Imperial College London

Department of Chemical Engineering and Chemical Technology

Characterisation of Organic Solvent Nanofiltration Membranes

By

Joanna Stawikowska

A thesis submitted in part fulfilment of the requirements for the degree of Doctor of Philosophy of Imperial College London and the Diploma of Imperial College London 2012

I certify that the work in this thesis is my own and that the work of others is appropriately acknowledged.

Abstract

Interests in application of organic solvent nanofiltration (OSN) technology based on synthetic membranes to molecular separation processes have been growing rapidly in recent years. The main classes of OSN flat sheet polymeric membranes are integrally skinned asymmetric (ISA) and thin film composite (TFC) membranes. A general goal of OSN membrane research is to improve membrane performance for specific non-aqueous applications, or to develop new separation processes. Most of the time the research is performed *via* trial–and–error methods, leading to extension of development time and increase of costs. This is partially because the structure of OSN membranes, particularly the size of their permeation pathway is largely unknown.

The filtration characteristics are mainly determined by the membrane structure, which is dependent on various fabrication methods as well as polymer chemistry. However, a direct correlation between these factors has not been understood in detail, because the current characterisation techniques have limitations in studying polymer structures with dimensions at the macromolecular level. The pore size in nanofiltration (NF) membranes is believed to be less than 2 nm, which is a lengthscale at the edge of most available material characterisation techniques. For this reason, advanced methods to study the membrane morphology need to be explored or developed with the aim of elucidating the NF membrane structure, transport mechanisms, and to understand the relationship between the membrane structure and the separation characteristics.

These objectives guided the work to development of a nanoscale characterisation method based on imaging the porous regions *via* probing the NF pores with nanoparticles (NP). Given that the probes provide high electron contrast, it is possible to map the pores formed between the polymer entanglements in the transmission electron microscope (TEM). This technique measures the pore size *in situ*, thus, a membrane is characterised during its operational state. The pore size was found to correlate well with the solute rejection and flux measured for a range of ISA and TFC membranes. The pore size distributions were then used together with a pore–flow model to simulate rejection curves.

A further insight into the membrane structure, particularly the surface structure, was provided by atomic force microscopy (AFM), particularly phase imaging. This method was applied to characterisation of polymer packing at the membrane surface, leading to analysis of the correlations between the phase shift, filtration parameters and membrane preparation methods.

Acknowledgments

First and foremost, I would like to thank my supervisor Prof. Andrew Livingston for his guidance throughout my PhD studies. I thank him for teaching me the "hypothesis driven research", respecting time that passes faster than a PhD student usually thinks, and especially for encouraging me to search for solutions far beyond the borders of my knowledge. I believe this work would not be achieved without his support.

Special thanks are also given to Maria Jimenez Solomon, Dr Yogesh Bhole, Jeong Kim, Dr Mahmoud Ardakani, Ecaterina Ware, Hector García Baleon, who contributed to the shape of this work.

Several parts of this work were consulted with experts, to whom I would like to thank for priceless scientific advises, therefore, I acknowledge Prof. David McComb, Dr. Joao Cabral, Prof. David Gidley, Prof. Ricardo García, Prof. José Calvo, and Dr Bart Hoogenboom.

I wish to also thank my colleagues from the research group, Dr Ludmila Peeva, Dr Iwona Soroko, Humera Siddique, Marcin Makowski, and Dr Sairam Malladi for their constant support, lengthy discussions and teaching me the experimental methods.

I wish to acknowledge the 7th Framework Programme of the European Commission's Marie Curie Initiative (NEMOPUR project, grant no. 214226-2) which enabled conduction of this work.

I would also like to express my deepest gratitude to my friends, family, especially my parents, ciocia Bogusia and wujek Marian, and Kuba for giving me their support, love and friendship.

Publications

Parts of this thesis have been published or are under revision for a publication:

J. Stawikowska, A. G. Livingston, **Nanoprobe imaging molecular scale pores in polymeric membranes**, Journal of Membrane Science, 413-414 (2012) 1-16

J. Stawikowska, A. G. Livingston, **Assessment of atomic force microscopy in characterisation of nanofiltration membranes**, Journal of Membrane Science, 425–426 (2012) 58-70

J. Stawikowska, M. F. Jimenez Solomon, Y. Bhole, A. G. Livingston, **Nanoparticle contrast agents to elucidate the structure of thin film composite nanofiltration membranes**, Submitted to Journal of Membrane Science

J. Stawikowska, J. F. Kim, A. G. Livingston, **Pore–flow calculations based on pore size distributions in polyimide membranes determined by a nanoprobe imaging technique**, Submitted to Chemical Engineering Science

Contents

Abstract **3**

Acknowledgments **4**

Publications **5**

Contents **6**

List of figures **10**

List of tables **12**

Nomenclature **13**

CHAPTER 1 ..... **17**

1. Literature review **17**

1.1 Organic solvent nanofiltration 18
1.2 Membrane formation and morphology 19
1.2.1 Membrane formation 20
1.2.1.1 Integrally skinned asymmetric membranes 20
1.2.1.2 Thin film composite membranes 22
1.2.2 Membrane morphology 25
1.2.2.1 Multi-layer morphology of integrally skinned asymmetric membranes 25
1.2.2.2 Morphology of thin film composite membranes 26
1.2.2.3 Nodules and pores 27
1.2.2.4 Macrovoids 29
1.3 Nanofiltration transport 30
1.3.1 Membrane filtration characteristics 30
1.3.2 Transport models 31
1.3.2.1 Solution–diffusion model 32
1.3.2.2 Pore–flow model 33
1.3.2.3 Log-normal pore size distribution 33
1.3.2.4 The extended Nernst–Planck pore–flow model 34
1.4 Nanostructural characterisation of nanofiltration membranes 38
1.4.1 Atomic force microscopy 39
1.4.1.1 Principles of atomic force microscopy 40
1.4.1.2 Microscope resolution 41
1.4.1.3 Phase imaging 42
1.4.1.4 Application of atomic force microscopy to membranes 45
1.4.2 Transmission electron microscopy 48
1.4.2.1 Contrast formation in transmission electron microscopy 49
1.4.2.2 Transmission electron microscopy characterisation of polymeric membranes 52
1.4.3 Positron annihilation lifetime spectroscopy 55

1.4.3.1 Principle of positron annihilation lifetime spectroscopy 56
1.4.3.2 Application of positron annihilation lifetime spectroscopy to membranes 57
1.4.4 Liquid–liquid displacement porosimetry 59
1.4.4.1 Principle of liquid–liquid displacement porosimetry 60
1.4.4.2 Pore size measurement in membranes 61
CHAPTER 2 63
2. Research motivation and strategy 63
CHAPTER 3 68
3. Development of nanoprobe imaging technique 68
3.1 Summary 68
3.2 Materials and methods 70
3.2.1 Membrane preparation 70
3.2.2 Dense film preparation 70
3.2.3 Estimation of P84 co-polyimide molecular weight 71
3.2.4 Membrane functional performance 71
3.2.5 Solute size calculations 72
3.2.6 Preparation of osmium dioxide nanoparticles 72
3.2.7 Sample preparation for TEM imaging 73
3.2.8 TEM imaging and analysis 73
3.3 Results and Discussion 74
3.3.1 Chemical structure of P84 co-polyimide 75
3.3.2 Nanofiltration performance 75
3.3.3 Characterisation of nanoparticle probes 77
3.3.4 Probing the nanopores 82
3.3.5 Electron microscopy projection mechanisms 84
3.3.6 Skin layer thickness 88
3.3.7 Mapping of polymer porous phases 91
3.3.8 Effect of specimen thickness on imaging contrast 94
3.3.9 Pore size estimation 95
3.3.10 Consideration of molecular architecture of membrane separating layer 100
3.3.11 Solute transport through membrane M1 101
3.4 Conclusions 104
CHAPTER 4 105
4. Assessment of the pore–flow model 105
4.1 Summary 105
4.2 Materials and methods 106
4.2.1 Membranes: preparation and filtration tests 106
4.2.2 Filtration of OsO_2 and Au nanoparticles 106
4.2.3 Inductively coupled plasma mass spectrometry 107
4.2.4 TEM imaging of Os and Au nanoparticles 107
4.2.5 Pore–flow model 107

4.3 Results and discussions 108
4.3.1 Pore flow rate calculations based on the pore size distribution and the skin layer thickness measured by the nanoprobe imaging technique 108
4.3.2 Rejection calculation based on the pore size distribution 112
4.3.3 Discrete approach 115
4.3.4 Particle size analysis in permeate 120
4.3.5 Continuous approach 124
4.3.6 Comparison of the computed rejection with the experimental measurements 126
4.4 Conclusions 129
CHAPTER 5 130
5. Characterisation of thin film composite membranes 130
5.1 Summary 130
5.2 Materials and methods 131
5.2.1 Membranes 131
5.2.1.1 Support preparation for coating with PTMSP 131
5.2.1.2 Preparation of PTMSP/P84 composite membrane 131
5.2.1.3 Preparation of PA/P84 composite membranes 132
5.2.2 Membrane functional performance 132
5.2.3 Preparation of OsO_2 nanoparticles 133
5.2.4 Filtration of OsO_2 nanoparticles 133
5.2.5 TEM imaging 134
5.2.6 Scanning electron microscopy 134
5.3 Results and discussions 135
5.3.1 Chemical structure and properties of polymers comprising the TFC membranes 135
5.3.2 Functional performance of TFC membranes 136
5.3.3 Membrane permeation with OsO_2 nanoparticles 138
5.3.4 Structural characterisation of TFC layer 141
5.3.4.1 PTMSP/P84 composite membrane 142
5.3.4.2 PA/P84 composite membrane 143
5.3.5 Pore size distribution 146
5.3.6 Relationship between the pore size and nanofiltration performance 150
5.3.7 Detection of nanoscale defects 151
5.4 Conclusions 154
CHAPTER 6 155
6. Assessment of atomic force microscopy for characterisation of nanofiltration membranes 155
6.1 Summary 155
6.2 Materials and methods 157
6.2.1 Membrane preparation 157
6.2.2 Nanofiltration experiments 158

6.2.3 AFM characterisation 158
6.2.3.1 AFM set-up 158
6.2.3.2 Surface roughness analysis 159
6.2.3.3 Nodule size measurement 159
6.2.3.4 Pore size measurement 160
6.2.3.5 Phase image analysis 160
6.3 Results and discussion 161
6.3.1 Nanofiltration performance 161
6.3.2 Surface topography 162
6.3.2.1 Roughness analysis 162
6.3.2.2 Nodule size measurement 164
6.3.2.3 Questionable pore size measurements 169
6.3.3 Correlation of surface topography with nanofiltration performance 172
6.3.4 Analysis of phase images 173
6.3.5 Correlation of phase lag with nanofiltration performance 181
6.4 Conclusion 182
7. Conclusions and future directions 184
References 191

List of figures

Figure 1.1 Filtration spectrum of membranes. 17
Figure 1.2 Two types of membranes used in OSN. 19
Figure 1.3 Membrane formation process. 21
Figure 1.4 Schematic of the interfacial polymerisation process. 23
Figure 1.5 SEM images of a P84 co-polyimide membrane revealing the multi-layer structure. 26
Figure 1.6 TEM image of cross-section of the composite PA film supported by a polysulfone microporous membrane. 27
Figure 1.7 Schematic representation of formation of interconnected clusters and nodules. 29
Figure 1.8 Schematic representation of molecular transport through a membrane. 32
Figure 1.9 Diagram of AFM during scanning the sample surface. 41
Figure 1.10 Electron–optical system and contrast formation mechanisms in TEM. 51
Figure 1.11 TEM image of cross-section of the assymetric P84 co-polyimide membrane. 54
Figure 1.12 TEM image of the Pt–C replica of the surface of the assymetric cellulose acetate membrane. 55
Figure 1.13 Principle of depth–profile PALS applied to assymetric membranes. 58
Figure 1.14 Schematic representation of pore types. 60
Figure 1.15 Scheme of the set-up used in liquid–liquid displacement porosimetry. 61
Figure 3.1 SEM image of asymmetric membrane. 74
Figure 3.2 Molecular structure of P84 co-polyimide. 75
Figure 3.3 NF performance of P84 co-polyimide membranes. 76
Figure 3.4 OsO_2 NP fabrication and probing the nanopores. 78
Figure 3.5 TEM characterisation of OsO_2 NP stabilised with PS in various solvents. 80
Figure 3.6 Conceptual model of the membrane structure with lodged NP and the corresponding projection. 83
Figure 3.7 Diagrams of possible particle arrangements in the 3–D polymer blocks sampled from the membrane cross-sections, and their corresponding high magnification projections. 86
Figure 3.8 Measurement of the skin layer thickness. 90
Figure 3.9 TEM images of skin layer cross-sections. 93
Figure 3.10 Effect of the specimen thickness on image contrast. 95
Figure 3.11 Nanoporous structure of the skin layer cross-sections and the pore size distributions. 97
Figure 3.12 Cross-sectional morphologies and corresponding 2D–FFT power spectra. 99
Figure 3.13 2–D FFT power spectra analysis. 101
Figure 3.14 Separation of OsO_2 NP using membrane M1. 103
Figure 4.1 Flow rate distributions. 109
Figure 4.2 Distributions of the fractional pore flow rate calculated using the pore size (diameter) measured by TEM. 111

Figure 4.3 Flow charts representing calculation methodology in the discrete and continuous simulations. 113
Figure 4.4 PS molecular diameter in relation to MW in toluene. 115
Figure 4.5 Overall PS rejections calculated in the discrete approach methods using the bulk solvent viscosity (μ_0), and the solvent viscosity corrected to pore viscosity ($\mu_{p,i}$). 118
Figure 4.6 Size and rejection of OsO_2 NP. 121
Figure 4.7 Cross-sectional TEM image of membrane M3 after filtering with Au NP. 123
Figure 4.8 Overall PS rejection estimated using the integration function and the log-normal pore size distribution computed based on the pore size distribution measured by the nanoprobe imaging technique. 125
Figure 4.9 Comparison of computed particle rejections based on PDF and r_{max} with plots of the experimental particle rejection. 128
Figure 5.1 Chemical structures. 136
Figure 5.2 Rejection curves of TFC membranes. 137
Figure 5.3 Permeability measurements of feeds containing OsO_2 NP in comparison to a pure solvent. 139
Figure 5.4 Electro-micrographs of PTMSP/P84 composite membrane. 143
Figure 5.5 Electro-micrographs of PA/P84 composite membrane. 145
Figure 5.6 TEM cross-sectional images of composite separation layers probed from the surface side of the membranes. 147
Figure 5.7 High magnification TEM cross-sectional images of the composite separation layers. 148
Figure 5.8 Measured pore size distribution in the composite layers. 149
Figure 5.9 Correlation of solute rejection with pore size. 151
Figure 5.10 TEM cross-sectional images of the membranes probed with OsO_2 NP to detect the nanoscale defects. 152
Figure 6.1 Electro-micrographs of the CNT tip supplied by Nanosensors™. 158
Figure 6.2 Rejection curves of membranes M4, M5 and M6 in acetone. 162
Figure 6.3 AFM topographical images revealing changes in the nodular structure. 167
Figure 6.4 Nodule size analysis. 168
Figure 6.5 Pore size measurements analysis and possible misinterpretation. 171
Figure 6.6 The pore size correlation graphs. 172
Figure 6.7 Correlation of the surface topography with NF performance. 173
Figure 6.8 Analysis of the phase images. 176
Figure 6.9 Attractive–region phase images 179
Figure 6.10 Energy dissipation analysis. 180
Figure 6.11 Data determined from the phase images versus NF performance. 181

List of tables

Table 3.1 Solvent physico-chemical parameters and solubility difference values between solvent and polystyrene (at 25°C) 81
Table 3.2 Summary of the quantitative features acquired by the nanoprobe imaging technique 98
Table 4.1 Integrated average pore flow rate calculated from the fractional pore flow rate histograms. 110
Table 4.2 Estimations of the molecular diameter of PS oligomers solvated in toluene 114
Table 4.3 Estimated membrane porosity from Equation 4.10 120
Table 4.4 Size and concentration analysis of Au and OsO_2 NP in permeate 123
Table 5.1 Summary of the NF performance parameters 138
Table 5.2 Permeability of a solvent containing OsO_2 NP in comparison to a pure solvent measured at the permeated volume of 50 mL 141
Table 6.1 Membrane nomenclature and dope solution composition. 157
Table 6.2 NF membrane characteristics 162
Table 6.3 A quantitative summary of the surface roughness 164
Table 6.4 Numerical summary of the estimated values of median and mean of the nodule surface area and the mean diameter. 169
Table 6.5 Surface phase lag analysis 177
Table 6.6 Attractive mode phase image analysis 179

Nomenclature

Abbreviations

AFM	Atomic force microscopy
Au	Gold
BET	Burnauer, Emmett and Teller
C–C	Carbon–carbon
CCD	Charge–couple device
CNT	Carbon nanotube
DMF	Dimethylformamide
DMSO	Dimethyl sulfoxide
ESEM	Environmental scanning electron microscopy
FFT	Fast Fourier transform
ICP–MS	Inductively coupled plasma mass spectrometry
IPA	Isopropanol
LLDP	Liquid–liquid displacement porosimetry
MF	Microfiltration
MW	Molecular weight
MWCO	Molecular weight cut-off
NF	Nanofiltration
NMP	N-methyl-2-pyrrolidone
NP	Nanoparticles
Os	Osmium
OSN	Organic solvent nanofiltration
OsO_2	Osmium dioxide
OsO_4	Osmium tetroxide
PA	Polyamide
PALS	Positron annihilation lifetime spectroscopy
PAN	Polyacrylonitrile
PDF	Probability density function
PDMS	Polydimethylsiloxane
PEG	Polyethylene glycol
PIM	Polymers with intrinsic microporosity
PS	Polystyrene
PSD	Power spectral density
Pt–C	Platinum – carbon
PTMSP	Poly(1-trimethysilyl-1-propyne)
RO	Reverse osmosis
SEM	Scanning electron microscopy
SRNF	Solvent–resistant nanofiltration

THF	Tetrahydrofuran
UF	Ultrafiltration
WAXS	Wide angle x-ray scattering

Symbols

$_i$	Subscript *i* refers to pore
$_j$	Subscript *j* refers to solute
$A(\omega)$	Cantilever tapping amplitude
A_0	Cantilever free amplitude
A_m	Membrane filtration area
C	Constant equal to 2.8 mg cm^{-2} kV^{-n}
c	Speed of light
c_f	Total solute concentration in feed
$count_i$, $count_{total}$	Number of analysed pores in pore–size–class, total number of analysed pores
$count_{p,i}$, $count_{f,i}$	Number of analysed particles in (permeate) particle–size–class, number of analysed particles in (feed) particle–size–class
$count_{p,total}$, $count_{f,total}$	Number of analysed particles in permeate, number of analysed particles in feed
$c_{p,i}$, $c_{p,j}$	Porewise solute concentration in permeate, solute concentration in permeate
$c_{p,total}$, $c_{f,total}$	Concentration of particles in permeate, concentration of particles in feed
$c_{r,j}$	Solute concentration in retentate
C_s	Spherical aberration
d	Specimen thickness
$d_{p,i}$	Pore diameter
d_{pol}	Polymer phase size
$D_{s,j}$	Solute diffusivity
d_{solv}	Solvent molecular diameter
E	Energy
E_{dis}	Dissipation energy
f_i	Ratio of number of pores in a pore–size–class to total number of pores
$f_R(r)$, $f_R'(r)$	Probability density function, finite probability density function
F_{ts}	Tip–surface net forces
H	Hamaker constant
I	Positron annihilation intensity
$J_{v,i}$	Volumetric flux
k	Boltzmann constant
K'	Coefficient related to nature of membrane in Darcy's law
k_s	Cantilever stiffness
l	Separation layer thickness (capillary length)
L	Permeability

l_d	Spatial resolution
l_{xy}	Lateral resolution
M_{solv}	Solvent molecular weight
Mw_j	Solute molecular weight
n	Constant equal to1.7
n_{e0}	Electron–optical index of refraction
N_i, N_{total}	Number of pores in a pore–size–class, total number of pores (area = 0.0014 m^2)
$P_{e,i}$	Peclet number
Q	Quality factor
q	Wavenumber
Q_{m_exp}	Experimental membrane flow rate (area = 0.0014 m^2)
q_{max}	Wavenumber of Fourier peak with the highest intensity
Q_{p_av}, $Q_{p_av_corr}$	Integrated average pore flow rate (bulk viscosity), integrated average pore rate (corrected pore viscosity)
$Q_{p,i}$, $Q_{pf,i}$	Pore flow rate, fractional pore flow rate
R	Tip radius of curvature
r^*	Mean pore radius
R_a	Average roughness
r_e	Electron radius
R_i, R_j	(Porewise) solute rejection, overall solute rejection
R_j^{exp}, R_j^{cal}	Experimental solute rejection, calculated solute rejection
R_{ku}	Surface kurtosis
r_{max}	Maximum radius of a solute/particle
$r_{p,i}$, r	Pore radius of a pore–size–class, pore radius
R_q	Root–mean–square roughness
$r_{s,j}$, $d_{s,j}$	Solute molecular radius, solute molecular diameter
R_{sk}	Surface skewness
R_z	Peak–to–valley height
s_p	Pooled standard deviation
S_y	Band width for rejection estimation
T	Temperature
t	Time
T_g	Glass transition temperature
V_f	Feed volume
$V_{m,j}$	Solute molar volume
V_p	Permeate volume
V_r	Retentate volume
z	Instantaneous tip position
z_c	Tip–sample distance
$\overline{Z}$	Depth of implantation energy

Greek symbols

γ	Interfacial tension
ΔE	Change in electron energy
Δh	Height difference between the highest points of adjacent features
δh_r	Vertical resolution
ΔP	Transmembrane pressure
Δr	Thickness of electron matrix
$\Delta \varphi$	Phase shift
ε	Porosity
λ_e	Electron wavelength
μ_0 , $\mu_{p,i}$	Solvent bulk viscosity, solvent viscosity in a pore
ξ	Image characteristic lenghtscale
ρ_0	Homogenous density of electron matrix in a pore
σ	Standard deviation
τ	Positronium lifetime
ϕ	Dimensionless solvent parameter in the Wilke–Chang equation
φ	Phase angle
ω	Cantilever driving frequency
ω_0	Cantilever resonance frequency
γ	Interfacial tension

Introduction

CHAPTER 1

1. Literature review

Membranes are an established separation technology in many industries such as wastewater treatment [1], desalination [2, 3], food production [4], gas separation [5], and recently in the synthesis of pharmaceuticals [6, 7] and the petrochemical purification [8, 9]. The membrane filtration spectrum (Figure 1.1), depending on the membrane pore size and the filtrate size, ranges from reverse osmosis (RO), nanofiltration (NF), ultrafiltration (UF) and microfiltration (MF). This thesis focuses on synthetic NF membranes and the detailed reviews on various membranes can be found in the literature [10, 11]. Polymeric NF membranes are important in molecular processes such as adsorption [12], template synthesis [13], catalysis [14, 15], or membrane permeation and separation [15-17]. Organic solvent nanofiltration (OSN), although a relatively young membrane technology, has already been well established in several industries and academic research centres.

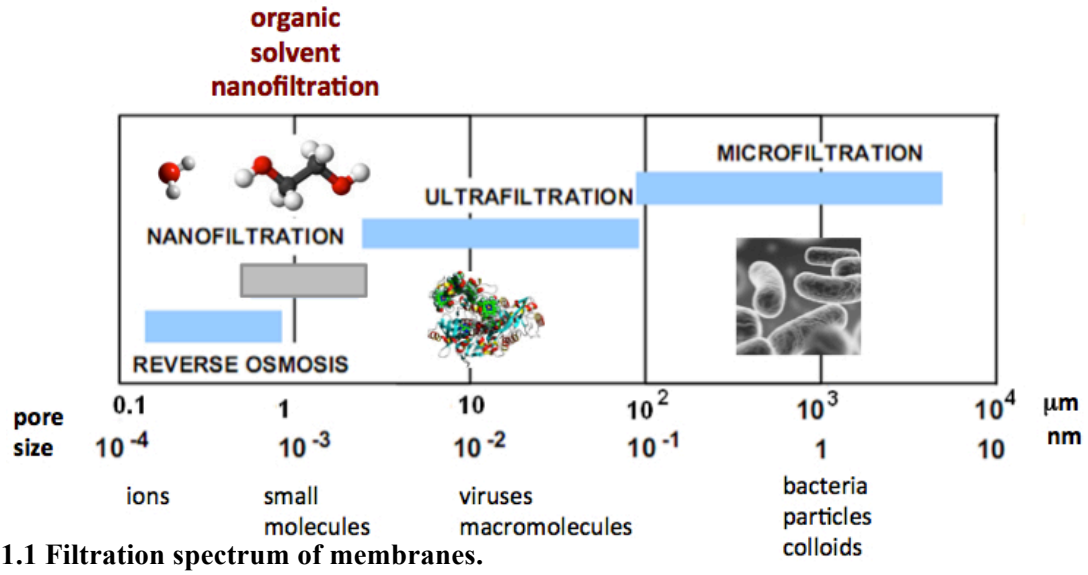


Figure 1.1 Filtration spectrum of membranes.

1.1 Organic solvent nanofiltration

OSN is a pressure driven process used to remove solutes, with molecular weights (MW) in the range 200 – 1000 g mol^{-1} from organic solvent feeds [18, 19]. An alternative terminology often encountered in the literature is solvent–resistant nanofiltration (SRNF). This emerging technology has been attracting interest among several industries as it offers significant savings in energy consumption in comparison to thermal processes such as distillation, which in addition may cause product degradation [20, 21]. The number of membranes developed for OSN has been constantly growing. The first commercial membranes became available in the mid 1990's followed by a rapid growth in a number of failed patents and academic publications on membranes and processes for OSN [18].

Both organic and inorganic membranes are used for filtrations in non-aqueous systems. These membranes can be produced as flat sheets or hollow fibres. Extensive reviews on membrane materials, which are stable in organic solvents, are available elsewhere [19, 22]. For the purpose of the experimental work described in this thesis, the background information is limited to flat sheet polymeric membranes.

1.2 Membrane formation and morphology

Fabrication of NF membranes, to achieve a specified performance, remains a challenging research goal for membrane technology. NF membranes require a nanostructure capable of molecular separation, which necessitates controlled generation of macromolecular architectures building the top separation layer. During the membrane formation process, polymer chains are formed into various nanostructures through the interfacial polymerisation reaction, coating, or phase inversion. The resulting architecture is strongly dependent on fabrication methods and polymer chemistry.

The main classes of flat sheet polymeric membranes used in OSN are integrally skinned asymmetric (ISA) (also termed as phase inversion or asymmetric membranes), and thin film composite (TFC) membranes. ISA membranes are composed of the same polymer and possess an asymmetric structure where the skin layer is present on top of the membrane (Figure 1.2a). TFC membranes consist of a microporous support and a thin film formed from a different polymer on top of the support (Figure 1.2b). Two of the crucial requirements for an OSN membrane material are stability in an organic solvent medium, and in contact with feed components. The other conditions include thermal stability, reliable purity grades for applications to food or pharmaceuticals, manufacturing price, ability to form a module from the membrane, resistance to compaction and fouling, reproducibility, and filtration performance [18, 19].

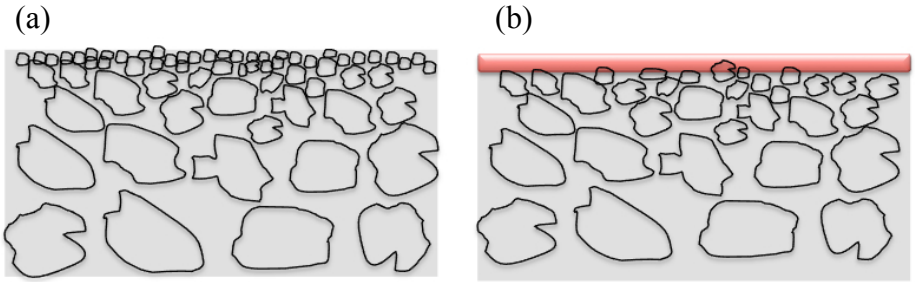


Figure 1.2 Two types of membranes used in OSN.
(a) Integrally skinned asymmetric membrane. (b) Thin film composite membrane.

1.2.1 Membrane formation

1.2.1.1 Integrally skinned asymmetric membranes

The ISA membrane, formed *via* phase inversion, is microporous and "open" on the side adhering to a non-woven backing. The polymer density gradually increases from the microporous side towards the "tight" surface side, where a skin layer is formed. The structure of the skin layer, interchangeable referred to as the separation layer, determines the NF performance [23, 24].

To prepare a membrane, a film of polymeric "dope" solution is cast on a non-woven backing, and then typically immersed in a non-solvent medium. The polymer in solution undergoes phase inversion, whereby the chains fold themselves into certain structures in order to reach more thermodynamically favourable configuration in reaction to solvent – non-solvent exchange [23, 24]. The phase inversion of ISA polymeric membranes can be induced by the following mechanisms: quenching, immersion in a non-solvent bath (immersion precipitation), solvent evaporation, or exposing the polymer film to non-solvent vapours [23]. Phase inversion through immersion precipitation, developed by Loeb and Sourirajan [25], is the most studied and used method for formation of ISA membranes and supports for TFC membranes. The first cellulose acetate membranes developed for desalination *via* RO in the early 60's became a base for development of the subsequent generations of ISA membranes.

The research focus in this work is on membranes prepared from P84 co-polyimide, which is a commercially available polymer with a glass transition temperature (T_g) of 331°C [26]. The P84 co-polyimide membranes posses superior performance in solvents such as toluene, methanol, ethyl acetate, and after crosslinking with 1,6 hexanediamine, even in dimethylformamide (DMF), N-methyl-2-pyrrolidone (NMP) and tetrahydrofuran (THF) [27, 28]. These membranes are relatively straightforward to produce as flat sheets, to crosslink, or to build

into a module [27, 28]. An important property is the ability to control the molecular weight cut-off (MWCO), defined as MW of a solute rejected by a membrane at 90%. By changing the dope solution composition membranes possessing different MWCOs in the range 200 – 1200 g mol^{-1} can be produced [29]. In addition to good separation properties, the membranes achieve high permeabilities; for instance, DMF permeability in the range 1 – 8 L m^{-2} h^{-1} bar^{-1} was measured after 120 h of continuous filtration [27].

To prepare a P84 co-polyimide membrane, typically, the dope solution comprising 18 – 26% (w/w) of the polymer dissolved in solvent such as NMP, dimethyl sulfoxide (DMSO) or DMF with the addition of a co-solvent such as 1,4 dioxane, acetone or THF, is cast on e.g. polyester or polypropylene backing material, followed by immersion in a water coagulation bath (Figure 1.3) to induce phase inversion [27, 29, 30]. During phase inversion, the polymer rich phase forms a membrane matrix, and the polymer lean phase transforms into pores. The process is mainly determined by kinetics of the liquid–liquid demixing, *i.e.* an exchange of a solvent by a non-solvent [31].

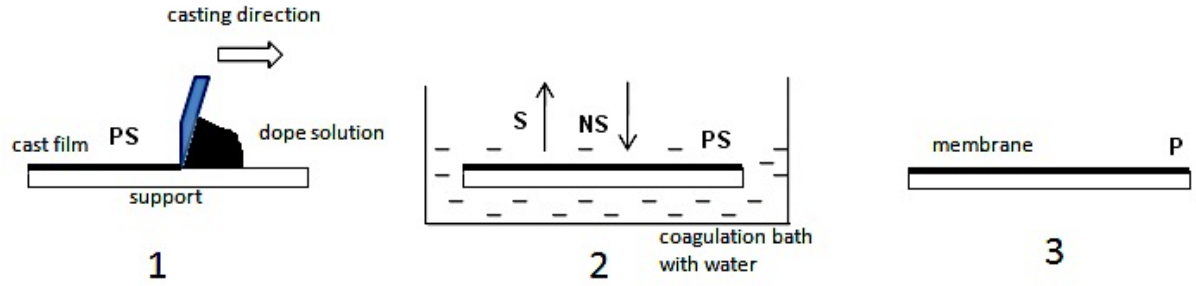


Figure 1.3 Membrane formation process.

1) Polymer solution (PS) is cast on a support material, 2) cast film immersed in coagulation bath where solvent (S) is exchanged with non-solvent (NS), 3) solidified polymer (P) film.

Soroko *et al.* [30] showed through experiments coupled to an evaporation–diffusion model that the skin layer thickness is related to the evaporation time of a volatile co-solvent. The longer the evaporation time, the thicker the skin layer formed, and thus the lower the flux was observed. The evaporation time, however, was not correlated with the solute rejection, and the

factors such as kinetics of the liquid–liquid demixing process and the mutual solubility parameters of a solvent, polymer, and a non-solvent were responsible for NF separation properties of the polyimide–based membranes.

The skin layer is tighter if the diffusion ratio of a solvent to a non-solvent is higher [32]. This effect can be explained at the macromolecular level. In a "poor" solvent, at low affinity of system is unstable [33], and so the solvent can leave the polymer film faster, leading to an increase in density of the skin layer. Studying the ternary phase diagram also helps to understand the skin layer formation by analysis of the miscibility region where the instantaneous liquid–liquid demixing takes place. At low miscibility of a solvent with a non-solvent, the liquid demixing is delayed and as a result the tighter polymer structure is formed [34]. The other phase inversion factors having an impact on the membrane structure include the type of non-solvent in which polymer solution precipitates, supersaturation conditions, temperature, humidity or additives [34, 35].

1.2.1.2 Thin film composite membranes

The second type of NF membranes, widely used for both aqueous and non-aqueous applications, is the TFC membrane. These membranes were developed as a follow-up to the phase inversion asymmetric membranes to meet demand in the growing desalination industry in the 80's [3]. One of the most important developments in this area was introduction of the interfacial polymerisation methods by Cadotte [36, 37]. The RO membranes produced by this technique dramatically improved the salt rejections performance and fluxes in comparison to ISA membranes [10]. In the interfacial polymerisation, as illustrated in Figure 1.4, the microporous membrane (e.g. polysulfone) is coated with an aqueous amine (*i.e.* reactive pre-polymer) solution that impregnates the surface pores, followed by immersion in a water–immiscible solution comprising reactant molecules such as acid chloride. The amine reacts with

acid chloride at the interface of the two immiscible liquid phases leading to polymerisation and formation of the highly crosslinked polymer network. The resulting composite film is very thin and highly crosslinked, thus it achieves high permeation rates of water and it is able to retain salt or other small molecules.

Permeability is also strongly related to surface chemistry, for instance a hydrophilic surface is required for RO applications [38], whereas a hydrophobic surface would be preferred for some of the non-aqueous systems [39]. Furthermore, to achieve high fluxes, a high surface area and porosity is required [40, 41]. Selectivity at the NF or RO level is directly related to internal packing of the molecular network, thus, often various monomers are tested in the interfacial polymerisation reaction to optimise the selectivity [16]. One of the most successful TFC membranes formed *via* interfacial polymerisation, was the one developed by Cadotte at FilmTec. The salt rejection of a single–pass of seawater was 99.5% with very high water fluxes [42]. This membrane was produced by reaction of phenylenediamine with trimesoyl chloride.

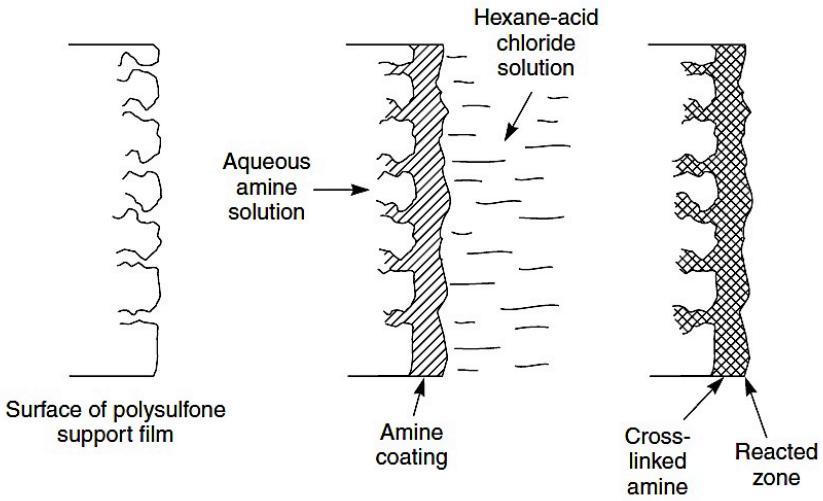


Figure 1.4 Schematic of the interfacial polymerisation process.

Surface of the microporous support membrane is coated with an aqueous amide solution followed by immersion in a hexane acid solution to induce polymerisation at the interface of two immiscible solutions resulting in formation of a densely crosslinked polyamide film. Adapted from [43].

Recently Jimenez Solomon *et al.* [44] developed a novel TFC polyamide (PA) composite membrane for OSN applications in solvents such as DMF, THF, methanol, and toluene. Good membrane performance in these organic solvents was possible due to performing the interfacial polymerisation reaction on top of the crosslinked P84 co-polyimide UF membrane. The post-treatment involving flushing with DMF, dramatically improved fluxes without compromising rejection, owing to dissolving the less crosslinked hydrogel-like layer; hence, the resistance to permeation was reduced without affecting the structure of the densely crosslinked separation layer.

TFC membranes can be also produced by coating a polymer solution *via* dip coating, spin coating or casting a diluted volatile solution containing a polymer on surface of a microporous support [45-48]. After solvent evaporation, a film of several microns thick is formed. The microporous support needs to be carefully chosen, as it greatly contributes to transport resistance, and thus it is recommended for an uncoated support that it has a flux of at least 10 times higher than the final composite membrane. Furthermore, the support membrane also needs to be finely porous to preserve the structure of the thin composite layer under high pressures [10]. The most successful solution–coated TFC membranes developed for non-aqueous applications are polydimethylsiloxane (PDMS) coated on polyimide (Matrimid 5218) or polyacrylonitrile (PAN) membranes [47, 49], or poly(1-trimethysilyl-1-propyne) (PTMSP) coated on PAN support [50]. Other polymers used as materials to form a composite layer include: polyacrylic acid, polyurethane, polyvinyl alcohol, polyethylene imine, polyphenylene oxide, or polyvinylidene fluoride. The properties of these materials and other advanced polymers are reviewed elsewhere [16, 19]. Silicone rubber coated membranes such as PDMS/PAN attracted lots of interest due to high fluxes of organic solvents permeating through highly swollen PDMS. Therefore, the swelling properties of PDMS, characterised with aid of the polymer–solvent solubility parameters, are related to the magnitude of the permeation flux, often

described by the solution–diffusion model [10, 51-53]. In the PDMS membrane film there are no fixed pores, rather there are highly interconnected interstitial spaces formed due to high mobility of the chains [10], given that T_g is equal to –90°C [54].

PTMSP composite membranes were successfully utilised in OSN due to high free volume fraction, about 20 – 27% [55], hydrophobic and glassy nature with T_g of 280°C [56], and stability in organic solvents such as acetone, ethanol and methanol [50]. Owing to trimethylsilyl side-groups, the structure is bulky and rigid, and so it possesses high porosity within the macromolecular packing [57, 58]. PTMSP membranes were originally used for pervaporation of water/alcohol mixtures [59, 60] or for gas separation [61].

1.2.2 Membrane morphology

1.2.2.1 Multi-layer morphology of integrally skinned asymmetric membranes

See-Toh *et al.* [62] and Soroko *et al.* [35] characterised the OSN P84 co-polyimide membranes using scanning electron microscopy (SEM). The low magnification image of the entire cross-section (Figure 1.5a) reveals the typical structural asymmetry found in ISA membranes. The macrovoids, with a finger-like shape, are commonly observed morphological features. The images (Figure 1.5b,c) show a spongy, interconnected porous structure with densely packed nodules present within the top region of the membrane. The region near the surface, the skin layer, has the densest structure that determines the separation characteristics. The thickness of the skin layer in ISA P84 co-polyimide membranes has been roughly estimated to be 70 nm [63]. Underneath the skin layer, there is an intermediate transition layer [64], where the skin layer merges with the microporous open region. For this reason, it is not straightforward to pin point the exact border between the skin layer and the open region.

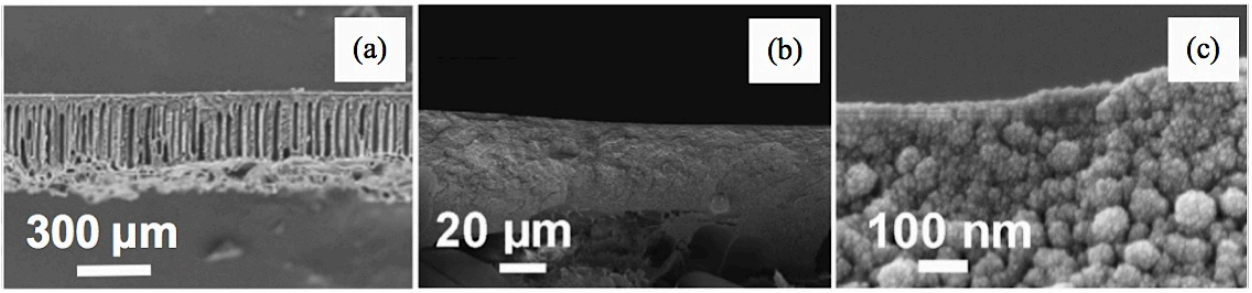


Figure 1.5 SEM images of a P84 co-polyimide membrane revealing the multi-layer structure.

(a) The entire membrane cross-section with a view of finger-like macrovoids (adapted from [35]). (b) Top region of the membrane cross-section where the skin layer is present, and (c) densely packed nodules and nodular aggregates. Adapted from [62].

1.2.2.2 Morphology of thin film composite membranes

The composite film, formed in the interfacial polymerisation reaction on top of a UF support, acts as the separation layer. Film formation is a complex process that involves controlling many reaction parameters, and thus alteration of any of the reaction factors, chemistry of reactants or the support material, leads to existence of different morphology across the composite film [65]. For this reason, elucidating the composite film structure is often an important research focus.

According to Freger and Srebnik [66] the structure of the PA film is non-uniform due to diffusion mechanisms taking place during the interfacial polymerisation. In this process, the reaction molecules polymerise into a densely crosslinked layer, *i.e.* the selective layer, at the interface of organic and aqueous solutions. As a result, this layer acts as a barrier hindering further diffusion of the reactant molecules, and so a less crosslinked and more permeable polymer network is formed on the outside of the highly crosslinked film, which then becomes a middle layer. For instance, the piperazine-based NF membrane has the thickness of the densely crosslinked layer about 20 – 50 nm, whereas the thickness of approximately 100 nm measures

the total interfacial film of this membrane. Owing to very thin active separation layer, there is low resistance across the film, thus the membrane can achieve high fluxes [67].

Pacheco *et al.* [68] described two types of structures of the PA composite film. The authors have found that the nanoscale morphology relates to the PA chemistry. If the PA interfacial layer is comprised from fully aromatic PA, the structure is heterogeneous with the ridge–and–valley type of surface (Figure 1.6a). If the PA chemistry is based on the semi-aromatic PA, the surface is smooth and it constitutes densely packed nodules (Figure 1.6b). The roughness of the film, composed of the fully aromatic PA, is very high; it reaches approximately 100 nm due to ridges and valleys. Separation takes place in the nodular-like compacted layer having the thickness 30 – 60 nm. The composite film formed from the polymerisation of the semi-aromatic PA is thinner, as it does not possess the ridge–and–valley structure. The thickness of the active layer measures only 40 nm and it constitutes of densely packed nodules.

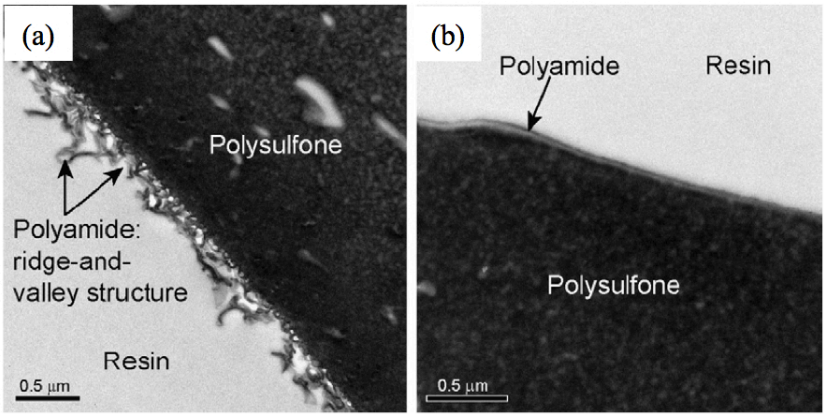


Figure 1.6 TEM image of cross-section of the composite PA film supported by a polysulfone microporous membrane.

(a) Ridge–and–valley structure of the PA film of the ESPA3 (RO) membrane (Hydranautics, US). (b) Nodular structure of the PA film of the NF270 (NF) membrane (Dow FilmTec, US). Adapted from [68].

1.2.2.3 Nodules and pores

Nodules are spherical features with diameters of well under 100 nm. They are formed from densely folded macromolecules, and often tend to aggregate into larger nodular clusters.

Finer nodules form the skin layer, whereas the larger aggregates build the membrane interior [69]. Although nodules are observed on the surface of both TFC and ISA membranes [69], in this review the interest is towards the nodular structures present in ISA membranes, as one of the objectives of the work, described in this thesis, is to study correlation of the nodule size with NF performance for a range of the P84 co-polyimide asymmetric membranes.

The first study on nodules in polymeric membranes was reported by Schultz and Asunmaa [70]. The authors analysed the nodular structures on surface of the ISA cellulose acetate membranes using transmission electron microscopy (TEM). Panar *et al.* [71] investigated in more detail the formation of nodules in cellulose acetate, PA and PA–hydrazide RO membranes. An innovative approach at that time was to freeze–dry the dope solutions and compare their morphologies with membrane cross-sections by TEM. The authors found that the specimens, *i.e.* the dope solutions and membranes, exhibited similar morphological characteristics; hence, they suggested that nodular micelles were pre-formed in the polymer dope solution from which the membranes were cast. They also deduced that the mass transport through the membrane occurred between the nodules, as in these regions, the polymer packing was believed to be less dense. Wienk *et al.* [23] described that the skin layer was built from densely packed folds or spheres of polymer chains formed into the nodular structures.

Wienk *et al.* [23, 72] have also suggested that nodules grow in response to simultaneous out-diffusion of a solvent and in-diffusion of a non-solvent. In this environment the macromolecules rapidly coil up and surround themselves with other polymer segments in order to reduce their contact surface area with the non-solvent. Under these conditions, the chains surround themselves and coil up forming segments of the nodular clusters, which are interconnected by entanglements of the adjacent nodules (Figure 1.7). On the surface of NF membranes, pores are formed within looser packing of the chains present between the nodules.

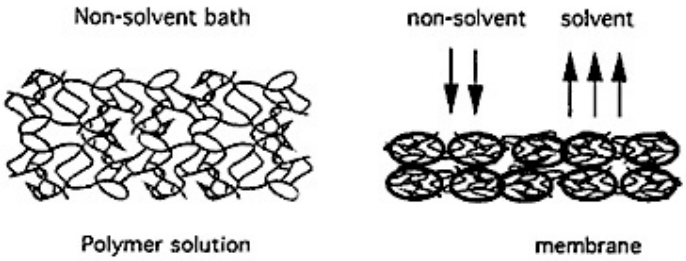


Figure 1.7 Schematic representation of formation of interconnected clusters and nodules.
In phase inversion the polymer chains tightly entangle leading to decrease of the interstitial spaces and formation of a dense nodular packing [23].

In a dense interfacial PA network, pores are formed between the chain segments constituting the macromolecular entanglements or between the macromolecular entanglements themselves [73, 74]. Furthermore, due to the highly crosslinked network, these pores tend to be non-interconnected [75, 76], and their size profile follows a bimodal size distribution [77].

1.2.2.4 Macrovoids

Macrovoids are finger-like large cavities that extend across the cross-section of ISA membranes (Figure 1.5a). In general, these features are considered undesirable as they may lead to decreasing mechanical strength, eventually resulting in membrane compaction [35]. Smolders *et al.* [78] postulated that the instantaneous liquid–liquid demixing was directly related to formation of the macrovoids. The macrovoids are formed due to rapid precipitation driven by large convective flows of a non-solvent towards the polymer film. To reduce the convective flows and minimise the macrovoid formation, the instantaneous demixing should be delayed. There are several methods used: increasing the polymer solution viscosity [62], selecting a non-solvent–solvent combination characterised by low miscibility between the liquids [79], or by adding inorganic fillers, *i.e.* additives, into the dope solution [35, 80].

1.3 Nanofiltration transport

1.3.1 Membrane filtration characteristics

Membrane performance is usually described by two parameters: solute rejection (R_j) (Eq. 1.1) and permeate flux (J_v) (Eq. 1.2):

$$R_j = \left(1 - \frac{c_{p,j}}{c_{r,j}}\right) \times 100\% \qquad \textit{Eq. 1.1}$$

$$J_v = \frac{V_p}{A_m t}, \qquad \textit{Eq. 1.2}$$

where $c_{p,j}$ and $c_{r,j}$ is concentration of a solute j in permeate and retentate, respectively. V_p is permeate volume, A_m is membrane filtration area, and t is time. Other useful parameters, used to describe membrane performance, are listed as following: permeability (L, Eq. 1.3), retention (Eq. 1.4) and mass balance (Eq. 1.5):

$$L = \frac{V_p}{P A_m t} \qquad \textit{Eq. 1.3}$$

$$\mathrm{Re}\,tention = \frac{c_{r,j} V_r}{c_{f,j} V_f} \times 100\% \qquad \textit{Eq. 1.4}$$

$$Mass\ balance = \frac{V_p c_{p,j} + V_r c_{r,j}}{V_f c_{f,j}} \times 100\% \qquad \textit{Eq. 1.5}$$

where P is feed pressure, $c_{f,j}$ is solute concentration in feed, V_r and V_f is volume of retentate and feed, respectively. A widely used membrane parameter is MWCO, which is defined as MW of a solute rejected by a membrane at 90%. In order to graphically describe the separation characteristics, the rejection curve is created. It is a plot of solute rejection in relation to solute

MW. In OSN tests, solute marker molecules such as alkenes, polyethylene glycols (PEG) or polystyrene (PS) oligomers are commonly used [81-83].

Because determination of the rejection curves using PEG or alkenes suffered from inconsistency due to linearity of the molecular structure of PEG and alkenes, See-Toh *et al.* [83] developed a method to characterise MWCO and selectivity of OSN membranes. The method was based on filtering a range of PS oligomers dissolved in an organic solvent and measuring solute concentrations using liquid chromatography. The main beneficiaries of this standardised test are membrane manufacturers, who use this method to optimise membranes that are under development, and end users who match a membrane to a particular process.

1.3.2 Transport models

Two models are used to describe transport of solutes through the NF membrane: solution–diffusion and pore–flow (Figure 1.8). In the solution–diffusion model, solutes diffuse through a membrane driven by a concentration gradient (Figure 1.8a). In the pore–flow model it is assumed that tiny fixed pores exist within the polymer matrix. Separation is achieved by "sieving" whereby solutes are excluded by a pore (Figure 1.8b); thus, rejection is directly related to the solute and pore size. In this work, the background information is rather focused on the pore–flow model, since the research described in this thesis is towards development of the pore probing technique. Nevertheless, the reader will be briefly introduced to the solution–diffusion model and provide the relevant literature.

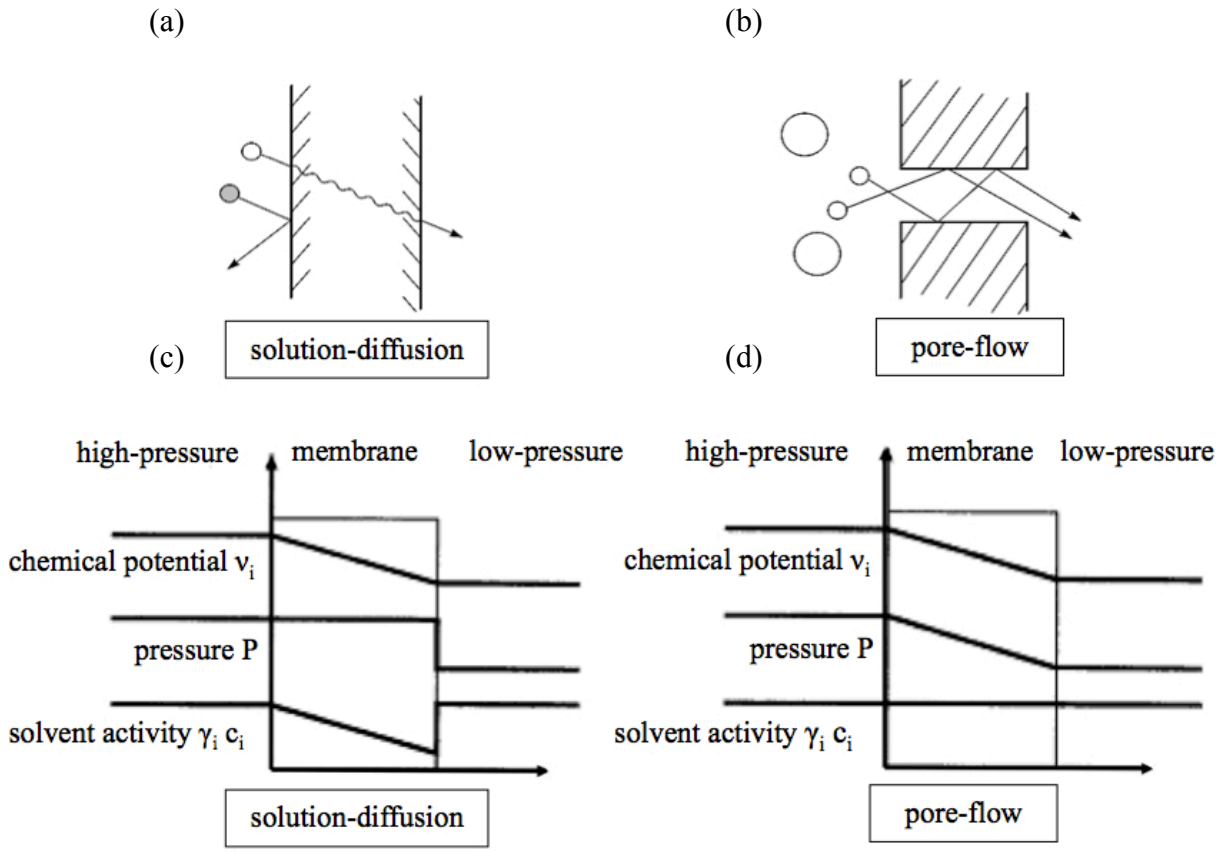


Figure 1.8 Schematic representation of molecular transport through a membrane.

(a) In the solution–diffusion transport a solute diffuses through a dense polymer network. (b) The pore–flow transport is based on the size–exclusion mechanism. (c) The driving force for the membrane transport in the solution–diffusion model is the concentration gradient (pressure is constant) (d) Driving force for the membrane transport in the pore–flow model is the pressure gradient (concentration is constant) [10].

1.3.2.1 Solution–diffusion model

The solution–diffusion model is based on the Fick's law of diffusion:

$$J_{v,j} = -D_j \frac{dc_j}{dx}, \qquad \textit{Eq. 1.6}$$

where $J_{v,j}$ is the flux of a compound j, D_i is the diffusion coefficient and dc_j/dx is the compound j concentration gradient. The minus sign indicates that the transport direction is down the concentration gradient. A membrane with the solution–diffusion transport is believed to possess highly interconnected free volume elements formed between the polymer chains, so the size of

the interstitial spaces is related to chain mobility. The solution–diffusion transport in membranes has been well described in the literature [84, 85].

1.3.2.2 Pore–flow model

The pore–flow model is based on the pressure–driven convective flow described by the Darcy's law:

$$J_{v,j} = K'c_j \frac{dP}{dx}, \qquad Eq.\ 1.7$$

where dP/dx is the pressure gradient through a porous membrane, c_j is the concentration of compound j and K' is a coefficient related to the nature of the medium [10]. The pore–flow model assumes that a membrane contains cylindrical fixed pores.

In the literature there are several models developed in the past that are still widely used today. Ferry's model, originally developed for UF membranes operating in aqueous systems, estimates retention of a spherical particle based on the pore and particle diameter. The model carries the assumption that the pores have uniform size and their shape is cylindrical [86]. The steric hindrance pore–flow model assumes that the rejection is calculated based on the pore diameter and the molecular size, under the assumption that all pores are uniform [87]. Zeman and Wales [88] developed further modifications of Ferry's model by implementing a parabolic velocity profile in the uniform cylindrical pores.

1.3.2.3 Log-normal pore size distribution

The main weakness in the aforementioned models is that they do not consider the realistic membrane structure, which is believed to comprise pores with various sizes represented by a continuous distribution such as the Gaussian or log-normal. Mochizuki and Zydney [89] have shown that there is a significant difference between values of the sieving coefficient

calculated for the Gaussian and log-normal pore size distributions. The subsequent review published by Zydney *et al.* [90] discussed various types of the log-normal probability density functions (PDF) used to describe the pore size distribution. It was concluded that the PDF proposed by Belfort *et al.* [91] was the most applicable, since it included the mean pore radius and the standard deviation. Van der Bruggen *et al.* [92] reported that the log-normal pore size distribution was the most applicable to predict the maximum retention of an organic molecule. Further work reported by Bowen and Welfoot [93] suggested truncating the log-normal PDF at the pore radius r_{max}. This operation was recommended to avoid integrating the rejection over the log-normal pore size distribution $(0 < r < \infty)$ up to infinity, since the small fraction of very large pores dominates the calculated overall rejection.

1.3.2.4 The extended Nernst–Planck pore–flow model

The extended Nernst–Planck pore–flow model, modified and described by Bowen and Welfoot with colleagues [94-97], was subsequently applied several times to the P84 co-polyimide membranes operating in organic solvents [27, 29, 62]. This model incorporates the pore size distribution described by the log-normal PDF. The computational formulas consider solvent–solute interactions by estimating the solute molecular diameter and the diffusivity in relation to a solvent medium. There are several publications in the literature suggesting that this model has been one of the most commonly chosen for predictive computations of OSN processes. It is assumed that the pore in a NF membrane is a capillary, and its diameter equals to pore size. In this case, the Hagen–Poiseuille equation defines the volumetric flux (J_v) on the assumption that a membrane constitutes of uniform capillaries [98]:

$$J_{v,i} = \frac{r_{p,i}^2 \Delta P \varepsilon}{8 \mu_0 l} , \qquad \textit{Eq. 1.8}$$

where ε is porosity, ΔP is the transmembrane pressure, l is capillary length, μ_0 is the solvent bulk viscosity, and $r_{p,i}$ is capillary radius. If a membrane possesses non-uniform pores described by the size distribution, sub-index i corresponds to a pore–size–class at which the volumetric flux is calculated using the above equation.

The porewise flow rate ($Q_{p,i}$) is calculated as following:

$$Q_{p,i} = \frac{\pi r_{p,i}^4 \Delta P}{8 \mu_0 l}. \qquad \textit{Eq. 1.9}$$

The former work described by Bowen and Welfoot [94] suggested that the solvent viscosity in a pore ($\mu_{p,i}$) varies with the pore radius according to the following formula:

$$\frac{\mu_{p,i}}{\mu_0} = 1 + 18\left(\frac{d_{solv}}{r_{p,i}}\right) - 9\left(\frac{d_{solv}}{r_{p,i}}\right)^2, \qquad \textit{Eq. 1.10}$$

where d_{solv} is the solvent molecular diameter. Then, the following set of equations is used to compute the overall solute rejection:

$$R_i = 1 - \frac{\Phi_i K_{c,i}}{1 - \left(1 - \Phi_i K_{c,i}\right)\left(\exp(-P_{e,i})\right)}, \qquad \textit{Eq. 1.11}$$

where Φ_i is a partition coefficient, and λ_i is a ratio between the solute and pore radius:

$$\Phi_i = \left(1 - \lambda_i\right)^2 \qquad \textit{Eq. 1.12}$$

$$\lambda_i = \frac{r_{s,j}}{r_{p,i}}; \qquad \textit{Eq. 1.13}$$

therefore, it is assumed that the steric behaviour between the solute and pore wall occurs. Then, the solute convective $K_{c,i}$ and diffusive $K_{d,i}$ hindrance factors are expressed as following:

$$K_{c,i} = \left(2 - \Phi_i\right)\left(1 + 0.054\lambda_i - 0.988\lambda_i^2 + 0.44\lambda_i^3\right) \qquad \textit{Eq. 1.14}$$

$$K_{d,i} = 1 - 2.3\lambda_i + 1.154\lambda_i^2 + 0.224\lambda_i^3. \qquad \textit{Eq. 1.15}$$

The Peclet number ($P_{e,i}$) characterising the pore flow is defined as:

$$P_{e,i} = \frac{K_{c,i}}{K_{d,i} D_{s,j}} \left(\frac{r_{p,i}^2 \Delta P}{8 \mu_{p,i}} \right). \qquad \textit{Eq. 1.16}$$

The diffusivity $D_{s,j}$ of a solute with the radius $r_{s,j}$ is calculated using the Stokes–Einstein equation [99]:

$$D_{s,j} = \frac{kT}{6\pi \mu_{p,i} r_{s,j}}, \qquad \textit{Eq. 1.17}$$

where k is the Boltzmann constant and T is temperature. The Stokes–Einstein equation was originally derived to estimate diffusivity of large spherical molecules in dilute solutions. To provide a diffusion coefficient to the above equation, the Wilke–Chang formula may be used to estimate the solute diffusivity [100]:

$$D_{s,j} = 7.4 \times 10^{-8} \frac{T \sqrt{\phi M_{solv}}}{\mu_{p,i} V_{m,j}^{0.6}}, \qquad \textit{Eq. 1.18}$$

where M_{solv} is MW of a solvent molecule, ϕ is a dimensionless solvent parameter, and V_m is the solute molar volume. The Wilke–Chang correlation was originally proposed for engineering purposes of estimating diffusivity in solvents of small molecules [100]. Further modifications of the Wilke–Chang formula have been subsequently performed [101, 102]. One must note that the correlation possesses an error of ~10% [100] or ~20% [103, 104], thus it may influence values of the calculated rejection. Furthermore, combining Eqs.1.17 and 1.18 may bring an additional error to solute size calculations since the Stokes–Einstein should be applicable for large molecules, whereas the Wilke–Chang correlation has been derived for use of small molecules. Nevertheless, the equations are encountered frequently in the membrane science literature to calculate the solute diffusivity and size in NF systems, either aqueous or non-aqueous [29, 105].

If rejection $R(r)$ is a continuous function of the pore radius r, PDF is introduced to describe the pore size distribuion ($f_R(r)$) [91, 93]:

$$f_R(r) = \frac{1}{r\sqrt{2\pi b}} \exp\left[-\frac{\left(\log(r/r^*) + b/2\right)^2}{2b} \right] \qquad \textit{Eq. 1.19}$$

$$b = \log\left[1 + \left(\frac{\sigma}{r^*} \right)^2 \right]. \qquad \textit{Eq. 1.20}$$

To calculate the function $f_R(r)$, the mean pore radius (r^*) and the standard deviation (σ) need to be known. Since PDF has a log-normal profile, the probability values are estimated for r rising up to infinity; therefore, in order to define a finite PDF for the pore radii $0 < r < r_{max}$, where r_{max} is an upper limit of the distrubution, a new PDF $f'_R(r)$ is to be employed by scaling the distribution:

$$\frac{f'_R(r)}{f_R(r)} = \frac{1}{\int_0^{r_{\max}} f_R(r) dr}. \qquad \textit{Eq. 1.21}$$

Now, the overall rejection over the pore radii $0 < r < r_{max}$ is calculated using the following expression [93]:

$$R_T = \frac{\int_0^{r_{\max}} f'_R(r) r^4 R(r) / \mu(r)\, dr}{\int_0^{r_{\max}} f'_R(r) r^4 / \mu(r)\, dr}. \qquad \textit{Eq. 1.22}$$

1.4 Nanostructural characterisation of nanofiltration membranes

Materials possessing pores smaller than 2 nm are known as microporous, whereas pores larger than 2 nm occur in mesoporous materials [16]. According to this definition, a NF membrane belongs to the group of microporous materials. It is challenging to characterise NF membranes, as the most important feature of interest, the pore size, is believed to be approximately 1 nm [94, 106]; hence, this is a lengthscale localised at the edge of the nanoscale (1 – 100 nm), and consequently the NF pores are often termed as 'nanopores'.

Mass transport in a NF membrane occurs through the permeation pathways such as fixed nanopores or interstitial free volume elements. However, there is no clear definition of the permeation pathway, since the structure of the NF membrane has not been elucidated in detail. It is common to describe a pore as a region where lower entanglement of the polymer chains is present [72]. For instance, in the interfacially polymerised PA network, pores or free volume elements exist between the polymer chains or between larger complexes of the entangled chains [73, 74]. In membranes prepared from polymers with intrinsic microporosity (PIM), the interconnected free volume elements act as the permeation pathways. The microporous structure is formed due to sites of contortion present in a rigid backbone [107]. In thermoplastic polymers such as PDMS, there are different types of permeation pathways. These are the interstitial spaces formed between the chains building the polymer matrix, which swell while in contact with an organic solvent or due to the temperature increase [33, 108]. This class of thermoplastic polymeric membranes are identified as the non-porous dense membranes [19].

In glassy polymers, where polymer chain configurations are fixed, and if the pore–flow transport is assumed, flux and rejection are believed to derive from the pore size, porosity, and thickness of the separation layer. These structural characteristics can be controlled by polymer type and membrane formation parameters [16, 106]. Therefore, progress in this area might lead

to a better control of the membrane formation *via* improvement in understanding the physical and functional properties.

Work on characterisation of the NF membrane structure has a long history. Previous studies used atomic force microscopy (AFM) [96, 97, 109-111], positron annihilation lifetime spectroscopy (PALS) [63, 112-114] and transmission electron microscopy (TEM) [64, 68, 71, 115, 116]. These techniques analyse a membrane in a dry state. Some attempts to image membranes using AFM in a liquid medium were performed by Johnson *et al.* [117]. In terms of *in situ* characterisation techniques, credit should be given to liquid–liquid displacement porosimetry (LLDP), a method developed to measure the pore size in UF membranes [110]. It is important to acknowledge several other membrane structural characterisation techniques such as Burnauer, Emmett and Teller (BET) gas adsorption–desorption [118-120], wide angle X-ray scattering (WAXS) [121, 122], mercury porosimetry [123], scanning electron microscopy (SEM) [64], environmental scanning electron microscopy (ESEM) [64, 124], or thermoporometry [125]. However, after a careful review of the literature, it has been assessed that PALS, AFM, TEM, and LLDP are the most useful in characterisation of pores in NF ISA and TFC membranes, as other techniques were mainly applied to MF, UF or gas separation membranes. Therefore, in the following paragraphs there are critical reviews of AFM, TEM, PALS, and LLDP aiming to provide a solid base for the research motivations and discussions of the experimental results described in this thesis.

1.4.1 Atomic force microscopy

The first AFM has been developed by Binnig *et al.* [126] and soon after that it was applied to characterisation of material surfaces [127]. In the 90s' Bowen *et al.* thoroughly explored AFM to image surface morphologies of polymeric membranes [128, 129]. Since then,

studies have been mainly focused on characterisation of TFC membranes [96, 109-111, 130], and a few ISA NF membranes [97]. The papers about application of AFM to membranes usually describe studies involving measurement of the pore size [110, 131], nodule size [69, 132-135], and surface roughness [130, 136]. In addition, the research interests were also directed towards analysis of the surface–colloid interactions aiming to understand the membrane affinity to fouling [137].

1.4.1.1 Principles of atomic force microscopy

AFM belongs to the group of scanning probe microscopies, employed to profile surfaces in a 3–D manner. In AFM a cantilever equipped with a sharp tip scans the specimen surface with the aid of the piezoelectric system. A laser beam reflects from the cantilever and travels to the photodiode detection system to register the cantilever deflections in order to convert them into a 3–D image (Figure 1.9). AFM can operate in various modes [138]; the most commonly used are the contact mode, the tapping mode (also known as the intermittent tapping mode), and the non-contact mode [139]. In the contact mode, the tip is continuously in contact with the surface. The constant setpoint amplitude, *i.e.* force applied on the cantilever, is maintained at all times, thus, a signal transmitted from the cantilever deflections provides an input to create the surface profile. In the contact mode, scanning is fast and relatively easy to set up. The disadvantage is that large tips, with a radius of curvature more than 5 nm, sought to be employed; therefore, image resolution is normally lower than when ultra sharp tips, with a radius of curvature significantly lower than 5 nm, are used. The reason they are not applicable to the contact mode scanning is that thin tips are subjected to higher forces and friction; therefore, they may be immediately worn off.

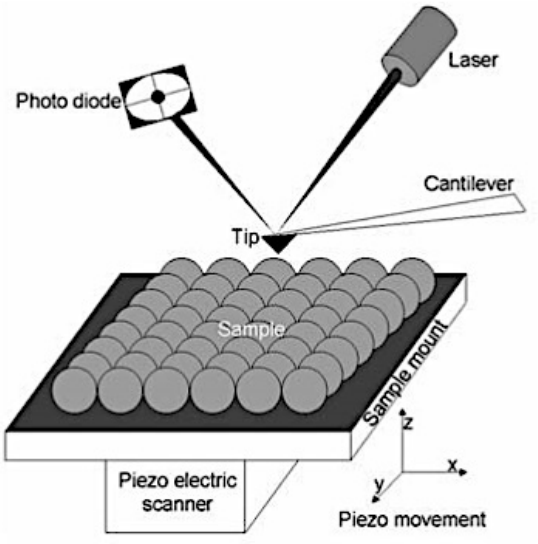


Figure 1.9 Diagram of AFM during scanning the sample surface.

In the tapping mode the cantilever is driven close to its resonance frequency at the constant setpoint amplitude, and its response amplitude or phase angle is registered on the detector. This operational mode is suitable for analysis of biological samples or soft materials such as polymers. A special function of the tapping mode is phase imaging, which is able to detect any variations in phases present on the surface. Some of the material phases detectable by phase imaging include: stiffness, composition, adhesion energy, crystallinity, viscoelasticity, plasticity index, elastic modulus [140, 141].

In the non-contact mode a tip is kept away from the surface by controlling the tip–surface force. The piezoelectric system moves vertically to maintain the constant tip–surface force to create the surface profile.

1.4.1.2 Microscope resolution

The tapping and non-contact modes are considered as high resolution methods, since ultra sharp tips can be used, which dramatically improve the resolution [117]. Furthermore, it is also possible to produce a cantilever with a single-walled carbon nanotube (CNT) tip with a

diameter of ~ 1 nm [142]. The application of these high aspect ratio tips significantly enhances image resolution [143, 144].

The vertical resolution of the microscope can reach as low as 0.1 nm [145], whereas the lateral resolution (l_{xy}) is significantly poorer, especially in materials with high roughness. The magnitude of the lateral resolution can be estimated using the following equation [146]:

$$l_{xy} = \sqrt{2R}\left(\sqrt{\delta h_r} + \sqrt{\delta h_r + \Delta h}\right), \qquad Eq.\ 1.23$$

where δh_r is the vertical resolution and Δh is the height difference between the highest points of the adjacent features. In modern microscopes δh_r reaches sub-angstroms [147], thus, the lateral resolution mainly depends on the tip radius (R) and the sample roughness.

The spatial resolution is strongly affected by the tip–surface convolution effect, which is influenced by the size and shape of the tip [139, 148]. If an image suffers from the tip–surface convolution effect, concave features become smaller, and convex – larger. A contaminated tip with e.g. a dust particle, also leads to artefacts produced along direction of the scanning.

For good image quality, the parameters such as scan speed and force play important roles. Higher contact force may provide higher resolution; however, it may also lead to distortion of the surface or result in production of undesired noises. It is also very important to select a cantilever with a suitable stiffness. The higher the spring constant, the higher the resonance frequency, and the higher force can be applied on the tip. Usually several tips are used before selecting the one with the most suitable stiffness.

1.4.1.3 Phase imaging

Phase imaging is an extension of the tapping mode. It is used to enhance the contrast of fine features, or to distinguish material phases to provide additional information beyond the topographical projections. Until extensive research work in this field was carried out in the last

decade, the main use of phase imaging was to visualise surfaces, and beyond this, the phase shift signals were not interpreted in detail. Nowadays, many publications report applications of phase imaging to studying the surface energy dissipation profiles [149], variations in surface composition [140], charge [150], crystallinity [151], and material mechanical properties [152, 153]. In the field of synthetic membranes phase imaging has been mainly used to characterise block co-polymer membranes [48], to identify the hydrophilic domains in proton exchange membranes [154], or to study surface hydrophobicity [130].

To use phase imaging for the quantitative analysis of material viscoelasticity [140], a comprehensive insight into the operational parameters of the tapping mode such as the free and setpoint amplitudes, drive frequency, and the cantilever properties (quality factor, tip radius, stiffness constant or resonance frequency) is crucial. Phase angle (φ) contrast (Eq. 1.24)) is produced due to the dissipation energy (E_{dis}) generated in response to the force transmitted from the cantilever tip onto the surface in an oscillation cycle [155, 156]:

$$\sin\varphi = \frac{\omega}{\omega_0}\frac{A(\omega)}{A_0} + \frac{QE_{dis}}{\pi A_0 A(\omega)}. \qquad \textit{Eq. 1.24}$$

In this equation ω_0 and ω is correspondingly the cantilever resonance and driving frequency, Q is the cantilever quality factor, and $A(\omega)$ and A_0 are the tapping and free amplitudes, respectively. For convenience of the analysis, in most of the AFM softwares the phase angle equal to 90° is expressed as 0°, and thus the part of Eq. 1.24 is then changed into the cosine function [157]:

$$\cos\varphi = \frac{\omega}{\omega_0}\frac{A(\omega)}{A_0} + \frac{QE_{dis}}{\pi A_0 A(\omega)}. \qquad \textit{Eq. 1.25}$$

Eqs. 1.24 and 1.25 consist of two terms: elastic ($A(\omega)/A_0$) and dissipative (Q and E_{dis}). Since the first term stays constant during the imaging, the phase contrast mainly depends on the second term [158]. To deduce the tip–surface dissipation energy Eq. 1.24 is expressed as [159]:

$$E_{dis} = \left(\sin\varphi - \frac{A}{A_0} \right) \frac{A}{A_0} F_E \qquad \textit{Eq. 1.26}$$

$$F_E = \frac{\pi k_s A_0^2}{Q}, \qquad \textit{Eq. 1.27}$$

where k_s is the cantilever stiffness.

When the probe is far away from the surface and there are no tip–surface interactions, the cantilever oscillates with the frequency ω equal to its resonance frequency ω_0, and so the phase angle becomes 90° (in the AFM images generated by for example WSxM software [160], the real phase angle 90° corresponds to 0°). As the probe approaches the surface, the cantilever starts oscillating in the attractive region, resulting in reduction of the amplitude and shifting the driving frequency below the resonance frequency and in consequence, the phase angle becomes greater than 90°. Analogously to the Lennard–Jones potential plot [161], the long range attractive tip-surface net forces are negative ($F_{ts} << 0$). While the tip is approaching the sample surface, the cantilever enters the repulsive region, where the net force is positive ($F_{ts} >> 0$), the driving frequency shifts above the resonance frequency, and the phase angle shifts below 90° [162]. This description can be summarised using Eq. 1.28 [163] and Eq. 1.29 [162]:

$$\tan\varphi = \frac{\omega\omega_0 / Q}{\omega_0^2 - \omega^2} \qquad \textit{Eq. 1.28}$$

$$F_{ts}(z_c, z) = -\frac{HR}{6(z_c + z)^2}, \qquad \textit{Eq. 1.29}$$

where H is the Hamaker constant, R is the tip radius, z_c is the tip–sample distance and z is the instantaneous tip position during the oscillation.

1.4.1.4 Application of atomic force microscopy to membranes

It is obvious that the opportunity to measure the pore size is very attractive in the membrane science field, to correlate the membrane structural characteristics with the filtration parameters. The pore size has been mainly measured in commercial TFC NF or RO membranes. Bowen and colleagues [96, 97, 109] described several studies focussed on measurement of the pore size using AFM, and its correlation with the solute rejection. Otero *et al.* [110] used three techniques to measure and compare the pore size of two different TFC NF membranes: AFM, LLDP and the steric pore–flow model. The pore size obtained by LLDP has been found to be the largest. AFM measurements and the steric pore flow–model calculations have resulted in very comparable pore sizes in the range of 0.38 – 0.56 nm. Hilal *et al.* [131] also used AFM to measure the pore size in five different NF TFC membranes designated for aqueous applications. The authors claimed that the measured pore size was as small as 0.2 nm. Although, some authors recognise the tip–surface convolution effect, none of the paper discusses the impact of the lateral resolution on the pore size measurements in NF membranes. This issue will be investigated in detail in the 'Results and discussion' section.

The application of AFM to studying the topography of polymeric membranes has led the membrane scientists to analyse the nodular structures. Fritzsche *et al.* [164] were the first to report the research on membrane nodules using AFM. The surface morphology of an ISA polyvinylidene fluoride MF membrane was described to consist of nodular aggregates with pores located in their interstitial regions. Khulbe *et al.* [165] studied nodules of a polyphenylene oxide ISA membrane in the tapping mode. The authors acquired high resolution images that allowed characterising the nodule size with good precision. Some other studies investigated the impact of the membrane formation parameters during the phase inversion on the nodule size. Khayet *et al.* [132] showed that amount of water added to the dope solution comprising polyvinylidene fluoride, dissolved in dimethylacetamide, had a strong impact on the nodule size. The pore and

nodule size was larger when higher water content was added to the casting solution. The water fluxes were also higher for membranes that had larger nodules. Hamza *et al.* [166] observed that an increase in methanol content in the methanol–chloroform solvent mixture used for preparation of sulfonated poly(2,6-dimethyl–l,4 phenylene oxide)–polyethersulfone composite membranes, resulted in larger nodules. It was explained that the polymer–solvent interaction parameter controlled the nodule size.

Surface roughness is an important structural property of NF and RO membranes. It has been shown that it can be related to colloidal fouling [137, 167], and to membrane formation parameters such as type of solvent in a dope solution [168], or the evaporation time allowed prior to phase inversion [136]. Surface roughness can be presented as average roughness (R_a) (Eq. 1.30), root–mean–squared (RMS) roughness (R_q) (Eq. 1.31), or peak–to–valley height (R_z) (Eq. 1.32). Surface skewness (R_{sk}) (Eq. 1.33) is a measure of height distribution symmetry. Negative skew values correspond to dominance of valleys, associated with a porous-like surface; whilst positive skew values suggest a surface dominated by peaks. Surface kurtosis (R_{ku}) (Eq. 1.34) describes sharpness of the height distribution. Kurtosis values lower than 3, (the Gaussian distribution corresponds to a kurtosis of 3) indicate a flat and repetitive surface, while values greater than 3 suggest that the height distribution is sharp. An additional parameter used is surface area ratio (R_{ar}), which is a ratio between the actual and projected surface areas [169].

$$R_a = \frac{1}{n}\sum_{i=1}^{n} Z_i \qquad \textit{Eq. 1.30}$$

$$R_q = \sqrt{\frac{1}{n}\sum_{i=1}^{n} Z_i^2} \qquad \textit{Eq. 1.31}$$

$$R_z = Z_{\max} - Z_{\min} \qquad \textit{Eq. 1.32}$$

$$R_{sk} = \frac{1}{nR_q^3}\sum_{i=1}^{n} Z_i^3 \qquad \textit{Eq. 1.33}$$

$$R_{ku} = \frac{1}{nR_q^4}\sum_{i=1}^{n} Z_i^4 , \qquad \textit{Eq. 1.34}$$

where Z_i is height at point i, n is number of points in an image and Z_{max} and Z_{min} are the highest and the lowest Z value, respectively [139].

Bossou *et al.* [130] studied roughness of six different aqueous NF TFC membranes in the contact and tapping modes, acquiring images with very good quality. The average roughness increased with an increase of the scan size; hence, it was recommended that for the purpose of comparison, membranes should be scanned over the same size. Phase shift was also measured in the tapping mode. A small phase shift corresponded to a large contact angle, thus, to more hydrophobic surfaces of the membranes. Since the studied membranes were fabricated from different polymers using various preparation methods, it cannot be absolutely deduced, whether the surface roughness is a crucial factor influencing the solute rejection, or another property, such as for instance solute–surface electrostatic interactions, is also significant.

An interesting study reported by Stamatialis *et al.* [136] involved correlation of the surface roughness of asymmetric cellulose-based membranes with the solvent evaporation time. An increase in the evaporation time during membrane preparation resulted in lower surface roughness. Furthermore, the lower the peak–to–valley distance, the higher rejection the membranes showed. Vrijenhoek *et al.* [167] studied the impact of surface roughness on colloidal fouling and flux decline for the NF TFC PA membranes. AFM images showed that more particles adhered to the surface of rougher membranes than to smoother ones. The membranes with higher roughness and higher affinity for particle fouling were characterised by greater flux decline. The authors rationalised that colloidal particles tended to accumulate more in "valleys" present on the rougher surfaces resulting in blocking the pores. The affinity to fouling was characterised by measuring the forces acting between a particle, *i.e.* colloid, and the surface. The experiments were performed by moving the cantilever, with an immobilised colloid on its tip,

towards the surface while simultaneously recording the forces, *i.e.* adhesion forces, in relation to the tip–surface distance. Stronger forces corresponded to stronger colloidal interactions between the particle and the surface, thus, the higher affinity for membrane fouling was expected to exist [130].

1.4.2 Transmission electron microscopy

TEM is one of the most powerful imaging techniques in terms of resolution. However, there are two main challenges in application of TEM to polymeric materials. The electron–optical contrast is greatly affected by elements possessing low atomic numbers present in materials such as polymers, which comprise low atomic number elements. Furthermore, soft organic samples are very sensitive to ionizing radiation transferred from the electron beam. The ionizing radiation is responsible for beam damage, commonly occurring in organic specimens and leading to alteration of their phases [170], or even chemical composition [171]. Nevertheless, TEM has been used in characterisation of polymers for several decades. The literature offers numerous publications describing the application of TEM to polymers [13, 172-174]. Careful sample preparation and knowledge of the image formation mechanisms certainly help in correct interpretation of the contrast origin and its relationship with the sample structure.

Although TEM has been used in characterisation of polymers, it has not been frequently applied to imaging of synthetic membranes; presumably because of the problems associated with generating a sufficient contrast at the high magnifications required to provide the necessary resolution to distinguish nanoscale phases in polymeric NF membranes. Nevertheless, the excellent work on characterisation of interfacially polymerised films in NF or RO composite membranes was reported by Freger [67, 115] and Bartels *et al.* [175]. ISA membranes have only been characterised at the microscale [64].

1.4.2.1 Contrast formation in transmission electron microscopy

A high energy electron beam travelling through the electron–optical system of lenses (Figure 1.10a) is transmitted through an ultrathin specimen with a thickness of less than 100 nm. The image contrast is formed by interaction of electrons with atoms building the specimen (Figure 1.10b,c). If a sample is crystalline or semicrystalline, the crystal orientation gives rise to the Bragg diffraction. The objective aperture localised next to the objective lens blocks high angles of the electron waves scattered from the specimen, hence atomic lattice configurations can be evaluated.

If a sample is stained with heavy elements, high electron densities induce the Rutherford scattering that produces dark contrast on a projection (Figure 1.10b). The other type of the image contrast (Figure 1.10c) is generated from amorphous samples such as polymers, where spatial variations in electron densities are very low; therefore, the projection mechanism detects the modulations in phase and energy of an incident electron beam [170].

In polymers, there are two methods to generate the image contrast: heavy element stains and phase variations. Heavy element staining is based on affinities governed by chemical or physical interactions of an element or a compound to a certain phase in the specimen. The most common staining compounds are osmium tetroxide (OsO_4) and ruthenium tetroxide (RuO_4). OsO_4 reacts covalently with unsaturated double C–C bonds existing, for instance, in rubbers and latexes. The most commonly described utility of staining with OsO_4 is undertaking the micro-phase characterisation of triblock co-polymers such as, for example, polystyrene–polybutadiene–polystyrene. Herein, the contrast is produced owing to enhancement of electron scattering over the polybutadiene domains where OsO_4 reacts with unsaturated C–C bonds, resulting a high content of heavy atoms, in comparison to the polystyrene domains where the staining agent does not bind.

The OsO_4 staining of rubbers has also been found useful in the TEM sample preparation utilised to harden specimens [176]. In addition, OsO_4 has been used in staining of semicrystalline materials comprising crystalline and amorphous phases, which are differentiated based on the preferential absorption of the contrast agent to one of the phases. For instance, in semicrystalline polyethyleneterephthalate OsO_4 preferentially absorbs into the amorphous phases revealing polymer morphologies by generating contrast variations [177].

RuO_4 stains latexes or resins owing to its high oxidative affinity to aromatic rings, thus, the phases containing these sites result in enhanced contrast [172]. Other commonly utilised staining compounds include iodine, uranyl acetate, or phosphotungstic acid. All of them to some extend preferentially localise in certain regions inducing higher electron scattering and contrast enhancement [170, 173].

The second type of the contrast formation mechanism is based on the phase modulation of scattered electron waves across an amorphous specimen. The contrast intensity is characterised by a relative phase shift ($\Delta\varphi$) (Eq. 1.35), which is measured in relation to a reference wave that would pass through vacuum. The phase shift is then dependent on an electron–optical index of refraction (n_{e0}), specimen thickness (d) and the electron wavelength (λ_e) [170].

$$\Delta\varphi = \frac{2\pi}{\lambda_e}\left(n_{e0} - 1\right)d \qquad \textit{Eq. 1.35}$$

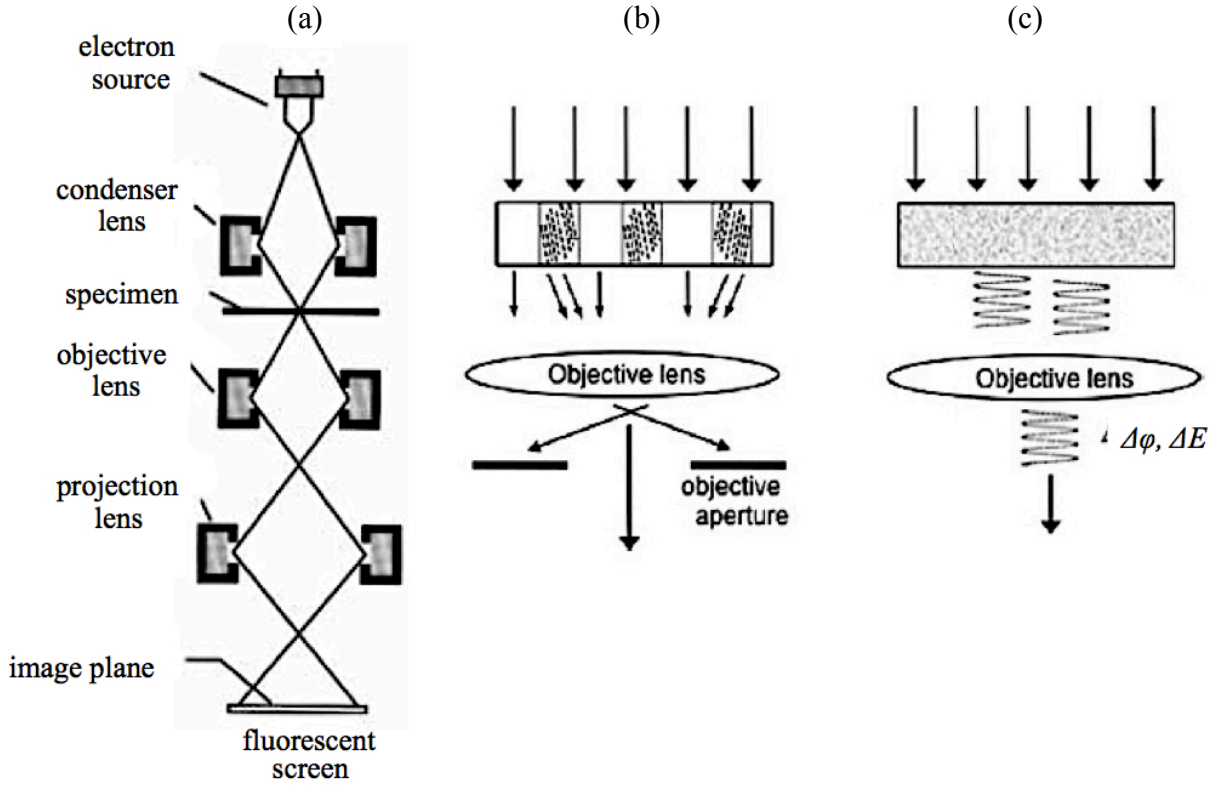


Figure 1.10 Electron–optical system and contrast formation mechanisms in TEM.

(a) Electron–optical system consisting of the main three groups of lenses controlling alignment of the electron beam: condenser, objective and projection. (b) An image is formed by diffracted electrons from the atomic lattices or due to variations in electron densities (contrast source: crystalline, semicrystalline phases or heavy element stain). (c) An image is formed due to changes in electron phase ($\Delta\varphi$) or energy (ΔE) as a result of variations in specimen density or thickness [170].

Because the phase shift information is lost while a signal is transformed through a charge–couple device (CCD), various techniques are used to convert the phase shift into the amplitude. One of the most commonly explored methods in imaging of polymers is defocusing the beam by controlling the objective lenses [170, 178]. This methods was used to reveal the morphology of block polymers [179-181], lamella in semicrystalline polymers [182, 183], or inorganic–organic composites [184]. The theoretical approach and experimental procedures of the phase contrast imaging of polymers are well discussed in publications of Thomas *et al.* [178-180, 183, 185].

The spatial resolution (l_d) (Eq. 1.36) of a microscope, *i.e.* a smallest feature that a microscope can detect, is limited by the spherical aberration C_s of the objective lens and the acceleration voltage given by the electron wavelength λ_e. JOEL 2010, a model of the microscope under which most of the specimens in the studies were imaged, has a spatial resolution limit of 0.23 nm, calculated based on the accelerated voltage of 200 kV and C_s of 1 mm [186].

$$l_d = 0.66\left(C_s\lambda_e^3\right)^{1/4} \qquad \textit{Eq. 1.36}$$

1.4.2.2 Transmission electron microscopy characterisation of polymeric membranes

TEM imaging of polymer membranes is a complex characterisation technique, as it requires lots of expertise in image interpretation and sample preparation. To prepare a good membrane specimen, first a sample needs to be embedded in a resin, sectioned using an ultramicrotome and often stained to generate a contrast on polymeric structures. Probably due to complexity of the sample preparation, TEM is rather rarely chosen to analyse the membrane structure.

One of the first reported applications of TEM to the characterisation of polymeric membranes was in the 80's, when Bartels and Kreuz [175] imaged cross-sections of several RO TFC membranes by electron microscopies. TEM was used to analyse polyurea TFC membranes prepared by the interfacial polymerisation of polyethyleneimine and 2,4-toluene di-isocyanate. In this study TEM assisted the SEM imaging in order to measure accurately thickness of the polyurea film. The researchers embedded specimens in a resin followed by staining with chemicals such as uranyl acetate and lead citrate. It was shown that staining dramatically improved contrast between the membrane macrophases. A low operating voltage of 80 kV was used, presumably to reduce beam damage occuring to the specimens. Xue *et al.* [187] characterised the ion–exchange Nafion membranes to image ionic cluster domains having sizes

in the range of 25 – 50 Å. Owing to staining the membrane with RuO_4, good contrast of the clusters was acquired at the accelerated voltage of 120 kV.

The work of Freger *et al.* [67] has brought significant progress in understanding the structure of the interfacial PA films. The relationship between the interfacial polymerisation conditions and the nanoscale heterogeneity was elucidated from the cross-sectional TEM images of PA composite membranes used for NF and RO processes. The images of the membranes stained with uranyl nitrate and sodium tungstate acquired at the accelerating voltage of 120 kV, allowed for differentiation of the extremely thin PA layer from the polysulfone support. Moreover, an insight into the PA film provided further information on the carboxyl–rich and carboxyl–free domains and the interface, described as a sharp boundary or an intermediate layer, between these domains. The structure of the intermediate core layer appeared to be the densest, thus, it was suggested that herein the selectivity was created. Two types of TFC PA membranes were investigated: high–pressure and high–flux. In the high–pressure membrane the intermediate active layer appeared to be about 200 – 300 nm thick; whereas a thickness of only 20 – 50 nm was measured for the high–flux membranes. In further work, Freger *et al.* [115] observed that TEM performed on samples stained with uranyl nitrate assisted in the characterisation of structures formed during the graft polymerisation of acrylic monomers on RO and NF membranes. The findings showed that a thin layer of the grafted monomers was present on surfaces of the investigated membranes.

Patterson *et al.* [64] carried out a structural characterisation study of the P84 co-polyimide membranes used for OSN processes. The cross-sectional image, presented in Figure 1.11, reveals three morphologically different layers: the skin layer built from densely packed nodules, a microstructured transition layer where densely packed nodular structures transform into the loosely packed matrix, and the porous bulk layer. The skin layer thickness was not measured as there were no definite borders between the layers.

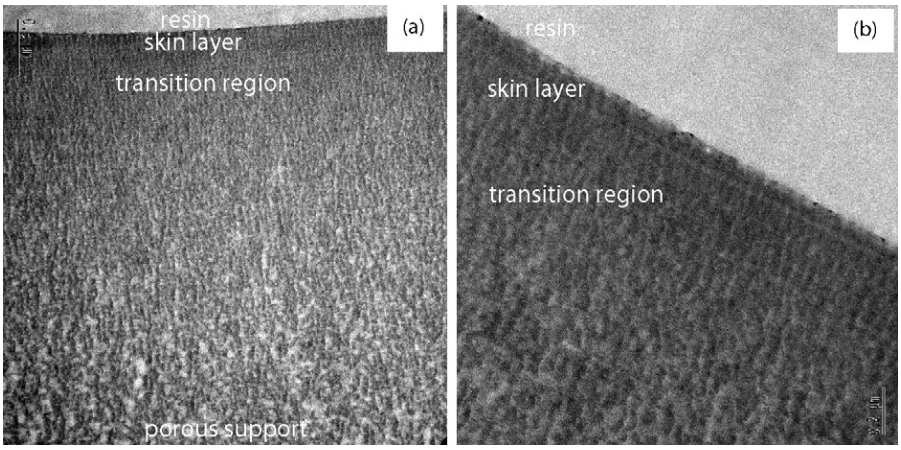


Figure 1.11 TEM image of cross-section of the assymetric P84 co-polyimide membrane.
Adapted from [64] (poor quality of the online print does not allow to read the scale bar).

Pacheco *et al.* [68] have recently published TEM images of the TFC PA membranes used for RO and NF processes. The interesting outcome observed after filtering 10 and 30 nm gold nanoparticles (NP) dispersed in water through the membranes followed by imaging the membrane top layer. The images indicated that NP had higher affinity to accumulate on the ridges than in the valleys building the surface of the PA film (Figure 1.6a); therefore, the findings suggested that the transport occurred preferentially through the ridges [188].

TEM characterisation studies have been mostly based on cross-sectional imaging. The surface can be only imaged *via* replication methods, *i.e.* masking of the membrane surface, because the membrane is too thick for the electron beam to transmit. One of the methods involves carbon deposition onto a membrane surface using a thermal vacuum evaporation process, followed by extraction of a replica from the surface, and imaging under TEM. To enhance contrast the carbon replica can be shadowed by platinum, gold or palladium *via* sputtering [172]. The replicas, providing the highest resolution, are produced by depositing platinum–carbon (Pt–C) vertically to the surface [69]. If a carbon replica is peeled off from the sample surface, it can be easily damaged, thus, in-direct replication, whereby, for instance, templates made of acetyl cellulose (soluble in methyl acetate) or cellulose acetobutyrate (soluble

in acetone) are prepared. Firstly, a template is prepared by pressing a foil against the surface, then it is peeled off, followed by the Pt–C shadowing. The Pt–C layer is then easily separated from the template foil, which is then dissolved in an organic solvent. The thickness of the replica should be below 50 nm to acquire good images [173].

Although, the surface replication of membranes is not a common technique, there is a noteworthy study published by Schultz and Asunmaa [70], who measured sizes of the nodules building the surface of the cellulose acetate membrane. The image of the replica, as presented in Figure 1.12, clearly shows the membrane nodular morphology.

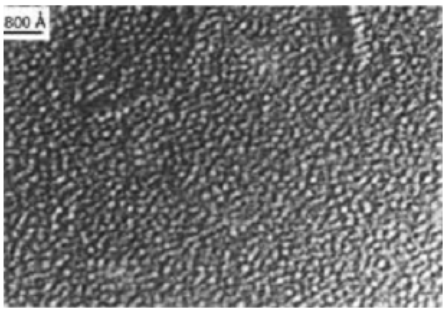


Figure 1.12 TEM image of the Pt–C replica of the surface of the assymetric cellulose acetate membrane.
Adapted from [189].

1.4.3 Positron annihilation lifetime spectroscopy

Positron annihilation lifetime spectroscopy (PALS) measures size of free volume elements in porous materials in a non-destructive way. This method has been used to characterise porous semiconductors, metals, and composites [190-192]. It has also found application to probe porous polymers to study size of free volume elements or cavities [193]. PALS and depth–profile PALS have been frequently used to characterise RO, NF and gas separation polymeric membranes in order to measure the pore size (averaged over the surface and bulky pores) [190, 194], and to estimate the thickness of membrane layers [113, 114].

1.4.3.1 Principle of positron annihilation lifetime spectroscopy

A positron annihilates with an electron in a free volume cavity to form a positronium, of which lifetime (τ) is measured. ^{22}Na is used as a positron source that is implanted into the material porous phases [33]. Typically lifetimes (τ_3 and τ_4) and intensities (I_3 and I_4) of the ortho-positronium, of which spins are parallel, are analysed. The lifetime is very sensitive to local electron densities, and thus to pore/void size in a porous material. The intensity is related to a fraction of free volume elements [195].

The positronium lifetime is related to pore radius (r) by the expression shown in Eq. 1.37, under the assumption that pores are spherical [196, 197]:

$$\frac{1}{\tau} = \pi r_e^2 \rho_0 \left(\frac{\Delta r}{r + \Delta r} + \frac{1}{2\pi} \sin \frac{2\pi r}{r + \Delta r} \right), \qquad \textit{Eq. 1.37}$$

where, r_e is the classical electron radius, c is the speed of light, ρ_0 is homogenous density and Δr is an electron layer thickness of 0.1656 nm [198].

PALS combined with a slow positron beam of controllable energy is known as depth–profile PALS. By changing the energy (from 1 keV to 60 keV), a sample can be probed at various depths up to few microns [195]. Algers *et al.* [199] proposed a formula correlating the implantation energy with depth ($\bar{Z}$) in amorphous polymers:

$$\bar{Z} = \frac{CE^n}{\rho}, \qquad \textit{Eq. 1.38}$$

where C and n are constants correspondingly equal to 2.8 mg cm^{-2} kV^{-n} and 1.7, ρ is polymer density (units g cm^{-3}) and E is an incident positron energy (units keV). According to Eq. 1.38, the energy of the positron beam increases as a sample is penetrated more deeply. The implantation depth of the positron beam is strongly related to specimen chemistry and density; therefore, if the same energy is used to penetrate various materials, the positron beam may reach different depths.

1.4.3.2 Application of positron annihilation lifetime spectroscopy to membranes

Depth–profile PALS has been frequently used to characterise TFC NF membranes to evaluate differences in porosities across a composite film and a top region of a support membrane [113, 114]. In most of the studies, the investigated membranes were commercial; therefore, material chemistries were largely unknown, and consequently, the impact of chemistry on the implantation depth, at which porosities were evaluated, could not be fully understood. Nevertheless, the values of R– and S–parameters in function of the incident positron energy, which corresponded to the positron implantation depth, were analysed.

The R–parameter is related to free volume, and thus it describes porosity, whereas the S–parameter is sensitive to material chemistry and structural changes [63]. Plots of the parameters can be studied to elucidate the multi-layer architectures of TFC NF membranes [112-114]. De Baerdemaeker *et al.* [113] have estimated, from the analysis of the positronium lifetime, the average pore radius in various commercial TFC NF membranes used in aqueous systems. Two size ranges of the pore radius have been measured: 1.25 – 1.55 Å and 3.20 – 3.95 Å.

Cano-Odena *et al.* [63] used the depth–profile PALS to characterise ISA P84 co-polyimide NF membranes and commercial Starmem^{TM} membranes. The results indicated that with increasing polymer concentration in the dope solution, the thickness of the resulting top layer increases. The schematic representation of the membrane cross-section and the R–parameter profile is depicted in Figure 1.13. The plot presenting the correlation of the R–parameter with the positron implantation depth distinguishes three sub-layers building the membrane top layer. There is a surface layer reaching the depth of 0.07 μm, an intermediate layer extending from the depth of 0.07 μm to 0.5 μm, and a transition layer linking the top layer with the microporous support. The surface layer is described to be the densest and responsible for the separation.

The plot depicted in Figure 1.13b indicates that at initial implantation energy, the R–parameter values are high. This trend suggests that some fractions of positrons annihilated with electrons localised on the surface resulting in longer positronium lifetimes. At the depth of 0.07 μm, low value of the R– parameter implies low porosity. Further away from the dense surface layer, at the depth ranging from 0.2 μm to 0.5 μm, the R–parameter continuously increases, suggesting a gradual increase in the porosity up to the depth of 0.5 μm, where the R–parameter stabilises indicating the existence of the transition open sub-layer.

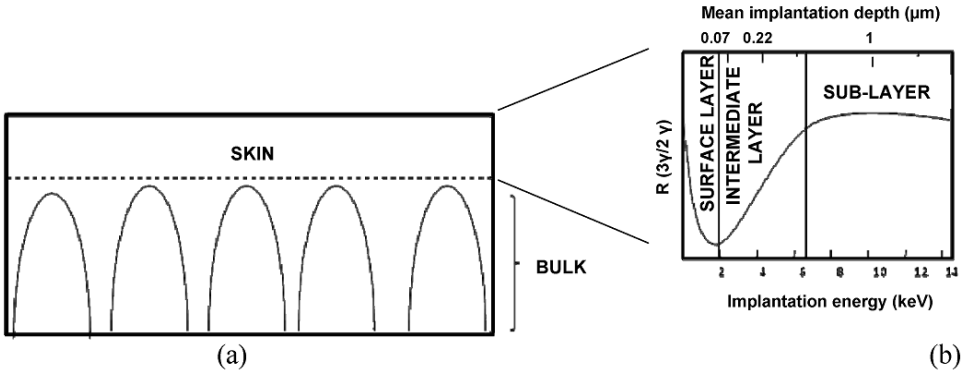


Figure 1.13 Principle of depth–profile PALS applied to assymetric membranes.

(a) Schematic drawing of the asymmetric membrane cross-section and (b) the corresponding profile of the R–parameter versus implantation energy. The lower the R–parameter value, the smaller pores in a material exist [63].

Although, depth–profile PALS offers an interesting outcome such as the characterisation of the multi-layer structure, unfortunately a correlation of the positronium lifetime with the membrane permeability or MWCO has not been found in the Starmem™ membranes [63]. Perhaps, it was due to the fact that during the removal of a conditioning agent and drying the membrane, the pores collapsed and material changed structure in an uncontrolled manner. Furthermore, the S–parameter data neither showed any correlation. Given that the S-parameter is sensitive to changes in chemical composition, this could explain the lack of correlation between the MWCO values and the S–parameter as the Starmem™ membranes may have been formed from different polymers, of which composition was not disclosed.

As this paper is the only one that analysed polyimide based ISA NF membranes using PALS, it is difficult to reach conclusion about the usefulness of this technique. The published results demonstrated that the positronium intensities measured for the P84 co-polyimide membranes were very low, implying that formation of positronium in this polymer was insignificant. Unfortunately, the presence of low annihilation intensities significantly reduces reliability of this technique as the variability of the data increases in reference to average intensity values.

In a further study reported by Chen *et al.* [114], the technique showed good correlation between the structural and functional characteristics determined for the TFC PA membranes with PAN supports. The cavity radius and the R–parameter profile correlated well with the pervaporation performance of 70% (w/w) isopropanol/aqueous mixture.

1.4.4 Liquid–liquid displacement porosimetry

LLDP evaluates the effective pore size of open through pores, *i.e.* permeation pathways which reach through the separating layer; hence, it characterises pores contributing to fluid transport. The main advantage of this method over other membrane structural characterisation techniques is that LLDP analyses a membrane *in situ*. In contrast, other pore measurement techniques may misleadingly consider in analysis a bottle–open or a blind pore. The descriptive scheme of the pore types in membranes is presented in Figure 1.14.

LLDP is carried out when a fluid is transported through pores; thus, real operating conditions are introduced, avoiding analysis of the dead–end or collapsed pores, which may exist in a dry membrane. It uses low pressure of about 5 – 6 bar (for UF membranes), therefore, the test does not cause damage to the membrane structure. In comparison, gas liquid displacement

porosimetry uses much higher pressures of approximately 60 bar [200]. However, LLDP applied to NF membranes may require pressures of more than 60 bar and the operating pressure, for instance, for the P84 co-polyimide membranes is reported to be between 5 – 50 bar [28]; consequently, there is high risk of damage to these membranes during the test. Nevertheless, LLDP has been used to measure the pore size in commercial NF PA composite membranes with polysulfone supports [110] .

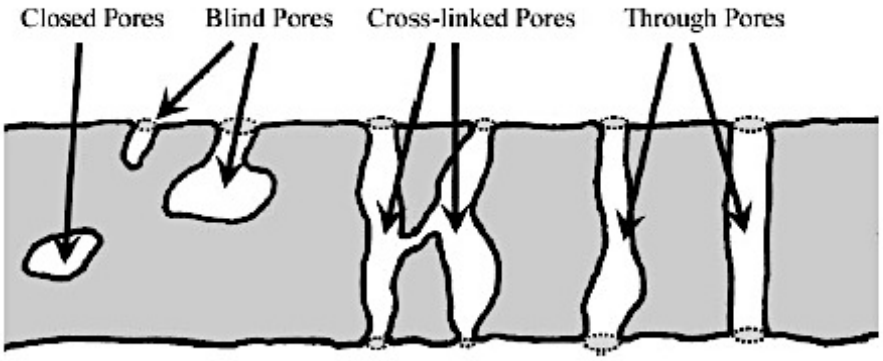


Figure 1.14 Schematic representation of pore types.
Reproduced from [201].

1.4.4.1 Principle of liquid–liquid displacement porosimetry

In LLDP the membrane is first filled with a wetting liquid (alcohol rich phase), which is then displaced with a displacing liquid (aqueous phase). The pore radius (r) is determined by the modified Washburn equation known as the Cantor equation [110]:

$$P = \frac{2\gamma}{r}, \qquad \textit{Eq. 1.39}$$

where P is the applied pressure and γ is the interfacial tension. It is assumed that the contact angle between the liquid–liquid interface and the membrane material is zero [202]. The pore radius distribution is determined from the Hagen–Poiseuille equation (Eq. 1.40) which correlates

the volumetric flow rate (Q) with the number of pores (N) having radius r, on the assumption that pores are cylindrical.

$$Q_i = \sum_{k=1}^{i} \frac{N_k \pi r_k^4 P_i}{8\mu l} \qquad \textit{Eq. 1.40}$$

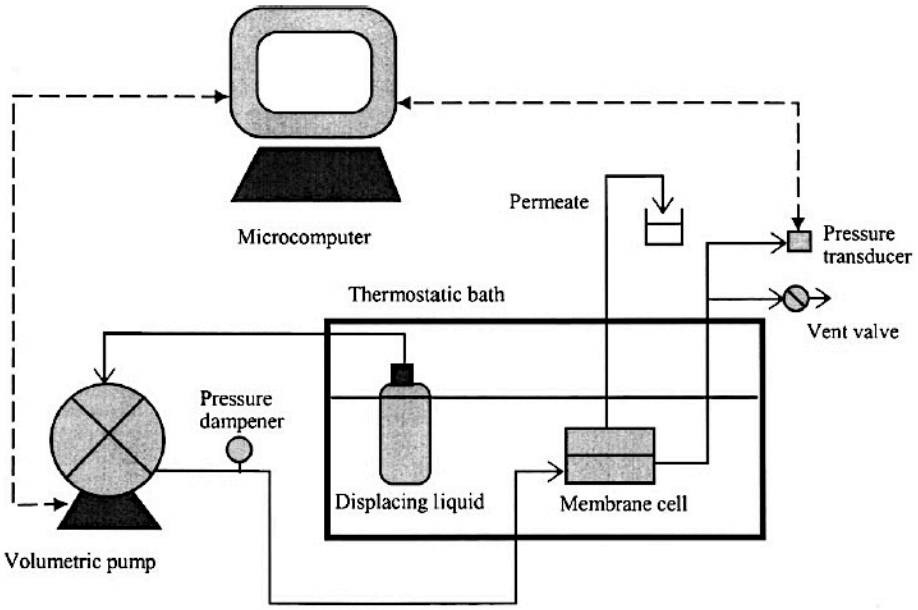


Figure 1.15 Scheme of the set-up used in liquid–liquid displacement porosimetry.
Reproduced from [200].

1.4.4.2 Pore size measurement in membranes

LLDP is very effective to evaluate the pore size in MF and UF membranes [200]. However, the technique may not be as accurate when applied to NF membranes, as it requires very high pressure for use in nanoscale porous materials. Otero *et al.* [110] used LLDP to test two commercial TFC PA membranes prepared on polysulfone supports. The average pore radii measured for AFC–40 and AFC–80 membranes (PCI membranes, UK) was equal to 0.56 ± 0.12 nm and 0.41 ± 0.43 nm, respectively. The authors commented that the pore sizes estimated using LLDP were significantly larger than the pore sizes computed through the steric pore–flow model. The difference in the comparative analysis was presumably associated with the difficulty in filling finer pores in the LLDP experiment; thus, the averaged pore size was overestimated.

The molecular Stokes radius of an isobutanol molecule is 0.31 – 0.34 nm, which is comparable to the size of finer pores, resulting in insufficient wetting of small pores, and invalidating the Cantor equation because the flow at the molecular level does not behave as the macroscopic capillary flow.

The high viscosity of isobutanol also has an impact on the application of the Hagen–Poiseuille equation to calculation of the pore radius distribution, as the pressure required to displace the wetting fluid would be significantly higher. Furthermore, surface chemistry also has an important impact. Although the Cantor equation assumes that the contact angle between the wetting fluid and the membrane is zero, this assumption is unlikely to be valid for more hydrophilic membranes. Therefore, it is crucial to select suitable wetting and displacing fluids in order to increase the accuracy of the results, especially for membranes with finer pores.

CHAPTER 2

2. Research motivation and strategy

Nanofiltration (NF) processes require a membrane of which the separating layer is built from a nanostructure capable of permeation of solutes in a selective manner. It is a challenging research goal in the membrane technology to control generation of the macromolecular arrangements in a top skin layer during the membrane formation process to achieve required molecular separation characteristics. It is also difficult to characterise polymeric nanostructures in a top separating layer, but on the other hand progress in this area might lead to better control of membrane formation, and ultimately better understanding of the physical and functional properties of membranes.

Most of the time the research is performed *via* trial–and–error methods leading to extension of development time and increase in costs. This is partially because the structure of the OSN membranes, particularly the size of the permeation pathways, is largely unknown. The distribution of the permeation pathway size is a membrane characteristic that determines the selectivity and contributes to the magnitude of flux [94]. Therefore, knowledge of the pore size distribution would significantly improve the development process. Additionally, a technique that can measure the transport–active pore size could elucidate transport behaviour and contribute to prediction of the solute rejection using computational methods.

Often studies on NF modelling are focused on fitting simulation plots into experimental results. Development of new predictive models is limited mainly due to unknown parameters such as the pore size distribution, the separation layer thickness, porosity, and information on solvent–solute, solvent–membrane and solute–membrane interactions. The pore–flow model, such as the extended Nernst–Planck pore–flow model, modified and described by Bowen *et al.*

[95-97, 203], has not been critically assessed for application to the OSN P84 co-polyimide membranes, although it has been frequently used to model these membranes. The proposed pore–flow model can only be investigated on a system in which the detailed membrane structure is known, and the functional performance is controlled by, de facto, the membrane structure.

OSN P84 co-polyimide membranes prepared *via* phase inversion are excellent candidates to carry out systematic characterisation in an attempt to relate their macromolecular structures to NF characteristics [29, 62]. Given that these membranes can be fabricated from the same polymer, there are no chemical differences between them; hence, a series of membranes with a range of MWCO values provides an excellent control material for development of new characterisation techniques, with no risk of artefacts occurring due to differences in the membrane chemistry.

Work on characterisation of the NF membrane structure has a long history. The most useful techniques include atomic force microscopy (AFM), transmission electron microscopy (TEM), positron annihilation lifetime spectroscopy (PALS), and liquid–liquid displacement porosimetry (LLDP). The surfaces of NF membranes have been continuously analysed using AFM since the 1990's; however, the studies have mainly focused on estimation the pore size and surface roughness of thin film composite (TFC) membranes [96, 109-111, 130], or commercial integrally skinned asymmetric (ISA) membranes [97]. However, this technique cannot differentiate between surface cavities and active pores contributing to solute transport. Furthermore, the resolution of AFM is limited by size of the cantilever tip [148]; thus, it may be difficult to measure pore sizes at the scale of a nanometre or less [109-111]. Therefore, the ability of measuring the pore size using AFM is questioned, as the lateral resolution achieved by a conventional probe is not sufficient to detect the transport–active pores.

Therefore, it is proposed to analyse the membrane surface in the tapping mode using a cantilever equipped with a carbon nanotube (CNT) tip, which has the potential to provide

additional resolution, enabling measurement of the nodule size, roughness, and possibly the pore size. These analyses could yield more detailed understanding of the molecular architectures and their impact on MWCO and the flux. Therefore, this works assesses the use of AFM combined with an ultra-high resolution CNT probe in characterisation of NF membranes, and the phase imaging methods in analysis of the polymer packing in membranes. When studying membranes, phase imaging can be applied to analyse the localised viscoelastic maps of surfaces to elucidate the polymer chain packing. Given that the phase lag can be related to material stiffness [204], this study will test the hypothesis that it can also provide information on the arrangement and entanglement of the polymer chains, in order to relate these surface properties to membrane NF performance. Nodules have been mainly studied for ultrafiltration (UF) and microfiltration (MF) membranes [132-135], with less attention to ISA NF membranes. To the best of my knowledge, there has not been any systematic study of the nodular structures of a range of ISA NF membranes fabricated from the same polymer, and which possesses varying NF characteristics.

TEM is a most powerful imaging technique in terms of resolution. This technique, although it is often applied to characterisation of polymeric materials, does not provide detailed information about their nanostructure due to the fact that polymers do not generate sufficient electron contrast for imaging of their morphologies at the nanoscale [173]. ISA membranes have only been characterised at the microscale [64], and TEM has been applied to TFC membranes to evaluate the thickness, but not the structure, of their polyamide (PA) top layers [115]. The literature review on the application of TEM to polymeric NF membranes suggested that this microscopy has not been fully explored, and therefore, the methods to enhance the contrast of the porous phases present in the membranes are proposed to be able to “see” the macromolecular configurations and to measure *in situ* the transport–active pore size.

PALS provides information about size of free volume elements in polymeric films; however, it does not measure dimensions of the transport–active pores that contribute to membrane transport. The so-called S–parameter obtained through slow positron beam techniques can be acquired in relation to membrane depth, so changes in material structure with depth can be evaluated [205]. However, these analyses are strongly related to material chemistry [63], and hence a comparison of membranes having different chemical compositions does not yield reliable results.

The publication about the characterisation of the P84 co-polyimide membranes [63] was carefully reviewed with the field experts to deduce that the measured positronium intensities were very low, thus the data suggested that this polymer was not suitable to undertake PALS analysis and this spectroscopy was not further explored.

In terms of *in situ* characterisation techniques, credit should be given to LLDP, a method developed to measure the pore size in UF membranes [110]. However, at the NF level, the Cantor equation ($P = 2\gamma r^{-1}$, where r is pore radius), used to estimate the pore size ($2r$) of 1 nm, would require a pressure of 68 bar (based on a surface tension between immiscible liquids of γ = 1.7 dyne cm^{-1}), leading possibly to mechanical damage of membranes due to high pressure. Furthermore, the equations used to estimate the pore size carry too many assumptions that in fact cannot be valid for the NF transport, which behaviour is no longer alike the macroscopic capillary flow.

To date, none of the characterisation methods described above estimate the pore size in a reliable manner and are able to distinguish pores which are active in the solute/solvent transport (these pores are termed as ‘transport–active pores’) from “dead–end” pores. A method to relate the NF membrane functional characteristics, such as flux and rejection, to the membrane nanoscale structure, has not yet been reported. In order to progress understanding of the

molecular architectures of the separating layers of polymeric membranes, new high resolution characterisation techniques are required. Hence, this work will be focused on development of new approaches for the characterisation of NF membranes; both ISA and TFC membranes. An *in situ* technique, based on probing the pores with high contrast agents and high resolution TEM, will be proposed to measure the transport–active pore size and the separation layer thickness. Given the detailed membrane structure, it will be possible to assess the pore–flow model for applications to OSN membranes and processes. Furthermore, the characterisation studies will be performed on AFM combined with a high aspect ratio single-walled CNT tip that has potential to enhance the resolution significantly. The research will explore two paths: high resolution topographical imaging to quantitatively analyse the surface features, and the phase imaging to map variations in macromolecular packing across various membranes.

CHAPTER 3

3. Development of nanoprobe imaging technique

3.1 Summary

It is essential to develop a novel *in situ* structural characterisation technique, as there are no available methods able to image nanopores, which actively participate in the membrane transport, with dimensions in the range of 0.5 – 2 nm. Other techniques such as atomic force microscopy (AFM) and positron annihilation lifetime spectroscopy (PALS) do not measure transport–active pore sizes, since the characterisation is not performed when a membrane is operating in filtration. Transmission electron microscopy (TEM) facilitates the imaging of materials with sub-nanostructures. However, the major problem in TEM imaging at this scale is insufficient electron contrast of polymers, which has made distinguishing their structural phases at the nanoscale not practically feasible. Therefore, a research direction for novel TEM methods applied to the characterisation of nanofiltration (NF) polymeric membranes is to focus on contrast enhancement between the free volume and polymer phases comprising the membrane. Furthermore, the ability to do so with the membrane in its active state would additionally contribute to elucidation of membrane transport.

Here a development path of the *in situ* structural characterisation technique is described. The technique was applied to characterise the pores in organic solvent nanofiltration (OSN) membranes. Nanopores in integrally skinned asymmetric (ISA) P84 co-polyimide membranes were filled with high contrast osmium dioxide (OsO_2) nanoparticles (NP), whose spatial arrangement was mapped under TEM. Due to the uniquely small size range of these probes, they targeted nanopores in the membrane skin layer; thus, the pore size distribution and even polymer chain structures could be evaluated. The pore size was found to correlate well with the

membrane NF performance, and the molecular separation mechanism of the OSN P84 co-polyimide membrane was shown to be due to size exclusion of larger NP.

3.2 Materials and methods

3.2.1 Membrane preparation

ISA membranes, assigned with nomenclatures M1, M2, and M3, were cast from dope solutions comprising 24% (w/w) P84 co-polyimide (HP Polymers, Austria) dissolved in a mixture of dimethylformamide (DMF) and 1,4 dioxane (dioxane) at the solvent ratios of 1:2, 2:1, and 4:1, correspondingly for membranes M1, M2, and M3. Dope solutions were stirred for 24 – 48 h until homogenous solutions were obtained, and then left overnight to degas. The membrane films were cast at a knife height of 300 μm on polyester non-woven backing material (Hollytex 3329, USA) taped to a glass plate. The cast film was then held for 30 s before immersion in a water coagulation bath, where phase inversion was induced and membranes formed. After an hour, the membranes were removed from the water coagulation bath and immersed in isopropanol (IPA) for solvent exchange to remove water. In the next step, the membranes were conditioned for 24 h in polyethylene glycol (PEG) 400 (Fisher Scientific, UK) with a molecular weight (MW) of 400 g mol^{-1} dissolved in IPA at a volume ratio of 3:2 (PEG:IPA), followed by air drying.

3.2.2 Dense film preparation

A dope solution comprising 24 % (w/w) of P84 co-polyimide dissolved in a mixture of DMF:dioxane at a ratio of 2:1 was cast on a glass plate with the casting knife set at a height of 300 μm. Subsequently, the film was placed in a vacuum oven at 80°C for 24 h to induce the dry phase inversion process, whereby solvent evaporates from the cast polymer film resulting in a homogenous, non-porous dense film.

3.2.3 Estimation of P84 co-polyimide molecular weight

The polymer MW was measured based on a series of polystyrene (PS) standards (Agilent Technologies, UK) using gel permeation chromatography (Waters™ GPC equipped with Waters Styragel® HT4 Column). A mobile phase comprising 0.03 M lithium bromide (Sigma–Aldrich, UK) dissolved in *N*-methyl-2-pyrrolidone was used.

3.2.4 Membrane functional performance

NF experiments were carried out in a METcell cross–flow system (Evonik–Membrane Extraction Technology, UK) in toluene at an applied pressure of 10 bar. During the first 30 min of filtration the PEG conditioning agent was removed by filtration of pure toluene. The rejection curves were then evaluated by filtration of a mixture of PS oligomers, *i.e.* GPC standards supplied from Agilent Technologies, UK, comprising PS 580 (Mp = 580 g mol^{-1}, Mw = 635 g mol^{-1}, Mw/Mn = 1.09, as provided by the supplier) and PS 990 (Mp = 990 g mol^{-1}, Mw = 1040, Mw/Mn = 1.11, as provided by the supplier), and α-methylstyrene dimer (Sigma-Aldrich, UK) dissolved in acetone at concentrations of 1 g L^{-1} each. Concentrations of PS oligomers in feed and permeate samples were measured using an Agilent HPLC with a UV/Vis detector set at a wavelength of 264 nm, combined with an ACE 5-C18-300 column (Advanced Chromatography Technologies, UK). The mobile phase employed comprised 35% v/v analytical grade water, 65% v/v tetrahydrofuran (THF) and 0.1% v/v trifluoroacetic acid.

3.2.5 Solute size calculations

Solute diameters ($d_{s,i}$) of the PS species were determined using the Stokes–Einstein equation (Eq. 1.17, [99]) and the Wilke–Chang equation (Eq. 1.18, [100]). Solute size in toluene was determined by solving the above formulas given that the MW of a toluene molecule at 20°C is 92.14 g mol^{-1}, the dimensionless solvent parameter ϕ is equal to 1 [98], and the solute molar volume is estimated using the Group Contribution Method [106].

3.2.6 Preparation of osmium dioxide nanoparticles

Fabrication of OsO_2 NP was supported by a PS oligomers mixture comprised of PS 580 and PS 990 (Agilent Technologies, UK). PS was coated onto walls of a round bottom flask, and exposed in its close proximity to vapours of 4% (w/w) osmium tetroxide (OsO_4) aqueous solution (Agar Scientific, UK) (Figure 3.4a). The reaction time was 4 h at room temperature. The complex of PS and the staining agent became black, indicating that OsO_4 was reduced to OsO_2 in the presence of air. The gravimetric ratio of OsO_2 to PS was 5/1. This ratio was measured by first weighting PS alone prior to staining with OsO_4 vapours, then by weighing the final product of the PS with the formed OsO_2 NP, and consequently the mass of OsO_2 solids was calculated by subtracting the weight of PS prior to the staining. A solvent (toluene, THF, acetone) was then added to form a dispersion of the OsO_2 NP to achieve the final concentration of OsO_2 NP of 2 mg mL^{-1}. The dispersions were then sonicated for 30 min prior to being used in filtration.

3.2.7 Sample preparation for TEM imaging

Polyester backing material was peeled off from a membrane snapped after freezing in liquid nitrogen. Each membrane section, with a size of 2 x 2 mm, was embedded in an Agar resin prepared from glycidylether, dodecenyl succinic anhydride, N,N–dimethylbenzenemethanamine and methyl nadic anhydride (Agar Scientific, UK) mixed at ratios provided in the supplier's instructions, followed by curing at 60°C for 24 h. The resin blocks containing the membranes were then sectioned at a thickness of 50 nm using a PT–XL Ultramicrotome with a Diatome Ultra 45° knife (TAAB, UK), and specimens were placed on TEM copper grids (Agar Scientific, UK).

3.2.8 TEM imaging and analysis

A JEOL 2010 high resolution TEM, with the spherical aberration coefficient C_s of 1 mm, was used to characterise specimens at an accelerating voltage of 200 kV with objective lens defocus set at –64 nm. Pore size was estimated using Image J software [206] followed by image processing with 'fast Fourier transform (FFT) band pass filter' in order to remove low frequency noises and reconstruct the pores. Pore size distributions were acquired using the 'Analyse Particles' tool under the following optimised conditions: minimum size of 0.4 nm (the smallest NP detected by TEM) and minimum *circularity* of 0.8 defined as following:

$$circularity = 4\pi \frac{area}{perimeter^2}. \qquad Eq.\ 3.1$$

3.3 Results and Discussion

In this study, the focus is on the characterisation of ISA P84 co-polyimide membranes for OSN processes, and specifically on relating their nanoscale structural characteristics to their functional performance. The performance, microscale morphology and formation mechanisms of the membranes have been previously reported elsewhere [26, 27, 29-31]. The mean pore size was estimated to be in the range of 0.30 – 1.32 nm through experimentally obtained solute rejection measurements in organic solvent systems, and using the pore–flow model [29]. The morphology of a typical ISA P84 co-polyimide membrane acquired by scanning electron microscopy (SEM) is presented in Figure 3.1, where microscale structural changes are observed in relation to membrane depth. The bulk of the membrane thickness of approximately 200 μm has a highly porous structure, while the skin layer, which contributes to molecular separation, is much thinner; its thickness measures less than 0.2 μm.

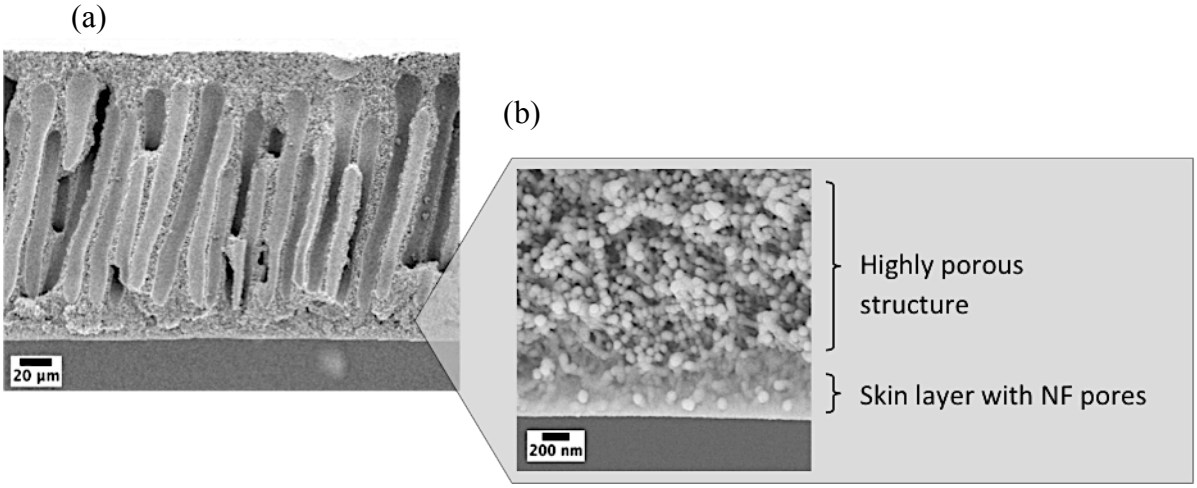


Figure 3.1 SEM image of asymmetric membrane.

(a) Cross-section of membrane M1 showing the typical asymmetrical morphology. (b) High magnification view of the region where highly porous structure changes into the dense skin layer where NF pores are present. Membrane cross-section is shown with the skin layer at the bottom, since the nanoprobes, as explained later, are filtered from the open side of the membrane to analyse the skin layer structure.

3.3.1 Chemical structure of P84 co-polyimide

Figure 3.2a presents the chemical structure of the P84 co-polyimide and Figure 3.2b shows a 3–D model of a fragment of the polymer chain built in ChemBio 3D Ultra 12.0 software. The theoretical chain cross-sectional diameter and the length of the extended polymer chain were estimated to be 0.664 nm and 275 nm, respectively. Calculations were based on the molecular geometry through estimation of the bond lengths and angles computed by the software, and the P84 MW of 62,000 g mol^{-1} measured experimentally using GPC.

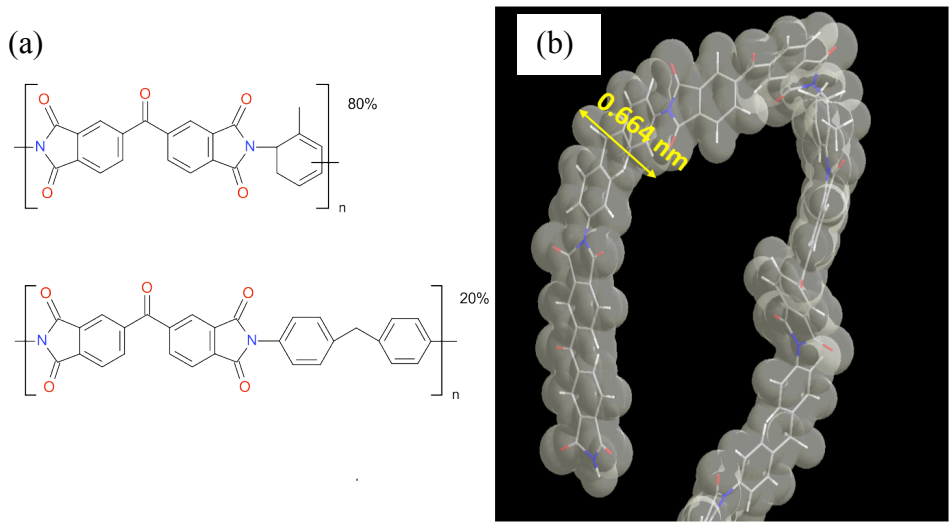


Figure 3.2 Molecular structure of P84 co-polyimide.

(a) Chemical structure of two units composing P84 co-polyimide. (b) 3–D representation of a fragment of the polymer chain built in ChemBio 3D Ultra 12.0 software.

3.3.2 Nanofiltration performance

Three ISA OSN membranes, assigned the nomenclature M1, M2 and M3, were used to validate the characterization technique. In terms of functional filtration performance, quantified by the solute rejection and flux, membrane M1 corresponds to tight, M2 to medium, and M3 to

open. The membranes were prepared from dope solutions comprising P84 co-polyimide dissolved in a solvent mixture of DMF and dioxane at various ratios, while keeping the polymer concentration constant. Higher DMF content in the dope solution results in lower rejection and higher flux [29], and it is by changing the dope composition that the tight, medium and open membrane characteristics respectively were obtained. The functional performance, determined in toluene, is described by the rejection curves and flux measurements presented in Figure 3.3. For comparison purposes, relative membrane separation performance was described using the estimated rejection of a solute with MW of 500 g mol^{-1}, corresponding to a molecular diameter of 0.77 nm. The resulting average values of the solute rejection R_{500} ± standard deviation estimated for membranes M1, M2 and M3 were 92 ± 3%, 63 ± 6% and 27 ± 2%, respectively, while toluene fluxes were measured to be 34.8 ± 7.0 L $m^{-2} h^{-1}$, 90.6 ± 5.3 L $m^{-2} h^{-1}$ and 143.6 ± 9.1 L $m^{-2} h^{-1}$ for membranes M1, M2 and M3, respectively. As expected, the higher R_{500} of the membrane, the lower the flux. These membranes were selected for the present study because they differ only in their observed functional performance – their chemical composition is identical. This is important, since it means that differences in features observed under imaging cannot be attributed to differences in chemical composition, and so they can be correlated directly with the functional performance.

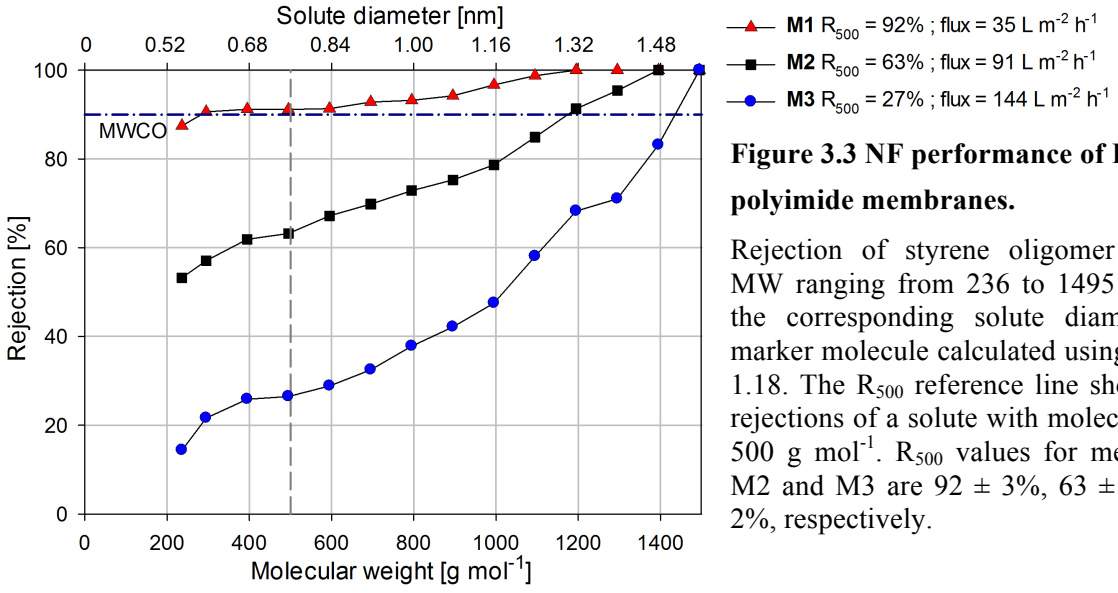


Figure 3.3 NF performance of P84 co-polyimide membranes.

Rejection of styrene oligomer solutes with MW ranging from 236 to 1495 g mol^{-1}, with the corresponding solute diameter of each marker molecule calculated using Eq. 1.17 and 1.18. The R_{500} reference line shows estimated rejections of a solute with molecular weight of 500 g mol^{-1}. R_{500} values for membranes M1, M2 and M3 are 92 ± 3%, 63 ± 6% and 27 ± 2%, respectively.

3.3.3 Characterisation of nanoparticle probes

The proposed strategy for visualising the membrane architecture with TEM was to develop a novel pore probing method. The key to achieving this non-trivial task was to fabricate NP probes with the following properties: high contrast, a size distribution within the NF range, and existence as a homogenous, stable dispersion. Material phase contrast is necessary to attain high resolution TEM images, and can be achieved by selecting a base material containing high atomic number elements [207]. OsO_2 was selected because of its known ability to generate high contrast in electron microscopy imaging of polymeric materials [208, 209].

Figure 3.4a presents schematically a representation of the NP fabrication methodology. The mechanism believed to provide a stable dispersion is known as 'polymeric stabilisation' [210], whereby the polymer chains associate with the NP surface and neutralise inter–particle forces. A good solvent yields effective particle dispersion due to un-coiling of the polymer chains. TEM images (Figure 3.4b,c) show that stabilisation of OsO_2 NP is crucial for their homogenous dispersion in toluene. Toluene was selected due to high polystyrene solubility and good stability of the membranes in this solvent. An important consideration is what happens to the PS molecules associated with the NP, when the NP enter the nanoporous regions of the membrane during filtration. It is possible that the PS remains associated with the NP, or that it becomes separated as the membrane polymer begins to interact with the NP and stabilise them under intimate contact. A further possible effect is charge on the surfaces of the NP, and its interaction with the membrane. The assumption is adopted that in a low dielectric solvent such as toluene, charge effects are negligible. Although the ratio of OsO_2 to PS is quite high (5/1 w/w), it cannot be discounted that some amount of PS stabiliser may enter the pores together with OsO_2 NP. Due to the difficulty of discounting the effect of PS in the pores, the hypothesis was posited

that if this effect were present, it would occur uniformly to all the samples. For these reasons, these issues are recognised as a source of uncertainty in the estimations of pore sizes.

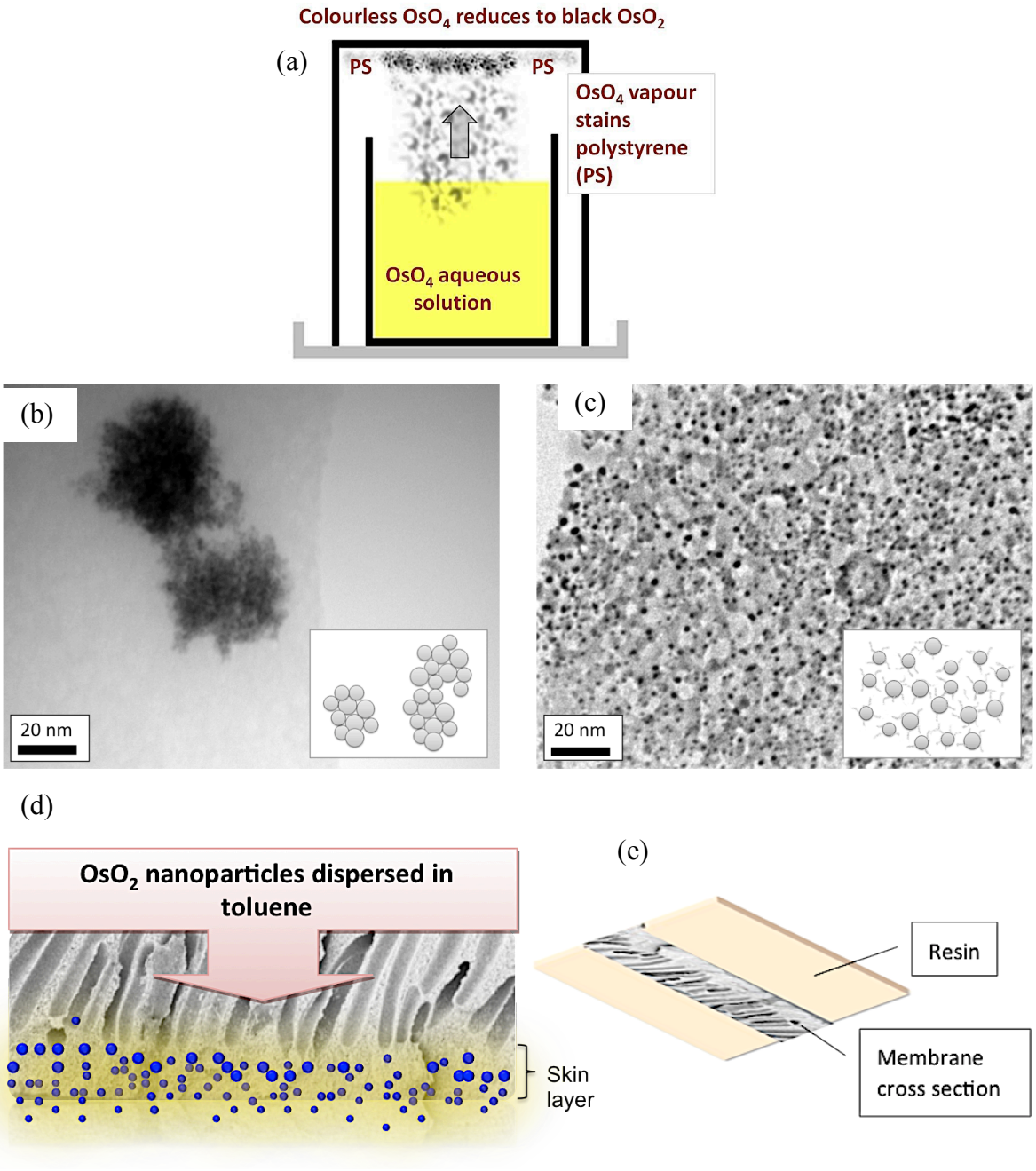


Figure 3.4 OsO_2 NP fabrication and probing the nanopores.

(a) Preparation of OsO_2 NP through absorption of OsO_4 vapours into the PS. (b) TEM image of OsO_2 NP without using PS stabilisers. The NP show a high degree of agglomeration as demonstrated in the inset. (c) TEM image of homogenously dispersed OsO_2 NP. The inset demonstrates the stabilisation mechanisms due to uncoiled PS chains repelling the particles. (d) Schematic diagram of filtration of OsO_2 NP from the open side of the membrane (NP size is exaggerated for descriptive purposes). (e) Schematic diagram of membrane cross-sections embedded in a resin and sectioned for TEM imaging.

Figures 3.4b,c show that OsO_2 NP, obtained from OsO_4 aqueous solution *via* deposition and reduction, followed by dispersion in toluene, were in a suitable size range to simulate NF solutes. This study also tested other commonly used solvents in OSN such as THF and acetone in order to investigate the impact of solvents on the NP morphology. The analysis of the TEM images revealed that the OsO_2 NP had an average diameter of 1.17 ± 0.28 nm in toluene, 1.32 ± 0.33 nm in THF, and 1.01 ± 0.33 nm in acetone.

The images and the size distributions of the OsO_2 NP dispersed in these three solvents are shown in Figure 3.5. In toluene (Figure 3.5a) and THF (Figure 3.5b) NP were homogenously dispersed on a TEM grid, allowing for relatively straightforward imaging; whereas NP extracted from acetone (Figure 3.5c) were covered by PS, resulting in accumulation into larger complexes. This sample was difficult to image, since occurrence of the NP–PS clusters caused problems in finding a good dispersion so the particles could be individually projected. Nevertheless, with some effort and time it was still possible to acquire good quality electro-micrographs of the OsO_2 NP extracted from acetone.

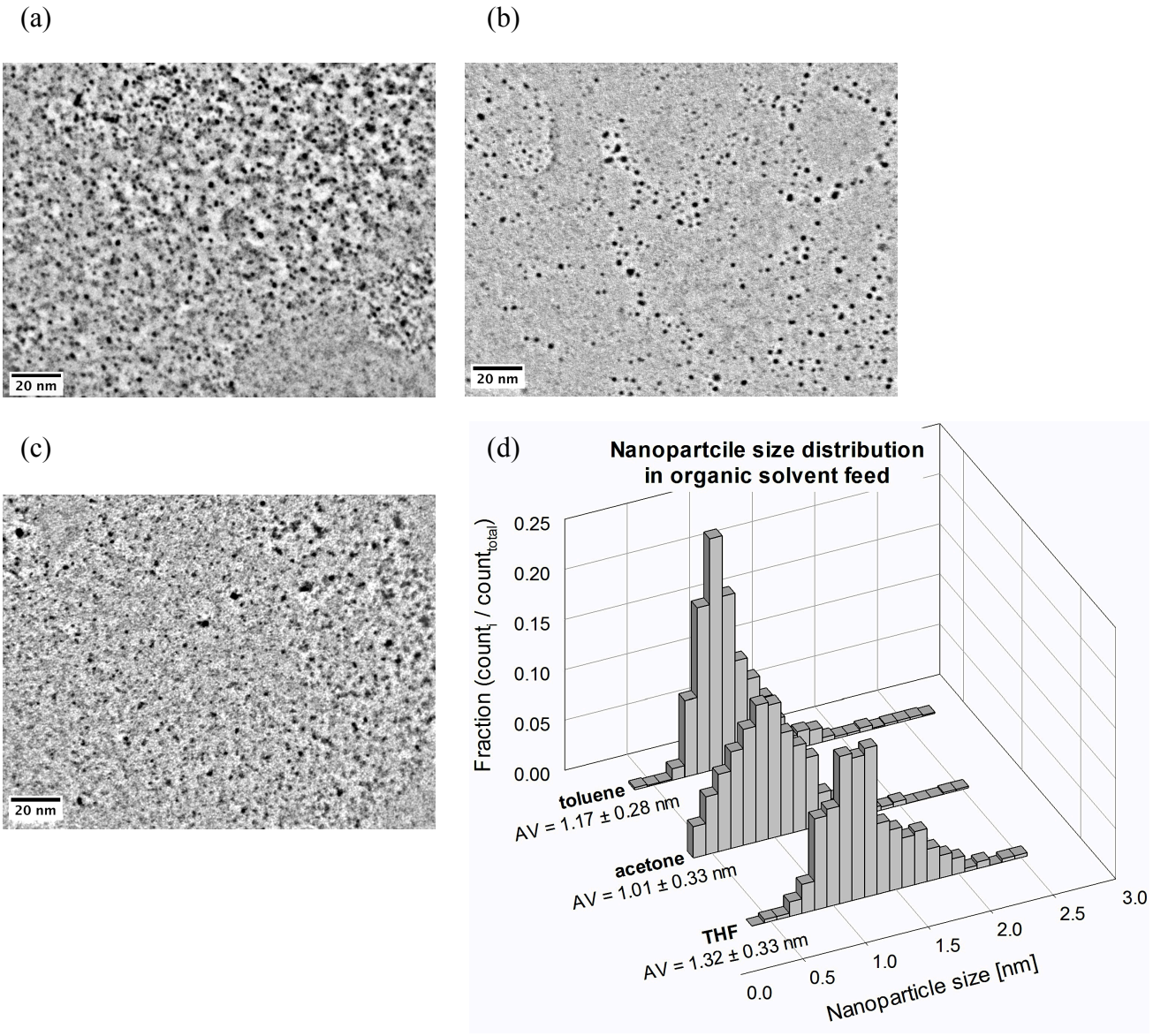


Figure 3.5 TEM characterisation of OsO_2 NP stabilised with PS in various solvents.
(a) TEM image of NP sampled from toluene, (b) THF, (c) acetone. (d) NP size histograms.

Although the difference in the mean NP size is notable, the focus should be rather on the size range. The distributions presented in Figure 3.5d show that the NP size extends from 0.4 nm to approximately 2.5 nm, indicating that they are in a suitable size range for probing the NF pores.

The morphology of the NP differed in terms of the type of solvent used to stabilise the colloids. Table 3.1 lists several physical properties of THF, acetone, and toluene that may be related to NP stabilisation using PS. High vapour pressure and low solubility could be associated with PS precipitation, causing the stabilisers to cluster, and effectively leading to obstructing signals from the NP required to generate high magnification electro-micrographs. Given that acetone has the highest vapour pressure and the highest difference between the polymer and solvent solubility parameters among the three solvents, these properties could be related to rapid precipitation of PS. However, the parameter that may have the strongest impact on the NP morphology is dielectric constant. Since acetone has significantly higher dielectric constant than THF and toluene, the dielectric strength may be responsible for moderate aggregations of the NP in this solvent. With regards to this effect, THF and toluene is recommended as solvents to disperse OsO_2 NP and test the membranes.

Table 3.1 Solvent physico-chemical parameters and solubility difference values between solvent and polystyrene (at 25°C)

Property	THF	acetone	toluene	Ref.
Vapour pressure (mmHg)	143	181.7	22	[211]
Viscosity (cP)	0.456	0.306	0.550	[211, 212]
Solubility difference between solvent and PS ($MPa^{1/2}$)	3.8	4.9	3.1	[213]
Dielectric constant	7.6	20.7	2.4	[214, 215]

The smallest NP detected in the TEM projections had a size of 0.4 nm. Given that OsO_2 single crystals have a tetragonal structure, with lattice parameters of a = 4.500 ± 0.004 Å and c = 3.184 ± 0.004 Å, and a unit cell volume of 64.476 $Å^3$ [216], the volume of a 0.4 nm diameter OsO_2 NP would be 64 $Å^3$, assuming that the diameter corresponds to an average lattice

parameter of the tetragonal structure. This implies that the smallest NP revealed by the TEM corresponds approximately to a single unit cell of OsO_2. Furthermore, using a material density of 11.44 g cm^{-3} [217] and the OsO_2 MW of 222.23 g mol^{-1}, calculations were performed to estimate that a 0.4 nm particle theoretically consisted of two OsO_2 molecules. The size distribution from 0.4 nm to 2.5 nm, as shown in the histograms in Figure 3.5, suggested that these NP were suitable for probing NF membranes with various pore sizes. Finally, a stable dispersion was achieved by fabrication of the OsO_2 NP with use of low MW PS. These stabilisers, solvated by (preferably) toluene or THF, were able to disperse the colloids.

3.3.4 Probing the nanopores

In order to identify transport–active pores, OsO_2 NP were filtered through the membranes from the open side towards the skin layer (Figure 3.4d) on hypothesis that larger NP would be retained at the transition between the open region of the membrane and the skin layer, while smaller NP would enter the skin layer. These smaller NP might pass right through the skin layer pores into the permeate, or be trapped in this layer itself. Filtration experiments were carried out from the open side of the membrane, resulting in gradual filling of transport–active pores, and so the quantity of OsO_2 NP occupying any region is related to the pore size and porosity of the region. Hence, a significantly lower number of the NP enter the skin layer, and the majority of them occupy the microporous region. Because polymer chains are entangled more tightly, the skin layer is much denser; and only small NP (with sizes equal or smaller than the pore sizes) can be lodged into the interstitial spaces between the polymer molecules.

Figure 3.6a schematically demonstrates the structure of a polymeric region with OsO_2 NP lodged into spaces between polymer molecules. Whether NF scale pores in membranes prepared from glassy polymers are fixed cavities formed in the polymeric network, or are free volume

present between single polymer chains, is yet to be established. The imaging approach hypothesised that a NF pore is a cavity formed between entangled bundles of polymer chains forming the skin layer. The width of a permeation pathway within a single interstitial space, which is transport–active, is then considered to be the "pore size". Possibly not all of the pores become blocked by NP, since some NP pass to the permeate as OsO_2 NP were found downstream. Because the polymer phases are "transparent" in the electro-micrographs, the pore size is estimated by mapping and quantifying the size of OsO_2 NP distributed within the porous phases of the polymeric matrix.

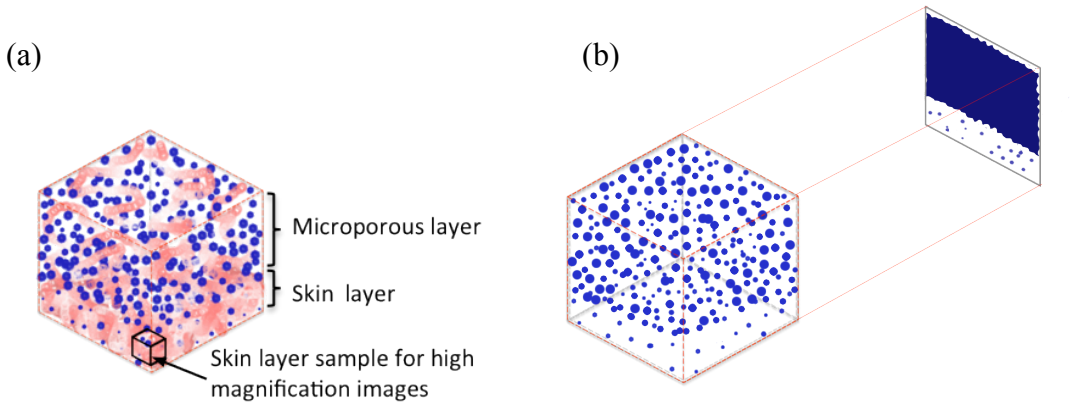


Figure 3.6 Conceptual model of the membrane structure with lodged NP and the corresponding projection.

(a) 3–D diagram of the polymer chain arrangements (red) densely packed at the skin layer and loosely at the microporous region. OsO_2 NP (blue) occupy the interstitial spaces between the polymer macromolecules. (b) Expected nature of a 2–D projection of a specimen consisting of two regions. The region highly packed with the NP results in an intensive overlap of the NP resulting in a non-contrast projection; the region moderately packed with the NP provides good imaging contrast between individual projections of NP and the polymer. The difference in contrast between the microporous region (highly packed) and the skin layer (moderately packed) is used to estimate the skin layer thickness.

3.3.5 Electron microscopy projection mechanisms

TEM imaging was carried out on samples collected from the permeate, feed, and the membrane cross-sections. It is relatively straightforward to image and measure the NP size in dilute solutions (feed and permeate); however, it is challenging to characterise the multi-phase system comprising the membrane with lodged NP. This is because specimens need to be microtomed down to thicknesses below 100 nm, and a 3–D sample of the NP captured in the bright field image is transformed to 2–D statistical projection averaged over the entire specimen [185]. The skin layer, due to its dense structure, is expected to contain a small/moderate number of NP, in comparison to the microporous region, whose open structure permits lodging of a significantly higher density of NP. Thus, two distinctive regions are expected in the 2–D projection (Figure 3.6b): dark (due to high density packing of the NP that overlap on the image) and contrasted dark shapes on light background (dark shapes due to resolved images of NP from moderate density packing of the NP). The microporous layer, which is densely packed with NP, corresponds to an information poor region, because the overlapping particles resulting in a lack of contrast. The skin layer, in contrast, contains a moderate number of NP allowing the 2–D image to capture individual shapes. In turn, the difference in the projected intensities generates a sufficient contrast to measure the skin layer thickness.

To further elucidate and explain the information extracted from the high magnification TEM images, Figure 3.7 shows various possible projections that could be generated from different spatial arrangements of NP lodged in a 3–D specimen. The diagrams ignore bright low-contrast pattern typically generated from the polymers, since their amorphous nature does not provide any information in regards to mapping of the NP. The first possible scenario demonstrated in Figure 3.7a is for a single NP in the specimen, which would result in a single circular object visible in the electro-micrograph. Figure 3.7b demonstrates an arrangement where

particles perfectly align in a parallel direction to the electron beam, producing an image a single object. Figure 3.7c shows the 2–D projection of overlapping NP, resulting in a projection characterised by irregular and enlarged shapes in comparison to the original objects. Figure 3.7d shows an image of a specimen containing only a few NP, corresponding to a projection in which the shapes either overlap or remain separated. This example demonstrates the most probable imaging scenario for membranes M1 – M3, where a moderate number of NP are distributed within the specimens from the skin layer. The pore size distribution is estimated by measuring diameters of the circular–shaped objects acquired in the projections using the image analysis algorithm developed for the purpose of this study (see Section 3.2.8 for description). The last scenario (Figure 3.7e) shows a block densely packed with the NP. The projection suffers from the overlapping effect, and the poor contrast generated from the sample does not allow for good quality imaging and characterisation of the objects in the 3–D sample.

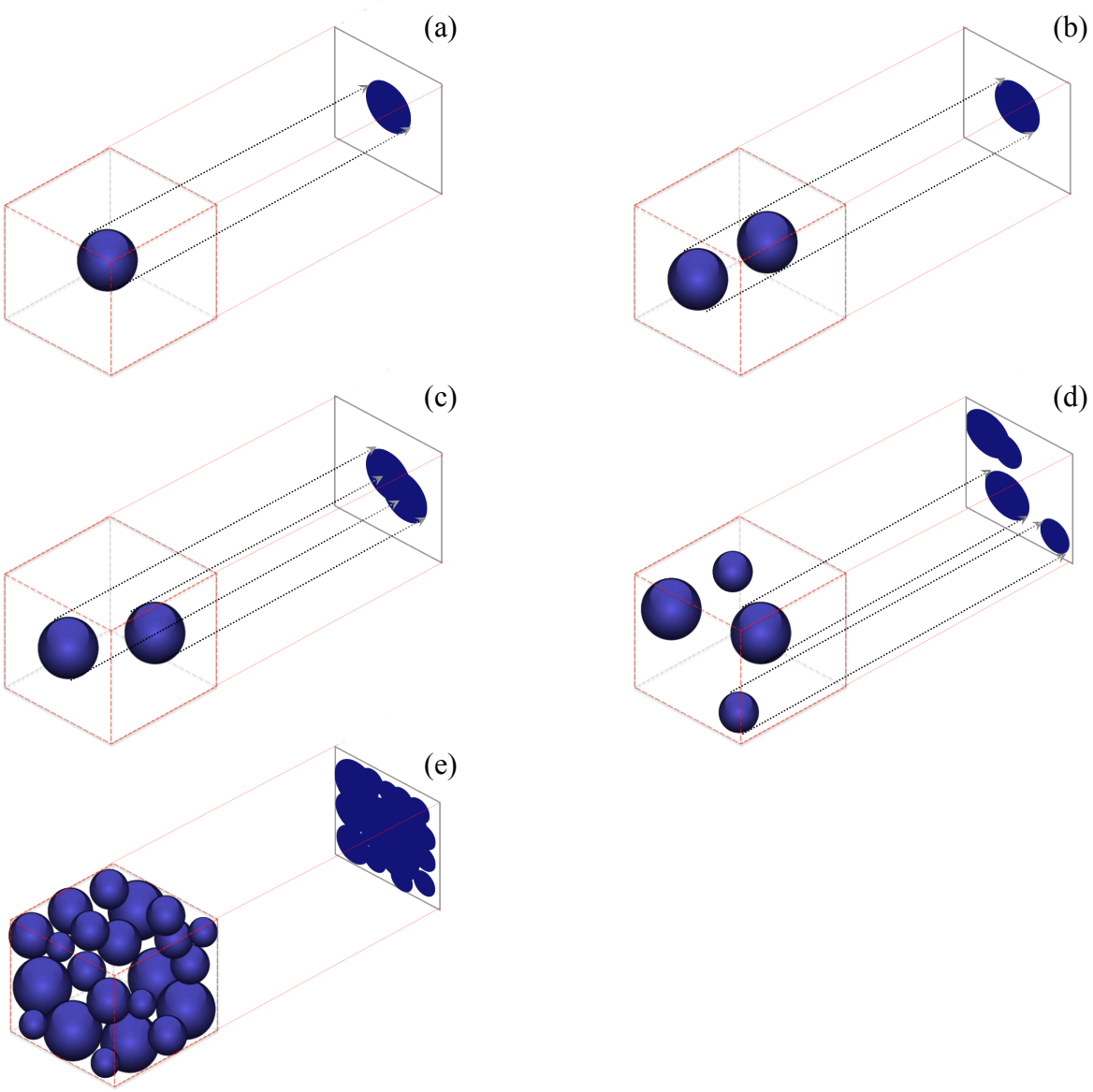


Figure 3.7 Diagrams of possible particle arrangements in the 3–D polymer blocks sampled from the membrane cross-sections, and their corresponding high magnification projections.

(a) An individual particle corresponds to an individual object. (b) Particles of the equal size overlap perfectly, and thus a single object is captured. (c) Particles do not overlap perfectly, resulting in an enlarged non-circular projection. (d) The system contains both overlapping and individual separated particles. In this case the circular objects can be selected for measuring of their diameters in the corresponding projections. This is the most probable scenario within the membrane skin layer. (e) A sample fully packed with the particle results in a projection that does not allow individual objects to be distinguished. Polymer phases in the electro-micrographs are “transparent”, and so they are visible as bright regions; therefore, for simplicity the polymer chains are not included in the diagrams. For demonstration purposes the magnification effects are also neglected.

Electron microscopy of the complex specimens, such as the embedded high–contrast NP within a polymeric film, requires sample preparation methods and imaging conditions to be constant. Variations in any of these parameters can mislead interpretations of the imaged features. The contrast described by a relative phase shift ($\Delta\varphi$), generated from the sample by scattered electrons, can be altered by the specimen thickness according to Eq. 1.35. This equation highlights the importance of maintaining constant specimen thickness, especially for the comparative analysis of amorphous materials, as variations can lead to erroneous interpretation of the contrast origin [218]. In this work, the ultramicrotomed nominal specimen thickness was set at 50 nm, with an apparatus tolerance of ± 5 nm. Therefore, the expected variations in contrast are attributed to physical properties of an imaged object. Furthermore, feature size can be dependent on the defocus value. Here, the objective lens defocus was set close to the Scherzer defocus (Δf_{Sch}) (Eq. 3.2) [218], as this is known to be the optimal value to reveal features with low spatial frequencies;

$$\Delta f_{Sch} = -1.2\sqrt{C_s \lambda_e} \qquad \textit{Eq. 3.2}$$

where C_s is the spherical aberration coefficient and λ_e is the electron wavelength. The calculated value for the microscope employed was estimated to be –62.4 nm, and thus for all images the objective lens was defocused by –64 nm (the value is related to the multiplicity of the single incremental step on the focus knob). Since the electro-micrograph is a projection of a 50 nm thick multiphase polymer–polycrystalline NP containing specimen, interpretation of the contrast requires good understanding of the electron scattering and imaging conditions. Defocusing is a commonly employed method to convert the phase signal into the amplitude [170, 178] to reveal morphology of block polymers [179-181], lamella in semicrystalline polymers [182, 183], or inorganic–organic composites [184]. In this work the images of the specimens were acquired slightly out of focus, maintaining identical imaging conditions each time, to phase shift the

amplitude of scattered electrons and generate a contrast with OsO_2 NP embedded in the polymer matrix. Owing to the high Z–number of osmium and the high electron beam voltage of 200 kV, sufficient contrast at high magnifications could be generated; however, this somewhat compromises sharpness of the polymer phases due to beam damage resulting in blurry contours of the NP rich domains.

3.3.6 Skin layer thickness

The asymmetric structure of the membrane cross-sections can be confirmed through the observed decrease in density of OsO_2 NP with depth (Figure 3.8a–c). The skin layer is indicated by the lighter areas located nearer to the surface. It appears due to a significant accumulation of the NP in the microporous region – skin layer transition, implying that the skin layer acts as a semi-barrier reducing transport of OsO_2 NP. The skin layer thickness measurements were taken from the images at points at around 20 nm distanced from each other, and this procedure was repeated on at least three independent samples prepared for each membrane. The measured values of the skin layer thickness are as follows: membrane M1 – 76 ± 10 nm, M2 – 116 ± 19 nm, and M3 – 165 ± 14 nm. Because the measurements were taken at several points of the same image and from independent samples, pooled standard deviation (s_p) was calculated using Eq. 3.3:

$$s_p = \sqrt{\frac{\sum\left(N_i - 1)\sigma_i^2\right)}{\sum N_i}}. \qquad \textit{Eq. 3.3}$$

N_i is number of measurements taken from each image and σ_i is standard deviation calculated for data obtained from each image. The high standard deviations present in the skin layer thickness are considered to be attributable to the nature of the membrane structure. Polymer chains forming the membrane tend to be progressively entangled towards the membrane surface. This

explains why there is no definite border between the skin layer and the more open interior layers. One can observe in the image of membrane M1 that there is more significant transition from the dense layer to the microporous region. The skin layer of this membrane is thinner, denser, and OsO_2 probes retained at its border accumulate to a greater extent resulting in higher contrast.

Figure 3.8d shows a graphical representation of the measured values of the skin layer thickness. The means were analysed using ANOVA test followed by the multiple comparison Tukey's test that through computing HSD value of 18.94 at $\alpha = 0.05$, and 24.55 at $\alpha = 0.01$, estimated p–value at these two levels to be less than 0.01; thus, the test implied that the means were statistically different. Next, by observing the trend of the investigated membranes, the skin layer thickness appears to be associated with the dope solution composition. The experimental methods were identical in terms of the membrane fabrication, TEM sample preparation, and imaging; the only one parameter which changed was a DMF:dioxane ratio in the dope solution. The data suggests that the skin layer thickness decreases with increasing dioxane content. Soroko *et al.* [31] studied the polymer–solvent interaction parameters for the P84:DMF:dioxane system and reported that the polymer solubility decreases with increasing dioxane content. At the macromolecular level, the solubility parameters can be translated into the degree of polymer entanglement; the lower the solubility parameter, the more entangled and compacted the polymeric structures are. This mechanism occurs due to the response of polymer molecules to a poor solvent, which forces them to coil up and surround themselves with other polymer segments to reduce their contact surface area with the non-solvent [72]. Consequently, the skin layer of a membrane prepared from the higher dioxane content dope solution is more compact, denser, and thus it is thinner.

The skin layer thicknesses determined in this study can be compared with PALS performed on the P84 co-polyimide membranes. Cano-Odena and co-workers [63] reported a

separation layer thickness of around 70 nm, which is within the range of the values measured in this study.

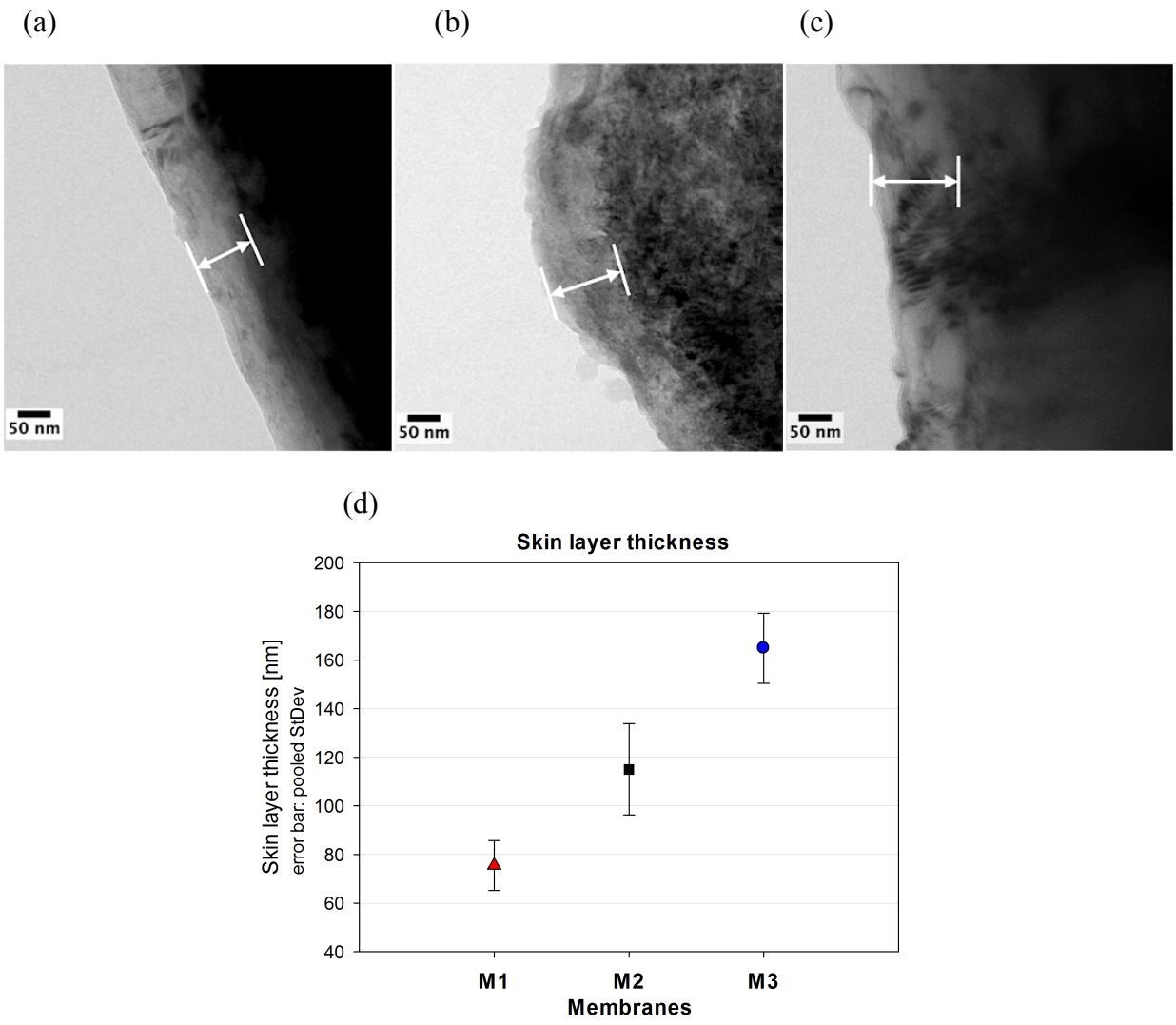


Figure 3.8 Measurement of the skin layer thickness.

TEM images of membrane cross-sections with samples including the skin layer and the microporous region. Thickness of the skin layer can be measured owing to the contrast generated by differences in density of lodged OsO_2 NP in the open and dense regions. (a) Membrane M1 with the skin layer thickness of 76 ± 10 nm. (b) Membrane M2 – 116 ± 19 nm. (c) Membrane M3 – 165 ± 14 nm. (d) Graphical representation of magnitudes of the skin layer thickness shows that the values are statistically different (multi-comparison Tukey's test, p–value < 0.01).

3.3.7 Mapping of polymer porous phases

Figure 3.9a–c shows images of the skin layer. Dark areas (referred as 'preferential transport paths') can be clearly observed, suggesting an increase of OsO_2 NP content in these regions. OsO_2 NP are thought to accumulate along the preferential transport paths due to gradual reduction of pore sizes towards the membrane surface. These features are consistently observed in the cross-sectional images of membranes M1 – M3 with the nanoprobes filtered through the membrane from the open side (Figure 3.9a–c), and so their origin is asserted to be related to the membrane structural properties, rather than to coincidental marks arising from sample artefacts, thickness variations or contamination.

Because there was a risk of image misinterpretation, additional control studies were carried out. The first experiment aimed at identification of the preferential transport paths. If a solution carrying the OsO_2 NP is permeated from the skin layer–side (tight–side filtration), dark regions would not occur, since the pore size increases with depth from the surface, and the NP would not be expected to accumulate. To test this hypothesis, membrane M1 was subjected to a tight–side filtration with a toluene dispersion of OsO_2 NP. The resulting electro-micrograph presented in Figure 3.9d does not reveal the presence of preferential transport paths within the skin layer. Rather, dark regions are observed in the resin used to secure the membrane, which suggests that the larger NP remain at the membrane surface and cannot penetrate the tight separating layer. This implies that, when probing the pores from the tight side, only the small NP were able to pass through the skin layer and enter the membrane. These NP simply permeated through the membrane with little accumulation, since the deeper interior regions are more open than the skin layer. This sample provides further indication that the skin layer has a significantly denser structure in comparison to the layers underneath.

To bring additional evidence that the maps of OsO_2 NP correspond to the distribution of pores in the skin layer, and to show that the obtained results are not artefacts of the imaging technique, an additional control experiment is reported. A non-porous membrane (a dense film), of which the casting solution had an identical chemical composition to membrane M2, was prepared. This was fabricated by so-called 'dry phase inversion' in which solvent evaporates from a cast film at elevated temperature resulting in a homogenous non-porous structure [219]. Because this film has a non-porous structure, no flux was expected, and so no OsO_2 NP were expected to be incorporated. Consistent with predictions, no flux was registered while the membrane was used to filter a feed containing OsO_2 NP. A cross-sectional image of the non-porous film (Figure 3.9e) confirms that there are no dark regions distributed across the structure. This in turn confirms that the observed domains in Figure 3.9a–c are attributable to OsO_2 NP trapped in the transport–active pores of the skin layer, and are not artefacts of the imaging technique employed.

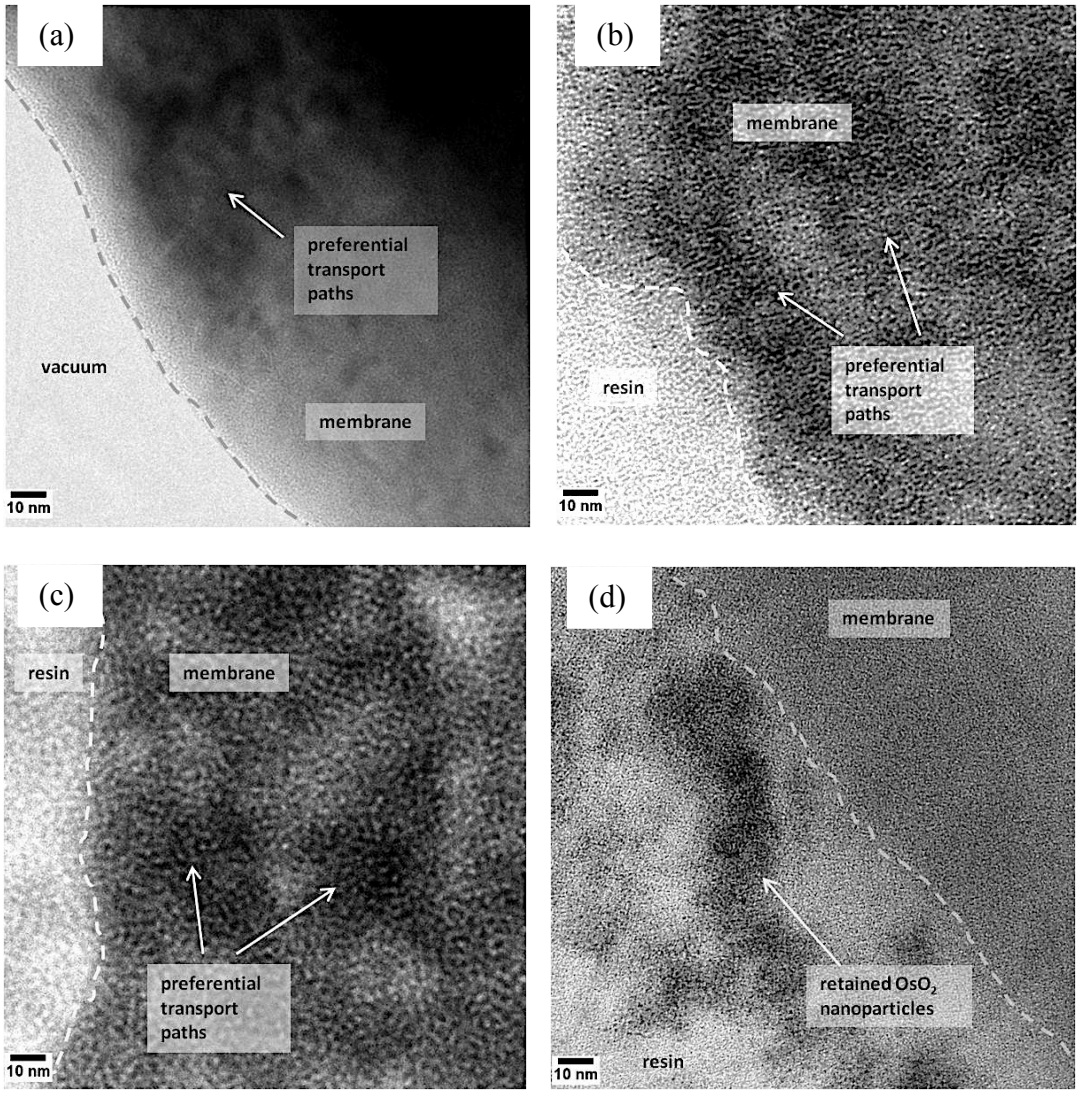


Figure 3.9 TEM images of skin layer cross-sections.

(a),(b),(c) OsO_2 NP filtered from the open side of membranes M1, M2, and M3, respectively (black areas correspond to NP rich regions – porous domains). (d) OsO_2 NP filtered from the skin layer side of membrane M1, which retained the majority of the NP. (e) Dense film through which OsO_2 NP did not penetrate because of the non-porous structure. (a) Resin detached from the membrane surface due to the high voltage of the electron beam; in (b) – (e) the resin remains attached to the sample; regardless of the presence of the resin next to the specimen, the skin layer structure remains the same. The dashed line is drawn to distinguish the membrane from the resin or vacuum.

3.3.8 Effect of specimen thickness on imaging contrast

According to the schematic drawings included in Figure 3.7 objects within a specimen can overlap and the resulting projection contrast may be insufficient to distinguish individual features; therefore, it is important to prepare samples for the images that are as thin as possible. Ideally the sample thickness should be within the size range of a feature of interest. For the purpose of this study a preferred specimen thickness would be below 2 nm, since the NP are within this size range. However, sample microtoming to achieve this thickness is not feasible, and instead the optimised sectioning thickness of 50 nm was consistently used to prepare the membrane specimens. There are several drawbacks related to the specimen thickness that can occur in the membrane systems: features overlapping effect, beam irradiation, mechanical damage during microtoming of thin specimens, and incoherent scattering of the electrons from amorphous polymeric phases. First, the microtoming of specimens below 50 nm was found to be very difficult, since the sectioned films were vulnerable to mechanical damage, tended to fold, and as a result they were often not suitable to perform electron microscopy. Secondly, thin specimens were extensively affected by the electron beam due to irradiation causing instability and drifting, which led to astigmatism and poor resolution. In spite of these difficulties, the images of the thinner specimens proved that the OsO_2 NP were more easily distinguishable, since they overlapped to a lesser extent. They provided good contrast in comparison to thick specimens of which multi-phase morphologies were barely captured.

To visualise this effect the cross-sectional images of membrane M1, subjected to the tight–side filtration with OsO_2 NP followed by sectioning at the thickness of 30 nm and 80 nm, are presented in Figure 3.10. In the 30 nm–thick specimen (Figure 3.10a) the NP can be distinguished both within the resin, where they are retained, and within the skin layer, into which they were lodged. In contrast, the 80 nm–thick specimen (Figure 3.10b) does not provide a

sufficient contrast to reveal individual NP lodged into the membrane. The lack of contrast is because the objects of interest overlap and amorphous polymeric phases scatter electrons in random directions hindering the transmitted signals from the NP. However, thicker specimens are significantly more stable under a high accelerating voltage, and remain undamaged by ultramicrotomy. These compromises led the next experimental step to select a sectioning thickness of 50 nm. With this thickness, after applying image processing methods used to increase the signal–to–noise ratio, the essential information was extracted and so at least some of the NP within the membrane sample could be mapped.

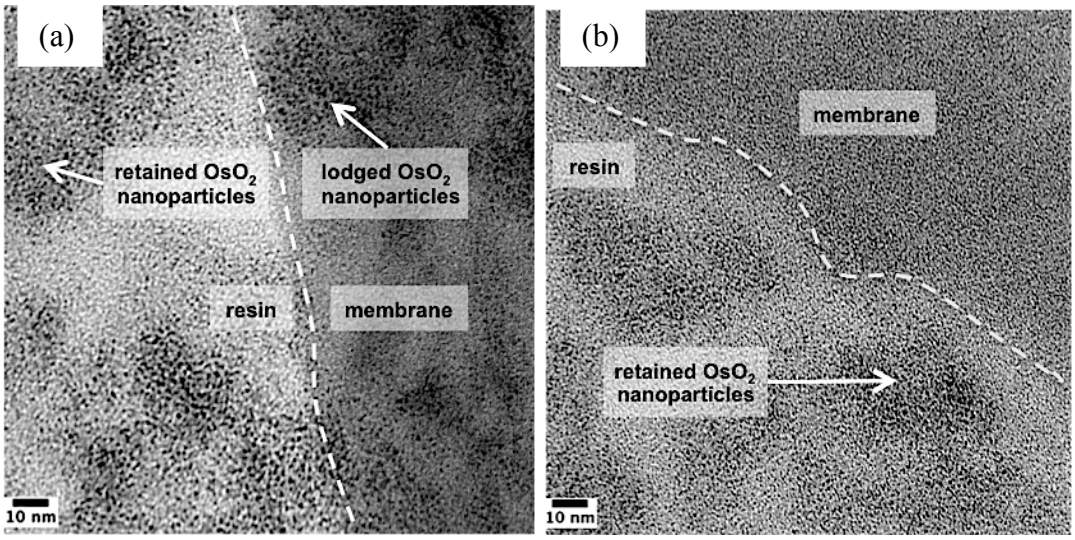


Figure 3.10 Effect of the specimen thickness on image contrast.

TEM images of the skin layer of membrane M1 microtomed at the thickness of (a) 30 nm, and (b) 80 nm. Specimen (b) does not have sufficient imaging contrast to allow projection of individual OsO_2 NP.

3.3.9 Pore size estimation

High resolution image analysis was performed on samples from membranes M1, M2, and M3. The cross-sectional images taken from the membranes' skin layer show three different morphologies that can be characterised by the size of the NP lodged in the interstitial spaces. Membrane M1 (Figure 3.11a) appears to have the finest arrangement, membrane M2

(Figure 3.11c) – medium, and membrane M3 (Figure 3.11e) – the coarsest with the largest black areas corresponding to the porous regions. The pore size distributions were estimated from the black circular areas found in the high magnification images (Figure 3.11a,c,e) processed by 'FFT band pass filtering' to remove low frequency noises arising from the beam irradiation. The pore size is assumed to be equal to the diameter of black circular areas corresponding to regions with distinctive OsO_2 NP visible in the images. This assumption has obvious pitfalls, as the transport mechanism of the NP through the pore is unclear. Specifically, it is unclear whether the particle is being carried in a convective flow of solvent, or is moving by diffusion. While the latter may seem more probable, recent work [220] has showed that the flow of solvents, with molecular diameters in the range of 0.3 – 0.7 nm, through pores of less than 1 nm appears to follow the Hagen–Poiseuille equation, *i.e.* convective flow. The experimental approach assumes that a free volume space, where a particle lodges, to be a pore, which is in the size range or larger than the particle size. Thus, the quoted pore sizes are crude estimates, and should be interpreted as such.

With this approach, the mean pore sizes were estimated to be 0.68 ± 0.13 nm, 0.98 ± 0.16 nm and 1.04 ± 0.24 nm (see Figure 3.11b,d,f for histograms), for membranes M1, M2 and M3, respectively. The pore size distribution was also measured for the membrane M1 after tight side filtration (filtration from the membrane surface side) and found to be 0.69 ± 0.16 nm. The results implied that there was no significant change in the pore size when measured with the NP lodged either from the open or tight side. However, a dramatic increase in flux was observed when the membrane was subjected to open–side filtration in comparison to tight–side filtration.

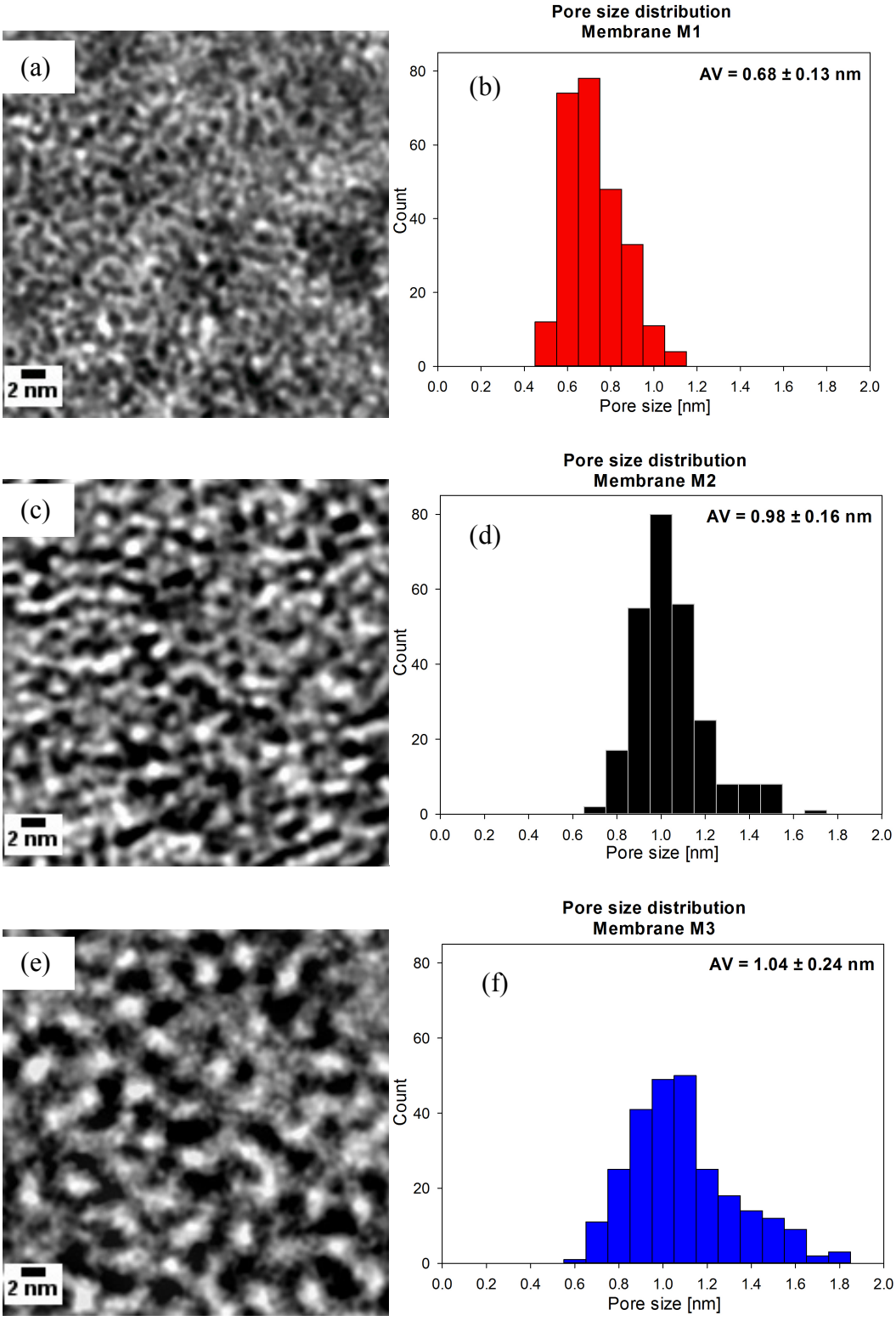


Figure 3.11 Nanoporous structure of the skin layer cross-sections and the pore size distributions.

(a),(c),(e) High magnification TEM images revealing pore size estimates for membranes M1, M2 and M3, respectively. (b),(d),(f) Estimated pore size distribution in the skin layer for membranes M1, M2 and M3, respectively.

The FFT spectrum combines all image intensities and shows them in a frequency profile. The spectrum helps to analyse repetitively occurring characteristic features in a TEM image. As further control information, analysis of 2–D FFT power spectra (Figure 3.12 shows original unprocessed electro-micrographs with corresponding 2–D FFT power spectra) demonstrates that the image of the non-porous dense film (Figure 3.12b) was affected by astigmatism, whereas other membranes show a typical circular FFT ring (see Figure 3.12d,f,h for membranes M1, M2, M3 lodged with OsO_2 NP, respectively). These discrete spectra provided further evidence that the morphologies observed through the TEM imaging of samples M1 – M3 is due to the nanoporous nature of the material.

Overall, one may accept that there are many pitfalls in the interpretation of TEM images of polymer systems due to electron scattering interferences and sample preparation artefacts. Furthermore, one may also acknowledge that the method used for estimating the pore size based on the observed 2–D images of the NP may create systematic offsets in the final estimates. However, these effects were attempted to be discounted through control experiments and repeating the analyses. When considering electro-micrographs shown in Figure 3.9 – 3.12 an assertion that artefacts would affect all images equally is accepted, thus, the reader's attention is wished to focus on the differences. The interesting finding is that the clear variations in the membrane nanostructure between the samples, which are derived from the images, can be correlated in a logical way to membrane functional performance (flux and rejection).

Table 3.2 Summary of the quantitative features acquired by the nanoprobe imaging technique

Membrane	Pore size (nm)	Polymer phase size (nm)	Skin layer thickness (nm)
M1	0.68 ± 0.13	0.93 ± 0.18	76 ± 10
M2	0.98 ± 0.16	1.68 ± 0.27	116 ± 19
M3	1.04 ± 0.24	3.23 ± 0.75	165 ± 14

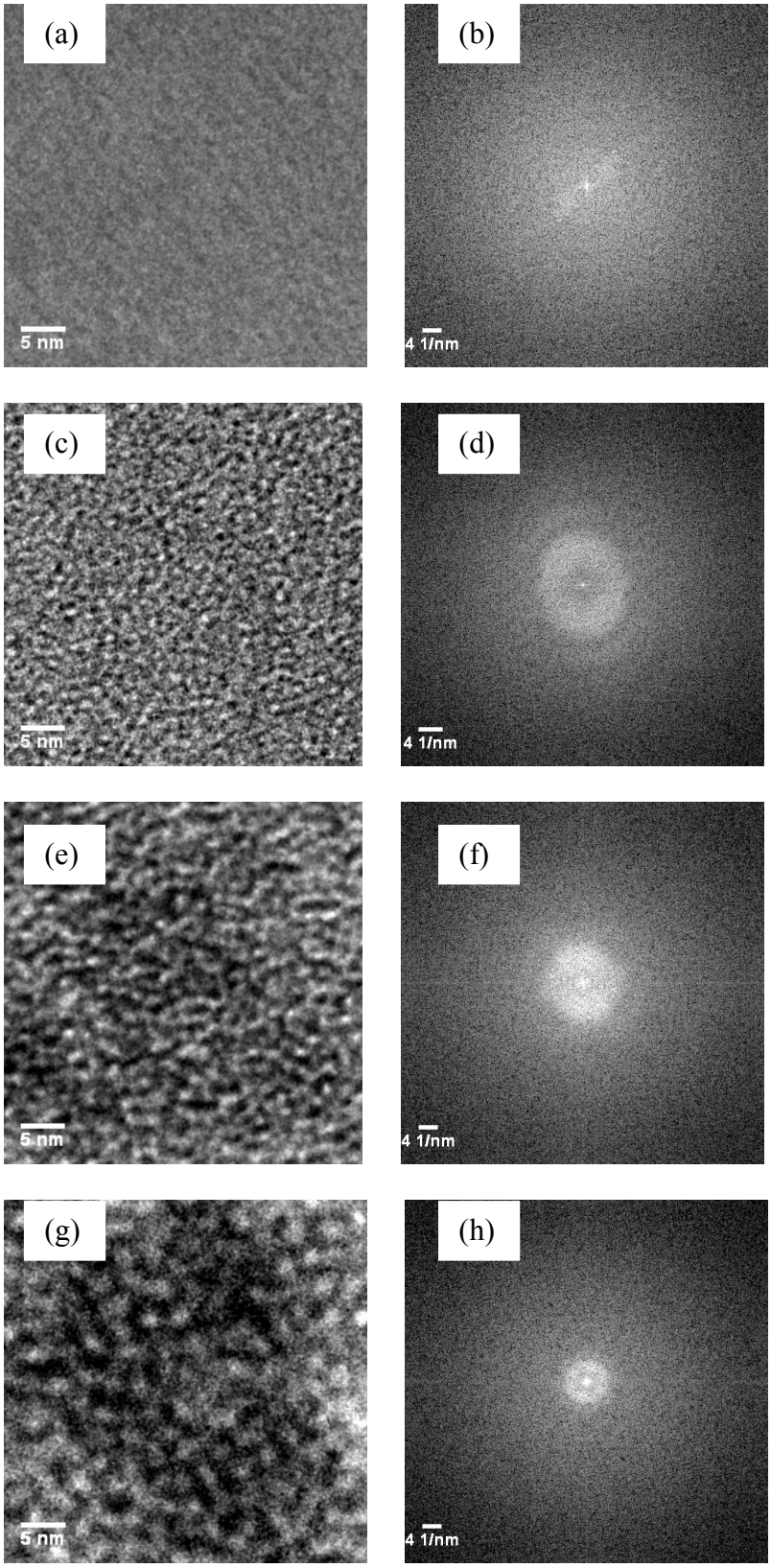


Figure 3.12 Cross-sectional morphologies and corresponding 2D–FFT power spectra.

(a),(b) Non-porous dense film (without OsO_2 NP). (c),(d) Membrane M1. (e),(f) Membrane M2. (g),(h) Membrane M3. Membrane M1 – M3 contain lodged OsO_2 NP.

3.3.10 Consideration of molecular architecture of membrane separating layer

In addition to the pore size distribution, the characterisation quantifies polymer phase dimensions (which correspond to bright regions in the images). On this basis, the polymer phase region is believed to be comprised of spirally entangled polymer chains forming a bundle. The maximum theoretical diameter of the P84 co-polyimide macromolecule was estimated to be 0.664 nm under the assumption that the polymer chain can be described as a flexible tube with a diameter and a length. The results obtained through the TEM imaging bring speculations that each bundle corresponds to several polymer chains. Therefore, the polymer phase size is correlated with the thickness of the polymer chain bundle, for which spatial dimensions can be evaluated through the 2–D FFT power spectra (Figure 3.12) and the characteristic lengthscale (ξ) calculated using the following equation:

$$\xi = \frac{2\pi}{q_{\max}}; \qquad \text{Eq. 3.4}$$

where $q_{max,i}$ is a wave number corresponding to the maximum Fourier intensity of the power spectrum peak estimated using a radial average profile of the 2–D FFT power spectrum (Figure 3.13). The estimated characteristic lengthscale ξ of 1.61 nm, 2.66 nm, and 4.27 nm was estimated for membranes M1, M2 and M3, respectively. Assuming that ξ is a sum of polymer and pore phase lengths, the spatial dimension of polymer phase (d_{pol}) can be estimated using the following expression:

$$d_{pol} = \xi - d_p \qquad \text{Eq. 3.5}$$

where d_p is the mean pore size determined for each membrane using TEM. Therefore, d_{pol} is equal to the following values: 0.93 ± 0.18 nm, 1.68 ± 0.27 nm and 3.23 ± 0.75 nm for membranes M1, M2 and M3, respectively.

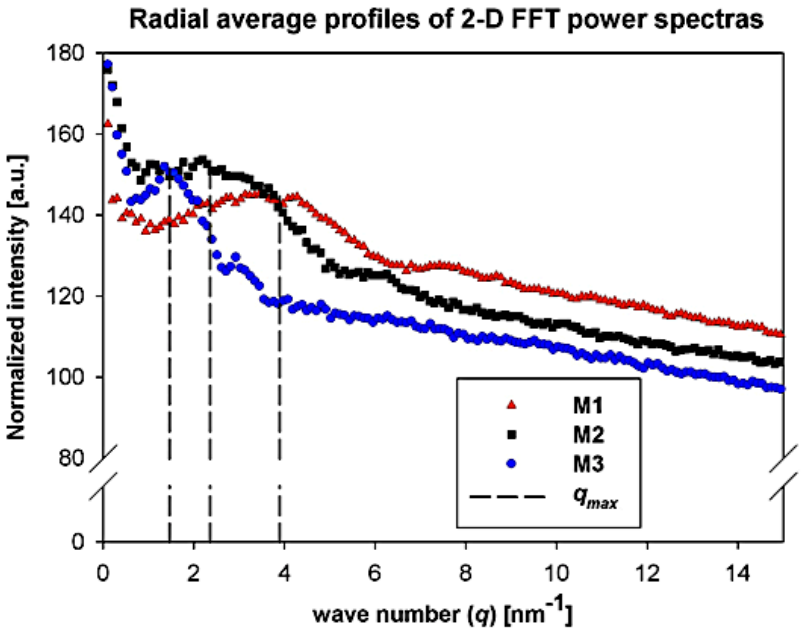


Figure 3.13 2–D FFT power spectra analysis.
Fourier intensity tuned by wavenumber q related to corresponding membrane morphologies.

3.3.11 Solute transport through membrane M1

The mechanism of solute transport through NF membranes still remains unclear, although it is frequently discussed in the literature [94, 221]. Nanoprobe imaging of NF pores may progress understanding of molecular transport through the membrane. The size distribution of NP in the permeate and the feed following filtration of OsO_2 NP through membrane M1 were measured by TEM. Figure 3.14 presents images of OsO_2 NP from the feed solution (Figure 3.14a), and permeate solution (Figure 3.14b). It is clear that the size distribution of OsO_2 NP in the permeate is within the pore size range of membrane M1; furthermore, both the pore and permeate NP distributions correspond to the lower end of the size range of OsO_2 NP present in the feed solution (Figure 3.14c). These analyses, thus, suggest that separation through the NF membrane fabricated from P84 co-polyimide is based on a size exclusion/steric mechanism,

where depending on size, larger NP are retained, while smaller ones permeate through the pores to the permeate.

Due to the possibility of characterising a membrane *in situ* and imaging the solute transport pattern the following hypothesis is proposed: nanometre pores can be described as spaces between polymer chains into which solutes enter while subjected to a transmembrane pressure gradient. Nanometre pores are uniformly distributed across the skin layer and are related to the degree of polymer entanglement and interspatial arrangement. The pores primarily determine the flux and rejection of the membrane. The porous structures are believed to form during liquid–liquid demixing, and consequently, are related to conditions of the phase inversion process. Previous studies on the effect of membrane preparation conditions on separation properties showed that varying the ratio of solvent to co-solvent in the dope solution had a greater impact on the NF performance of the membranes than changing polymer concentration [29]. Given that nanopores are uniformly distributed in the skin layer, the study has rejected the hypothesis that pores are interstitial spaces between nodules, where lower chain entanglement is present [72]. If nodules are dense spherical clusters of collapsed polymer chains (approximate size 20 nm [69]) and transport occurs between them, the distance between differentiated permeation transport paths would have corresponded to 20 nm given the size of the polymeric clusters. If this hypothesis were true these areas would have been visible, since the sample thickness was only 50 nm and contrast between nodules and interstitial spaces would have revealed their occurrence. In addition, the NP distribution within the skin layer, feed and permeate elucidates NF transport behaviour. This has been a subject of much debate in the membrane science field. The experiments suggest that the separation mechanism, at least for neutral solutes, is based on particle exclusion by steric hindrance mechanisms in the membrane skin layer.

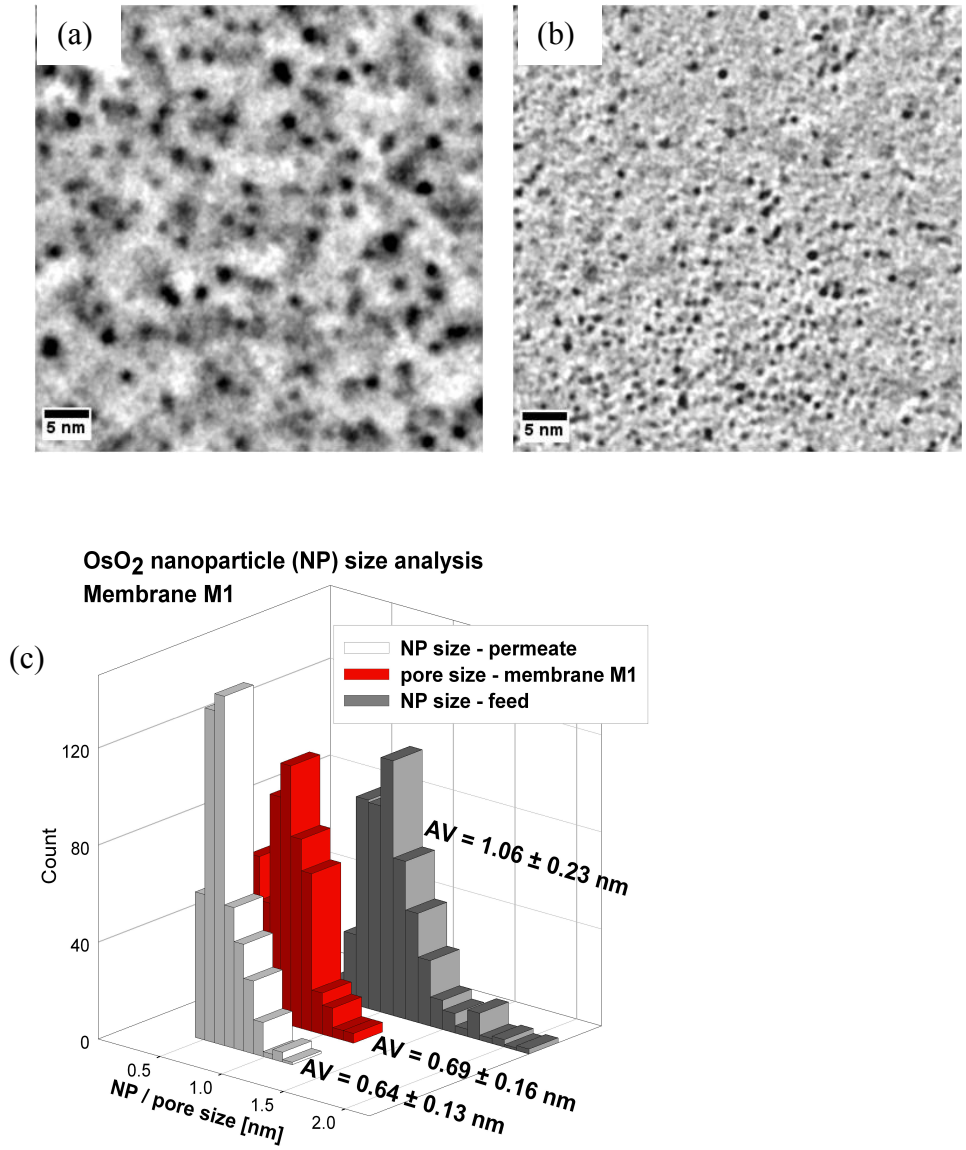


Figure 3.14 Separation of OsO_2 NP using membrane M1.

(a) Sample of OsO_2 NP from the feed. (b) OsO_2 NP found in the permeate. (c) Comparison of OsO_2 NP size distribution in the permeate, pores of membrane M1, and the feed.

3.4 Conclusions

The experimental work described in this chapter has demonstrated a new characterisation technique, which allows for estimation of pore size distributions in polymer films at sub-nanometre resolution. It has unique application to membranes as *in situ* probing is performed in conditions identical to the filtration process. A high contrast nanoprobe, *i.e.* OsO_2 NP, suitable to fill the pores in NF membranes and to provide contrast in TEM, was fabricated and tested. The lodged OsO_2 NP into porous regions in the skin layer generate sufficient contrast to measure the transport–active pore size. Hence, the significant advantage of this method is possibility to analyse the pores contributing to solvent and solute transport unlike other conventional membrane characterisation techniques.

A correlation between the pore size distribution and the separation properties for a range of OSN membranes prepared from the same polymer has been found. This correlation and the data of particle size analysis in feed and permeate have suggested that the separation mechanism in NF membranes fabricated from P84 co-polyimide is based on size exclusion of the permeating solutes by their size. Therefore, the next step in the research aims to introduce the obtained pore size distributions into a pore–flow model to run a computational analysis of transport through the P84 co-polyimide membranes.

CHAPTER 4

4. Assessment of the pore–flow model

4.1 Summary

One of the main challenges in modelling organic solvent nanofiltration (OSN) is to choose and apply a suitable transport model to predict the separation performance of a membrane. Although pore–flow models have often been applied to describe membrane performance, it is difficult to obtain some key parameters, including the transport–active pore size distribution, which is a governing characteristic in determining the selectivity. Nanoprobe characterisation, as described in Chapter 3, is an imaging technique developed to measure the pore size and the skin layer thickness *in situ* based on filling the membrane pores with high contrast nanoparticle (NP) agents. The objective of this chapter is to assess the applicability of a pore–flow model combined with the pore size distribution determined by the nanoprobe imaging technique, to predict the polystyrene or NP rejection. Various simulation approaches were employed in this work. The findings indicate that the simulated rejection using the log-normal probability density function (PDF) to describe the pore size distribution for a range of P84 co-polyimide membranes resulted in better predictions for spherical rigid particles than it did for polystyrene solutes.

4.2 Materials and methods

4.2.1 Membranes: preparation and filtration tests

The analyses carried out to meet objectives of this chapter were based on the membranes M1, M2 and M3, and the filtration tests as described in Chapter 3, Section 3.2 and 3.3.

4.2.2 Filtration of OsO_2 and Au nanoparticles

Two aqueous suspensions of Au NP with nominal diameters of 2 nm and 5 nm, without any stabilisers, were purchased from Chemquest, UK. The suspensions were mixed to increase their particle distribution followed by ten-fold dilution with water to achieve Au final concentration of 50 ppm. OsO_2 NP stabilised with polystyrenes (PS) in toluene at a concentration of 150 ppm (w/w, OsO_2/toluene). OsO_2 NP were fabricated according to the protocol described in Section 3.2.6. 30 mL of a NP suspension were filtered in a dead-end MET-cell (Evonik Membrane Extraction Technology, UK) under constant stirring at a pressure of 10 bar, followed by filtering 100 mL of the corresponding pure solvent (water prior to Au NP filtration and toluene prior to OsO_2 NP filtration), to remove the conditioning agent polyethylene glycol (PEG).

4.2.3 Inductively coupled plasma mass spectrometry

The permeate and feed aqueous solutions containing Au NP were diluted five–fold, without undertaking further sample preparation methods prior to the inductively coupled plasma mass spectrometry (ICP–MS) analysis. OsO_2 NP suspensions in toluene were heated to dryness, and samples were then treated overnight with fresh aqua regia to digest PS stabilisers. Next, water was added to dilute the suspensions five–fold with reference to initial concentrations of the permeate and feed samples. Concentrations of Au and Os were determined using ICP–MS, at detector wavelengths of Au: 267.595 nm and Os: 228.226 nm. Au and Os standards were purchased from Esslab, UK, and MBH Analytical, UK, respectively.

4.2.4 TEM imaging of Os and Au nanoparticles

A drop of the permeate and feed NP samples were placed on copper grids coated with carbon film (Agar Scientific, UK) and left until the solvent evaporated. The imaging methods as described in Section 3.2.8 were used to characterise the NP specimens.

4.2.5 Pore–flow model

The pore–flow model described in Section 1.3.2.2 was used to calculate solute and particle rejections based on the pore size distribution determined for membranes M1 – M3 using the nanoprobe imaging technique (data from Section 3.3.9).

The pore flow rates were calculated based on the pore size distribution as included Section 3.3.9, and the data of the skin layer thickness from Section 3.3.6.

4.3 Results and discussions

4.3.1 Pore flow rate calculations based on the pore size distribution and the skin layer thickness measured by the nanoprobe imaging technique

The pore size distribution and the skin layer thickness estimated using the nanoprobe imaging technique is introduced into the Hagen–Poiseuille equation to calculate the pore flow rate (Eq. 1.9). Although it is likely that the pore has a channel-like tortuous structure, because it is probably formed between bundles of polymer chains, the pore is assumed to be cylindrical. It is also assumed that the thickness of the skin layer corresponds to the capillary length *l*, as in the Hagen–Poiseuille equation.

The calculations incorporated the pore size histograms correlating the count with the pore–size–class. Thus, the calculated flow rate became the fractional pore flow rate ($Q_{pf,i}$) (Eq. 4.1), that is equal to the magnitude of flow rate through a pore with radius $r_{p,i}$, multiplied by a fraction (f_i) of the pore–size–class (in the entire distribution) to which this pore belongs. The pore–size–classes are presented in the histograms (Figure 3.11b,d,f) where the height of the bars corresponds to $count_i$, that is a number of analysed pores belonging to a particular pore–size–class. Therefore, the value f_i was normalised, by calculating it as a ratio of $count_i$ to the total number of analysed pores (equal to 260) in the histograms. The fractional pore flow rate is calculated using the following equation:

$$Q_{pf,i} = f_i \frac{\pi r_{p,i}^4 \Delta P}{8 \mu_0 l} \quad , \qquad \textit{Eq. 4.1}$$

where ΔP is the transmembrane pressure of 10 bar equal to the magnitude of pressure used in the experimental filtration, μ_0 is the solvent bulk viscosity (for toluene 0.59 x 10^{-3} Pa s at 20°C), and l is the skin layer thickness (theoretically a channel length) measured using TEM. $Q_{p,i}$ and so

$Q_{pf,i}$ are dependent on solvent viscosity, and the solvent bulk viscosity μ_0 can be modified, using the viscosity correction formula (Eq. 1.10), to the pore viscosity $\mu_{p,i,}$ resulting in one order of magnitude lower values of the pore flow rates, as the corrected pore viscosity is strongly related to pore radius.

The analysis first compared the impact of the pore size on the pore flow rate at a constant channel length equal to 100 nm. Subsequently, the channel length was altered from 10 nm to 200 nm to investigate which factor is more significant (channel length or pore size). The graphs presented in Figure 4.1 show the flow rate distributions in relation to the pore size and the channel length. At values close to 100 nm the impact of the pore size is more significant than the channel length. Thus, the plots suggest that an analysis of the fractional pore flow rate carried out in relation to the measured pore radius, at a channel length of approximately 100 nm and a pressure of 10 bar, is essential in elucidating transport in the OSN membranes using the pore–flow model.

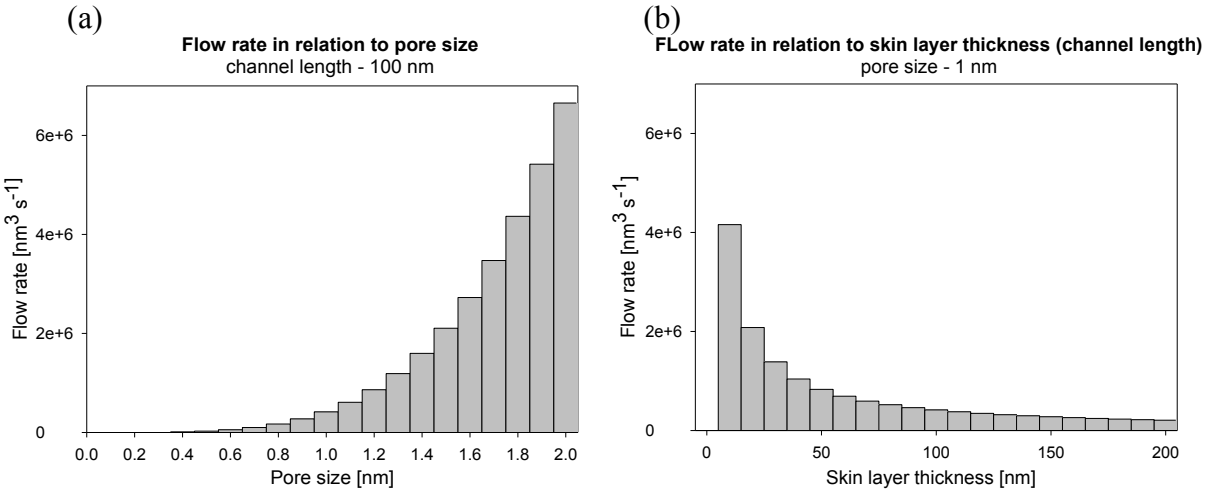


Figure 4.1 Flow rate distributions.

(a) Flow rate in relation to pore size (diameter). (b) Flow rate in relation to skin layer thickness (capillary length). Calculations were based on the transmembrane pressure of 10 bar and the bulk viscosity of toluene.

Figure 4.2 compares the fractional pore flow rate distributions in relation to the pore size. Two data sets for the fractional pore flow rate are presented: the first calculated with the solvent bulk viscosity, and the second calculated with the corrected pore viscosity. The pore viscosity

has an enormous effect on the pore flow rate, resulting in values one order of magnitude lower than the pore flow rates calculated using the solvent bulk viscosity. In order to compare the mean pore flow rate, one can introduce the integrated averaged pore flow rate (Q_{p_av}), which can be expressed as a sum of the fractional pore flow rates:

$$Q_{p_av} = \sum_i Q_{pf,i} \qquad \textit{Eq. 4.2}$$

Because the flow rate for the specific membrane area cannot be calculated without knowing the porosity; instead, the integrated averaged pore flow rate has been estimated using both the bulk and pore viscosities. A comparison of values shown in Table 4.1 implies that Q_{p_av}, calculated using the bulk viscosity, is approximately three times higher for membrane M1, and eight for membranes M2 and M3, than $Q_{p_av_corr}$, calculated using the corrected pore viscosity. This behaviour is directly associated with the viscosity correction formula, which estimates higher viscosity at smaller pore sizes. One may notice that the fractional pore flow rates calculated with the corrected pore viscosity (membrane M1, Figure 4.2b) are equal to 0 for the pore sizes of 0.5 and 0.6 nm, whereas the fractional pore flow rates calculated using the bulk viscosity (membrane M1, Figure 4.2a) for the same pore sizes are equal to ~ 6 and 20 $nm^3\ s^{-1}$, respectively. According to Eq. 1.10 the viscosity magnitude becomes negative for the pore diameter smaller than the size of solvent molecule, which is 0.7 nm for toluene [222]. Thus, for the pore diameters smaller than 0.7 nm the fractional pore flow rate is assigned to be 0.

Table 4.1 Integrated average pore flow rate calculated from the fractional pore flow rate histograms.

Data sets	Bulk viscosity		Corrected pore viscosity	
Membrane	Integrated averaged pore flow rate Q_{p_av}		Integrated average pore flow rate $Q_{p_av_corr}$	
	($nm^3\ s^{-1}$)	($L\ h^{-1}$)	($nm^3\ s^{-1}$)	($L\ h^{-1}$)
M1	145×10^3	5.22×10^{-16}	47.29×10^3	1.70×10^{-16}
M2	400×10^3	14.41×10^{-16}	48.80×10^3	1.76×10^{-16}
M3	396×10^3	14.27×10^{-16}	48.06×10^3	1.73×10^{-16}

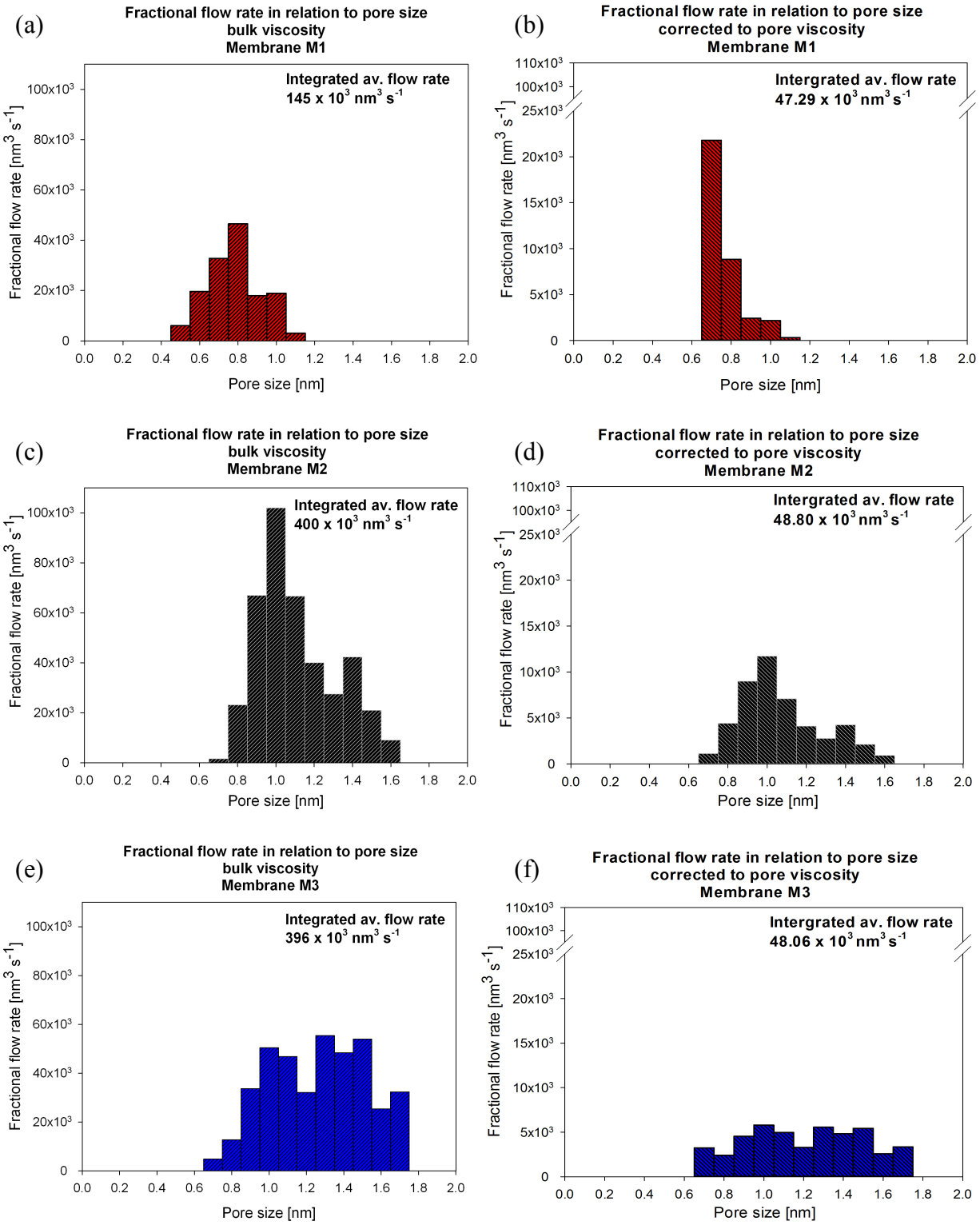


Figure 4.2 Distributions of the fractional pore flow rate calculated using the pore size (diameter) measured by TEM.

(a),(c),(e) Plots of the pore flow rates created using bulk viscosity, and (b),(d),(f) corrected to pore viscosity.

4.3.2 Rejection calculation based on the pore size distribution

Two approaches were undertaken to calculate the rejection: (*i*) 'discrete' and (*ii*) 'continuous'. Figure 4.3 presents flow charts representing the calculation methodology for the discrete (Figure 4.3a) and continuous (Figure 4.3b) approach. In the 'discrete' approach, the overall rejection was calculated based on the pore size distribution, *i.e.* histograms, and the experimentally measured flow rates at the membrane area A_m = 0.0014 cm^2, *i.e.* equal to the filtration cell surface area. In the 'continuous' approach the overall rejection was integrated over the continuous pore size distribution, described using the PDF computed *via* Eqs. 1.19 – 1.21. The integration was truncated at the pore radius r_{max}, which was approximated by the radius of the largest OsO_2 NP or Au NP found in the corresponding permeates.

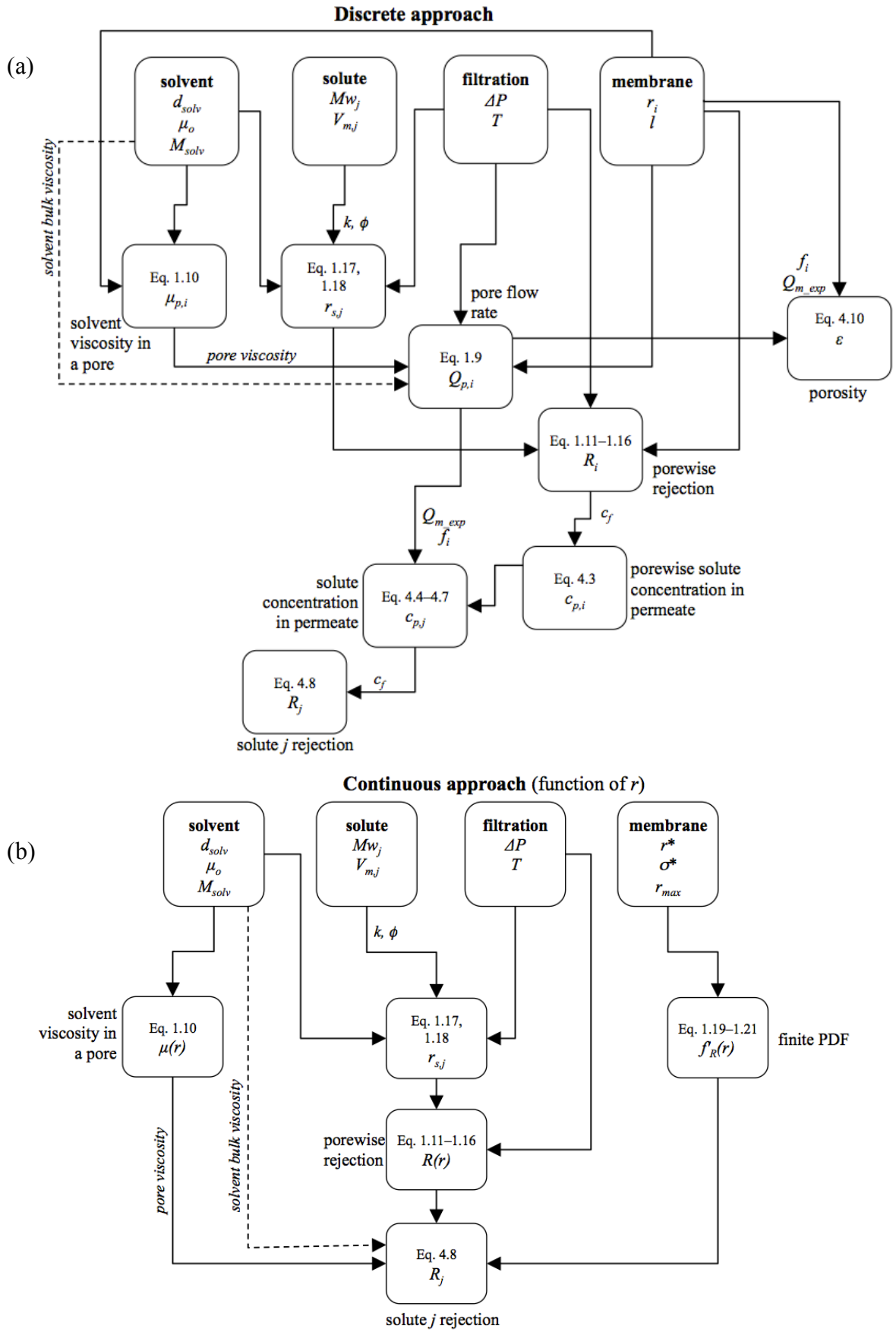


Figure 4.3 Flow charts representing calculation methodology in the discrete and continuous simulations.

To compute the pore–flow model equations, the solute size (molecular diameter) can be calculated *via* Eqs. 1.17 and 1.18. The molar volume ($V_{m,j}$) of each PS solute estimated using the Group Contribution Method [106] gives a required input for calculation of the solute diffusivity *via* Eq. 1.18. Table 4.2 lists the molecular diameter and molar volume values determined for PS oligomers solvated by toluene. The relationship between the solute diameter and molecular weight (Mw_j) is graphically presented in Figure 4.4.

Table 4.2 Estimations of the molecular diameter of PS oligomers solvated in toluene

PS molecular weight Mw_j (g mol^{-1})	Molar volume $V_{m,j}$ (cm^3 gmol^{-1})	Calculated PS diameter $d_{s,j}$ (nm)
236	183.4	0.47
295	258.4	0.58
395	349.3	0.69
495	440.2	0.80
595	531.1	0.89
695	622.0	0.98
795	712.9	1.06
895	803.8	1.14
995	894.7	1.22
1095	985.6	1.29
1195	1076.5	1.36
1295	1167.4	1.43
1395	1258.3	1.49
1495	1349.2	1.56

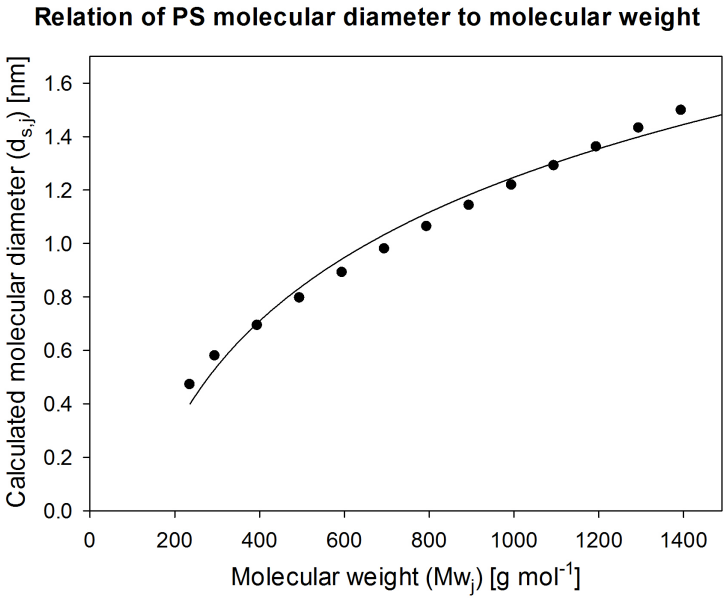


Figure 4.4 PS molecular diameter in relation to MW in toluene.

4.3.3 Discrete approach

In the discrete approach the pore size distributions determined by the nanoprobe imaging technique were employed for calculations of the overall rejection. The porewise permeate concentration ($c_{p,i}$) was calculated using the following expression:

$$c_{p,i} = (1 - R_i) c_f , \qquad \textit{Eq. 4.3}$$

where c_f is solute concentration in feed. The overall permeate concentration of each solute ($c_{p,j}$) was defined using the mass balance expression:

$$Q_{m_\exp} c_{p,j} = \sum_i N_i Q_{p,i} c_{p,i} , \qquad \textit{Eq. 4.4}$$

where N_i is the number of pores in each pore–size–class in the membrane area A_m = 0.0014 m^2 (filtration surface area used in the experiments). The total volumetric flow rate (Q_{m_exp}), measured experimnetally over the membrane surface area A_m, was equal to 0.049 L h^{-1} for

membrane M1, 0.127 L h^{-1} – M2, and 0.201 L h^{-1} – M3. The experimental flow rate can then be expressed as a sum of the volumetric pore flow rates at each pore–size–class given by:

$$Q_{m_\exp} = \sum_i N_i Q_{p,i} . \qquad \textit{Eq. 4.5}$$

Because the fraction (f_i) is a ratio of the number of pores in each pore–size–class to the total number of pores, its value is defined as following:

$$f_i = \frac{count_i}{count_{total}} = \frac{N_i}{N_{total}} . \qquad \textit{Eq. 4.6}$$

The symbols $count_i$ and N_i are ascribed to the number of pores in each pore–size–class, correspondingly in the histograms (Figure 3.11b,d,f) and in the tested membrane coupons; whereas $count_{total}$ and N_{total} represent respectively the total number of pores in the histograms (Figure 3.11b,d,f) and in the tested membrane coupons. Subsequently, Eqs. 4.3 – 4.6 were combined into the expression relating the porewise permeate concentration with the fraction of pore–size–class and the volumetric pore flow rate:

$$c_{p,j} = \frac{\sum_i f_i c_{p,i} Q_{p,i}}{\sum_i f_i Q_{p,i}} \; ; \qquad \textit{Eq. 4.7}$$

to finally calculate the overall solute rejection using:

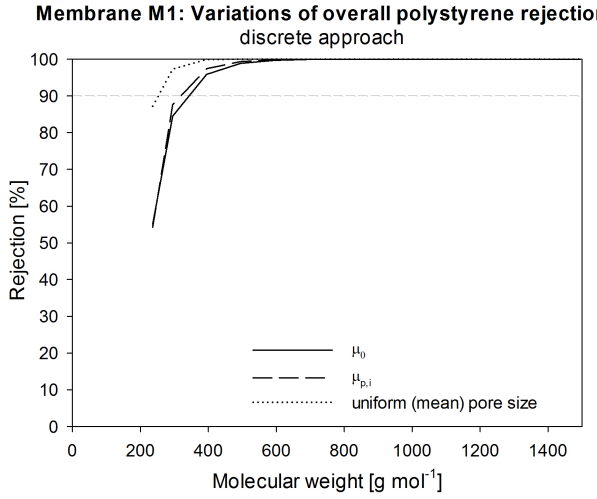
$$\mathrm{R}_j = 1 - \frac{c_{p,j}}{c_f} . \qquad \textit{Eq. 4.8}$$

Figure 4.5 presents plots of the calculated overall rejection in relation to solute MW. The rejection curves were computed using the solvent bulk viscosity and the corrected pore viscosity over the pore size distributions. In addition, the graphs include the rejection plots simulated for a hypothetical membrane having uniform pore sizes. This isoporous membrane is considered as a perfect membrane, which is expected to provide an ideal selectivity. In the simulations, the mean pore size estimated by the nanoprobe imaging was used. The purpose of including these plots was to demonstrate how the presence of size distribution impacts the rejection. One can observe

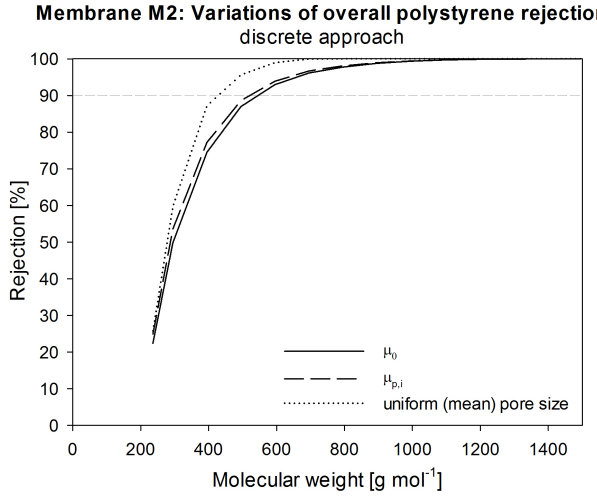
that the selectivity (a curve slope) of the ‘uniform pore size curve’ is significantly steeper and rejection shifts towards higher values.

The simulation employing the corrected pore viscosity results in only a minimal increase in the rejection. The reason for this insignificant change is related to the solute diffusivity. While the Wilke–Chang and Stokes–Einstein equations (Eqs. 1.17 and 1.18) were combined through the diffusion coefficient to calculate the PS diameter, rejection was no longer dependent on solvent viscosity in a pore. Despite the fact that the pore viscosity, in the discrete methods, is included in the rejection calculations *via* the expression computing the Peclet number (Eq. 1.16) and the pore flow rate $Q_{p,i}$ (Eq. 1.9), the rejection plots (Figure 4.5) do not show significant difference in the overall PS rejection.

(a)



(b)



(c)

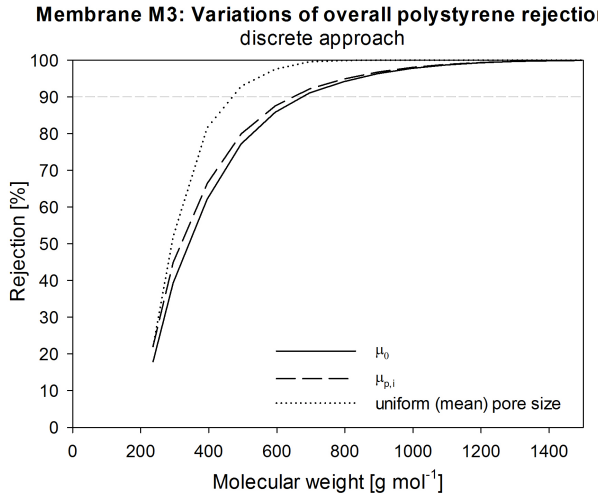


Figure 4.5 Overall PS rejections calculated in the discrete approach methods using the bulk solvent viscosity (μ_0), and the solvent viscosity corrected to pore viscosity ($\mu_{p,i}$).

From the pore size distribution and the experimentally measured volumetric flow rate (Q_{m_exp}), the membrane porosity can be calculated by estimating the number of pores in each pore–size–class:

$$N_i = f_i N_{total} = f_i \frac{Q_{m_\exp}}{\sum_i f_i Q_{p,i}} \; ; \qquad \textit{Eq. 4.9}$$

hence, porosity could be estimated as a ratio of total pore area to membrane area A_m of the filtration coupon:

$$\varepsilon = \frac{\sum_i N_i \pi r_i^2}{A_m} \; . \qquad \textit{Eq. 4.10}$$

Table 4.3 presents the porosity values arranged in two categories: data obtained using the solvent bulk viscosity and the corrected pore viscosity. A comparison of the data indicates that the calculated porosity using the corrected pore viscosity is one order of magnitude higher than the porosity calculated using the bulk viscosity. The porosity values of 41.2% or 73.8% are rather unrealistic, and the porosities estimated using the bulk viscosity are considered more probable. One has to note that the pore viscosity formula is a relatively arbitrary rough estimation of the fluid viscosity in a fine pore, and should be treated as such. Unfortunately, there is no available experimental technique to validate these porosity values and these estimates are used for the purpose of assessment and discussion of the pore–flow model equations, and should not be considered as accurate experimentally derived values.

The above discussion does not assert that the viscosity in a pore is comparable to its bulk value, since there are reported studies showing evidence that the viscosity increases with decreasing pore radius [94, 223]. However, one of the conclusions of this work is a concern that the applied viscosity estimation represented by Eq. 1.10 may not be relevant to OSN systems, since the solvent molecular diameter is comparable to the pore size in NF membranes. Additionally, one should consider the formula assumes that a single layer of solvent molecules

adheres to a pore wall. While this may be true for a water molecule given its polarity, it may not be relevant for a toluene molecule, which is considered non-polar.

Table 4.3 Estimated membrane porosity from Equation 4.10

Porosity ε (%)		
Membrane	Bulk viscosity	Pore viscosity
M1	2.5	7.4
M2	4.9	41.2
M3	9.0	73.8

4.3.4 Particle size analysis in permeate

OsO_2 NP size distributions were measured in the permeate and feed solutions (Figure 4.6a). The mean diameter of the OsO_2 NP in the permeate of membrane M1 was 0.64 ± 0.13 nm, M2 – 0.74 ± 0.13 nm, and M3 – 1.09 ± 0.15 nm, whereas the mean size in the feed was equal to 1.17 ± 0.28 nm. In addition, the size analysis allowed estimation of the diameter of the largest particle able to permeate the separation layer ($2*r_{max}$). In the permeate of membrane M1 the size of the largest OsO_2 NP ($2*r_{max_OsO2NP}$) was equal to 1.22 nm, membrane M2 – 1.30 nm, and membrane M3 – 1.68 nm. These values for maximum radius r_{max} are required to truncate the integration function in order to compute the overall solute/particle rejection (R_T) using the continuous pore size distribution described by the log-normal PDF. The concentration of OsO_2 NP in the permeate and feed solutions measured using ICP–MS (essentially the concentration of Os was measured) allowed estimation of the overall rejections of OsO_2 NP, and these were found to be 86.12%, 69.26%, and 54.36% for membranes M1, M2, and M3, respectively. Given the particle size distribution and the total concentration of OsO_2 NP in the permeate ($c_{p,total}$) and feed

($c_{f,total}$), the rejection R_i, calculated for each particle–size–class, was determined using the following equation:

$$R_i = 1 - \frac{c_{p,total}}{c_{f,total}} \frac{count_{p,i}}{count_{f,i}} \frac{count_{f,total}}{count_{p,total}}, \qquad Eq.\ 4.11$$

where $count_{p,i}$ and $count_{f,i}$ are the count of the particles in particle–size–class i, corresponding to the permeate and feed samples, and $count_{p,total}$ and $count_{f,total}$, in the permeate or feed samples respectively, are the total number of the analysed particles from the TEM images.

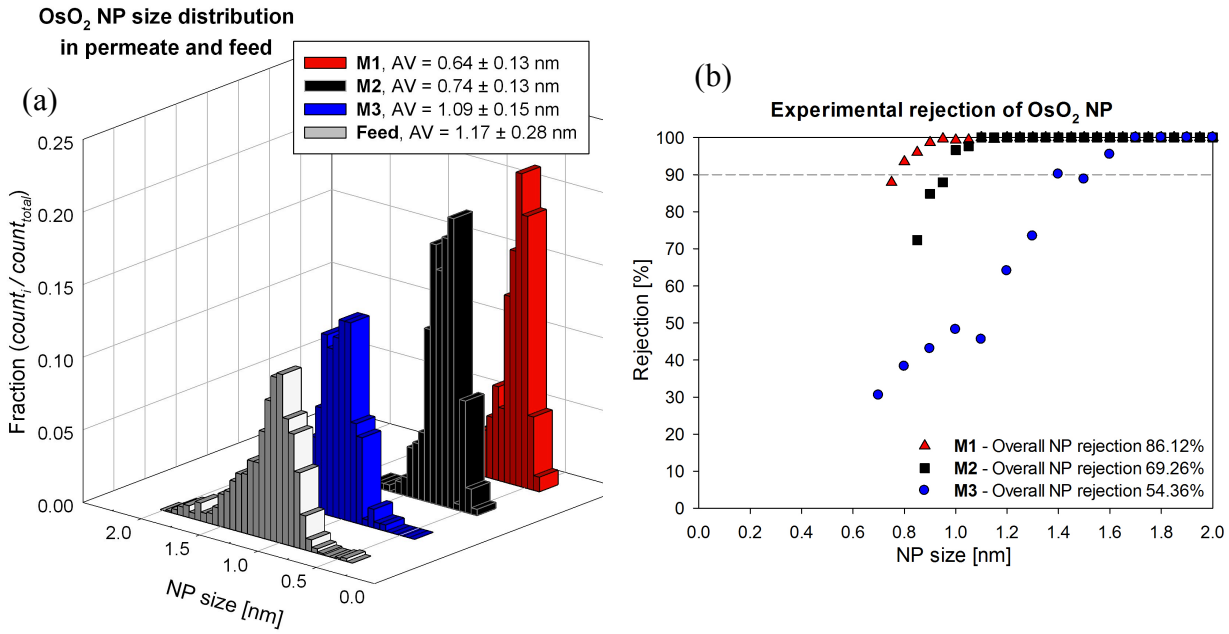


Figure 4.6 Size and rejection of OsO_2 NP.

(a) OsO_2 NP size distribution in the permeate and feed solutions of membranes M1 – M3. (b) Particle rejection curves evaluated for membranes M1 – M3 using the OsO_2 NP size distribution and the total concentration of OsO_2 solids in the permeate and feed samples.

Bowen and Welfoot [93] reported that the pore size distribution described by the log-normal PDF has a "tail" of large pores that can largely influence the overall solute rejection, even if a number of large pores is very low. Therefore, a further control study was undertaken to examine whether the "tail" of the log-normal pore size distribution, as described by PDF (Eqs.

1.19 and 1.20), was also a characteristic for the P84 co-polyimide NF membranes. To eliminate the "tail" effect, the integration function (Eq. 1.22) should be truncated at r_{max}. In the previous paragraph r_{max} was estimated from the size distribution of the OsO_2 NP. An additional experiment was performed due to uncertainty whether the largest OsO_2 NP found in a permeate corresponded, in fact, to the r_{max} (as OsO_2 NP could be still too small to find r_{max}).

The proposed methodology was to filter Au NP with sizes ranging from the upper NF up to the lower UF region. A mixture of Au NP with the mean size of 4.74 ± 1.63 nm was filtered through the membranes to estimate size distributions of the permeated NP. Because Au NP were large, high rejections measured by ICP–MS were indeed observed: 97.92% for membrane M1, 97.64% – M2, and 96.66% – M3. The mean sizes of Au NP, measured from the TEM images, corresponding to samples M1, M2 and M3, were equal to 2.06 ± 0.58 nm, 3.57 ± 1.23 nm and 3.88 ± 1.36 nm, respectively. To estimate the diameter ($2*r_{max_AuNP}$) of the largest Au NP found in the respective permeates, the particles were imaged and their sizes were measured using TEM. The values of $2*r_{max_AuNP}$ were estimated to be 3.94 nm, 7.38 nm, and 7.58 nm for membranes M1, M2 and M3, respectively. The estimations assumed that the size of Au NP with a radius r_{max_AuNP} corresponded to the largest pore, and thus to the end of "tail" of the log-normal distribution. This is where the integration was then truncated.

Given the large sized Au NP might permeate due to leakage through defects in the membranes instead of large pores, an additional control TEM imaging of the membranes after filtration with Au NP was conducted. The experiment was undertaken to test whether the particles were actually lodged in the membranes, on the hypothesis that if large Au NP were found in the membranes, it was due to the "tail" effect caused by the log-normal profile of the pore size distribution. Figure 4.7 presents a cross-sectional view of membrane M3 after filtration with Au NP. A majority of the NP (larger than the pores) were retained at the membrane surface; however, a small fraction of the NP (smaller or equal to the pore size) could actually enter the

membrane. This behaviour was also observed consistently for the membranes M1 and M2, although significantly less Au NP were lodged into these membranes and a higher number of the particles were retained at the surface. This observation reflects the overall rejection of Au NP listed in Table 4.4.

Table 4.4 Size and concentration analysis of Au and OsO_2 NP in permeate

NP sample	Au NP conc. ($mg\ L^{-1}$)	Au NP size mean ± σ (nm)	Overall rejection of Au NP (%)	OsO_2 NP conc. ($mg\ L^{-1}$)	OsO_2 NP size mean ± σ (nm)	Overall rejection of OsO_2 NP (%)
M1 permeate	0.232	2.06 ± 0.58	97.92	4.145	0.64 ± 0.13	86.12
M2 permeate	0.264	3.57 ±1.23	97.64	9.178	0.74 ± 0.13	69.26
M3 permeate	0.373	3.88 ± 1.36	96.66	13.626	1.09 ± 0.15	54.36
Feed	11.155	4.74 ± 1.63	-	29.855	1.17 ± 0.28	-

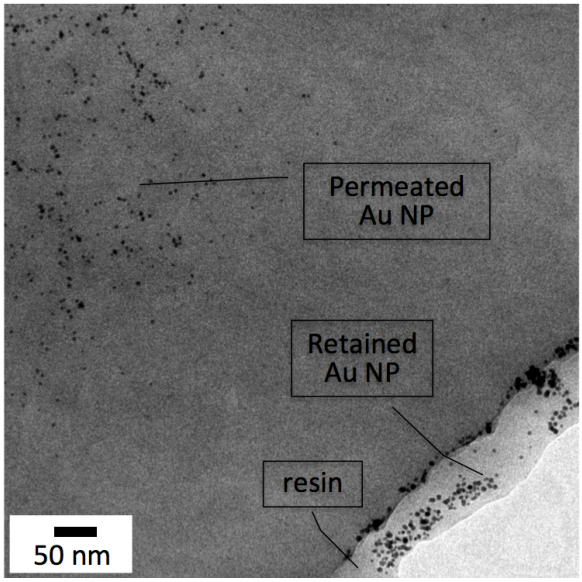


Figure 4.7 Cross-sectional TEM image of membrane M3 after filtering with Au NP.

The image confirms that the particle permeation is due to the presence of a small fraction of the large pores rather than due to leakage in the filtration cell.

4.3.5 Continuous approach

An alternative approach to the discrete method is integration of the porewise rejection; thus, the term 'continuous approach' is used through the discussion. The aim is to analyse the influence of the PDF using various standard deviation (σ) and r_{max} values. The impact of σ on the PDF in simulations of the porewise rejection and the volumetric flux has been previously considered by Bowen and Welfoot [93]. In our study, on the other hand, the objective was to assess whether the pore flow model was able to predict rejections comparable to the experimental values. This comparison was possible as the pore size distributions of the studied membranes were defined. Figure 4.8a–c present the porewise rejection curves estimated based on the PDF using the mean pore size, σ and r_{max} values (r_{max_AuNP} and r_{max_OsO2NP}). In all cases, rejection did not decrease dramatically after introduction of r_{max_AuNP} estimated from the Au NP distribution. This implies that the frequency of pore dimensions close to r_{max_AuNP} was very low. The different behaviour in the simulations was observed when σ was doubled. In this scenario, the pore size distribution was very broad and its peak shifted towards larger pores that dominated the porewise rejection due to the r^4 averaging. As a result, the overall rejection dramatically decreased due to higher values of probability in the "tail" region of the PDF (Figure 4.8d–f). Furthermore, the shape of the simulated rejection curves became flattened, indicating a drop in membrane selectivity.

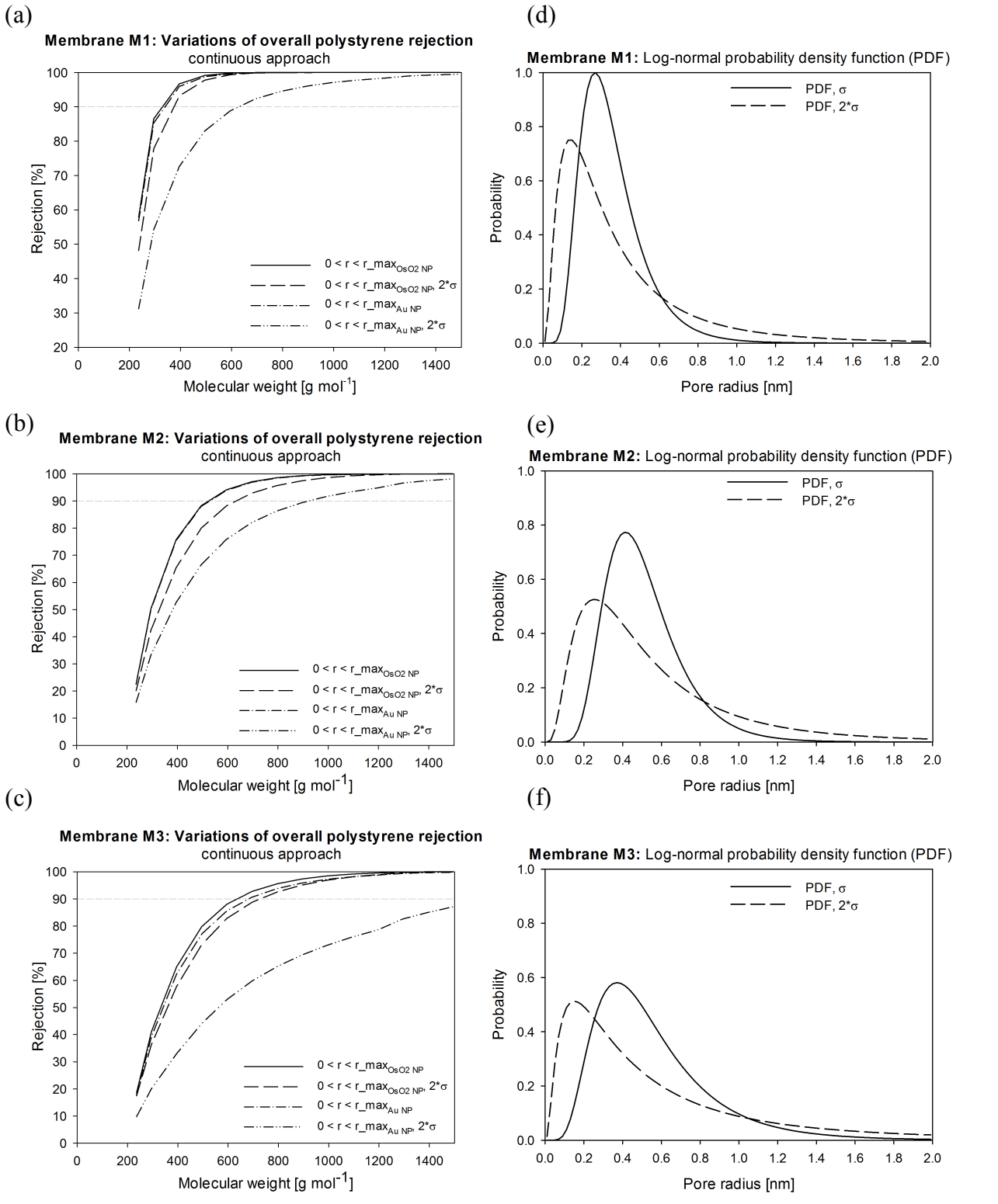


Figure 4.8 Overall PS rejection estimated using the integration function and the log-normal pore size distribution computed based on the pore size distribution measured by the nanoprobe imaging technique.

(a)(b)(c) Various scenarios of the estimated rejection corresponding to membranes M1, M2 and M3. (d)(e)(f) Log-normal pore size distribution estimated corresponding to membranes M1, M2 and M3 using the PDF at single σ and at double σ.

4.3.6 Comparison of the computed rejection with the experimental measurements

The calculated rejection curves obtained *via* the discrete and continuous approaches show various outcomes. In general, the discrete methods resulted in higher rejection values in comparison to the continuous approaches. The continuous methods that employed the log-normal PDFs led to lower rejection due to a small fraction of large pores being localised within the "tail".

The next step of the analysis involved comparison of the simulation outcomes with the experimental NF data. There were two experimental sets of results: PS and OsO_2 NP rejection plots (Figure 3.3 and 4.6b). The experimental rejection values evaluated for the PS solutes dissolved in toluene were significantly lower than the rejections estimated using the discrete approach. Furthermore, a series of the rejection curves, simulated in the continuous approach under the assumption that the pore size distribution follows the log-normal PDF, do not predict with good accuracy the experimental results evaluated with the PS solutes. One of the most likely reasons for this discrepancy is that the PS molecular diameter may change when the molecule is subjected to high viscous forces in a narrow channel. As the PS molecule is a relatively rigid molecule [224], and has a linear structure, lower rejections are probable in comparison to a bulky molecule or a rigid spherical particle. Since the impact of confined space on molecular diameter is not taken into account in any of the pore–flow model formulas, this hypothesis led to undertaking the following part of the comparative analysis.

In order to exclude the potential variability in the molecular diameter of a solute permeating through a confined channel, the experimental rejection (Figure 4.6b) was measured using OsO_2 NP, which are rigid and spherical particles. The experimental rejection plots show that the rejection measured for the NP was higher than for the PS solutes (Figure 4.6b vs. Figure 3.3). The values were compared at a particle size equal to a PS molecular diameter. Given that

the particles maintain their spherical shape and size in a confined space, whilst PS may slightly coil leading to reduction of the molecular diameter in comparison to its bulk diameter, higher rejection of the particles was indeed expected. By considering this effect, the rejection curves, simulated in the continuous approach, were compared with the experimental results, obtained by filtering the OsO_2 NP from the surface side of the membrane. Figure 4.9 presents particle rejection plots of the experimental results and the computed values determined through PDF truncated at two values of r_{max}, equal to the radius of the largest OsO_2 NP (r_{max_OsO2NP}) and Au NP (r_{max_AuNP}) respectively, which were found in the permeates from M1–M3.

The rejection curves simulated based on r_{max_OsO2NP} used single σ, whereas the curves truncated at r_{max_AuNP}, used $2*\sigma$. The reason for selecting this combination was to localise the experimental rejection values in the regions confined by the simulated NP rejection curves. The graphical analysis has suggested that the pore–flow model simulations using the pore size distribution, determined by the nanoprobe imaging, predicts the particle rejection fairly well. The pore–flow model computations seems to give better rejection predictions for rigid spherical particles than for linear molecules, which may change their geometry due to impact of the membrane structure and/or the chemistry.

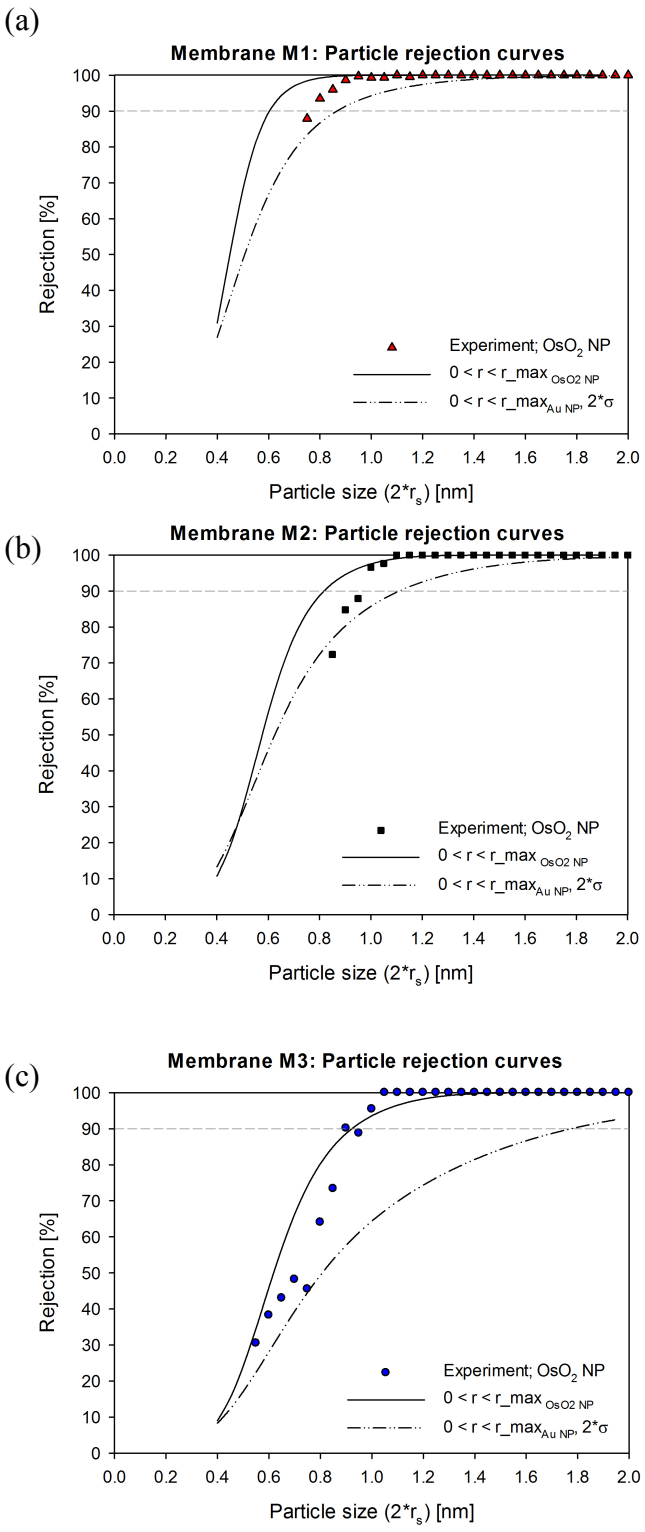


Figure 4.9 Comparison of computed particle rejections based on PDF and r_{max} with plots of the experimental particle rejection.

4.4 Conclusions

This chapter presents a critical assessment of the pore–flow model computations applied to OSN P84 co-polyimide membranes. The input data required for the simulations was produced by the nanoprobe imaging technique. The main value of this approach was the possibility to analyse the pores participating in NF transport; therefore, the effective membrane nanostructure was characterised. The pore size distribution and the skin layer thickness, determined in Chapter 3, were used in this study to calculate the pore flow rate. It was found that it was not only strongly dependent on the pore radius, but also on the solvent viscosity in a pore, especially when the pore viscosity correction formula was employed in the computations. The porosity estimations suggested that introduction of the pore viscosity correction formula resulted in unrealistic porosity values; and the reader is advised to use this correction with care in application to OSN modelling.

The second part of the work involved application of the pore size distribution in computation of the rejection plots using two simulation methods: discrete and continuous. In the discrete methods, the rejection was determined from the mass transfer for each pore–size–class. The rejection plots showed significantly higher rejections in comparison to the experimental PS rejection curves. In further analysis, the continuous approach used the log-normal PDF to describe the pore size distribution. The rejection was strongly dependent on the pore radius, standard deviation of the mean pore radius and r_{max}, a pore radius value at which the integration function was truncated. The final comparative analysis suggested that the continuous method with the log-normal PDF yielded a good prediction of the OsO_2 NP rejection, whereas a high discrepancy was observed between the simulations and the PS experimental rejection. This finding implied that the pore–flow model is more applicable to spherical and rigid particles, than to semi-rigid or compliant molecules of which size can be altered in confined transport channels.

CHAPTER 5

5. Characterisation of thin film composite membranes

5.1 Summary

Successful application of the nanoprobe imaging technique to characterisation of the P84 co-polyimide membranes directed the research to thin film composite (TFC) membranes prepared from glassy polymers. This class of the membranes has recently attracted a lot of interest in organic solvent nanofiltration (OSN) processes [44, 58]. This chapter describes findings on characterisation of two TFC membranes comprising polyamide (PA) and poly(1-trimethysilyl-1-propyne) (PTMSP) top layers.

PA separation layer can be formed by interfacial polymerisation on a crosslinked P84 co-polyimide support. This composite membrane, termed in this chapter as PA/P84, has recently been shown to be very promising for OSN applications, since its chemistry can be independently modified to enhance flux and improve selectivity [44]. PTMSP is an interesting polymer for conducting nanostructural imaging due to its intrinsic high free volume [55]. PTMSP composite membranes have also been successfully applied to OSN processes [50, 58]; therefore, the PTMSP film formed on the P84 co-polyimide support (termed in this work as PTMSP/P84) would be an interesting sample to interrogate with nanoprobe imaging using the nanoparticles (NP) contrast agents.

Furthermore, this study intends to test the hypothesis whether the measured pore size could be correlated with the membrane filtration parameters. The membranes were characterised in terms of the permeation pathway (‘pore’) size and separation layer morphology. The estimated pore size correlates well with the solute rejection, implying that pore flow models may be useful for describing the transport through the membranes.

5.2 Materials and methods

5.2.1 Membranes

5.2.1.1 Support preparation for coating with PTMSP

The dope solution to cast the ultrafiltration (UF) support membrane, comprised 22% (w/w) P84 co-polyimide (HP Polymers, Austria), dissolved under constant stirring in a mixture of dimethylformamide (DMF) and 1,4 dioxane (dioxane) at a 4/1 solvent ratio of DMF/dioxane. Next, the solution was left overnight at room temperature to degas. The polymer dope solution was cast on a polyester backing material at a blade height of 300 μm (Hollytex 3329, USA) using a lab bench–casting machine. The cast film was then left for evaporation for 30 s, and subsequently immersed in a water coagulation bath to induce the polymer phase inversion by a rapid exchange of the solvent mixture with water. After an hour, the membrane was placed for several hours in isopropanol (IPA) to remove water, followed by overnight conditioning in polyethylene glycol (PEG) with a molecular weight (MW) of 400 g mol^{-1} (Fisher Scientific, UK) dissolved in IPA at a 3/2 ratio of PEG / IPA.

5.2.1.2 Preparation of PTMSP/P84 composite membrane

PTMSP polymer was purchased from ABCR GmbH & Co.KG, Germany, and it was used without any additional preparative steps. Prior to coating the support membrane with the PTMSP solution, PEG was removed by soaking the membrane at least twice in toluene for 30 min. Although traces of PEG might still be present in the interior of the support, it was important to remove it completely from the surface. Several trials showed that soaking a membrane in toluene was sufficient to remove PEG, as the coated PTMSP solution did not

appear to precipitate while in contact with the support surface.

After immersion in toluene an excess of the solvent on the surface was wiped off and the support membrane was attached to a glass plate. 2.5% (w/w) PTMSP was dissolved in toluene under constant stirring until a homogenous solution was achieved, followed by 5 – 6 h of degasing at room temperature. The polymer solution was then cast on the surface of the support membrane using a blade set at a height of 200 μm and a speed of 2.82 m min^{-1}. Immediately after casting, the membrane was placed in an oven at 80°C for 2 h where PTMSP film was formed (appeared uniformly transparent) on the top of the P84 co-polyimide UF membrane.

5.2.1.3 Preparation of PA/P84 composite membranes

PA/P84 TFC membranes were prepared according to the methodology developed and described by Jimenez Solomon *et al.* [44]. A solvent resistant crosslinked P84 co-polyimide UF membrane impregnated with PEG (MW of 400 g mol^{-1}) was used as a support for formation of the PA composite layer. In the interfacial polymerisation process the PA top layer was produced by the reaction of an aqueous phase comprising m-phenylenediamine with an organic phase containing trimesoyl chloride. As described elsewhere [44], TFC membranes were post-treated with DMF as an "activating solvent" in order to have toluene flux.

5.2.2 Membrane functional performance

TFC membranes were tested in the cross-flow system in the following membrane – solvent – pressure combinations: PTMSP/P84 – acetone – 10 bar, and PA/P84 – toluene – 30 bar. NF characteristics were measured for a mixture of polystyrene (PS) oligomers and α-methylstyrene dimer dissolved in a corresponding solvent used to test the membranes. The

detailed filtration procedure and the rejection measurement methods are included in Section 3.2.4.

5.2.3 Preparation of OsO_2 nanoparticles

The preparation methods for the OsO_2 NP are described in Section 3.2.6.

5.2.4 Filtration of OsO_2 nanoparticles

Filtration of OsO_2 NP was carried out in a dead-end MET-cell system (Evonik Membrane Extraction Technology, UK). Prior to filtration, the PEG conditioning agent was removed by flushing a solvent to collect at least 100 mL in a permeate. 60 mL of feed solution comprising OsO_2 NP, PS stabiliser and a solvent were filtered through the membranes driven by a nitrogen pressure of 10 bar (for testing the PTMSP/P84 membrane) and 30 bar (for the membrane PA/P84, previously treated with DMF to activate toluene flux). The PA/P84 membrane did not permeate toluene unless treated with DMF by immersion for at least 15 min. Permeabilities of the pure solvent, and then of NP dispersions in the solvent, were measured at the start of filtration, after collecting 20 mL, and 50 mL of a permeate.

In addition, the PA/P84 membrane was subjected to open-side filtration, whereby a membrane coupon was placed in a cell in an opposite manner (the open side of the membrane was facing the feed). This experiment was performed on the membrane not treated with DMF. The flux through the untreated membrane was only present during the open-side filtration. Due to the suspicion that that the composite layer might be delaminated, the additional test was undertaken by subjecting exactly the same membrane coupon to the tight-side filtration. There

was no toluene flux, thus the control test indicated that the open-side filtration did not destroy or detach the dense composite layer in the untreated TFC membrane.

5.2.5 TEM imaging

Samples for TEM were prepared according to the methods described in Section 3.2.7 and TEM images were acquired and analysed using the methods described in Section 3.2.8.

5.2.6 Scanning electron microscopy

Scanning electron microscopy (SEM) was performed using a LEO 1525 field emission gun SEM. Membranes for microscopy were not conditioned in PEG, since the presence of PEG could affect interpretation of the images. Membranes were snapped in liquid nitrogen to achieve a cross-sectional surface without plastic deformation. The samples were then coated with chromium in an Emitech K550X sputter coater for 1 min at a deposition rate of 15 nm min^{-1} and a plasma current set at 75 mA. The electro-micrographs were acquired at an EHT voltage of 20 kV using an InLens detector set at a working distance between 10 mm and 13 mm depending on the charging effects.

5.3 Results and discussions

5.3.1 Chemical structure and properties of polymers comprising the TFC membranes

Figure 3.2a presents the chemical structure of P84 co-polyimide, used to form the UF supports of PTMSP/P84 and PA/P84 TFC membranes. Although the same polymer was used to fabricate the support membranes, the processing methodology varied. The support for the PTMSP layer was uncrosslinked, whereas the support for the PA/P84 membrane was crosslinked with diamines [44]. Chemical structures of PA and PTMSP are presented in Figure 5.1a and 5.1b, respectively. PTMSP is a hydrophobic glassy polymer with a high free volume fraction of 20 – 27% [55], and thus it is often compared with polymers of intrinsic microporosity [107]. Owing to trimethylsilyl side-groups the structure is bulky and rigid, enabling it to retain a loose macromolecular packing [57]. PTMSP membranes were originally used for pervaporation of water/alcohol mixtures [59, 60] or for gas separation [61]. They showed good resistance in organic solvents such as acetone, ethanol and methanol [50], although they often suffered from flux decline [225].

In this study PA film was formed by interfacial polymerisation, where the monomers reacted at the interface of two immiscible solutions until a thin membrane film was formed. The reaction was completed when a dense highly crosslinked film attached to the support became a barrier against further diffusion of the reactive molecules. As a result the produced PA film was very thin, and characterised by a highly crosslinked polymer network and good chemical stability, making it a suitable membrane material for OSN applications.

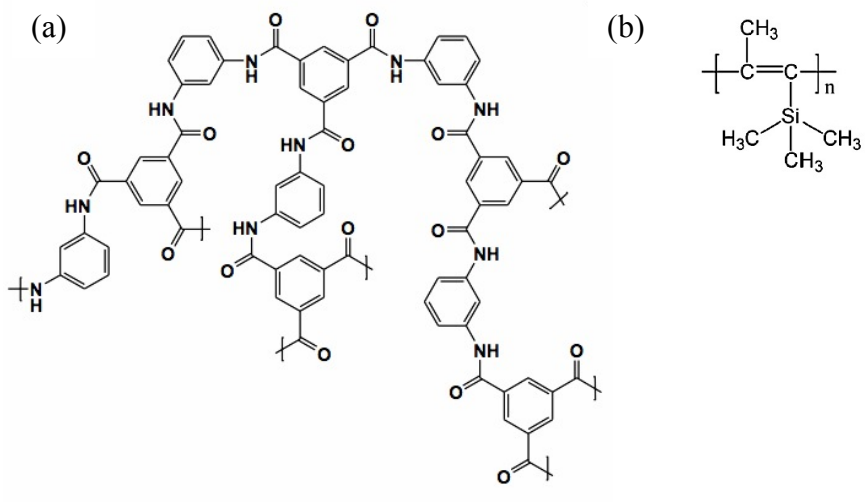


Figure 5.1 Chemical structures.
(a) Polyamide (PA) formed by interfacial polymerisation. (b) Poly(1-trimethylsilyl-1-propyne) (PTMSP).

5.3.2 Functional performance of TFC membranes

The membranes were tested in the cross-flow filtration system with tight side facing the feed to evaluate their NF performance in solvents chosen to match their intended applications. Figure 5.2 presents rejection curves determined from at least three different membrane coupons prepared from the same membrane batch, thus, the error bars correspond to standard deviation of the rejection means estimated for the tested coupons. The rejection plots suggest that the TFC membranes operate within the NF range, whereas the P84 support membrane used for the PTMSP film shows significantly lower rejections. As expected, PA/P84 TFC membrane highly rejects all tested solutes, consistent with the previously reported results [44]. Table 5.1 presents a summary of the measured filtration parameters such as permeability, flux, MWCO and rejection of α-methylstyrene dimer. The dimer rejection is significantly higher for PA/P84 membrane than for the PTMSP/P84 membrane.

Because the functional performance of the PTMSP composite membrane formed on a P84 support has not been reported previously, a control rejection curve, determined individually

for the support membrane, was included. This membrane underwent the same fabrication methods (soaking in toluene and thermal treatment) as the P84 support prior to coating with the PTMSP polymer solution. The control was performed to show that a defect-free top layer was formed.

The previous work carried out on PTMSP TFC membranes with a support prepared from polyacrylonitrile (PAN) showed a rejection of 85% of Remazol Brilliant Blue R (MW of 625.5 g mol^{-1}) dissolved in acetone and filtered at 10 bar [50]. In our study the estimated rejection of a solute with the comparable MW was 85 ± 3%. Therefore, the rejection obtained did not significantly differ from the rejection of the previously developed membrane, at least for molecules with an equivalent MW of Remazol Brilliant Blue R. This comparison has implied that PTMSP has an intrinsic pore size that remains constant, even if polymer concentration in a dope solution changes, or a membrane undergoes thermal treatment.

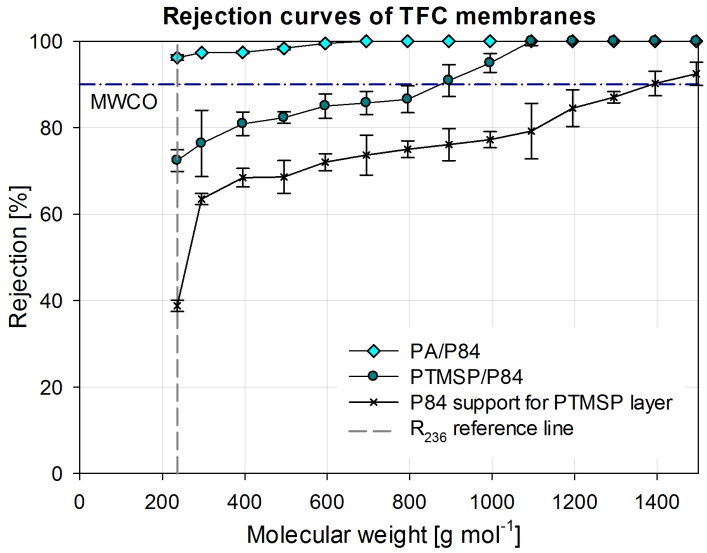


Figure 5.2 Rejection curves of TFC membranes.

Solute rejections were evaluated using PS oligomers dissolved in toluene (for PA/P84 membrane) and acetone (for PTMSP/P84 membrane). A rejection curve of the P84 support membrane is included for purposes of control. The rejection curve of the PA/P84 membrane was provided thanks to a courtesy of M.F. Jimenez–Solomon.

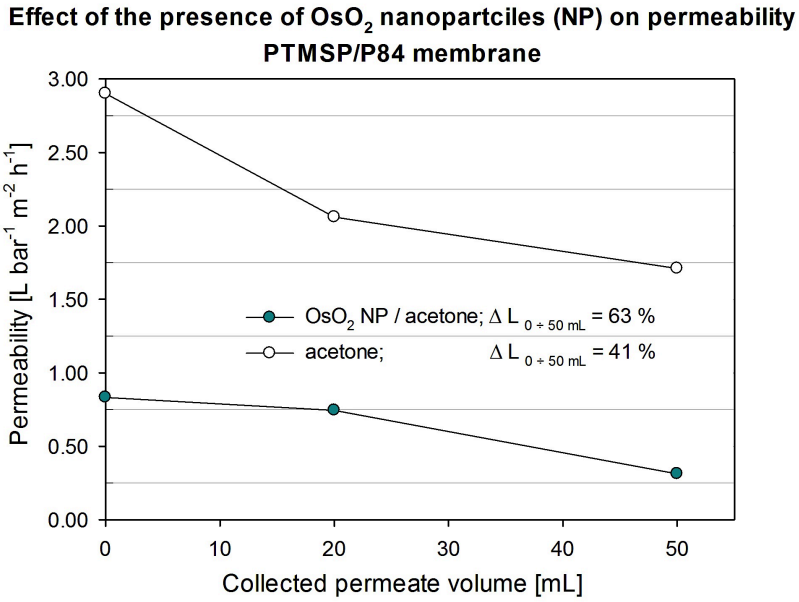
Table 5.1 Summary of the NF performance parameters

Membrane	Solvent	Permeability ($L\ m^{-2}\ h^{-1}\ bar^{-1}$)	Flux ($L\ m^{-2}\ h^{-1}$)	MWCO ($g\ mol^{-1}$)	Rejection of α-methylstyrene dimer with MW 236 $g\ mol^{-1}$ R_{236} (%)
PTMSP/P84	acetone	0.7 ± 0.2	7 ± 2	880	72 ± 3
P84 support		25.3 ± 1.8	253 ± 18	1400	39 ± 1
PA/P84	toluene	0.3 ± 0.0	9 ± 0	<236	96 ± 1

5.3.3 Membrane permeation with OsO_2 nanoparticles

The objective of analysing the permeation of OsO_2 NP was to investigate the impact of the NP on solvent permeability. The hypothesis was stated that the NP block the pores and reduce the flux. The permeability of pure solvent was compared to permeability of an OsO_2 NP/solvent suspension. The measurements were conducted in reference to the filtered volume of permeate, with the tight side facing the feed: at the start (0 mL), after 20 mL and 50 mL were collected downstream. NP were dispersed in the same solvent and the same pressure was used as during the filtration of PS solutes for each tested membrane. Despite continuous stirring in a dead-end filtration cell to reduce cake formation, solids accumulated on the membrane surface once the entire solvent from the feed solution passed through the membrane. Deposition of the OsO_2 NP was attributed to the size distributions of NP and pores. It was expected that the majority of the NP would have been retained on the membrane surface due to small pores present in the active layer of the membranes at the tight side. Figure 5.3 presents the permeability profiles in relation to the permeated volume of a pure solvent and a solvent carrying the NP filtered through the PTMSP/P84 (Figure 5.3a) and PA/P84 (Figure 5.3b) membranes. Both plots indicate that the permeabilities of feeds containing OsO_2 NP were significantly lower in comparison to the pure solvents.

(a)



(b)

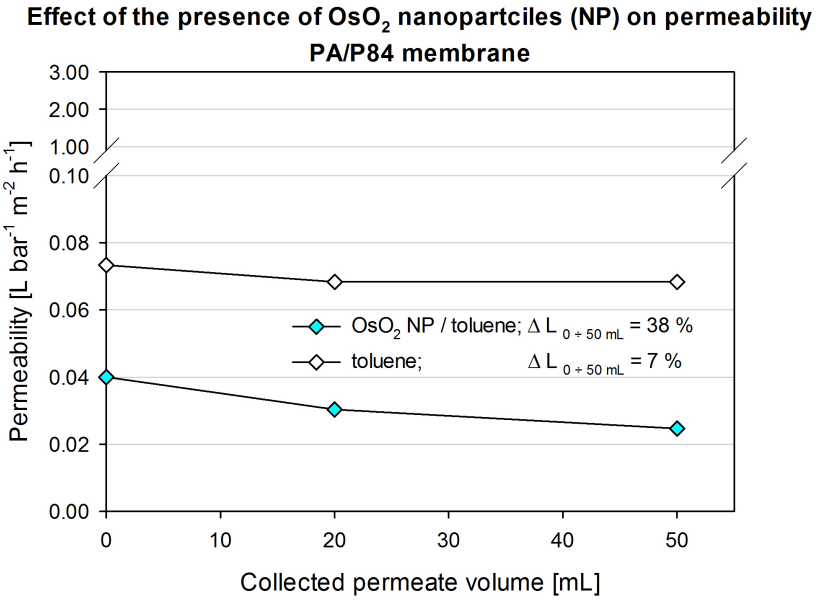


Figure 5.3 Permeability measurements of feeds containing OsO_2 NP in comparison to a pure solvent.

(a) PTMSP/P84 membrane, (b) PA/P84 membrane. The permeability of a solution carrying the OsO_2 NP is significantly lower than the permeability of a pure solvent. In both cases, the permeability decrease ($\Delta L_{0 \div 50\,mL}$) measured between the start of the filtration and when 50 mL were collected in the permeate was higher for the feed comprising OsO_2 NP than for a pure solvent.

The permeability values measured when 50 mL of the permeate were collected (Table 5.2) decreased by 81% and 64% for PTMSP/P84 and PA/P84 membranes, respectively. It is not recommended that the permeability magnitudes for the two membranes are compared since different solvents were used to disperse the nanoprobes; rather, the permeability decline is compared in order to have an overview on the effect of the NP on the mass transfer during the nanoprobing filtration. It was evident that the presence of the NP dramatically reduced the permeation rate. Furthermore, there was a significantly higher decrease in the permeability ($\Delta L_{0 \div 50\ mL}$) of the feeds containing OsO_2 NP measured between the start of the filtration and after 50 mL had been collected in the permeate than for pure solvents monitored in reference to the same permeated volume. The permeability decreases ($\Delta L_{0 \div 50\ mL}$) estimated for pure solvents and membranes PTMSP/P84 and PA/84 were 41% and 7% respectively, and for the feeds containing OsO_2 NP were – 63% and 38%, respectively.

Explaining the flux decline in terms of membrane macromolecular structure, two mechanisms are considered: compaction of polymer chains leading to reduction of interstitial free volume, and pore clogging. The PA/P84 membrane has very low tendency to compaction, most likely due to highly crosslinked structure of the PA network, which preserves the polymeric matrix even at high transmembrane pressures. In contrast, the PTMSP/P84 membrane is characterised by high compaction, given the significant decline of pure solvent flux in comparison to the PA/P84 membrane, suggesting that the interstitial free volume spaces undergo reduction due to polymer chain relaxation [226] or chain scission [58]. The second potential cause for the permeability decline is pore clogging, in which particles or solutes block the pores due to reduction of the permeation channel/pore width or due to tortuosity. High tortuosity may lead to adsorption of solutes/particles on the pore wall, as in depth–filtration [10]. The macromolecular porous phases in PTMSP and PA separating layers may have poor

interconnectivity between the pores, and thus they may possess a high number of dead-end pores enhancing the clogging effect, and consequently the permeability decline. The high magnification images presented in the following sections of this chapter show that the OsO_2 NP after entering the membrane stay in the pores.

Concentration polarisation may also have an impact on permeability reduction. In the study undertaken by Peeva *et al.* [227] OSN Starmem^{TM} 122 membranes showed high reduction in permeability in response to an increase in solute concentration which in turn enhanced concentration polarisation. Based on the simplified solution–diffusion model [228, 229] and the experimental work of Peeva *et al.* osmotic pressure also contributes to flux reduction at increased solute concentration. Therefore, concentration polarisation and osmotic pressure may also contribute simultaneously with the pore clogging and compaction effects to the observed flux decline.

Table 5.2 Permeability of a solvent containing OsO_2 NP in comparison to a pure solvent measured at the permeated volume of 50 mL

	Permeability ($L\ bar^{-1}\ m^{-2}\ h^{-1}$)		Permeability decrease between pure solvent and solvent with OsO_2 NP (%)
Membrane	Pure solvent	OsO_2 NP / solvent	
PTMSP/P84 (acetone)	1.7	0.3	81
PA/P84 (toluene)	0.1	~ 0.02	64

5.3.4 Structural characterisation of TFC layer

TEM cross-sectional images of the TFC membranes provided information on the nanostructure of the composite separation layer. Particularly, the low magnification images were

used to measure the thickness of the composite layer, to characterise the morphology, and the interface between the top layer and the UF support.

5.3.4.1 PTMSP/P84 composite membrane

Images presented in Figure 5.4 show that the PTMSP layer integrates well with the P84 support. Several factors require careful considerations while preparing the composite membrane. Since the P84 co-polyimide support was conditioned with PEG to retain its open structure, the PTMSP solution could not be cast directly on the support membrane without prior removal of the conditioning agent. The reason for this was that toluene, present in the PTMSP dope solution, also dissolved PEG, which in turn induced precipitation of PTMSP, resulting in an inability to form a uniform film. The cast film delaminated immediately if PEG was still present on the surface of the support. Therefore, prior to casting, the support membrane had to be immersed in pure toluene in order to dissolve and wash out the conditioning agent. This procedure removed PEG from at least the membrane surface. Although PEG still remained in the membrane interior, it did not affect formation of the PTMSP film. The dope solution was immediately cast on the support with the surface still wetted with some toluene. The presence of toluene was crucial to provide a good interfacial bond between the support and the PTMSP film. Finally, thermal treatment promoted adhesion of the PTMSP film to the support. The composite layer did not delaminate, as creases were not observed even after 18 h of filtration at a pressure of 30 bar.

The thickness of the PTMSP layer measured from the TEM image (Figure 5.4a) is 430 ± 10 nm. It can be clearly observed that the composite film is very uniform and adheres well to the support membrane. The interface can be observed because there is a slight agglomeration of OsO_2 NP between the support membrane and the top film. The SEM image (Figure 5.4b) also shows a cross-sectional view of the PTMSP/P84 membrane; however, the picture does not imply whether the composite layer contains defects or if it binds uniformly to the support membrane

without any discontinuities. Instead, SEM allows us to visualise the microscale morphologies and distinguish the composite layer from the support membrane.

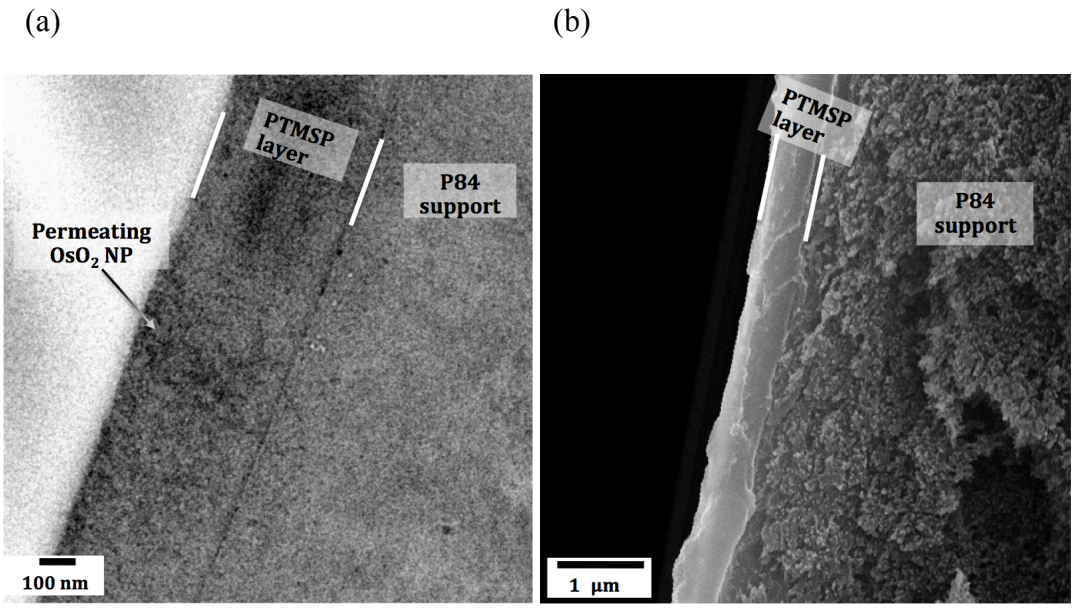


Figure 5.4 Electro-micrographs of PTMSP/P84 composite membrane.

(a) TEM cross-sectional view of the specimen probed with OsO_2 NP from the surface side shows a defect-free interface between the PTMSP layer and the P84 support. (b) SEM image presents the microscale morphological differences between the PTMSP layer and the P84 support.

5.3.4.2 PA/P84 composite membrane

TEM cross sectional images of the PA/P84 TFC membrane provide an insight into the composite membrane structure before and after the treatment with DMF, the activating procedure necessary to obtain toluene flux. According to the previous work describing development of the PA TFC membrane formed on the P84 support, flushing with DMF did not affect the structure of the separating layer [44]. The solute rejection stayed constant and only the solvent flux increased due to reduction in resistance across the membrane. It was suggested that treating the membrane with DMF results in dissolving small molecular fragments of PA leading to a permanent change of the membrane structure. According to Freger [67, 230] the polymer density across the PA film is non-uniform due to the mechanisms taking place during the

interfacial polymerisation reaction. The reactant molecules form a dense selective layer at the interface between the organic and aqueous solutions. This dense layer becomes a barrier hindering diffusion of the reactant molecules, and a less crosslinked and more permeable hydrogel-like polymer network is formed near the UF support and on the outer most surface. The multi-layer morphology of the interfacially polymerised film in Freger's study was distinguished under TEM by staining with uranyl nitrate and sodium tungstate. In contrary Pacheco *et al.* [68] did not observe any loose and less crosslinked PA layer adhering to the polysulfone support. There was only a dense PA film possessing a nodular structure. The TEM images suggested that the resin present in the polysulfone pores might be misleadingly considered as a loose PA network.

To build on the previously reported findings, the nanoprobe imaging technique was used to characterise the cross-section of the composite PA membrane that was treated with DMF in order to compare it to the morphology of the untreated membrane. The hypothesis was that if there were a loose PA film at the interface between the support and the dense PA film, it would be possible to image it with the aid of the high contrast nanoprobes. The imaging approach was based on providing contrast generated from the difference in accumulation of the OsO_2 NP owing to variations in the pore size and porosity between the PA film and the P84 support, and not on the difference between charges or chemical composition as in the aforementioned publications. Because there was no toluene flux through the untreated PA/P84 membrane, two experimental strategies were conducted. The first filtration was directed from the tight side of the DMF–treated membrane (typical filtration), and in the second experiment the filtration direction was from the open side of the untreated membrane.

Freger and colleagues routinely used DMF to detach the PA film from the support [231, 232]. The membrane characterisation studies implied that after this procedure the PA morphology stayed intact. In agreement with the cited publications no changes in the PA firm

itself were observed, except at the interface between the composite film and the support membrane. Filtration of the OsO_2 NP–toluene feed through the DMF–treated and untreated membranes and the subsequent TEM imaging (Figure 5.5) revealed that flushing with DMF caused delamination of the PA layer from the P84 support (Figure 5.5a), whereas the untreated membrane had integral morphology (Figure 5.5b). Relatively high magnification images could be acquired thanks to variations in content of the NP lodged into the PA film and the support (due to changes in the pore size and porosity). In Figure 5.5a one can observe a void filled with the resin that solidified during the sample preparation. The nanoprobes permeated further into the loose support membrane where the pores were too large to retain the particles. The dense PA film seems to be saturated with OsO_2 NP that clogged inside the pores of the highly crosslinked matrix providing a good contrast. The untreated PA/P84 membrane (Figure 5.5b) conversely has higher image contrast on the P84 support than on the PA film. The image agrees with the hypothesis that the PA dense film rejected the majority of the NP which accumulated below the composite film.

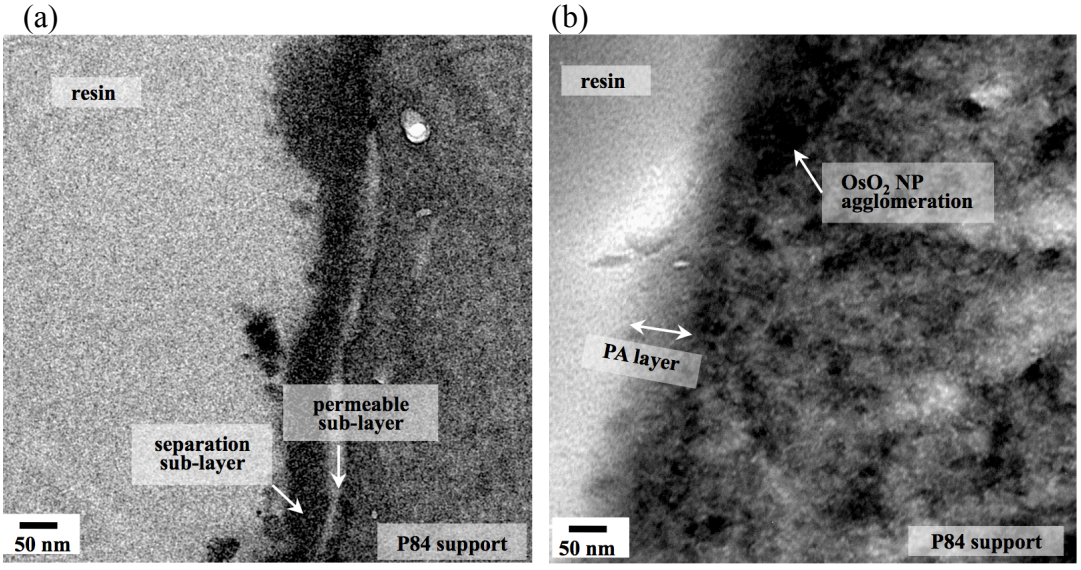


Figure 5.5 Electro-micrographs of PA/P84 composite membrane.

(a) TEM cross-sectional image of the PA/P84 membrane after filtration from the surface side, (b) and the open side. By comparing the specimens prepared by filtering the NP at two opposite directions, the permeable and separation sub-layers, composing the composite PA film, can be distinguished.

Good contrast between the PA composite film and the P84 support was achieved due to the difference in accumulation of the nanoprobes. This effect allowed measurement of the separation layer thickness, which is equal to 53 ± 6 nm and 55 ± 8 nm for the membrane subjected to correspondingly tight- and open-side filtration. The thickness measurements were taken from the images at points distanced from each other at around 20 nm, and this procedure was repeated on at least three images capturing different regions of the analysed top layers. These results imply that both thicknesses, measured from the membrane specimens subjected to filtrations at opposite directions, are comparable. Therefore, the quantitative comparison suggests that the PA film delaminated (Figure 5.5a) and the gap present between the PA film and the P84 support is a void filled with the resin. This observation agrees with the findings attained from the TEM characterisation undertaken by Pacheco *et al.* [68].

5.3.5 Pore size distribution

Pores in the membranes that are probed with OsO_2 NP are considered in this work as permeation pathways participating in the NF transport; whereas the pore size, estimated using the nanoprobe imaging technique, is equal to the diameter of a particle occupying this transport–active channel. In asymmetric membranes these permeation pathways or channels are assumed to be formed between bundles of the polymer chains [233]. In the PA separating film there are two types of pores: free volume elements present between segments of chains building the polymeric network and larger voids formed between macromolecular aggregates [234].

Figure 5.6 presents TEM images of cross-section of the separation layer in the TFC membranes studied. In the electro-micrograph of the membrane PTMSP/P84 (Figure 5.6a) one can observe large dark irregular regions that are attributable to high accumulations of OsO_2 NP. Because the PTMSP matrix has high intrinsic microporosity, a high number of nanoprobes were

able to enter the polymer network, and thus large accumulations are observed. The PA/P84 TFC membrane (Figure 5.6b), in contrast, does not contain as many NP as the membrane PTMSP/P84 (Figure 5.6a). Given the dense structure of PA, only small probes were able to travel through the separating layer.

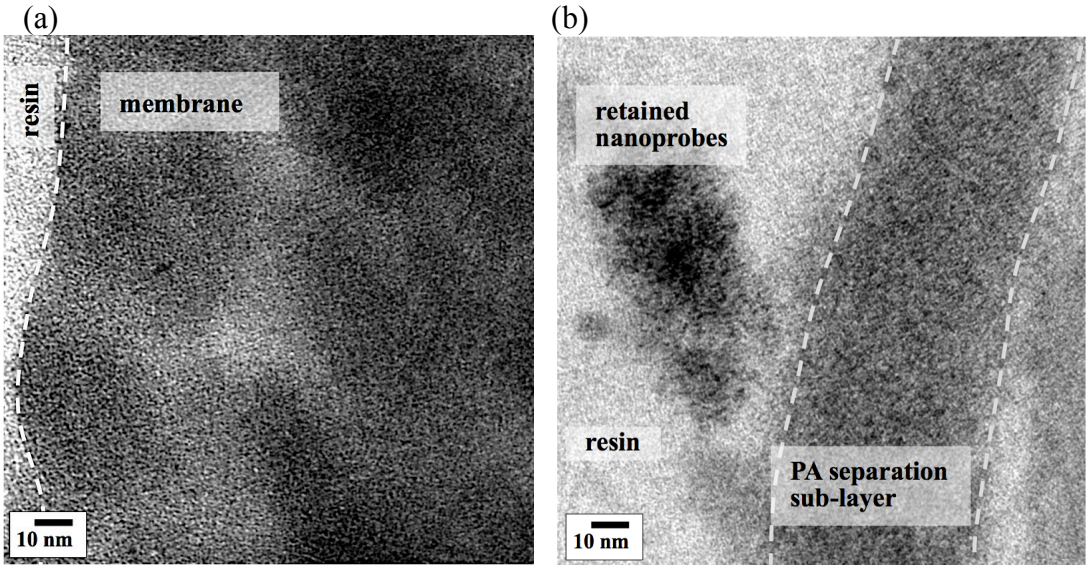


Figure 5.6 TEM cross-sectional images of composite separation layers probed from the surface side of the membranes.
(a) PTMSP film, (b) PA film.

Figure 5.7 presents high magnification images, capturing 30 nm by 30 nm regions of the membrane separation layer. The bright and dark domains are observed in the projections. Since the phases composed of polymer chains scatter very weak electron signals, they correspond to bright areas; whereas the dark regions are attributable to the presence of high contrast OsO_2 NP. The pore size was estimated from the circular-shape objects corresponding to projections of the non-overlapping particles. Because the diameter of a particle lodged into a cavity or a void is assumed to correspond to the size of the transport–active pore, it is important to analyse only the circular regions, since these domains correspond to the NP distributed in a 3–D specimen projected onto a 2–D image as single non-merged objects. The pore size distributions determined

for the membranes under study are presented in Figure 5.8. It was expected based on analysis of the selectivity performance (Figure 5.2) that the pore size distributions would have been wide, given rather flat profile of the rejection curves. The mean pore size for the membrane PTMSP/P84 was measured to be 0.69 ± 0.13 nm, and for PA/P84 – 0.56 ± 0.10 nm.

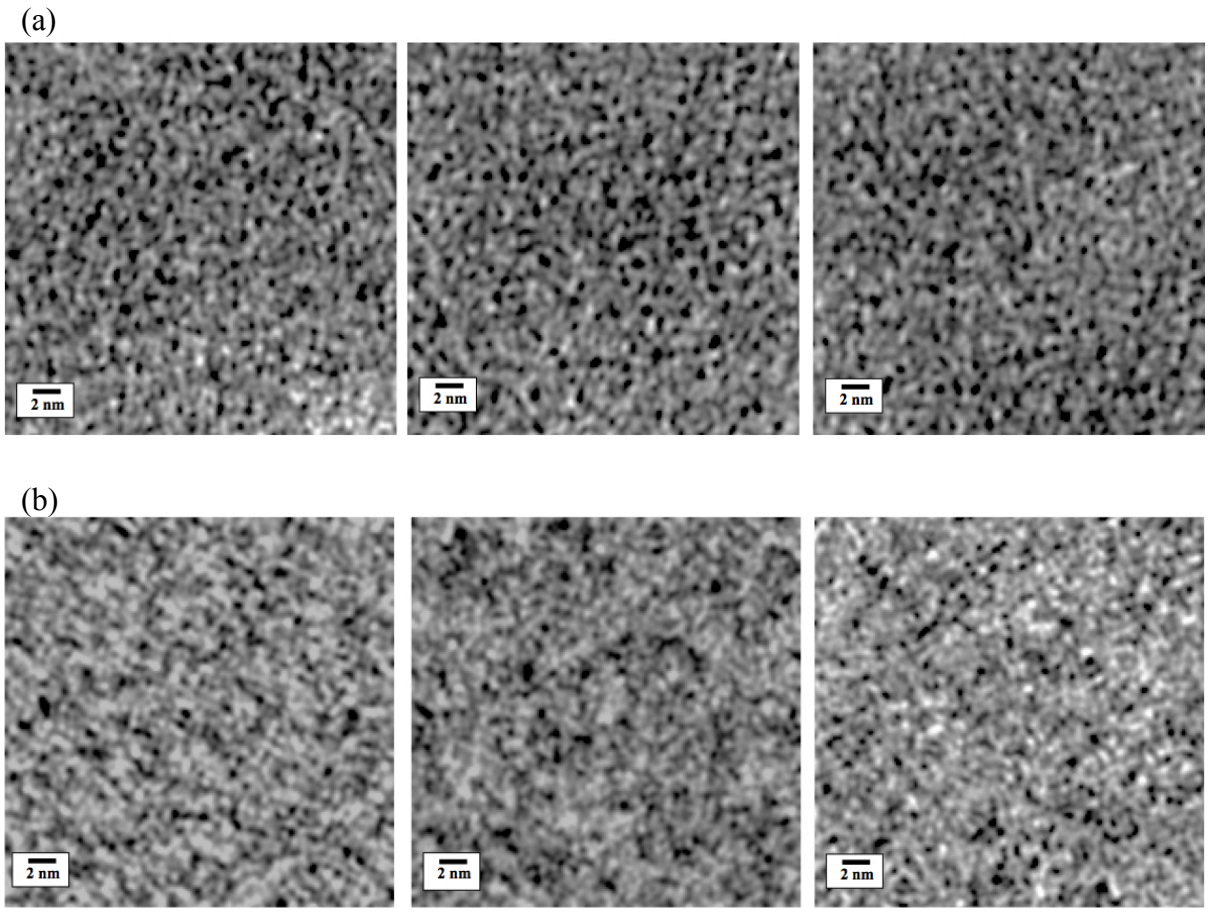


Figure 5.7 High magnification TEM cross-sectional images of the composite separation layers.
Three images acquired from different regions: (a) PTMSP composite layer and (b) PA composite layer.

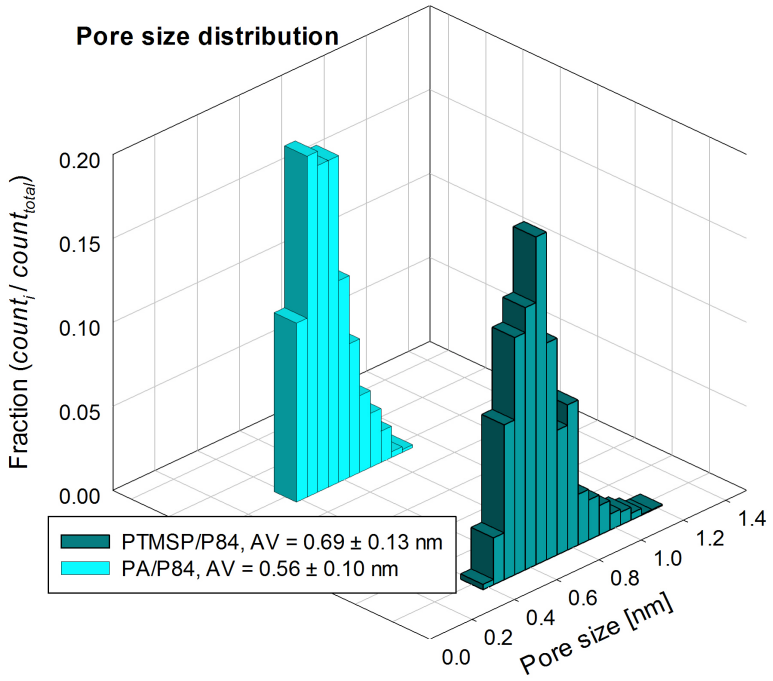


Figure 5.8 Measured pore size distribution in the composite layers.

To compare the pore size estimated using the nanoprobe imaging technique with other experimental methods, the literature was reviewed to find the void size data in glassy polymeric membranes composed of PTMSP and PA. The results of positron annihilation lifetime spectroscopy (PALS) indicated that the distribution of free volume elements had a bimodal profile. The estimated pore size ranges for the PTMSP film were 0.68 ± 0.07 nm and 1.36 ± 0.01 nm [77], and for the PA film they equalled 0.42 nm – 0.48 nm and 0.70 nm – 0.9 nm [234]. A comparison of the PALS with the nanoprobe imaging data suggests that the mean pore size determined in our study belongs to the lower range of the diameters estimated by PALS. The reason for this may be associated with the assumption stating that a pore is circular in the positronium lifetime formula, which calculates the pore radius [196, 197]. However, free volume elements present in a polymeric matrix are more likely to be irregular in shape, and so the pore size estimated from the nanoprobe imaging would be indeed smaller than a diameter estimated from the positronium lifetime formula.

5.3.6 Relationship between the pore size and nanofiltration performance

Given that the molecular transport through the dense polymeric membranes occurs through free volume elements or spaces not occupied by the chains [77], the relationship between the nanostructure and the NF performance can be investigated through analysis of the pore size and rejection of solutes dissolved in the same solvent as used for dispersions of OsO_2 NP. It is critical to maintain identical filtration conditions during the nanoprobing and the NF experiments, since functional properties of a polymeric membrane operating in various solvents and at different pressures may change [27]. For instance, the transmembrane pressure has a strong impact on solute rejection due to membrane compaction [29].

To relate nanostructure of the separating layer to NF performance, rejection of α-methylstyrene dimer with MW of 236 g mol^{-1} was plotted against the mean pore size (Figure 5.9). Rejection of the marker molecule increased with larger pore size. Furthermore, the results have also implied that the membrane permeability is associated with the pore size. Therefore, it is possible that a pore flow model governs the permeation and selectivity in the PTMSP and PA films. The literature describes the transport through PTMSP films to be in the transition region between the solution–diffusion and pore–flow [84, 235]. The solute permeation mechanism through the PA composite membranes is still under discussion [236]. However, in the recent work published by Singh *et al.* [237], transport through the PA composite membrane was analysed leading to a conclusion that the pores are not well interconnected and the transport happens *via* both the solution–diffusion and pore–flow.

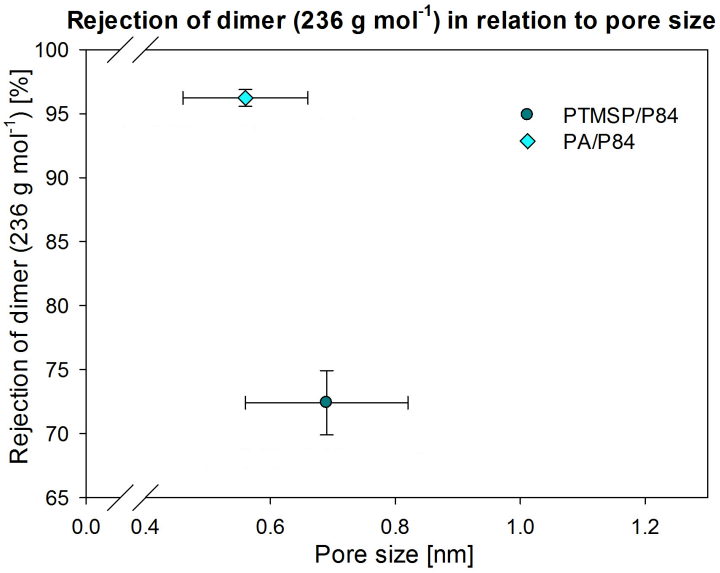


Figure 5.9 Correlation of solute rejection with pore size.

Relationship between rejection of α-methylstyrene dimer (dimer) with MW of 236 g mol^{-1}, and the mean pore size measured using TEM. Error bars correspond to standard deviation from the mean values.

To relate the nanostructure of the separation layer to the NF performance, rejection of α-methylstyrene dimer with MW of 236 g mol^{-1} was correlated with the mean pore size (Figure 5.9). It appears that the rejection of the marker molecules was strongly correlated with the mean pore size determined using the nanoprobe imaging technique. Furthermore, the results have also implied that the membrane permeability is associated with the pore size. Finally, based on the correlation, it is likely that the pore–flow model governs the transport through the PTMSP and PA films.

5.3.7 Detection of nanoscale defects

Defects in the membrane structure are often responsible for low reproducibility of NF characteristics. It is normally difficult to identify a cause accountable for poor performance, since membrane fabrication requires many steps. The nanoprobe technique is able to provide

insight into causes of low reproducibility, as it is a characterisation method based on *in situ* imaging of the transport; thus, any structural defects associated with solute permeation and selectivity can be detected. An advantage of the nanoprobe imaging over the other structural characterisation techniques such as for instance AFM or PALS, is an ability to look into the architecture and transport patterns across the separation layer and to help identify the cause of a defect.

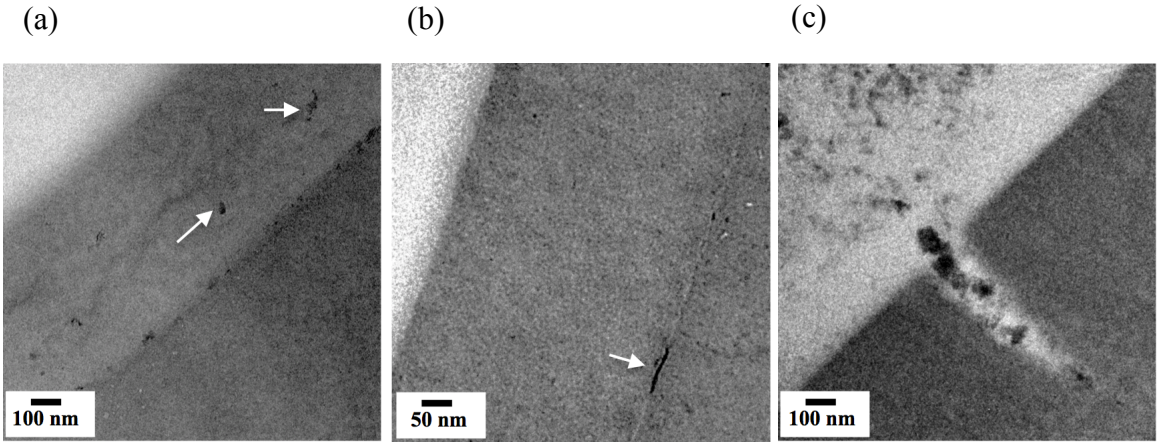


Figure 5.10 TEM cross-sectional images of the membranes probed with OsO_2 NP to detect the nanoscale defects.

(a) Irregular cavities found in the PTMSP layer due to the presence of air bubbles in the polymer solution used to cast the film. (b) The defect found at the interface between the PTMSP layer and the P84 support. (c) An example of discontinuity in the skin layer of a P84 asymmetric NF membrane, through which some of the OsO_2 NP were leaking. This type of defect could exist due to mechanical damage.

Figure 5.10 presents three examples of the defects detected using the nanoprobe imaging technique. The image in Figure 5.10a visualises cross-section of the PTMSP/P84 membrane. One can observe that large voids are present in the PTMSP layer. The cause of their existence is associated with insufficient degasing of the polymer solution, which after casting, still apparently contained air bubbles that transformed into voids. The second case is presented in Figure 5.10b, where insight into the interface between the PTMSP film and the support membrane is shown. The defect at the interface was revealed owing to the excessive accumulation of high contrast NP

within its free volumes. The last example presents a cross-sectional image of the P84 co-polyimide asymmetric membrane (Figure 5.10c) that supposedly was mechanically damaged on the surface. Because the NP were prone to permeation through this discontinuity, as depicted in the image, solutes could also leak through this defect leading to low rejection.

5.4 Conclusions

The study has demonstrated that the nanoprobe imaging technique, based on filtering NP high contrast agents, can be applied to characterise TFC membranes used for OSN processes. The pore size distributions were measured and correlated with the membranes' functional performance, implying that the selectivity of the OSN TFC membranes, composed of the glassy polymers such as PA and PTMSP, was highly related to the pore size. This correlation has suggested that the pore–flow model presumably governs the transport through these membranes. Furthermore, the membranes' cross-sectional images enabled detailed estimations of the thickness of the PA composite layer. An insight into the PA/P84 membrane has revealed that the composite layer delaminated from the support due to the treatment with DMF undertaken to activate the toluene flux.

Given that the membranes were characterised *in situ*, various nanoscale defects could be detected *via* imaging of excessive accumulations of high contrast NP in regions where the imperfections were formed. Therefore, this technique is recommended to characterise membranes under development, in order to find causes responsible for poor reproducibility.

CHAPTER 6

6. Assessment of atomic force microscopy for characterisation of nanofiltration membranes

6.1 Summary

Shortly after atomic force microscopy (AFM) became a common technique for characterisation of surfaces; it was applied to image morphologies of polymeric membranes. The main interest has been in analysis of the nodule size, the pore size and the roughness. Because nanofiltration (NF) membranes comprise nanostructures with dimensions within the lateral resolution of the microscope, the interpretation of NF membrane features remains challenging. This chapter describes and critically discuss the outcomes from experiments performed on NF membranes using AFM combined with carbon nanotube (CNT) probes, which are able to increase significantly the microscope resolution. The surface roughness, nodule and pore size were analysed for a range of the P84 co-polyimide integrally skinned asymmetric (ISA) NF membranes formed in the phase inversion process, and compared with the experimentally measured separation performance. Furthermore, a new concept for the membrane characterisation through quantitative analysis of the phase images is proposed. The phase imaging analysis aims to elucidate the macromolecular packing at the membrane surface, and correlate it with the membrane functional performance.

AFM combined with the CNT probe has a potential to provide additional resolution, allowing measurement of the nodule size, roughness, phase lag and possibly the pore size, with higher accuracy in comparison to the studies that used a conventional probe that was significantly larger than the CNT tip. These analyses could yield more detailed understanding of the molecular architectures resulting from the phase inversion process and their impact on the

molecular weight cut-off (MWCO) and flux. A significant part of this study is intended to analyse the phase images to search for further information about the macromolecular packing building the membrane surface.

6.2 Materials and methods

6.2.1 Membrane preparation

All membranes were prepared from P84 co-polyimide of which the chemical structure is shown in Figure 3.2a (HP Polymers, Austria) without any additional purification processes. Dope solutions were prepared with the following compositions: 24% (w/w) P84 dissolved in a mixture of dimethylformamide (DMF) and 1,4 dioxane (dioxane) at the solvent ratios of 1:2, 2:1 and 3:1 (corresponding to membranes M4, M5 and M6, Table 6.1). The detailed membrane preparation procedure is included in Section 3.2.1.

Membranes for AFM characterisation were prepared using exactly the same methods as described above; however, the difference was that they were directly cast on a glass plate and they were not conditioned with polyethylene glycol (PEG), as PEG would have affected the results of the analyses. Furthermore, directly prior to the AFM imaging the samples were exposed to a flow of nitrogen to remove traces of dust or other potential contaminants that could be transported to the cantilever probe and obstruct the measurements.

A non-porous dense film was prepared according to methods described in Section 3.2.2.

Table 6.1 Membrane nomenclature and dope solution composition.

Membrane	Polymer wt. concentration in a dope solution (%)	DMF: dioxane solvents ratio in a dope solution
M4	24	1:2
M5	24	2:1
M6	24	3:1
Dense film	24	2:1

6.2.2 Nanofiltration experiments

NF characteristics were measured on a mixture of polystyrene (PS) oligomers and α-methylstyrene dimer dissolved in acetone and filtered at a feed pressure of 10 bar. The detailed filtration procedure and the rejection measurement methods are included in Section 3.2.4.

6.2.3 AFM characterisation

6.2.3.1 AFM set-up

AFM was performed on a Veeco AFM Dimension 3100 with Nanoscope VI controller. Samples were attached to glass slides using a double sided tape. The scans were performed in an air medium. The images were scanned in the tapping mode using cantilevers with single- or double-walled CNT (Nanosensors, Switzerland) (Figure 6.1) having, according to the supplier, a nominal diameter of 2 nm, spring constant (k_s) of 2.8 N m^{-1}, and the quality factor (Q) of 280. Scanning was performed at a speed of 2 Hz, and scan size of 500 nm for standard images (analysis of nodule size and roughness) and 200 nm for higher magnification images (analysis of the pore size). A sampling resolution of 512 points per line was selected. The cantilever was tuned at the free amplitude of 1V (A_0 = 24 nm, relative setpoint of 0.8).

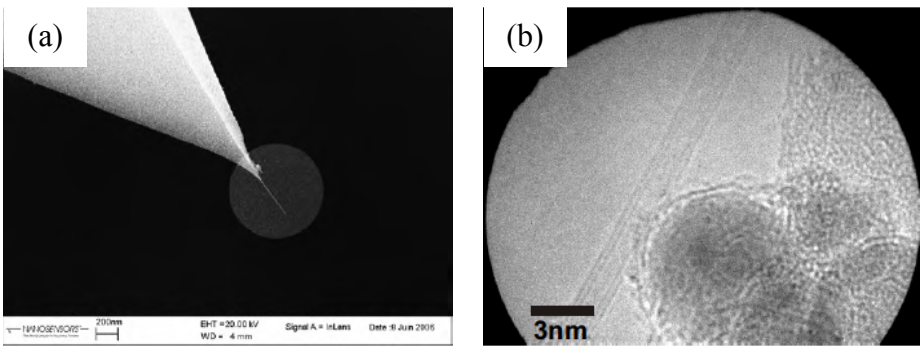


Figure 6.1 Electro-micrographs of the CNT tip supplied by Nanosensors™.

(a) SEM image of a silicon probe with grown CNT tip (scale bar 200 nm). (b) TEM image of a double-walled CNT. Both images adapted from the Nanosensors™ supplier information that was received together with the tips.

6.2.3.2 Surface roughness analysis

Surface roughness is an important structural property of NF membranes. The root–mean–square (RMS) roughness (R_q) (Eq. 1.31) was measured, since it averages the difference between peaks and valleys across the surface. Further roughness analysis included estimations of the magnitudes of the peak–to–valley height (R_z) (Eq. 1.32), surface skewness (R_{sk}) (Eq. 1.33), surface kurtosis (R_{ku}) (Eq. 1.34) and the surface area ratio (R_{ar}) The formulas used to estimate these parameters are included in Section 1.4.1.4.

Since surface roughness is dependent on the size of the scanned area [130], it is essential to estimate the roughness characteristics from images with a constant surface area. Therefore, all estimates came from images with a scan size of 500 nm x 500 nm followed by averaging from at least three images acquired from different regions of the same sample.

6.2.3.3 Nodule size measurement

WSxM software [160] was used to estimate the nodule size. The topographical images were convoluted using a wavelet transform [238]. The wavelet coefficient was set to 2 nm as it resulted in suitable amplification of the desired structural features, such as contours of the nodules, without lateral alteration of sizes and shapes of these features. Images were then transferred into the intensity profiles and further analysed in the J Image software [206], using the particle analysis functions which allow for quantification of the surface areas of each nodule; herein, a nodule is to be assumed as a flat “grain”. For diameter calculation, the circularity (C) as defined by Eq. 3.1, was computed. If a circularity factor greater than 0.8 was detected, then the nodule surface area was used to estimate the diameter.

6.2.3.4 Pore size measurement

Pore size was estimated from the high magnification images in conjunction with the digitally stored line height profiles from which sizes of depressions were estimated. In each case at least 100 cavities were measured to obtain the mean pore size and standard deviation. This is a well-known procedure, commonly reported in the literature, used to measure the pore size [109].

6.2.3.5 Phase image analysis

The phase lag angle was analysed in terms of RMS phase lag (P_q), peak–to–valley phase lag (P_z), phase lag skewness (P_{sk}), and kurtosis (P_{ku}). These parameters can be estimated with use of Eqs. 1.30 – 1.34 (Section 1.4.1.4). In addition, the characteristic lengthscale (ξ) was determined in order to numerically analyse variations between the images. The characteristic lengthscale (Eq. 3.4) was obtained from the wave number (q_{max}) evaluated using the power spectral density (PSD) of the phase lag maps.

6.3 Results and discussion

6.3.1 Nanofiltration performance

NF characteristics of membranes M4, M5, and M6 were evaluated in acetone at a pressure of 10 bar using the PS markers. The plot of rejection curves, presented in Figure 6.2, provides estimates of MWCO, which is defined as the molecular weight (MW) of a solute rejected at 90 %. The MWCO estimated for membrane M4 is 240 g mol^{-1}, for M5 is 430 g mol^{-1}, and for M6 is 1000 g mol^{-1}, and the acetone permeation fluxes measured after 4 h are: 19 ± 1. L m^{-2} h^{-1} (M4), 91 ± 5 L m^{-2} h^{-1} (M5), and 164 ± 14 L m^{-2} h^{-1} (M6). The NF characteristics obtained under the same filtration conditions can be attributed to differences in the membranes' nanostructure, since all three membranes were fabricated from the same polymer. Previous work describes how the membrane functional performance can be varied in a controllable manner by varying the solvent – co-solvent ratio of the solvent mixture used to dissolve the polymer in a dope solution [29, 31, 62]. In the phase inversion process of the P84 co-polyimide membranes, an increase of dioxane content in the polymer solution results in decrease of flux and MWCO. The next paragraphs explore whether the flux and rejection can be related in a systematic manner to the surface characteristics of the P84 co-polyimide asymmetric membranes characterised in the tapping mode.

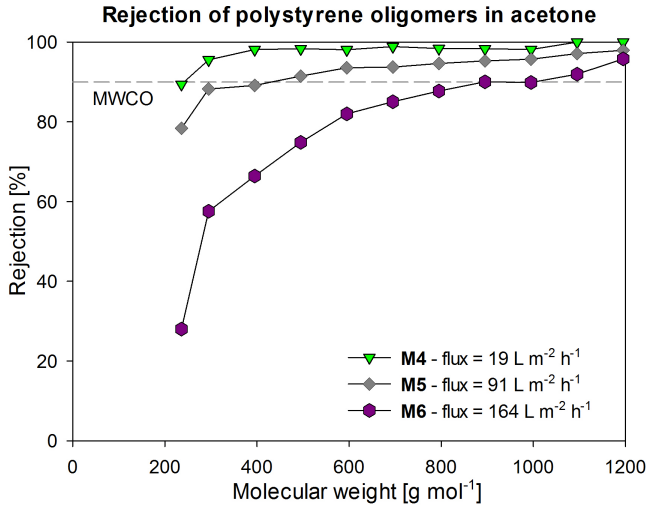


Figure 6.2 Rejection curves of membranes M4, M5 and M6 in acetone.

Table 6.2 NF membrane characteristics

Membrane	MWCO ($g\ mol^{-1}$)	Flux ($L\ m^{-2}\ h^{-1}$)
M4	240	19 ± 1
M5	430	91 ± 5
M6	1000	164 ± 14
Dense film	-	0

6.3.2 Surface topography

6.3.2.1 Roughness analysis

There are many parameters that can be used to analyse the surface roughness. RMS, peak–to–valley, skewness, kurtosis, and surface area ratio were selected for analysis. Table 6.3 presents the roughness parameters, which clearly show trends in relation to dioxane content in the dope solution. The higher the content of dioxane in the dope solution, the lower the RMS roughness, peak–to–valley height, and surface area ratio. Dioxane as a poor solvent for the P84 polymer induces chain entanglement, triggering chains to coil up tightly, leading to reduction of

their surface area and decreasing the distance between “peaks” and “valleys”; thus, the RMS roughness is lower in comparison to the membranes formed from a dope containing less dioxane. Presumably this effect occurs due to the response of the macromolecules to the unfavourable low solubility environment, where the chains are prone to minimisation of the surface area while in contact with a poor solvent.

An intriguingly high RMS roughness value was measured for the non-porous dense film. Given that the film was cast on a glass plate, very low surface roughness was expected. Instead, high RMS roughness and peak–to–valley height were measured. This might occur since the solvent evaporation during the heat treatment of the cast film resulted in non-uniform topography of the surface.

The surface skewness, describing the shape of the height distribution, is positive for all membranes, suggesting that the surface comprises peaks rather than cavities. The skewness value decreases in the following order: M4 > M5 > M6. This trend implies that with increasing dioxane content in the dope solution, the chains organise themselves into tighter complexes resulting in smaller depressions. The surface kurtosis value as an indicator of sharpness of the height distribution was estimated to be above 3 for membranes M4 and M5, and below 3 for membrane M6; implying that membrane M6 has a significantly less sharp height distribution, and characterised by repetitive flat features, in comparison to membranes M4 and M5.

Table 6.3 A quantitative summary of the surface roughness

Membrane	RMS roughness R_q (nm)	Peak-to-valley height R_z (nm)	Skewness R_{sk}	Kurtosis R_{ku}	Surface area ratio R_{ar}
M4	0.790 ± 0.023	7.665 ± 1.286	0.219 ± 0.003	3.448 ± 0.042	1.036 ± 0.011
M5	1.171 ± 0.046	10.230 ± 1.867	0.202 ± 0.001	3.493 ± 0.074	1.056 ± 0.014
M6	1.738 ± 0.034	12.771 ± 0.657	0.107 ± 0.003	2.900 ± 0.039	1.068 ± 0.022
Dense film	1.686 ± 0.030	14.785 ± 3.471	0.3695 ± 0.045	12.3832 ± 0.089	1.065 ± 0.021

6.3.2.2 Nodule size measurement

Nodule size was estimated from the height–images (Figure 6.3) produced in the tapping mode. It can be observed that the topography systematically changes and the features become finer with increasing dioxane content in the dope solution. The topographical image of the non-porous dense film (Figure 6.3d) shows a visually smoother surface in comparison to the membranes M4 – M6 (Figure 6.3a–c), although the peak–to–valley height and RMS roughness (Table 6.3), measured for this sample, is very high. The surface of the dense film does not contain nodular-like structures in comparison to the membranes M4 – M6. Instead, there are occasionally occurring “hills”, which are possibly formed due to irregular evaporation of the solvent mixture from the film during the heat treatment.

The nodule size was estimated by “drawing” a cross-sectional profile line across the height–images, and measuring the peak widths by transversely moving a cursor across the 2–D surface contour. Despite it is the most common method, this type of analysis does not take measurements from the entire scanned surface area, and selection of the profile line and peaks is somewhat at the discretion of the investigator and so may be inconsistent. Following initial attempts with 2–D surface profiles, a method using a WSxM AFM image processing software

was developed. In the developed algorithm an entire image is analysed (see schematic representation in Figure 6.3e) with high consistency; therefore, deviations occuring due to a human discretion are excluded. Each image was convoluted using the 'wavelet analysis' at a wavelet scale of 2 nm, which was found to be the optimum to enhance the nanoscale objects. This scale was also considered as fairly realistic in relation to size of the CNT tip which was 2 nm in diameter. A smaller value of the wavelet scale could result in over-processing of an image. With this transform, the images became flattened by means of equalising *Z*–height, resulting in enhancement of intensities over the regions of nodules and depressions to become more distinctive. The wavelet–filtered images were then transformed by the image processing software (J Image) where the following functions were used: 'find maxima' to localise nodules in the image, and 'analyse particles' to estimate the nodule area. Since the nodules measured using this method had low values of circularity (defined by Eq. 3.1) between 0.48 and 1, it might be misleading to consider them as spheres and to calculate their diameter. Hence, the data is presented in form of the distributions of the nodule areas (Figure 6.4a). The estimated average nodule areas for membranes M4, M5 and M6 are correspondingly 109 ± 75 nm^2, 156 ± 92 nm^2, and 205 ± 120 nm^2. The standard deviation values are relatively high due to wide distribution of the nodule size, and so multiple measurements were taken in order to conduct the statistical analysis.

The nodule diameter was calculated from features possessing a circular-like shape, with the condition of circularity greater than 0.8 being applied. The estimated mean diameters of the circular nodules for membranes M4, M5 and M6 correspondingly are 9.3 ± 3.6 nm, 11.8 ± 4.0 nm, and 13.2 ± 4.2 nm. Figure 6.4b presents the mean diameters calculated at the 95% confidence level. The values estimated for populations at each category are statistically significant according to an ANOVA test with a p–value computed for each pair of means considerably lower than 0.05. It is clear that the data is statistically significant and the mean

nodule sizes fit into the trend, which is that with increasing dioxane content in the dope solution, the nodule size decreases.

It is not straightforward to elucidate the impact of the dope solution composition on the nodule size, since the detailed mechanism of nodule formation is still not fully understood. Reuvers *et al.* [239, 240] proposed that nodule formation is driven by the nucleation and growth during the metastable demixing process. Wienk *et al.* [23, 72], however, commented that the demixing process is too rapid to allow for the nucleation and growth required for nodular aggregates to form; thus, it was suggested that nodules grow in response to the simultaneous out-diffusion of the solvent and in-diffusion of the non-solvent. In this environment the molecules rapidly coil up and surround themselves with other polymer segments to reduce their contact surface area with the non-solvent. Soroko *et al.* [31] calculated the polymer–solvent interaction parameters for ranges of the P84 co-polyimide/DMF/dioxane systems and numerically confirmed that the polymer solubility decreases with increasing dioxane content. Furthermore, the miscibility of the solvent mixture with water is related to the affinity of the solvent mixture towards water. Because the affinity of dioxane towards water is lower than for DMF, with increasing dioxane content, the demixing process is delayed in the ternary phase diagram [31]. The second mechanism that causes the delayed demixing can be found at the macromolecular level. In response to a poor solvent, polymer chains become highly entangled, leading to slowing down the demixing between the solvent (the DMF/dioxane mixture) and the non-solvent (water in a coagulation bath). Given that the nodule size is related to the dioxane content in the dope solution, the trend that with higher dioxane content, the nodule size decreases is observed. Therefore, it can be summarised that dioxane, as a poor solvent, enhances entanglement of the polymer chains during the demixing process, leading to smaller and denser packing of the nodular clusters on the membrane surface.

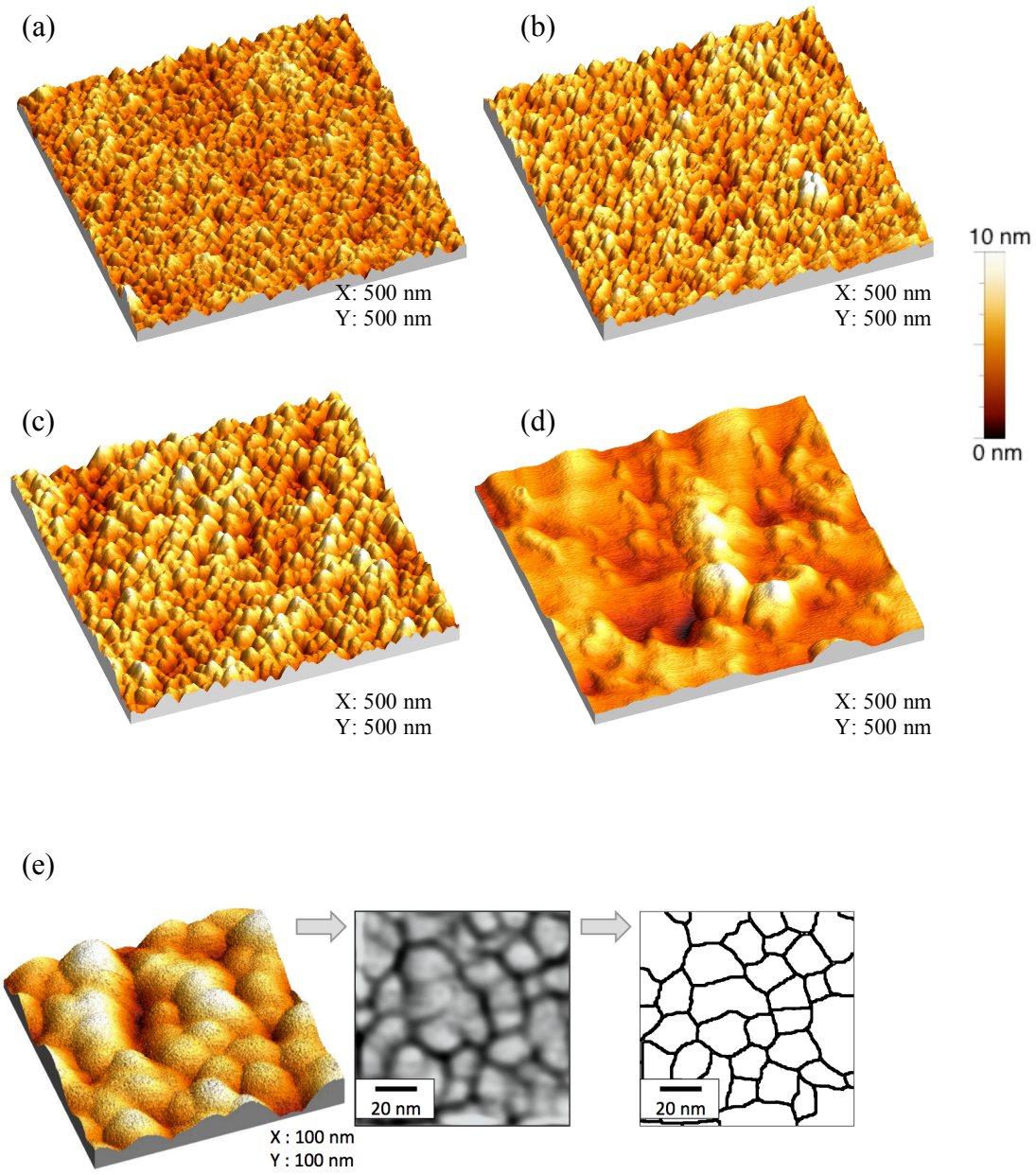


Figure 6.3 AFM topographical images revealing changes in the nodular structure.

(a) Membrane M4. (b) Membrane M5. (c) Membrane M6. (d) Non-porous dense film. (e) 3-D topographical image of membrane M6 and corresponding nodular pattern created to quantify the areas of nodules. X,Y – size of the scanned surface regions, Z-scale in the images is multiplied by a factor 2 for purpose of visualisation.

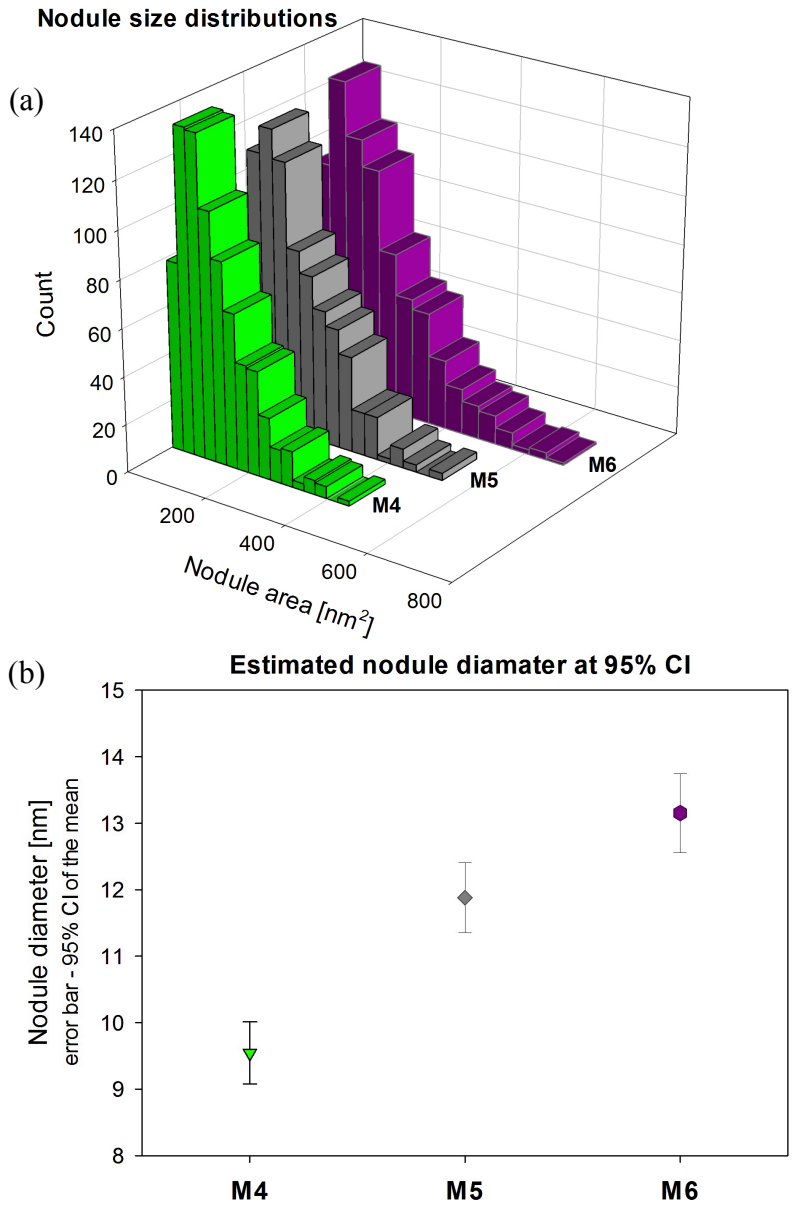


Figure 6.4 Nodule size analysis.

(a) Nodule size (by area) distribution. (b) Interval plot of nodule diameter estimated at 95% confidence level (CI). The mean nodule size for the studied membranes is statistically different according to the ANOVA test and the calculated P-value is considerably lower than 0.05.

Table 6.4 Numerical summary of the estimated values of median and mean of the nodule surface area and the mean diameter.

Membrane	Median (nm^2)	Mean (nm^2)	Nodule diameter (nm)
M4	94.2	108.6 ± 75.4	9.3 ± 3.6
M5	139.1	156.3 ± 91.8	11.8 ± 4.0
M6	178.9	204.5 ± 119.9	13.2 ± 4.2

6.3.2.3 Questionable pore size measurements

The pore size was measured from the 2–D profile line stored in the topographical images as shown in Figure 6.5a,b. Because this method is the most common procedure to measure the pore size, it was also applied to analyse the membranes for the purpose of assessment. The estimated mean pore size from at least 100 data measurements taken from each membrane image are as following: 1.53 ± 0.32 nm (M4), 1.65 ± 0.47 nm (M5), 2.07 ± 0.70 nm (M6). The pore–flow model (relevant formulas are included in Section 1.3.4.4) described by Bowen and Welfoot [94] was used to estimate the pore size. The model was also applied by See-Toh *et al.* [29] to computational analysis of transport and structure of OSN P84 co-polyimide membranes. To estimate the mean pore size based on the flux and rejection data, the fitting of calculated solute rejection (R_j^{cal}) into the experimental solute rejection (R_j^{exp}) was adopted from the paper of See-Toh *et al.* [29]:

$$S_y = \sqrt{\frac{\sum_1^n \left(R_j^{\exp} - R_j^{cal}\right)^2}{n-1}} \qquad \textit{Eq. 6.1}$$

The iteration of the pore size by fitting of R_j^{cal} into R_j^{exp} was completed when a minimum value of S_y was achieved. The calculated mean pore sizes in that manner were 0.38 nm for membrane M4, 0.42 nm for M5, and 0.76 nm for M6. This suggests that the pore size measured by AFM is significantly overestimated in comparison to the theoretical predictions. Since AFM tends to rather underestimate dimensions of the cavities as graphically demonstrated in Figure 6.5c, the

measurements might carry some level of uncertainty because they could be taken from at least some fraction of surface depressions, which did not lead to transport–active pores. Since this technique brings so many uncertainties, it is of interest to look into the lateral resolution limits. To measure size of the cavities on the surfaces having average roughness comparable to dimensions of these cavities, one needs to employ a probe with a high aspect ratio and an extremely thin tip, preferably smaller than a pore, as it is believed that these factors mainly determine the lateral resolution.

The lateral resolution according to Eq. 1.23, was estimated to be 1.79 nm, 1.83 nm, and 2.18 nm correspondingly for membranes M4, M5, M6, at the vertical microscope resolution δh_r of 0.1 nm [145], and the nominal tip radius R of 1 nm that is equal to the radius of a single walled CNT. The analysis clearly indicates that is not possible to measure the pore size in NF membranes with sufficient precision, because calculated dimensions are notably below the microscope lateral resolution. Furthermore, one can erroneously measure the cavity size on the surface as a pore because it is unknown whether it is a transport–active pore or a depression. To bring an additional argument to this discussion a control sample, *i.e.* non-porous dense film, was included. Its dense structure was achieved as a result of the solvent evaporation during the heat treatment through the so-called 'dry phase inversion process'. Section 3.3.7 describes that the fabricated film showed no flux, confirming that the structure was tight and non-porous. However, surface characterisation using AFM has yielded very high RMS roughness and the mean "pore" size was estimated to be 3.45 ± 1.01 nm. This value is even higher than the "pore" size measured for the most open membrane M6. The surface RMS roughness was also two times higher than for the densest membrane – M4. Hence, it implies that the measured pore size from the 2–D height profile is strongly related to the surface roughness. This mechanism is illustrated in Figure 6.5d, where a tip with a diameter within the size range of the pores is scanning the

rough membrane surface. The pores are omitted due to insufficient resolution and only some depressions are detected, which are misleadingly considered as pores.

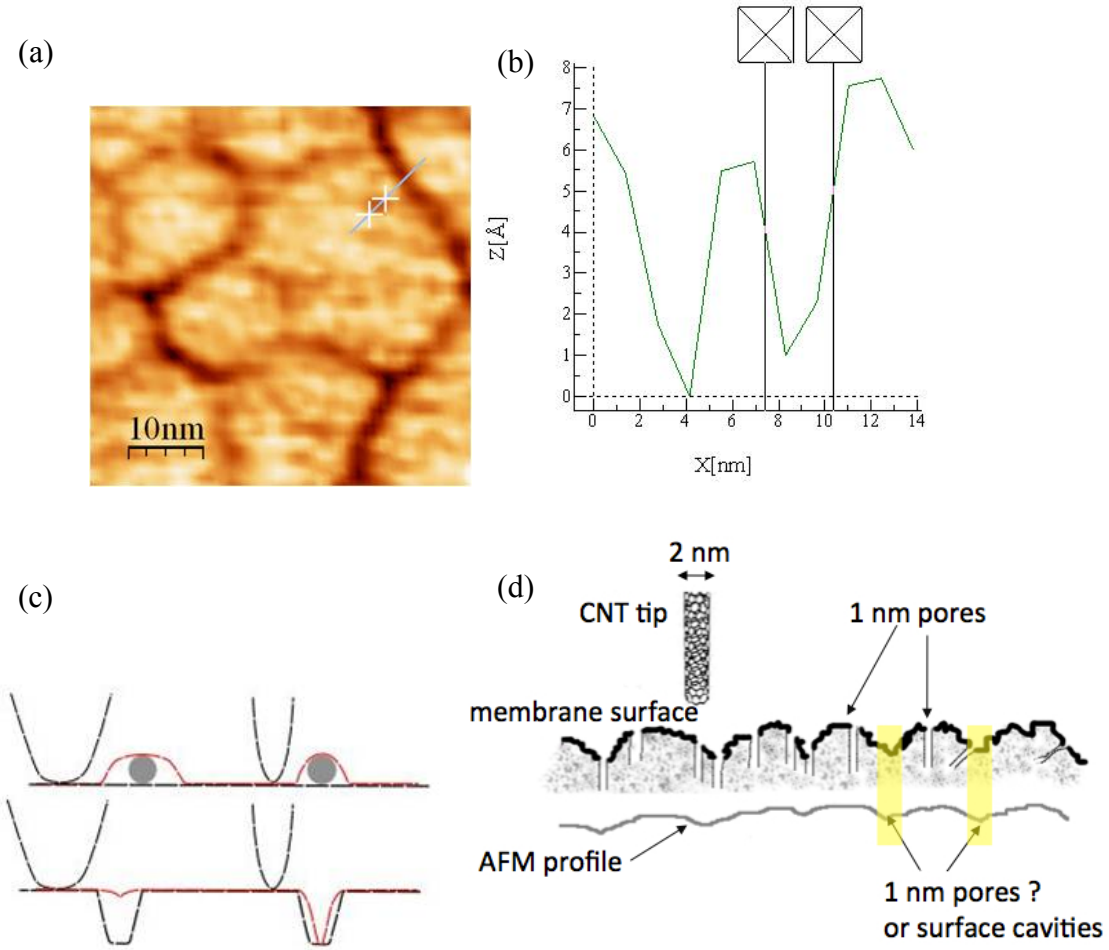


Figure 6.5 Pore size measurements analysis and possible misinterpretation.

(a) Graphical description of the methodology used to measure pore size using AFM software that generates (b) 2-D height profile, where the width of depression is estimated as the pore size. (c) Tip–surface convolution effect affects the size and shape of the concave and convex features. (d) Due to the tip-surface convolution effect the measurements taken from the membrane surface can lead to omission of some pores and misinterpretation of the pore size due to insufficient lateral resolution of the AFM probe.

Figure 6.6a demonstrates the correlation between the pore size and the RMS roughness determined for membranes M4 – M6 and the dense film. The higher the roughness, the higher the pore size that is measured using this technique. Although the technique may show the correlation between the pore size and the MWCO values as demonstrated in Figure 6.6b, special

care needs to be taken in interpretation of this trend, since as discussed above, the technique suffers from several pitfalls that can mislead the pore size analysis.

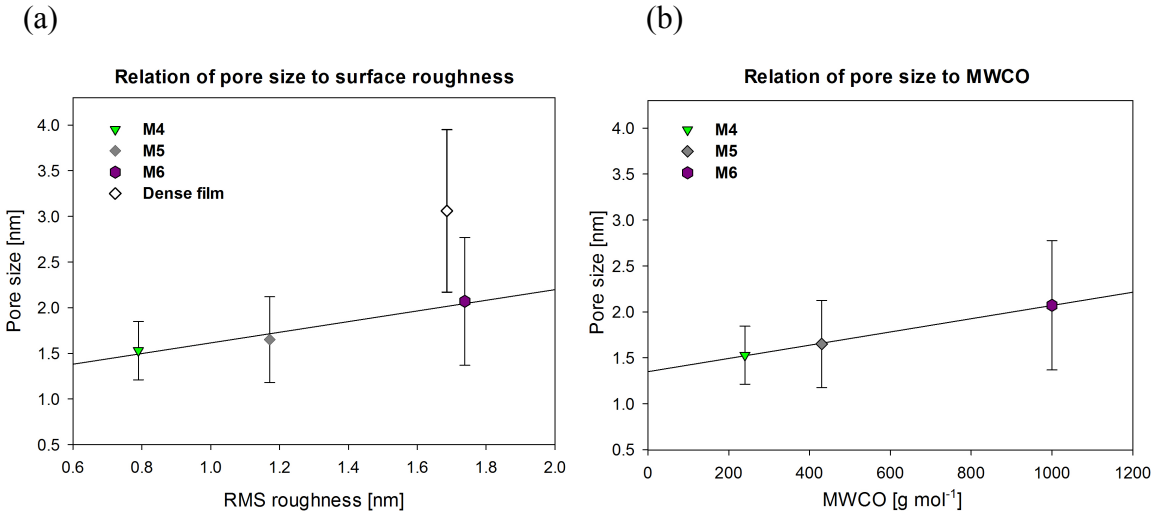


Figure 6.6 The pore size correlation graphs.

(a) The pore size measured for membranes M4, M5, and M6 is strongly correlated with the surface roughness, whereas the pore size of the dense film does not fit into this trend. (b) Although the plot shows good correlation between the pore size and the MWCO values, it is suspected that the pore size could be misinterpreted as it is strongly related to the surface roughness.

6.3.3 Correlation of surface topography with nanofiltration performance

AFM characterisation provides many parameters that can be studied to test correlations with flux or MWCO. The above paragraphs suggest that the analysis of the pore size, although they showing a good linear correlation with MWCO, may be misleading. Hence, special care needs to be taken in interpretation of the pore size measured by AFM for the purpose of prediction of the NF performance. Further analysis of the data delivered from the topographical images, presented as the RMS surface roughness and the nodule size, has indicated a good correlation with the flux and MWCO (Figure 6.7). The nodule size is linearly related to the

membrane flux; the smaller the nodule size, the lower the flux. There are two possible explanations: *i*) smaller nodules indicate that the chain structures are more compacted with narrower interstitial channels or pores and so the lower flow rates are expected, or *ii*) smaller nodule sizes correspond to lower surface area, *i.e.* superficial area, and thus lower mass transfer through the surface. The roughness is correlated with the membrane flux and MWCO in a way that with increasing in the RMS roughness, the rejection decreases and the flux increases.

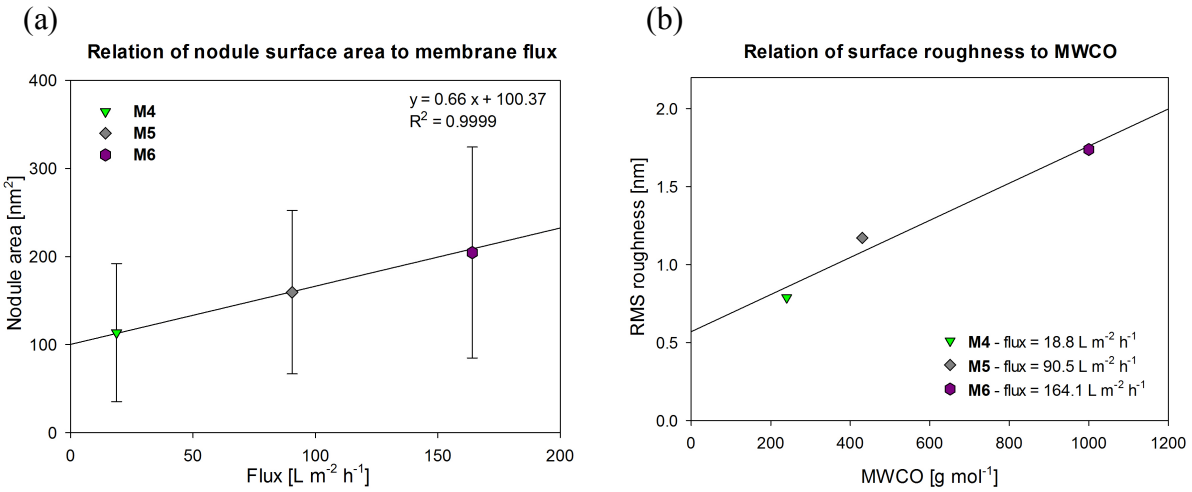


Figure 6.7 Correlation of the surface topography with NF performance.

(a) Correlation of the nodule size with the membrane flux. (b) Relation of the surface roughness to MWCO.

6.3.4 Analysis of phase images

An extension of the tapping mode is the phase imaging applied to map variations in the composition, friction, adhesion, and viscoelasticity of the surface based on the magnitude of the phase lag [241]. The phase lag of the oscillating cantilever at the constant amplitude is monitored in reference to the excitation signal. Since the phase lag is sensitive to changes in material properties independently from the topography, it provides a phase contrast that often offers higher resolution and detection strength than the standard height–images, which are produced

based on signals generated from the cantilever deflections. In this study, monitoring the phase lag gives maps of the viscoelasticity variations on the membrane surface, whose nanostructure results from entanglements of the polymer chains. Since the tapping mode provides very high resolution and the possibility to detect variations in material phases, this mode was adapted to study the polymer packing of the membranes composed of the same polymer, whilst arranged into different morphologies, as shown in the topographical images (Figure 6.3). A comparison of the height–images and the filtration performance indicates that the nanostructures vary systematically; and, if one would like to gain an insight into the macromolecular packing leading to this systematic variation, the phase imaging may provide useful information. The main variables studied to elucidate the packing degree of the polymer chains are phase lag, characteristic lengthscale and energy dissipation.

Figure 6.8a–d presents the phase contrast images of membranes M4 – M6 and the non-porous dense film. Arrangements of the phase–domains distributed along the surface become progressively finer with increasing dioxane content in a dope solution. It appears that a pattern of nodular structures, as observed in Figure 6.3, is comparable to the phase images. One of the methods to compare images containing the repetitive features is estimation of the characteristic lengthscale (ξ) (expressed by Eq. 3.4). This measure corresponds to the size of the feature that appears in an image with the highest frequency. PSD plots attained from the 2–D fast Fourier transform (FFT) profiles (2–D FFT rings are shown as insets in each of the phase images in Figure 6.8a–d) provide estimations of the characteristic lengthscale, which decreases with increasing dioxane content in the dope solution. The 2–D FFT spectrum of the dense film does not allow the image maximum wave number (q_{max}) to be attained, since the intensity peak was not observed in the PSD plots. This is because the phase image of the dense film does not show any distinctive domains, and thus it can be described as being homogenous in terms of viscoelasticity; this implies that the macromolecular packing does not exhibit any localised

nanoscale variations. The comparison of the height–image (Figure 6.3d) with the phase–image (Figure 6.8d) of the dense film indicates that the irregularly distributed “hills” observed on the topographical projection are not attributable to variations in polymer entanglement.

The magnitudes of the characteristic lengthscale and RMS phase lag, peak–to–valley phase lag, skewness, kurtosis are listed in Table 6.5. The value of RMS phase lag increases with dioxane content in the dope solutions from which the membranes were cast. Since the phase lag is related to the local viscoelastic properties, it can be associated with density of the membrane by means of the polymer entanglement. If the membrane is tighter, the chains exhibit denser packing, and in principle, the surface is expected to be stiffer and less compliant; thus, the viscoelasticity is lower, resulting in a lower value of the phase lag. The more compliant a material is in reaction to the force transmitted from the cantilever subjected to a constant setpoint amplitude, the more strongly it will respond, and as a result the amplitude is shifted further in its phase. A selection of the parameters for performing scanning and for analysing the recorded signals is not straightforward, and needs to be carefully considered. The scanning parameters need to be maintained constant at all times to compare independent samples. Furthermore, the phase lag is also strongly related to the quality factor and the resonance frequency of cantilevers, which often show tiny variations even within the same batch. Finally, one has to generate and understand the force–displacement curve in order to identify in which region, attractive or repulsive, the cantilever is operating. The attractive region was chosen as there, the cantilever deflections tend to be lower and thus the phase contrast is independent from the topography.

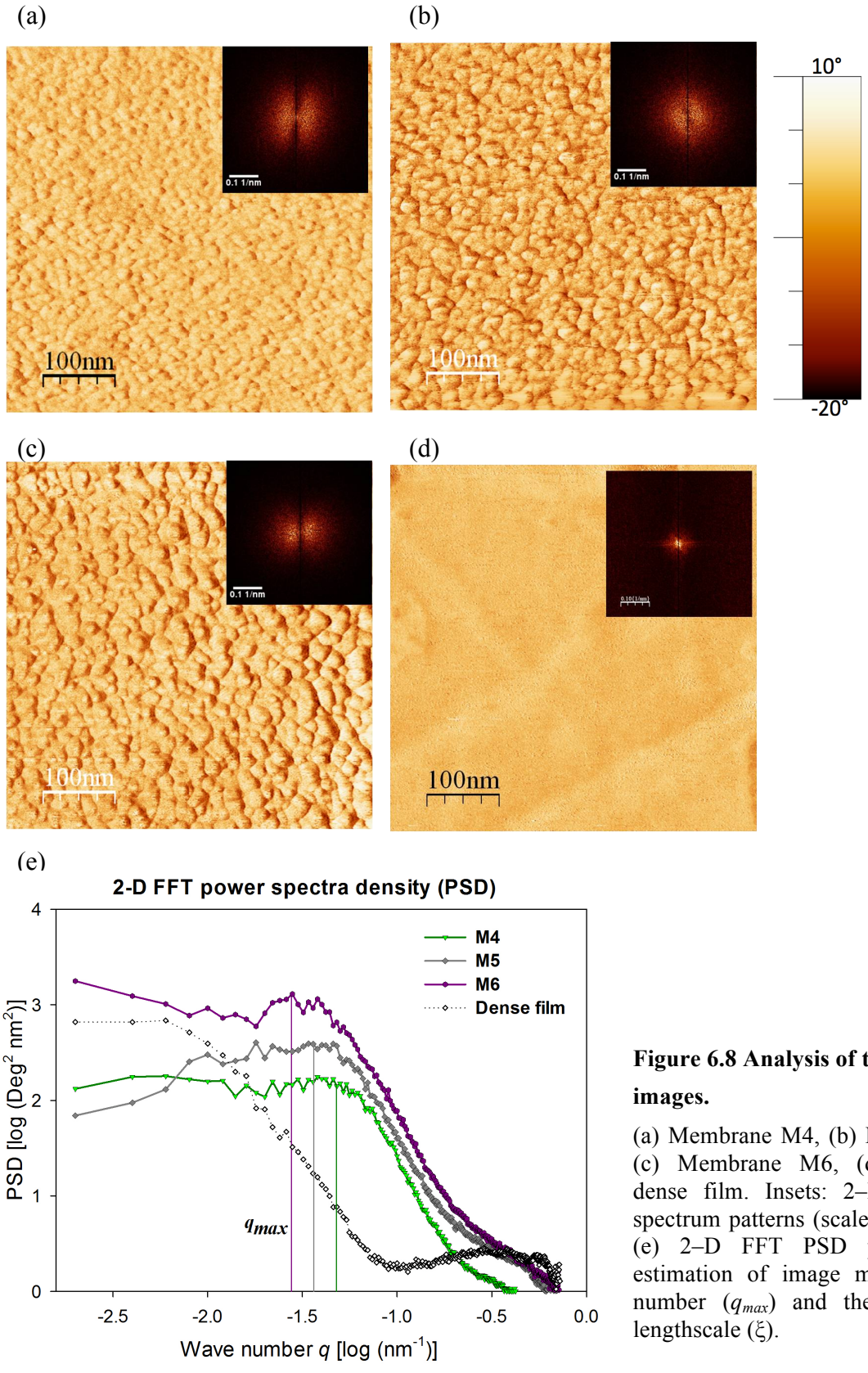


Figure 6.8 Analysis of the phase images.

(a) Membrane M4, (b) Membrane M5, (c) Membrane M6, (d) Non-porous dense film. Insets: 2–D FFT power spectrum patterns (scale bar: 0.1 nm^{-1}). (e) 2–D FFT PSD plot used for estimation of image maximum wave number (q_{max}) and the characteristic lengthscale (ξ).

Table 6.5 Surface phase lag analysis

Membrane	RMS phase lag P_q (°)	Peak-to-valley phase lag P_z (°)	Skewness P_{sk}	Kurtosis P_{ku}	Characteristic lengthscale ξ (nm)
M4	2.667 ± 0.199	21.672 ± 3.251	-0.853 ± 0.060	4.334 ± 0.189	21.0
M5	3.350 ± 0.231	25.119 ± 4.285	-0.615 ± 0.050	3.279 ± 0.121	27.6
M6	4.056 ± 0.250	51.411 ± 5.662	-0.719 ± 0.058	3.122 ± 0.103	36.2
Dense film	1.803 ± 0.052	42.316 ± 8.243	-0.615 ± 0.042	7.628 ± 0.240	-

Adhesion forces between the CNT probe and the surface are considered to have little effect on the phase shift in comparison to a silicon probe [242], as silicon tips experience greater Van der Waals attractive forces due to the large number of electrons accumulated on their tips [243]. Therefore, during scanning with the CNT tip the viscoelasticity is a dominant material property having an impact on the phase angle. The experimental observations suggested that the CNT tips operate more effectively in the attractive region. In the attractive region, the tip–sample interactions are lower than in the repulsive region where significant forces may lead to local penetration into soft surface of a sample resulting in topographical deformations in the image [242]. Taking this effect into account, the cantilever with the CNT tip was driven at frequency 10% lower than the resonance frequency in order to decrease the tapping force.

The phase contrast images processed to distinguish the regions, attained when the tip–surface interaction forces were attractive, are presented in Figure 6.9. The attractive regions, which appeared in the images as “islands”, were analysed in terms of inelastic interactions using the energy dissipation magnitudes. Variations in inelastic interactions between the tip and the surface correspond to changes of dissipated energy per cycle. Given that the energy dissipation

corresponds to material compliance, it can be related to tightness of the polymeric packing (see schematic representation in Figure 6.10a). Eqs. 1.26 and 1.27 (Section 1.4.1.3) determine values of the energy dissipation per cycle, which are presented as distributions in Figure 6.10b. The estimated mean values are: 15.343 ± 0.045 eV – membrane M4, 15.379 ± 0.077 eV – M5, 15.440 ± 0.093 eV –M6, and 15.326 ± 0.036 eV – dense film. It should be not surprising that the values are not dramatically different, since they come from compositionally identical samples. Nevertheless, there is a trend, in which the mean dissipated energy decreases with the membrane tightness. To support the numerical analysis the mean values estimated at 95% confidence level is included in an inset of Figure 6.10b. The graph suggests that the means are statistically different, and indeed, show a trend related to the composition of the dope solutions used to cast the membranes.

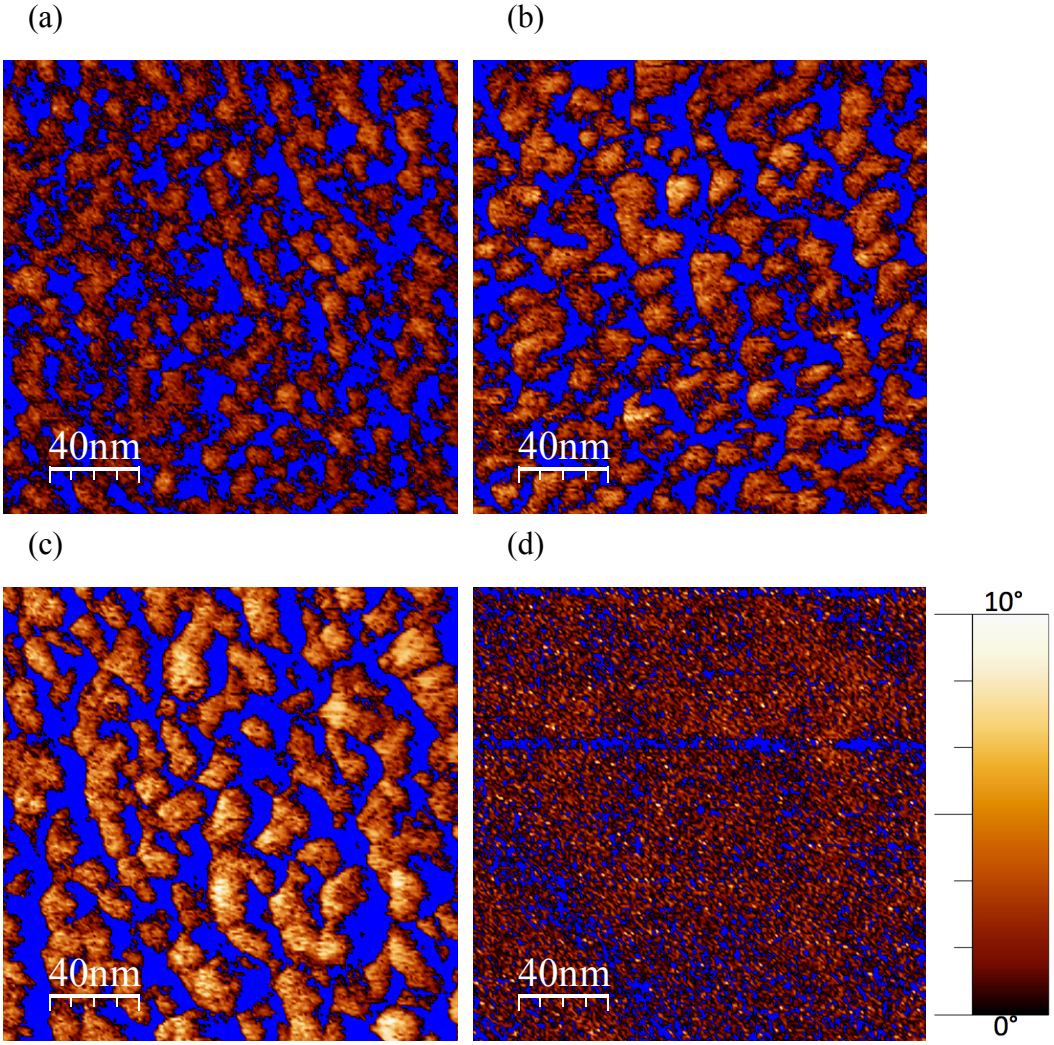
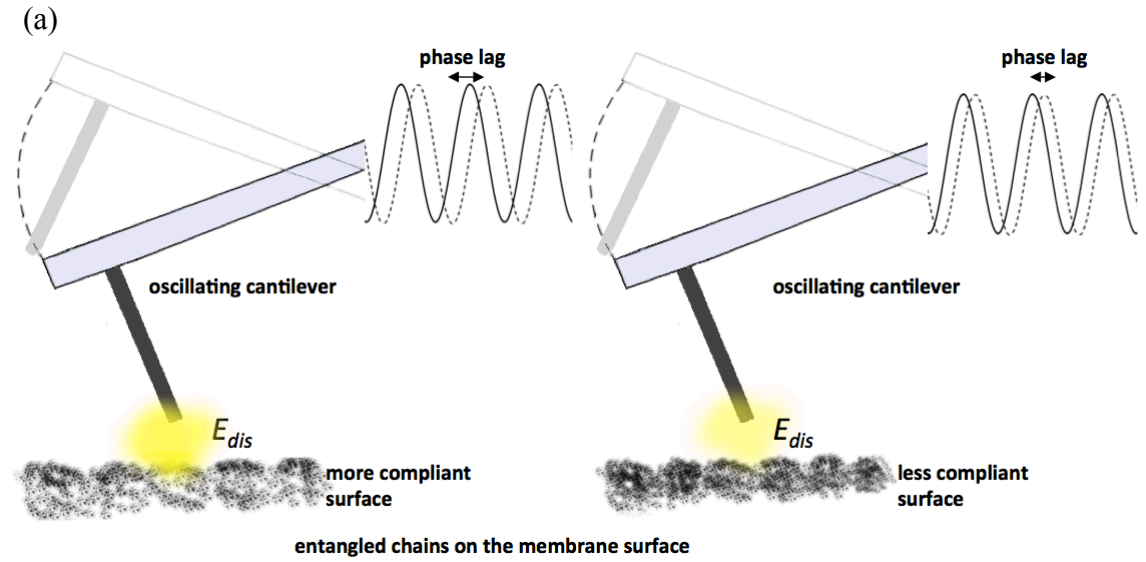


Figure 6.9 Attractive–region phase images

(a) M4, (b) M5, (c) M6, (d) non-porous dense film analysed in the attractive mode after application of the threshold to exclude the phase lag angles below 0° (marked blue).

Table 6.6 Attractive mode phase image analysis

Membrane	Area scanned in the attractive region (%)	Island-to island average distance (nm)	Average phase lag (°)	RMS phase lag P_q (°)	Energy dissipation per cycle E_{dis} (eV)
M4	55.4	4.01	1.948	1.434	15.343 ± 0.045
M5	55.5	4.08	2.496	1.680	15.379 ± 0.077
M6	59.0	3.69	2.721	1.764	15.440 ± 0.093
Dense film	52.4	-	1.234	1.085	15.326 ± 0.036



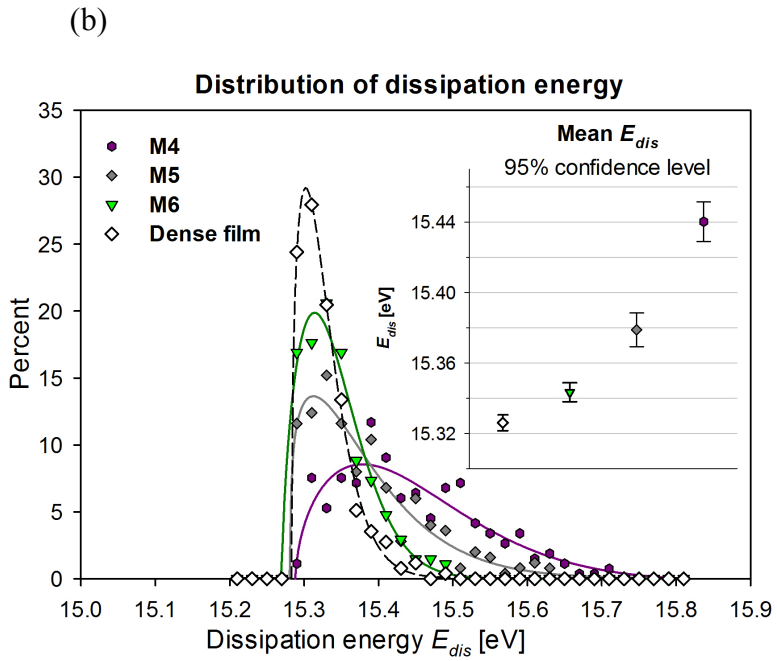


Figure 6.10 Energy dissipation analysis.

(a) Schematic drawing of the oscillating cantilever generating the dissipation energy. The magnitude of energy dissipation (E_{dis}) and phase lag are related to entanglement degree of the polymer chains and the surface compliance. (b) Distribution of the energy dissipation per cycle calculated in the attractive region, for membrane M4, M5, M6, and the dense film. An inset presents a plot of the means estimated at 95% confidence level.

6.3.5 Correlation of phase lag with nanofiltration performance

Beyond offering good contrast of nodular structures, phase imaging also provides information on the phase lag and the dissipation energy, which in turn help to elucidate the internal structure of the NF membranes. The interesting aspect is to correlate the phase lag and the characteristic lengthscale with the membrane functional performance. Figure 6.11 shows a graph in which the MWCO and flux are strongly related to the magnitudes determined from the phase images. One should note that the data derived from the height–images of the non-porous dense film was not correlated to the functional performance. The measured RMS surface roughness was very high; however, the dense film was intentionally fabricated to generate a non-porous and impermeable structure, and so low roughness was rather expected. In contrast to the topographical images, the phase lag of the dense film is significantly lower than estimated for the densest membrane M4; therefore, these results have strongly supported the hypothesis that the phase lag and the dissipation energy are indeed associated with the membrane tightness.

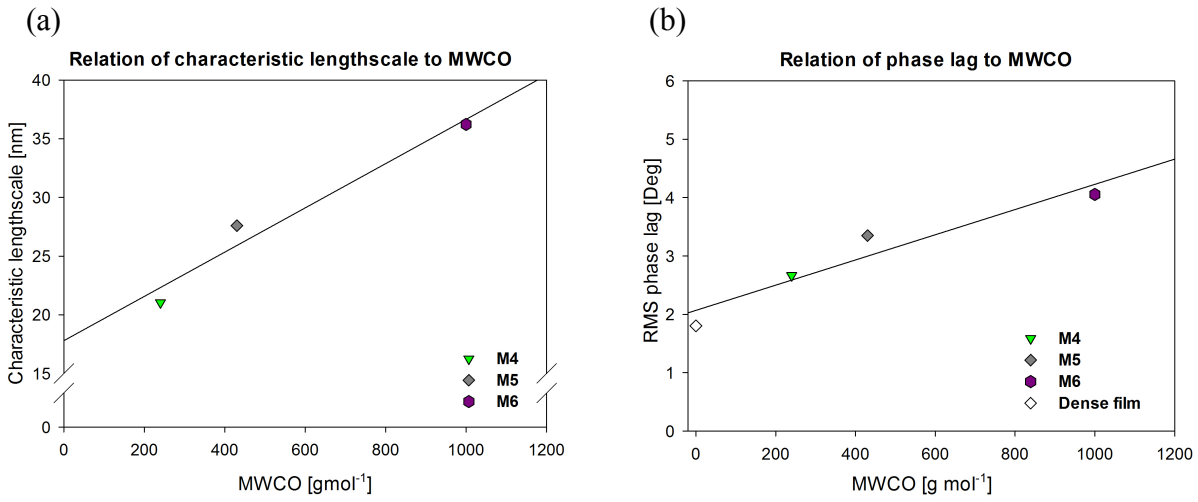


Figure 6.11 Data determined from the phase images versus NF performance.
(a) Relation of characteristic lengthscale to MWCO. (b) Relation of phase lag to MWCO.

6.4 Conclusion

In this work the application of AFM to characterisation of NF membranes has been assessed. The objective was to evaluate whether AFM can bring any valuable information to progress understanding of the membrane structure, which can be related to membrane formation methods as well as to the functional performance. A range of the P84 co-polyimide membranes was analysed using the topographical and phase images. The nodule size and roughness correlated well with the flux and MWCO for membranes that were cast from dope solutions comprising solvent mixtures at various ratios of solvent (DMF) to co-solvent (dioxane). It was found that a higher content of dioxane in a dope solution resulted in a smaller nodule size and consequently lower RMS roughness. This effect was associated with the phase inversion kinetics such as the delayed demixing process, and thermodynamics, particularly the polymer solubility. Both factors governed the final surface morphology of the membranes studied.

The possibility to obtain the pore size measurements in NF membranes using AFM has always been considered very attractive. Here, the AFM was combined with a CNT probe, which is the thinnest available probe, to increase resolution of the microscope. The results obtained through comprehensive analysis and control experiments have suggested that the measurements of the pore size using AFM alone may not provide actual information on transport–active pores due to lack of resolution, convolution effects and uncertainty whether a measured depression is a pore opening or a concave feature. The assessment has suggested that interpretation of AFM images needs to be performed with special care and rigorous characterising procedures. Therefore, the next chapter will include proposed paths that may still be worth to explore on behalf of these assessing studies.

Phase imaging, as an extension to the tapping mode, offers very interesting information describing the internal polymer packing at the membrane surface. The maps of the phase angle

and the dissipation energy distributions computed for each membrane have shown that the phase imaging, if performed with special attention to settings of the scanning parameters, provides further information on polymer chain entanglement, which cannot be determined from the topographical images. The control analysis of the phase shift measured for the dense film has shown that its magnitude is significantly lower than the phase shift measured for the membranes. Although an effect of the surface topography on the phase shift may be still present, nevertheless, the control studies have implied that the origin of the contrast in the phase images is rather attributable to variations in polymer packing. The magnitudes of the phase lag and the dissipation energy have shown to correlate with the flux and MWCO.

7. Conclusions and future directions

The conclusions and future research recommendations are divided in two parts. The first part is focused on the summary of the research results determined by the nanoprobe imaging technique and computations using the pore–flow model; whereas, the second part is related to application of atomic force microscopy (AFM) to the characterisation of nanofiltration (NF) integrally skinned asymmetric (ISA) membranes.

The main achievement of this work was development of an *in situ* membrane characterisation technique facilitating the size measurement of the permeation pathways or pores localised in the separation skin layer. The developed technique was based on filling the pores in NF membranes with high contrast nanoparticles (NP) dispersed in an organic solvent performed during filtration at a pressure of 10 bar. Thus, the identical conditions to the experimental filtration could be maintained during the nanoprobing. The core of these findings was ability to detect and measure the transport–active pores with dimensions at sub-nanoscale. This was realised by mapping the osmium dioxide (OsO_2) NP (developed and fabricated in-house) that filled the free volume spaces, *i.e.* membrane permeation pathways, present between bundles of the entangled polymer chains, using transmission electron microscopy (TEM). The undertaken TEM image analysis determined the pore size distribution and the skin layer thickness. The technique was applied to characterisation of the P84 co-polyimide ISA membranes (fabricated to achieve various separation performances), and also to two thin film composite (TFC) membranes composed of polyamide (PA) or poly(1-trimethysilyl-1-propyne) (PTMSP) top layers. The studies aimed to search for a correlation between the membrane structure, particularly the pore size, and the NF performance described by the solute rejection and the flux. It was found that the mean pore size correlated well with the polystyrene (PS) rejection. The pore size distributions

were observed to be rather wide; therefore, this finding explained the presence of a flat slope of the rejection curves evaluated for the studied membranes. Furthermore, the molecular separation based on size–exclusion mechanism in the membranes has been proposed, given that the permeated particle size distribution was comparable to the pore size distribution evaluated for a corresponding membrane.

A follow-up of the structural characterisation technique was assessment of the pore–flow model computed based on the evaluated pore size distributions. Here, the experimental rejection curves of PS solutes and OsO_2 NP were compared with the rejection curves simulated based on the pore size distributions combined with the pore–flow model. The comparative analysis suggested that the continuous method with the log-normal probability density function (PDF) yielded a good prediction of the OsO_2 NP rejection, whereas a high discrepancy was observed between the simulations and the PS experimental rejection. This finding has implied that the pore–flow model is more applicable to spherical and rigid particles, than semi-rigid or compliant molecules of which size can be altered in confined transport channels. The most probable reason for that is an arbitrary estimation of the solute size. The combination of the equations (Wilke–Chang and Stokes–Einstein) used for estimation of the solute size may bring an error to the calculations, since these correlations were originally derived for other applications than estimation of the solute diameter of a small molecule in a confined pore. Unfortunately, there are no other alternative methods for estimation of the solute size in the system required. The estimated porosity values using the pore–flow model combined with the experimentally measured pore size distributions and fluxes implied that the pore viscosity correction formula results in unrealistic porosity values. The outcome of this computation is a concern that the applied viscosity may not be relevant to OSN systems, since the solvent molecular diameter is comparable to the pore size in NF membranes.

There are two main issues associated with the nanoprobe imaging technique. A description of these concerns is important in order to indicate the future research directions to progress further developments. TEM imaging suffers from the particle overlapping effect, since a 3–D specimen is projected onto a 2–D electro-micrograph. This effect can be neglected in extremely thin samples, such as deposition of a single layer of NP or ultramicrotoming specimens with a low number of NP to very thin sections. This effect is however notable in specimens into which many particles are lodged. The best method to eliminate this pitfall is imaging the membrane specimens using 3–D tomography. This microscopy produces 3–D images by tilting the specimen at tiny angles, thus, many 2–D projections are combined *via* an image processing software to form a 3–D image.

Currently, low molecular weight (MW) PS are required to stabilise OsO_2 NP. However, the presence of PS stabilisers gives uncertainty in pore size measurements. Therefore, further work on development of the nanoprobes and understanding the stabilisation mechanisms are recommended. Firstly, one of the useful approaches would be the Zeta potential measurement of OsO_2 NP in various solvents. The tendency for the NP to agglomerate in various liquids can be studied using dynamic light scattering, which is a much faster technique than the TEM imaging. Next, the research should be directed into exploring other groups of stabilisers utilised in a broader spectrum of solvents including e.g. water, so NF membranes fabricated from various polymers can be characterised and their structure compared. For instance, it would be interesting to compare the structure of glassy polymers to rubbery polymers. It is likely, that with use of this technique the transport pattern across these two classes of membranes can be elucidated. To further analyse the transport behaviour across NF membranes prepared from various polymers, the size and concentration of permeated particles could be compared to size of the particles lodged into membranes.

An alternative approach to measuring the pore size, in an indirect manner, would be filling uncrosslinked P84 co-polyimide membranes with OsO_2 NP followed by dissolving these membranes in dimethylformamide (DMF) and sizing the extracted NP. Herein, a problem associated with particle agglomeration would remain, and further work would be required to re-stabilise the OsO_2 NP once they are suspended in DMF.

Given high toxicity of osmium tetroxide (OsO_4) compounds required to prepare OsO_2 NP, a further research on new nanoprobes such as e.g. quantum dots, would be highly recommended. This matter emits a particle size-dependent wavelength while irradiated with an UV light as well as it provides a good contrast for TEM imaging.

Finally, modelling the membrane structure using the advanced molecular dynamics models could bridge the pore size distribution determined using the nanoprobe imaging technique with the chemical structure of individual polymer chains. This is a very challenging research area, so a progress to "solve" the membrane structure would be very acknowledged. There is a prospect that the pore size measured using the nanoprobe imaging technique could provide a good reference for the simulations.

The work described in this thesis also assessed the application of AFM to NF membrane characterisation. During the research three hypothesis were tested: (*i*) The nodule size is correlative with the membrane functional performance; (*ii*) The pore size in NF membranes can be accurately measured using a cantilever equipped with a carbon nanotube (CNT) tip; (*iii*) Careful analysis of the phase images provides information on macromolecular packing on the membrane surface. The test of the first hypothesis showed that the nodule size, measured for a range of the P84 co-polyimide ISA membranes, correlated well with the flux and the molecular weight cut-off (MWCO), in a manner, that the higher the nodule size, the higher the flux and MWCO were observed. Furthermore, the nodule size was found to be correlative directly with

the polymer entanglement resulted by kinetics of the liquid–liquid demixing process present in the phase inversion. An increase of a co-solvent content resulted in a smaller nodule size, as the polymer chains tend to reduce their surface area and entangle more tightly while in contact with a poor solvent.

The possibility to measure the pore size using AFM has always attracted a lot of interests. Nonetheless, a significant improvement of the lateral resolution of the microscopy was achieved by introducing a CNT tip, that is a probe with a high aspect ratio and it is known to be the thinnest available tip to use in AFM, it was expected that the pore size could be measured with high accuracy. The experiments and comprehensive analysis have shown that the measurements of the pore size (~1 nm or smaller) in NF membranes using a conventional method, *i.e.* sizing depressions on the 2–D surface profile line, remains difficult. There is a risk that the analysed depressions from the surface contour may misrepresent transport–active pores. A direct reason for this uncertainty is insufficient lateral resolution, even though a CNT probe is utilised. An advanced approach to improve pore size measurements in NF membranes was proposed by Cheng *et al.* [244]. The authors studied a phase profile simultaneously with a topographical profile to confirm the presence of a pore. This is indeed a rational method worth to explore, however, one has to perform complex imaging steps. First, a force displacement curve should be generated to confirm in which region the cantilever is oscillating, attractive or repulsive. In the repulsive region one should consider that the phase angle is dependent on topography, therefore, its magnitude may not provide information on material phase. Secondly, a corresponding phase shift to a depression, visible on a topographical profile, has to be exactly zero to consider that there is no interaction between the tip and the surface, hence an indication for a pore opening. The force displacement curves (force vs. displacement and phase shift vs. displacement) should be performed at two regions: exactly at the pore opening and the non-porous region, in order to be able understand the signals (phase and deflection) sensed by a cantilever during scanning.

Phase imaging, as an extension to the tapping mode, offers very interesting information describing the internal polymer packing at the membrane surface. The maps of the phase angle and the dissipation energy distributions computed for each membrane have shown that the phase imaging, if performed with special attention to settings of the scanning parameters, provides information about the polymer chain entanglement, which cannot be actually determined from the topographical images. The magnitudes of the phase lag and the dissipation energy have demonstrated to be correlative with the flux and MWCO. The phase lag value indicates relative polymer chain entanglement and packing degrees. Dense membranes prepared from dope solutions comprising higher content of co-solvent (1,4 dioxane in case of the studied P84 co-polyimide membranes) show lower phase lag in comparison to membranes prepared from dopes with less 1,4 dioxane, implying that the pore size is related to lower polymer compliance. Since the polymer compliance, *i.e.* viscoelasticity, is related by some manner to the chain packing and entanglement, it is also related to the size of interstitial spaces or pores. Given the AFM findings and the macromolecular structure elucidated by the nanoprobe imaging, one can conclude that the pores in P84 co-polyimide membranes are formed between bundles of polymer chains or between the chains themselves, and kinetics and thermodynamics of the phase inversion process is related to the degree of polymer packing.

In the future research, AFM operating in the phase imaging could be used for analysis of a broader spectrum of the OSN polymeric membranes. Studying the surface of NF membranes fabricated from block co-polymers or blends in a quantitative manner would be particularly interesting to map the macrophases. For instance, one of the worth exploring research directions would be to prepare a membrane from hydrophilic–hydrophobic blends and characterise the surface in the phase imaging by mapping the separated macro-domains. In addition, cross-sectional images of this membrane after filling it with the high contrast nanoprobes dispersed in

either a hydrophilic or hydrophobic solvent would indicate across which domain the transport is inclined to exist in relation to a solvent type.

References

[1] T.A. Kurniawan, G.Y.S. Chan, W.-H. Lo, S. Babel, Physico-chemical treatment techniques for wastewater laden with heavy metals, Chem. Eng. J., 118 (2006) 83-98.

[2] M.A. Shannon, P.W. Bohn, M. Elimelech, J.G. Georgiadis, B.J. Marinas, A.M. Mayes, Science and technology for water purification in the coming decades, Nature, 452 (2008) 301-310.

[3] C. Fritzmann, J. Löwenberg, T. Wintgens, T. Melin, State-of-the-art of reverse osmosis desalination, Desalination, 216 (2007) 1-76.

[4] G. Daufin, J.P. Escudier, H. Carrère, S. Bérot, L. Fillaudeau, M. Decloux, Recent and emerging applications of membrane processes in the food and dairy industry, Food Bioprod. Process., 79 (2001) 89-102.

[5] I.P. Yampolskii, I. Pinnau, B.D. Freeman, Materials Science of Membranes for Gas and Vapor Separation, John Wiley and Sons, 2006.

[6] S. So, L.G. Peeva, E.W. Tate, R.J. Leatherbarrow, A.G. Livingston, Membrane enhanced peptide synthesis, Chem. Commun., 46 (2010) 2808-2810.

[7] E. Rundquist, C. Pink, E. Vilminot, A. Livingston, Facilitating the use of counter-current chromatography in pharmaceutical purification through use of organic solvent nanofiltration, J. Chromatogr., A 1229 (2012) 156-163.

[8] M. Takht Ravanchi, T. Kaghazchi, A. Kargari, Application of membrane separation processes in petrochemical industry: a review, Desalination, 235 (2009) 199-244.

[9] I. Sereewatthanawut, A.T. Boam, A.G. Livingston, Polymeric membrane nanofiltration and its application to separations in the chemical industries, Macromol. Symp., 264 (2008) 184-188.

[10] R.W. Baker, Membrane Technology and Applications, second ed., 2004.

[11] M. Mulder, Basic principles of membrane technology, second ed., Kluwer Academic Publishers, 1991.

[12] P.M. Budd, A. Butler, J. Selbie, K. Mahmood, N.B. McKeown, B. Ghanem, K. Msayib, D. Book, A. Walton, The potential of organic polymer-based hydrogen storage materials, Phys. Chem. Chem. Phys., 9 (2007) 1802-1808.

[13] C.R. Martin, Nanomaterials: A membrane-based synthetic approach, Science, 266 (1994) 1961-1966.

[14] C.J. Pink, H.-t. Wong, F.C. Ferreira, A.G. Livingston, Organic solvent nanofiltration and adsorbents; A hybrid approach to achieve ultra low palladium contamination of post coupling reaction products, Org. Process Res. Dev., 12 (2008) 589-595.

[15] N.B. McKeown, P.M. Budd, Polymers of intrinsic microporosity (PIMs): organic materials for membrane separations, heterogeneous catalysis and hydrogen storage, Chem. Soc. Rev., 35 (2006) 675-683.

[16] M. Ulbricht, Advanced functional polymer membranes, Polymer, 47 (2006) 2217-2262.

[17] T.C. Merkel, B.D. Freeman, R.J. Spontak, Z. He, I. Pinnau, P. Meakin, A.J. Hill, Ultrapermeable, reverse-selective nanocomposite membranes, Science, 296 (2002) 519-522.

[18] L.G. Peeva, M. Sairam, A.G. Livingston, Nanofiltration operations in nonaqueous systems, in: D. Enrico and G. Lidietta (Eds.), Comprehensive membrane science and engineering, Elsevier, Oxford, 2010, pp. 91-113.

[19] P. Vandezande, L. Gevers, I. Vankelecom, Solvent resistant nanofiltration: separating on a molecular level, Chem. Soc. Rev., 37 (2008) 365-405.

[20] L.S. White, Development of large-scale applications in organic solvent nanofiltration and pervaporation for chemical and refining processes, J. Membr. Sci., 286 (2006) 26-35.

[21] A. Boam, A. Nozari, Fine chemical: OSN—a lower energy alternative, Filt. Sep., 43 (2006) 46-48.

[22] A.G. Livingston, L.G. Peeva, P. Silva, Organic solvent nanofiltration, in: S.P. Nunes and K.-V. Peinemann (Eds.), Membrane Technology in the Chemical Industry, Wiley-VCH Verlag GmbH&Co. KgaA, Weinheim, Germany, 2006, pp. 203-228.

[23] I.M. Wienk, R.M. Boom, M.A.M. Beerlage, A.M.W. Bulte, C.A. Smolders, H. Strathmann, Recent advances in the formation of phase inversion membranes made from amorphous or semi-crystalline polymers, J. Membr. Sci., 113 (1996) 361-371.
[24] K.-V. Peinemann, V. Abetz, P.F.W. Simon, Asymmetric superstructure formed in a block copolymer via phase separation, Nat. Mater., 6 (2007) 992-996.
[25] S. Loeb, S. Sourirajan, Sea water demineralization by means of an osmotic membrane, Advances in Chemistry Series, 38 (1963) 117-132.
[26] I. Soroko, M. Sairam, A.G. Livingston, The effect of membrane formation parameters on performance of polyimide membranes for organic solvent nanofiltration (OSN). Part C. Effect of polyimide characteristics, J. Membr. Sci., 381 (2011) 172-182.
[27] Y.H. See Toh, F.W. Lim, A.G. Livingston, Polymeric membranes for nanofiltration in polar aprotic solvents, J. Membr. Sci., 301 (2007) 3-10.
[28] A.G. Livingston, Y.H. See-Toh, Method of separation, Imperial Innovations, Great Britain Pat. 2437519 (2007).
[29] Y.H. See-Toh, M. Silva, A. Livingston, Controlling molecular weight cut-off curves for highly solvent stable organic solvent nanofiltration (OSN) membranes, J. Membr. Sci., 324 (2008) 220-232.
[30] I. Soroko, M. Makowski, F. Spill, A. Livingston, The effect of membrane formation parameters on performance of polyimide membranes for organic solvent nanofiltration (OSN). Part B: Analysis of evaporation step and the role of a co-solvent, J. Membr. Sci., 381 (2011) 163-171.
[31] I. Soroko, M.P. Lopes, A. Livingston, The effect of membrane formation parameters on performance of polyimide membranes for organic solvent nanofiltration (OSN): Part A. Effect of polymer/solvent/non-solvent system choice, J. Membr. Sci., 381 (2011) 152-162.
[32] T.H. Young, L.W. Chen, A diffusion-controlled model for wet-casting membrane formation, J. Membr. Sci., 59 (1991) 169-181.
[33] L.H. Sperling, Introduction to Physical Polymer Science, fourth ed., Wiley Interscience, 2006.
[34] I.-C. Kim, H.-G. Yoon, K.-H. Lee, Formation of integrally skinned asymmetric polyetherimide nanofiltration membranes by phase inversion process, J. Appl. Polym. Sci., 84 (2002) 1300-1307.
[35] I. Soroko, A. Livingston, Impact of TiO2 nanoparticles on morphology and performance of crosslinked polyimide organic solvent nanofiltration (OSN) membranes, J. Membr. Sci., 343 (2009) 189-198.
[36] J.E. Cadotte, Evolution of composite reverse osmosis membranes, in: (Eds.), Materials Science of Synthetic Membranes, American Chemical Society, 1985, pp. 273-294.
[37] J. Cadotte, Interfacially synthesized reverse osmosis membranes, FilmTec Corporation, US Pat 4277344 (1981).
[38] D. Mukherjee, A. Kulkarni, W.N. Gill, Flux enhancement of reverse osmosis membranes by chemical surface modification, J. Membr. Sci., 97 (1994) 231-249.
[39] L. Sun, G.L. Baker, M.L. Bruening, Polymer brush membranes for pervaporation of organic solvents from water, Macromolecules, 38 (2005) 2307-2314.
[40] S.-Y. Kwak, S.G. Jung, S.H. Kim, Structure-motion-performance relationship of flux-enhanced reverse osmosis (RO) membranes composed of aromatic polyamide thin films, Environ. Sci. Technol., 35 (2001) 4334-4340.
[41] F.P. Cuperus, D. Bargeman, K. Smolders, A new method to determine the skin thickness of asymmetric UF-membranes using colloidal gold particles, J. Colloid Interface Sci., 135 (1990) 486-495.
[42] R.E. Larson, J.E. Cadotte, R.J. Petersen, The FT-30 seawater reverse osmosis membrane-element test results, Desalination, 38 (1981) 473.
[43] L.T. Rozelle, J.E. Cadotte, K.E. Cobian, C.V. Kopp Jr, Nonpolysaccharide membranes for reverse osmosis: NS-100 membranes, in: S. Sourirajan (Eds.), Reverse Osmosis and Synthetic Membranes, National Research Council Canada, Ottawa, Canada, 1977, pp. 249–262.
[44] M.F. Jimenez Solomon, Y. Bhole, A.G. Livingston, High flux membranes for organic solvent nanofiltration (OSN) - interfacial polymerization with solvent activation, J. Membr. Sci., 423–424 (2012) 371-382.

[45] H. Siddique, L. Peeva, K. Stoikos, G. Pasparakis, M. Vamvakaki, A.G. Livingston, Membranes for organic solvent nanofiltration based on pre-assembled nanoparticles, Ind. Eng. Chem. Res., In Press (2012).
[46] W.J. Koros, I. Pinnau, Membrane formation for gas separation processes, in: D.R. Paul and Y.P. Yampolskii (Eds.), Polymeric Gas Separation Membranes, CRC Press, Boca Raton, FL, 1994, pp. 209-272.
[47] L.E.M. Gevers, S. Aldea, I.F.J. Vankelecom, P.A. Jacobs, Optimisation of a lab-scale method for preparation of composite membranes with a filled dense top-layer, J. Membr. Sci., 281 (2006) 741-746.
[48] X. Li, C.-A. Fustin, N. Lefevre, J.-F. Gohy, S.D. Feyter, J.D. Baerdemaeker, W. Egger, I.F.J. Vankelecom, Ordered nanoporous membranes based on diblock copolymers with high chemical stability and tunable separation properties, J. Mater. Chem., 20 (2010) 4333-4339.
[49] L.E.M. Gevers, I.F.J. Vankelecom, P.A. Jacobs, Solvent-resistant nanofiltration with filled polydimethylsiloxane (PDMS) membranes, J. Membr. Sci., 278 (2006) 199-204.
[50] A.V. Volkov, V.V. Parashchuk, D.F. Stamatialis, V.S. Khotimsky, V.V. Volkov, M. Wessling, High permeable PTMSP/PAN composite membranes for solvent nanofiltration, J. Membr. Sci., 333 (2009) 88-93.
[51] I.F.J. Vankelecom, K. De Smet, L.E.M. Gevers, A. Livingston, D. Nair, S. Aerts, S. Kuypers, P.A. Jacobs, Physico-chemical interpretation of the SRNF transport mechanism for solvents through dense silicone membranes, J. Membr. Sci., 231 (2004) 99-108.
[52] E. Favre, P. Schaetzel, Q.T. Nguygen, R. Clément, J. Néel, Sorption, diffusion and vapor permeation of various penetrants through dense poly(dimethylsiloxane) membranes: a transport analysis, J. Membr. Sci., 92 (1994) 169-184.
[53] E.S. Tarleton, J.P. Robinson, M. Salman, Solvent-induced swelling of membranes - measurements and influence in nanofiltration, J. Membr. Sci., 280 (2006) 442-451.
[54] S.H. Maruf, D.U. Ahn, A.R. Greenberg, Y. Ding, Glass transition behaviors of interfacially polymerized polyamide barrier layers on thin film composite membranes via nano-thermal analysis, Polymer, 52 (2011) 2643-2649.
[55] N.A. Plate, A.K. Bokarev, N.E. Kaliuzhnyi, E.G. Litvinova, V.S. Khotimskii, V.V. Volkov, Y.P. Yampolskii, Gas and vapor permeation and sorption in poly (trimetylsilylpropyne), J. Membr. Sci., 60 (1991) 13-24.
[56] X.-Y. Wang, A.J. Hill, B.D. Freeman, I.C. Sanchez, Structural, sorption and transport characteristics of an ultrapermeable polymer, J. Membr. Sci., 314 (2008) 15-23.
[57] K. Nagai, T. Masuda, T. Nakagawa, B.D. Freeman, I. Pinnau, Poly[1-(trimethylsilyl)-1-propyne] and related polymers: synthesis, properties and functions, Prog. Polym. Sci., 26 (2001) 721-798.
[58] S. Claes, P. Vandezande, S. Mullens, P. Adriaensens, R. Peeters, F.H.J. Maurer, M.K. Van Bael, Crosslinked poly[1-(trimethylsilyl)-1-propyne] membranes: Characterization and pervaporation of aqueous tetrahydrofuran mixtures, J. Membr. Sci., 389 (2012) 459-469.
[59] T. Masuda, M. Takatsuka, B.-Z. Tang, T. Higashimura, Pervaporation of organic liquid-water mixtures through substituted polyacetylene membranes, J. Membr. Sci., 49 (1990) 69-83.
[60] K. Ishihara, Y. Nagase, K. Matsui, Pervaporation of alcohol/water mixtures through poly[1-(trimethylsilyl)-1-propyne] membrane, Makromol. Chem., Rapid Commun., 7 (1986) 43-46.
[61] L.M. Robeson, W.F. Burgoyne, M. Langsam, A.C. Savoca, C.F. Tien, High performance polymers for membrane separation, Polymer, 35 (1994) 4970-4978.
[62] Y.H. See-Toh, F.C. Ferreira, A.G. Livingston, The influence of membrane formation parameters on the functional performance of organic solvent nanofiltration membranes, J. Membr. Sci., 299 (2007) 236-250.
[63] A. Cano-Odena, P. Vandezande, K. Hendrix, R. Zaman, K. Mostafa, W. Egger, P. Sperr, J. De Baerdemaeker, I.F.J. Vankelecom, Probing the molecular level of polyimide-based solvent resistant nanofiltration membranes with positron annihilation spectroscopy, J. Phys. Chem. B, 113 (2009) 10170-10176.
[64] D.A. Patterson, A. Havill, S. Costello, Y.H. See-Toh, A.G. Livingston, A. Turner, Membrane characterisation by SEM, TEM and ESEM: The implications of dry and wetted microstructure on

mass transfer through integrally skinned polyimide nanofiltration membranes, Sep. Purif. Technol., 66 (2009) 90-97.
[65] A.K. Ghosh, E.M.V. Hoek, Impacts of support membrane structure and chemistry on polyamide - polysulfone interfacial composite membranes, J. Membr. Sci., 336 (2009) 140-148.
[66] V. Freger, S. Srebnik, Mathematical model of charge and density distributions in interfacial polymerization of thin films, J. Appl. Polym. Sci., 88 (2003) 1162-1169.
[67] V. Freger, Nanoscale heterogeneity of polyamide membranes formed by interfacial polymerization, Langmuir, 19 (2003) 4791-4797.
[68] F.A. Pacheco, I. Pinnau, M. Reinhard, J.O. Leckie, Characterization of isolated polyamide thin films of RO and NF membranes using novel TEM techniques, J. Membr. Sci., 358 (2010) 51-59.
[69] K.C. Khulbe, C.Y. Feng, T. Matsuura, Synthetic Polymeric Membranes Characterization by Atomic Force Microscopy, Springer, 2008.
[70] R.D. Schultz, S.K. Asunmaa, Ordered water and the ultrastructure of the cellular plasma membrane, Recent Progr. Surf. Sci., 3 (1970) 291 - 332.
[71] M. Panar, H.H. Hoehn, R.R. Hebert, The nature of asymmetry in reverse osmosis membranes, Macromolecules, 6 (1973) 777-780.
[72] I.M. Wienk, T. van den Boomgaard, C.A. Smolders, The formation of nodular structures in the top layer of ultrafiltration membranes, J. Appl. Polym. Sci., 53 (1994) 1011-1023.
[73] T.D. Nguyen, K. Chan, T. Matsuura, S. Sourirajan, Effect of shrinkage on pore size and pore size distribution of different cellulosic reverse osmosis membranes, Ind. Eng. Chem. Prod. Res. Dev., 23 (1984) 501-508.
[74] R.R. Sharma, R. Agrawal, S. Chellam, Temperature effects on sieving characteristics of thin-film composite nanofiltration membranes: pore size distributions and transport parameters., J. Membr. Sci., 223 (2003) 69-87.
[75] V.K. Sharma, P.S. Singh, S. Gautam, P. Maheshwari, D. Dutta, R. Mukhopadhyay, Dynamics of water sorbed in reverse osmosis polyamide membrane, J. Membr. Sci., (2009) 667-671.
[76] V.K. Sharma, P.S. Singh, S. Gautam, S. Mitra, M. R., Diffusion of water in nanoporous NF polyamide membrane, Chem. Phys. Lett., 478 (2009).
[77] V.P. Shantarovich, Y.P. Yampolskii, A.Y. Alentiev, Positron annihilation lifetime study of high and low free volume glassy polymers: Effects of free volume sizes on the permeability and permselectivity, Macromolecules, 33 (2000) 7453-7466.
[78] C.A. Smolders, A.J. Reuvers, R.M. Boom, I.M. Wienk, Microstructures in phase-inversion membranes. Part 1. Formation of macrovoids, J. Membr. Sci., 73 (1992) 259-275.
[79] M.A. Frommer, R.M. Messalem, Mechanism of Membrane Formation. VI. Convective Flows and Large Void Formation during Membrane Precipitation, Product R&D, 12 (2002) 328-333.
[80] R.M. Boom, I.M. Wienk, T. van den Boomgaard, C.A. Smolders, Microstructures in phase inversion membranes. Part 2. The role of a polymeric additive, J. Membr. Sci., 73 (1992) 277-292.
[81] L.S. White, Transport properties of a polyimide solvent resistant nanofiltration membrane, J. Membr. Sci., 205 (2002) 191-202.
[82] T. Tsuru, T. Sudoh, T. Yoshioka, M. Asaeda, Nanofiltration in non-aqueous solutions by porous silica–zirconia membranes, J. Membr. Sci., 185 (2001) 253-261.
[83] Y.H. See Toh, X.X. Loh, K. Li, A. Bismarck, A.G. Livingston, In search of a standard method for the characterisation of organic solvent nanofiltration membranes, J. Membr. Sci., 291 (2007) 120-125.
[84] J.G. Wijmans, R.W. Baker, The solution-diffusion model: a review, J. Membr. Sci., 107 (1995) 1-21.
[85] P. Silva, A.G. Livingston, Effect of solute concentration and mass transfer limitations on transport in organic solvent nanofiltration – partially rejected solute, J. Membr. Sci., 280 (2006) 889-898.
[86] J.D. Ferry, Ultrafilter membranes and ultrafiltration, Chem. Rev., 18 (1936) 373-455.
[87] X.-L. Wang, T. Tsuru, S.-i. Nakao, S. Kimura, The electrostatic and steric-hindrance model for the transport of charged solutes through nanofiltration membranes, J. Membr. Sci., 135 (1997) 19-32.

[88] L. Zeman, M. Wales, Steric rejection of polymeric solutes by membranes with uniform pore size distribution, Sep. Sci. Technol., 16 (1981) 275–290.
[89] S. Mochizuki, A.L. Zydney, Theoretical analysis of pore size distribution effects on membrane transport, J. Membr. Sci., 82 (1993) 211-227.
[90] A.L. Zydney, P. Aimar, M. Meireles, J.M. Pimbley, G. Belfort, Use of the log-normal probability density function to analyze membrane pore size distributions: functional forms and discrepancies, J. Membr. Sci., 91 (1994) 293-298.
[91] G. Belfort, P. Mikulasek, J.M. Pimbley, K.Y. Chung, Diagnosis of membrane fouling using a rotating annular filter. 2. Dilute particle suspensions of known particle size, J. Membr. Sci., 77 (1993) 23-39.
[92] B. Van der Bruggen, J. Schaep, D. Wilms, C. Vandecasteele, A comparison of models to describe the maximal retention of organic molecules in nanofiltration, Sep. Sci. Technol., 35 (2000) 169.
[93] W.R. Bowen, J.S. Welfoot, Modelling of membrane nanofiltration-pore size distribution effects, Chem. Eng. Sci., 57 (2002) 1393-1407.
[94] W.R. Bowen, J.S. Welfoot, Modelling the performance of membrane nanofiltration - critical assessment and model development, Chem. Eng. Sci., 57 (2002) 1121-1137.
[95] W.R. Bowen, J.S. Welfoot, Predictive modelling of nanofiltration: membrane specification and process optimisation, Desalination, 147 (2002) 197-203.
[96] W.R. Bowen, A.W. Mohammad, Characterization and prediction of nanofiltration membrane performance - a general assessment, Chem. Eng. Res. Des., 76 (1998) 885-893.
[97] W.R. Bowen, A.W. Mohammad, N. Hilal, Characterisation of nanofiltration membranes for predictive purposes - use of salts, uncharged solutes and atomic force microscopy, J. Membr. Sci., 126 (1997) 91-105.
[98] R.B. Bird, W.E. Stewart, E.N. Lightfoot, Transport Phenomena, 2nd ed., John Wiley & Sons, Inc., 2002.
[99] A. Einstein, Investigations on the theory of the Brownian movement, Dover, New York, 1956.
[100] C.R. Wilke, P. Chang, Correlation of diffusion coefficients in dilute solutions, AIChE J., 1 (1955) 264-270.
[101] K.A. Reddy, L.K. Doraiswamy, Estimating liquid diffusivity, Ind. Eng. Chem. Fundam., 6 (1967) 77-79.
[102] R.C. Reid, T.K. Sherwood, The Properties of Gases and Liquids, 2nd ed., McGraw-Hill, 1966.
[103] W. Hayduk, W.D. Buckley, Effect of molecular size and shape on diffusivity in dilute liquid solutions, Chem. Eng. Sci., 27 (1972) 1997-2003.
[104] J. Li, P.W. Carr, Accuracy of empirical correlations for estimating diffusion coefficients in aqueous organic mixtures, Anal. Chem., 69 (1997) 2530-2536.
[105] J. Geens, K. Peeters, B. Van der Bruggen, C. Vandecasteele, Polymeric nanofiltration of binary water - alcohol mixtures: Influence of feed composition and membrane properties on permeability and rejection, J. Membr. Sci., 255 (2005) 255-264.
[106] T. Matsuura, Synthetic Membranes and Membrane Separation Processes, CRC Press, Tokyo, 1993.
[107] P.M. Budd, N.B. McKeown, D. Fritsch, Free volume and intrinsic microporosity in polymers, J. Mater. Chem., 15 (2005) 1977-1986.
[108] J.P. Robinson, E.S. Tarleton, C.R. Millington, A. Nijmeijer, Solvent flux through dense polymeric nanofiltration membranes, J. Membr. Sci., 230 (2004) 29-37.
[109] R.W. Bowen, T.A. Doneva, Atomic force microscopy studies of nanofiltration membranes: surface morphology, pore size distribution and adhesion, Desalination, 129 (2000) 163-172.
[110] J.A. Otero, O. Mazarrasa, J. Villasante, V. Silva, P. Prádanos, J.I. Calvo, A. Hernández, Three independent ways to obtain information on pore size distributions of nanofiltration membranes, J. Membr. Sci., 309 (2008) 17-27.
[111] N. Hilal, H. Al-Zoubi, N.A. Darwish, A.W. Mohammad, Characterisation of nanofiltration membranes using atomic force microscopy, Desalination, 177 (2005) 187-199.
[112] K.-L. Tung, Y.-C. Jean, D. Nanda, K.-R. Lee, W.-S. Hung, C.-H. Lo, J.-Y. Lai, Characterization of multilayer nanofiltration membranes using positron annihilation spectroscopy, J. Membr. Sci., 343 (2009) 147-156.

[113] J. De Baerdemaeker, K. Boussu, N. Djourelov, B. Van der Bruggen, C. Dauwe, M. Weber, K.G. Lynn, Investigation of nanopores in nanofiltration membranes using slow positron beam techniques, Phys. Status Solidi C, 4 (2007) 3804-3809.
[114] H. Chen, W.-S. Hung, C.-H. Lo, S.-H. Huang, M.-L. Cheng, G. Liu, K.-R. Lee, J.-Y. Lai, Y.-M. Sun, C.-C. Hu, R. Suzuki, T. Ohdaira, N. Oshima, Y.C. Jean, Free-volume depth profile of polymeric membranes studied by positron annihilation spectroscopy: Layer structure from interfacial polymerization, Macromolecules, 40 (2007) 7542-7557.
[115] V. Freger, J. Gilron, S. Belfer, TFC polyamide membranes modified by grafting of hydrophilic polymers: an FT-IR/AFM/TEM study, J. Membr. Sci., 209 (2002) 283-292.
[116] A. Akthakul, R.F. Salinaro, A.M. Mayes, Antifouling polymer membranes with subnanometer size selectivity, Macromolecules, 37 (2004) 7663-7668.
[117] D.J. Johnson, S.A. Al Malek, B.A.M. Al-Rashdi, N. Hilal, Atomic force microscopy of nanofiltration membranes: Effect of imaging mode and environment, J. Membr. Sci., 389 (2012) 486-498.
[118] P. Prádanos, M.L. Rodriguez, J.I. Calvo, A. Hernández, F. Tejerina, J.A. de Saja, Structural characterization of an UF membrane by gas adsorption-desorption and AFM measurements, J. Membr. Sci., 117 (1996) 291-302.
[119] J.I. Calvo, P. Prádanos, A. Hernández, W.R. Bowen, N. Hilal, R.W. Lovitt, P.M. Williams, Bulk and surface characterization of composite UF membranes Atomic force microscopy, gas adsorption-desorption and liquid displacement techniques, J. Membr. Sci., 128 (1997) 7-21.
[120] M.J. Han, D. Bhattacharyya, Characterization of reverse osmosis cellulose acetate membranes by gas adsorption method: effect of casting variables and chlorine damage, J. Membr. Sci., 62 (1991) 325-346.
[121] S.A. Stern, Y. Mi, H. Yamamoto, K.S.C. Anne, Structure/permeability relationships of polyimide membranes. Applications to the separation of gas mixtures, Journal of Polymer Science Part B: Polymer Physics, 27 (1989) 1887-1909.
[122] Y.-H. Kim, H.-S. Kim, S.-K. Kwon, Synthesis and Characterization of Highly Soluble and Oxygen Permeable New Polyimides Based on Twisted Biphenyl Dianhydride and Spirobifluorene Diamine, Macromolecules, 38 (2005) 7950-7956.
[123] K. Li, Characterization of ceramic membranes, in: (Eds.), Ceramic Membranes for Separation and Reaction, John Wiley & Sons, Ltd, 2007, pp. 59-95.
[124] H. Reingruber, A. Zankel, C. Mayrhofer, P. Poelt, A new in situ method for the characterization of membranes in a wet state in the environmental scanning electron microscope, J. Membr. Sci., 399-400 (2012) 86-94.
[125] K.J. Kim, A.G. Fane, R. Ben Aim, M.G. Liu, G. Jonsson, I.C. Tessaro, A.P. Broek, D. Bargeman, A comparative study of techniques used for porous membrane characterization: pore characterization, J. Membr. Sci., 87 (1994) 35-46.
[126] G. Binnig, C.F. Quate, C. Gerber, Atomic force microscope, Phys. Rev. Lett., 56 (1986) 930-933.
[127] Y. Martin, C.C. Williams, H.K. Wickramasinghe, Atomic force microscope–force mapping and profiling on a sub 100-Å scale, J. Appl. Phys., 61 (1987) 4723-4730.
[128] W.R. Bowen, R.W. Lovitt, N. Hilal, P.M. Williams, Atomic force microscope studies of synthetic membranes, in: W.R. Bowen, R.W. Field, and J.A. Howell (Eds.), Proc. Euromembrane 95, ESMST, Bath, UK, 1995, pp. 136-139.
[129] R. Bowen, N. Hilal, R.W. Lovitt, P.M. Williams, Visualisation of an ultrafiltration membrane by non-contact atomic force microscopy at single pore resolution, J. Membr. Sci., 110 (1996) 229-232.
[130] K. Boussu, B. Van der Bruggen, A. Volodin, J. Snauwaert, C. Van Haesendonck, C. Vandecasteele, Roughness and hydrophobicity studies of nanofiltration membranes using different modes of AFM, J. Colloid Interface Sci., 286 (2005) 632-638.
[131] N. Hilal, A.W. Mohammad, B. Atkin, N.A. Darwish, Using atomic force microscopy towards improvement in nanofiltration membranes properties for desalination pre-treatment: a review, Desalination, 157 (2003) 137-144.

[132] M. Khayet, K.C. Khulbe, T. Matsuura, Characterization of membranes for membrane distillation by atomic force microscopy and estimation of their water vapor transfer coefficients in vacuum membrane distillation process, J. Membr. Sci., 238 (2004) 199-211.
[133] M. Khayet, C.Y. Feng, T. Matsuura, Morphological study of fluorinated asymmetric polyetherimide ultrafiltration membranes by surface modifying macromolecules, J. Membr. Sci., 213 (2003) 159-180.
[134] Y. Kim, D. Rana, T. Matsuura, W.-J. Chung, K.C. Khulbe, Relationship between surface structure and separation performance of poly(ether sulfone) ultra-filtration membranes blended with surface modifying macromolecules, Sep. Purif. Technol., 72 (2010) 123-132.
[135] A.K. Fritzsche, A.R. Arevalo, A.F. Connolly, M.D. Moore, V.C. Elings, M. Wu, The structure and morphology of the skin of polyethersulfone ultrafiltration membranes: A comparative atomic force microscope and scanning electron microscope study, J. Appl. Polym. Sci., 45 (1992) 1945-1956.
[136] D.F. Stamatialis, C.R. Dias, M. Norberta de Pinho, Atomic force microscopy of dense and asymmetric cellulose-based membranes, J. Membr. Sci., 160 (1999) 235-242.
[137] K. Boussu, A. Belpaire, A. Volodin, C. Van Haesendonck, P. Van der Meeren, C. Vandecasteele, B. Van der Bruggen, Influence of membrane and colloid characteristics on fouling of nanofiltration membranes, J. Membr. Sci., 289 (2007) 220-230.
[138] F.J. Giessibl, Advances in atomic force microscopy, Rev. Mod. Phys., 75 (2003) 949-983.
[139] P. Eaton, P. West, Atomic Force Microscopy, Oxford University Press, New York, 2010.
[140] R. Garcia, R. Magerle, R. Perez, Nanoscale compositional mapping with gentle forces, Nat. Mater., 6 (2007) 405-411.
[141] R. Garcia, C.J. Gómez, N.F. Martinez, S. Patil, C. Dietz, R. Magerle, Identification of nanoscale dissipation processes by dynamic atomic force microscopy, Phys. Rev. Lett., 97 (2006) 016103.
[142] S.S. Wong, A.T. Woolley, T. Wang Odom, J.-L. Huang, P. Kim, D.V. Vezenov, C.M. Lieber, Single-walled carbon nanotube probes for high-resolution nanostructure imaging, Appl. Phys. Lett., 73 (1998) 3465-3468.
[143] O. Krause, V. Bouchiat, A.M. Bonnot, A quantitative comparison of resolution, scanning speed and lifetime behavior of CVD grown single wall carbon nanotubes and silicon SPM probes using spectral methods, J. Phys.: Conf. Ser., 61 (2007) 628-632.
[144] C.V. Nguyen, Q. Ye, M. Meyyappan, Carbon nanotube tips for scanning probe microscopy: fabrication and high aspect ratio nanometrology, Meas. Sci. Technol., 16 (2005) 2138-2146.
[145] Bruker. Scanning probe/atomic force microscopy: technology overview and update. 2010 27/05/11]; Available from: bruker-axs.co.
[146] R. Garcia, Amplitude Modulation Atomic Force Microscopy, Wiley-VCH, Weinheim, 2010.
[147] J.H. Hafner, Probes in scanning microscopies, in: B. Bharat (Eds.), Handbook of Nanotechnology, Springer, Berlin, 2007, pp. 637-649.
[148] R. Lüthi, Meyer, M. Bammerlin, A. Baratoff, J. Lü, M. Guggisberg, H.J. Güntherodt, Resolution limits of force microscopy, in: D.R. Buddy and V.V. Tsukruk (Eds.), Scanning probe microscopy of polymers, American Chemical Society, 1998, pp. 300-311.
[149] R. García, J. Tamayo, A.S. Paulo, Phase contrast and surface energy hysteresis in tapping mode scanning force microsopy, Surf. Interface Anal., 27 (1999) 312-316.
[150] R.S. McLean, M. Doyle, B.B. Sauer, High-resolution imaging of ionic domains and crystal morphology in ionomers using AFM techniques, Macromolecules, 33 (2000) 6541-6550.
[151] B.B. Sauer, R.S. McLean, AFM and X-ray studies of crystal and ionic domain morphology in poly(ethylene-co-methacrylic acid) ionomers, Macromolecules, 33 (2000) 7939-7949.
[152] Z.W. Xu, Y.C. Liang, S. Dong, Y.Z. Cao, T.Q. Zhao, J.H. Wang, Q.L. Zhao, Phase contrast imaging of SEBS triblock copolymer studied by carbon nanotubes probe, Ultramicroscopy, 105 (2005) 72-78.
[153] S.N. Magonov, V. Elings, M.H. Whangbo, Phase imaging and stiffness in tapping-mode atomic force microscopy, Surf. Sci., 375 (1997) L385-L391.
[154] P.J. James, M. Antognozzi, J. Tamayo, T.J. McMaster, J.M. Newton, M.J. Miles, Interpretation of contrast in tapping mode AFM and shear force microscopy. A study of Nafion, Langmuir, 17 (2000) 349-360.

[155] B. Anczykowski, B. Gotsmann, H. Fuchs, J.P. Cleveland, V.B. Elings, How to measure energy dissipation in dynamic mode atomic force microscopy, Appl. Surf. Sci., 140 (1999) 376-382.
[156] J. Tamayo, R. García, Relationship between phase shift and energy dissipation in tapping-mode scanning force microscopy, Appl. Phys. Lett., 73 (1998) 2926-2928.
[157] B. Bhushan, J. Qi, Phase contrast imaging of nanocomposites and molecularly thick lubricant films in magnetic media, Nanotechnology, 14 (2003) 886.
[158] J.P. Cleveland, B. Anczykowski, A.E. Schmid, V.B. Elings, Energy dissipation in tapping-mode atomic force microscopy, Appl. Phys. Lett., 72 (1998) 2613.
[159] N.F. Martínez, R. García, Measuring phase shifts and energy dissipation with amplitude modulation atomic force microscopy, Nanotechnology, 17 (2006) S167-S172.
[160] I. Horcas, R. Fernandez, J.M. Gomez-Rodriguez, J. Colchero, J. Gomez-Herrero, A.M. Baro, WSXM: A software for scanning probe microscopy and a tool for nanotechnology, Rev. Sci. Instrum., 78 (2007) 013705-013713.
[161] L.E. Reichl, A Modern Course in Statistical Physics, third ed., Wiley-VCH, 2009.
[162] R. Garcia, A. San Paulo, Attractive and repulsive tip-sample interaction regimes in tapping-mode atomic force microscopy, Phys. Rev. B, 60 (1999) 4961.
[163] A.D. Dimarogonas, Vibration Engineering, West Publishing, New York, 1976.
[164] A.K. Fritzsche, A.R. Arevalo, M.D. Moore, V.B. Elings, K. Kjoller, C.M. Wu, The surface structure and morphology of polyvinylidene fluoride microfiltration membranes by atomic force microscopy, J. Membr. Sci., 68 (1992) 65-78.
[165] K.C. Khulbe, B. Kruczek, G. Chowdhury, S. Gagné, T. Matsuura, Surface morphology of homogeneous and asymmetric membranes made from poly(phenylene oxide) by tapping mode atomic force microscope, J. Appl. Polym. Sci., 59 (1996) 1151-1158.
[166] A. Hamza, G. Chowdhury, T. Matsuura, S. Sourirajan, Sulphonated poly(2,6-dimethyl-1,4-phenylene oxide)-polyethersulphone composite membranes. Effects of composition of solvent system, used for preparing casting solution, on membrane-surface structure and reverse-osmosis performance, J. Membr. Sci., 129 (1997) 55-64.
[167] E.M. Vrijenhoek, S. Hong, M. Elimelech, Influence of membrane surface properties on initial rate of colloidal fouling of reverse osmosis and nanofiltration membranes, J. Membr. Sci., 188 (2001) 115-128.
[168] K.C. Khulbe, T. Matsuura, G. Lamarche, H.J. Kim, The morphology characterisation and performance of dense PPO membranes for gas separation, J. Membr. Sci., 135 (1997) 211-223.
[169] J. Peltonen, M. Järn, S. Areva, M. Linden, J.B. Rosenholm, Topographical parameters for specifying a three-dimensional surface, Langmuir, 20 (2004) 9428-9431.
[170] M.R. Libera, R.F. Egerton, Advances in the transmission electron microscopy of polymers, Polym. Rev., 50 (2010) 321-339.
[171] A. Chapiro, Radiation Chemistry of Polymeric Systems, Plenum, New York, 1962.
[172] L.C. Sawyer, D.T. Grubb, G.F. Meyers, Polymer Microscopy, third ed., Springer, New York, 2007.
[173] G.H. Michler, Electron Microscopy of Polymers, third ed., Springer, Berlin, 2008.
[174] D.C. Martin, E.L. Thomas, Experimental high-resolution electron microscopy of polymers, Polymer, 36 (1995) 1743-1759.
[175] C.R. Bartels, K.L. Kreuz, A. Wachtel, Structure-performance relationships of composite membranes: Porous support densification, J. Membr. Sci., 32 (1987) 291-312.
[176] E.H. Andrews, J.M. Stubbs, A new freezing head for the ultramicrotomy of rubbers, J. R. Microsc. Soc., 82 (1964) 221-223.
[177] N.C. Watkins, D. Hansen, Morphology of melt-crystallized polyethyleneterephthalate, Text. Res. J., 38 (1968) 388-394.
[178] G.L. Christner, E.L. Thomas, Visualization of polymer interfaces by phase contrast (''defocus'') electron microscopy, J. Appl. Phys., 48 (1977) 4063.
[179] D.L. Handlin, E.L. Thomas, Visualization of ordered spherical microdomains of block copolymers by phase contrast electron microscopy, J. Mater. Sci. Lett., 3 (1984) 137-140.
[180] D.L. Handlin, E.L. Thomas, Phase contrast imaging of styrene-isoprene and styrene-butadiene block copolymers, Macromolecules, 16 (1983) 1514-1525.

[181] Y. Chen, Y. Chen, D. Yang, Crystallization and phase behavior of crystalline syndiotactic 1,2-polybutadiene/isotactic polypropylene blends in solution-cast thin films, Polymer, 47 (2006) 1667-1673.
[182] J. Petermann, H. Gleiter, Direct observation of amorphous and crystalline regions in polymers by defocus imaging, Philos. Mag., 31 (1975) 929 - 934.
[183] E.J. Roche, E.L. Thomas, Defocus electron microscopy of multiphase polymers: use and misuse, Polymer, 22 (1981) 333.
[184] Z.P. Luo, J.H. Koo, Quantification of the layer dispersion degree in polymer layered silicate nanocomposites by transmission electron microscopy, Polymer, 49 (2008) 1841-1852.
[185] E.L. Thomas, E.J. Roche, Critical evaluation of electron microscope evidence for order in glassy polymers, Polymer, 20 (1979) 1413.
[186] D.C. Martin, J. Chen, J. Yang, L.F. Drummy, C. Kübel, High resolution electron microscopy of ordered polymers and organic molecular crystals: Recent developments and future possibilities, J. Polym. Sci., Part B: Polym. Phys., 43 (2005) 1749-1778.
[187] T. Xue, J.S. Trent, K. Osseo-Asare, Characterization of Nafion membranes by transmission electron microscopy, J. Membr. Sci., 45 (1989) 261-271.
[188] F.A. Pacheco, I. Pinnau, M. Reinhard, J.O. Leckie. *Characterization of the nanostructure of isolated polyamide films of RO and NF membranes* in International Congress on Membranes and Membrane Processes. 2011, Amsterdam, The Netherlands.
[189] R.E. Kesting, A.K. Fritzsche, Polymeric gas separation membranes, Wiley Interscience, New York, 1993.
[190] A. Sousa, K.C. Souza, S.C. Reis, R.G. Sousa, D. Windmöller, J.C. Machado, E.M.B. Sousa, Positron annihilation study of pore size in ordered SBA-15, J. Non-Cryst. Solids, 354 (2008) 4800-4805.
[191] J.N. Sun, Y.F. Hu, W.E. Frieze, D.W. Gidley, Characterizing porosity in nanoporous thin films using positronium annihilation lifetime spectroscopy, Radiat. Phys. Chem., 68 (2003) 345-349.
[192] D.W. Gidley, H.-G. Peng, R.S. Vallery, Positron annihilation as a method to characterize porous materials, Annu. Rev. Mater. Res., 36 (2006) 49-79.
[193] R.A. Pethrick, Positron annihilation – A probe for nanoscale voids and free volume?, Prog. Polym. Sci. , 22 (1997) 1-47.
[194] C. Nagel, K. Günther-Schade, D. Fritsch, T. Strunskus, F. Faupel, Free volume and transport properties in highly selective polymer membranes, Macromolecules, 35 (2002) 2071-2077.
[195] K. Boussu, J. De Baerdemaeker, C. Dauwe, M. Weber, K.G. Lynn, D. Depla, S. Aldea, I.F.J. Vankelecom, Vandecasteele, B. van der Bruggen, Physico - chemical characterization of nanofiltration membranes, ChemPhysChem, 8 (2007) 370-379.
[196] S.J. Tao, Positronium annihilation in molecular substances, J. Chem. Phys. , 56 (1972) 5499-5510.
[197] M. Eldrup, D. Lightbody, J.N. Sherwood, The temperature dependence of positron lifetimes in solid pivalic acid, Chem. Phys., 63 (1981) 51-58.
[198] Y.C. Jean, P.E. Mallon, D.M. Schrader, Principles and Applications of Positron and Positronium Chemistry, World Scientific, Singapore, 2003.
[199] J. Algers, P. Sperr, W. Egger, G. Kögel, F.H.J. Maurer, Median implantation depth and implantation profile of 3–18 keV positrons in amorphous polymers, Phys. Rev. B, 67 (2003) 125404.
[200] J.I. Calvo, A. Bottino, G. Capannelli, A. Hernández, Comparison of liquid-liquid displacement porosimetry and scanning electron microscopy image analysis to characterise ultrafiltration track-etched membranes, J. Membr. Sci., 239 (2004) 189-197.
[201] H. Giesche, Mercury porosimetry: A general (practical) overview, Part. Part. Syst. Char., 23 (2006) 9-19.
[202] J.I. Calvo, A. Bottino, G. Capannelli, A. Hernández, Pore size distribution of ceramic UF membranes by liquid-liquid displacement porosimetry, J. Membr. Sci., 310 (2008) 531-538.
[203] W.R. Bowen, J.S. Welfoot, Modelling the performance of membrane nanofiltration--critical assessment and model development, Chem. Eng. Sci., 57 (2002) 1121-1137.

[204] W. Xu, P.M. Wood-Adams, C.G. Robertson, Measuring local viscoelastic properties of complex materials with tapping mode atomic force microscopy, Polymer, 47 (2006) 4798-4810.
[205] S.-H. Huang, W.-S. Hung, D.-J. Liaw, C.-L. Li, S.-T. Kao, D.-M. Wang, M.D. Guzman, C.-C. Hu, Y.C. Jean, K.-R. Lee, J.-Y. Lai, Investigation of multilayer pervaporation membrane by positron annihilation spectroscopy, Macromolecules, 41 (2008) 6438-6443.
[206] Image J - Image Processing and Analysis in Java, Open source software, http: //rsbweb.nih.gov/ij/, 2010.
[207] L. de Caro, E. Carlino, G. Caputo, P.D. Cozzoli, C. Giannini, Electron diffractive imaging of oxygen atoms in nanocrystals at sub-angstrom resolution, Nat. Nanotechnol., 5 (2010) 360-365.
[208] J.S. Hanker, F. Kasler, M.G. Bloom, J.S. Copeland, A.M. Seligman, Coordination polymers of osmium: the nature of osmium black, Science, 156 (1967) 1737-1738.
[209] A.-V. Ruzette, L. Leibler, Block copolymers in tomorrow's plastics, Nat. Mater., 4 (2005) 19-31.
[210] W.B. Russel, D.A. Saville, W.R. Schowalter, Colloidal Dispersions, Cambridge University Press, 1989.
[211] Chemical Engineering Research Information Center, *Pure Component Database*, Retrieved 11 Dec 2011.
[212] D.R. Lide, CRC Handbook of Chemistry and Physics: A ready-reference book of chemical and physical data, 73rd ed., CRC Press, 1992.
[213] C.M. Hansen, *Hansen solubility parameters a user's handbook [electronic resource]*, 2004, CRC Press.
[214] J.G. Speight, Perry's standard tables and formulas for chemical engineers, Mc Grow-Hill Companies, Inc., New York, 2003.
[215] M.K. Khayet, T. Matsuura, Membrane Distillation: Principles and Applications, Elsevier, Oxford, 2011.
[216] P.C. Yen, R.S. Chen, C.C. Chen, Y.S. Huang, K.K. Tiong, Growth and characterization of OsO2 single crystals, J. Cryst. Growth, 262 (2004) 271-276.
[217] C.-E. Boman, Precision determination of the crystal structure of osmium dioxide, Acta Chem. Scand., 24 (1970) 123-128.
[218] D.B. Williams, C.B. Carter, Transmission Electron Microscopy: A Textbook for Materials Science, Plenum Press, New York, 1996.
[219] R. Valadez-Blanco, A.G. Livingston, Solute molecular transport through polyimide asymmetric organic solvent nanofiltration (OSN) membranes and the effect of membrane-formation parameters on mass transfer, J. Membr. Sci., 326 (2009) 332-342.
[220] S. Karan, S. Samitsu, X. Peng, K. Kurashima, I. Ichinose, Ultrafast viscous permeation of organic solvents through diamond-like carbon nanosheets, Science, 335 (2012) 444-447.
[221] P. Silva, S. Han, A.G. Livingston, Solvent transport in organic solvent nanofiltration membranes, J. Membr. Sci., 262 (2005) 49-59.
[222] B. Van der Bruggen, J. Schaep, D. Wilms, C. Vandecasteele, Influence of molecular size, polarity and charge on the retention of organic molecules by nanofiltration, J. Membr. Sci., 156 (1999) 29-41.
[223] J. Israelachvili, P. McGuiggan, M. Gee, A. Homola, M. Robbins, P. Thompson, Liquid dynamics in molecularly thin films, J. Phys.: Condens. Matter 2(1990) SA89 - SA98.
[224] H.J. Zwijnenberg, S.M. Dutczak, M.E. Boerrigter, M.A. Hempenius, M.W.J. Luiten-Olieman, N.E. Benes, M. Wessling, D. Stamatialis, Important factors influencing molecular weight cut-off determination of membranes in organic solvents, J. Membr. Sci., 390-391 (2012) 211-217.
[225] A. Volkov, V. Volkov, V. Khotimskii, Membranes based on poly[(1-trimethylsilyl)-1-propyne] for liquid-liquid separation, Polym. Sci. Ser. A, 51 (2009) 1367-1382.
[226] Y.S. Kang, E.M. Shin, B. Jung, J.-J. Kim, Composite membranes of poly(1-trimethylsilyl-1-propyne) and poly(dimethyl siloxane) and their pervaporation properties for ethanol–water mixture, J. Appl. Polym. Sci., 53 (1994) 317-323.
[227] L.G. Peeva, E. Gibbins, S.S. Luthra, L.S. White, R.P. Stateva, A.G. Livingston, Effect of concentration polarisation and osmotic pressure on flux in organic solvent nanofiltration, J. Membr. Sci., 236 (2004) 121-136.

[228] I. Koyuncu, Reactive dye removal in dye/salt mixtures by nanofiltration membranes containing vinylsulphone dyes: effects of feed concentration and cross flow velocity, Desalination, 143 (2002) 243-253.
[229] E. Drioli, F. Laganà, A. Criscuoli, G. Barbieri, Integrated membrane operations in desalination processes, Desalination, 122 (1999) 141-145.
[230] V. Freger, Kinetics of film formation by interfacial polycondensation, Langmuir, 21 (2005) 1884-1894.
[231] V. Freger, Swelling and morphology of the skin layer of polyamide composite membranes: An atomic force microscopy study, Environ. Sci. Technol., 38 (2004) 3168-3175.
[232] S. Bason, Y. Oren, V. Freger, Ion transport in the polyamide layer of RO membranes: Composite membranes and free-standing films, J. Membr. Sci., 367 (2011) 119-126.
[233] J. Stawikowska, A.G. Livingston, Nanoprobe imaging molecular scale pores in polymeric membranes, J. Membr. Sci., 413-414 (2012) 1-16.
[234] S.H. Kim, S.-Y. Kwak, T. Suzuki, Positron annihilation spectroscopic evidence to demonstrate the flux-enhancement mechanism in morphology-controlled thin-film-composite (TFC) membrane, Environ. Sci. Technol., 39 (2005) 1764-1770.
[235] A.V. Volkov, D.F. Stamatialis, V.S. Khotimsky, V.V. Volkov, M. Wessling, N.A. Platé, Poly[1-(trimethylsilyl)-1-propyne] as a solvent resistance nanofiltration membrane material, J. Membr. Sci., 281 (2006) 351-357.
[236] D. Bhanushali, S. Kloos, D. Bhattacharyya, Solute transport in solvent-resistant nanofiltration membranes for non-aqueous systems: experimental results and the role of solute-solvent coupling, J. Membr. Sci., 208 (2002) 343-359.
[237] P.S. Singh, A.P. Rao, P. Ray, A. Bhattacharya, K. Singh, N.K. Saha, A.V.R. Reddy, Techniques for characterization of polyamide thin film composite membranes, Desalination, 282 (2011) 78-86.
[238] C. Gackenheimer, L. Cayon, R. Reifenberger, Analysis of scanning probe microscope images using wavelets, Ultramicroscopy, 106 (2006) 389-397.
[239] A.J. Reuvers, J.W.A. van den Berg, C.A. Smolders, Formation of membranes by means of immersion precipitation : Part I. A model to describe mass transfer during immersion precipitation, J. Membr. Sci., 34 (1987) 45-65.
[240] A.J. Reuvers, C.A. Smolders, Formation of membranes by means of immersion precipitation : Part II. the mechanism of formation of membranes prepared from the system cellulose acetate-acetone-water, J. Membr. Sci., 34 (1987) 67-86.
[241] R. García, R. Pérez, Dynamic atomic force microscopy methods, Surf. Sci. Rep., 47 (2002) 197-301.
[242] F.Z. Fang, Z.W. Xu, S. Dong, Study on phase images of a carbon nanotube probe in atomic force microscopy, Meas. Sci. Technol., 19 (2008) 055501.
[243] S.D. Solares, M.J. Esplandiu, W.A. Goddard, C.P. Collier, Mechanisms of single-walled carbon nanotube probe−sample multistability in tapping mode AFM imaging, J. Phys. Chem. B, 109 (2005) 11493-11500.
[244] S. Cheng, D.L. Oatley, P.M. Williams, C.J. Wright, Positively charged nanofiltration membranes: Review of current fabrication methods and introduction of a novel approach, Adv. Colloid Interface Sci., 164 (2011) 12-20.